MODELLING AND FAULT RIDE-THROUGH CONTROL OF GRID SUPPORTING INVERTER-BASED MICROGRID

by

ELUTUNJI BURAIMOH

M.Sc. and B.Tech. (Hons): Electronic and Electrical Engineering

Thesis submitted in the fulfilment of the requirements of the degree of

Doctor of Engineering in Electrical Engineering

in the Faculty of Engineering and the Built Environment

at the Durban University of Technology

Supervisor: Professor I. E. Davidson

January 2021

ABSTRACT

This thesis is focused on modeling and fault ride-through control, local load power delivery, and grid power exchange of power electronic interfaced Distributed Energy Resources (DERs) for grid supporting microgrids. Active and reactive power regulations are the requirements for a grid-supporting system operating as a current source, while frequency and voltage magnitude regulation in the grid-supporting system acting as a voltage source. Consequently, these are put into consideration as the primary control requirements for the inverter-based microgrid. To that end, two discrete-time models of a grid-feeding system and grid-forming system were developed to serve as controls for a single DER operating in grid-connected mode and islanded mode, respectively. Consequently, for the first set of mathematical models: grid feeding and grid forming were interfaced with a droop control to allow for parallel operation of additional DERs for power coordination within the microgrid for grid-connected and islanded operation. However, virtual impedance was incorporated into the grid-supporting system's droop control operating as a voltage source to emulate the link feeder's physical impedance to the main grid. Based on the developed grid supporting models, the microgrid primary control schemes effectively delivered power to the host grid and simultaneously contributed to the grid's frequency and voltage regulation. Furthermore, to ensure grid code compliance and ensure the microgrid provides ancillary services to the host grid, such as fault ride-through and reactive power compensation for voltage recovery, a novel technique is proposed in the microgrid's secondary control. The secondary control realizes the fault ride-through for the grid supporting system using a delay signal cancellation algorithm for negative sequence detection. The proposed control scheme actualizes grid code requirements by providing a secondary voltage control, which is active and more prominent in the transient period of faults without mode switching. The strategy's performance is further enhanced with an IGBT-Diodes switched AC reactor to improve the voltage and prevent the transient overcurrent in the microgrid during the grid fault. This ensures a continued supply of the microgrid's local sensitive load while meeting the grid code requirement. Similarly, the active power injection into the main grid is limited to maximize reactive power injection into the main network to support the grid voltage sag. The detection algorithm using the delayed signal cancellation algorithm is implemented to detect the instance of fault in 1.6% of the half-cycle under grid disturbance/fault to activate the proposed secondary control. This effectiveness and fault ride-through compliance of the developed control models were tested on an inverter-based microgrid system with an ideal voltage source DERs. Finally, to accommodate for the grid dynamics introduced to the DC link parameters of an ideal voltage source DER such as PV, the models were also implemented and assimilated for a solar PV sourced DER used with a grid supporting inverter-based microgrid. The injection of active power into the main grid is constrained by systematically shifting the MPPT operating point based on voltage

sag depth to maximize reactive power injection to support the grid voltage sag. The strategy developed in the PV sourced system also ensured that the DC-link voltage and AC grid current raises are suppressed while meeting microgrid load requirements. The models' implementation, DER primary control, and proposed secondary control schemes are established through detailed time-domain simulation studies using MATLAB Simscape Electrical™ and Control System™.

LIST OF PUBLICATIONS

The following publications emanate from this doctoral thesis.

E. Buraimoh, I. E. Davidson, and F. Martinez-Rodrigo. "Fault Ride-Through Enhancement of Grid Supporting Inverter-Based Microgrid Using Delayed Signal Cancellation Algorithm Secondary Control." Energies 12, no. 20 ,**2019**: 3994. [1].

E. Buraimoh and I. E. Davidson. "Fault Ride-Through Analysis of Current and Voltage Source-Models of Grid Supporting Inverter-Based Microgrid." published in the IEEE Canadian Journal of Electrical and Computer Engineering/Journal canadien de genie electrique et informatique ,**2020** 10.1109/CJECE.2020.3035036. [2]

E. Buraimoh and I. E. Davidson. "Investigation of the Low Voltage Ride-Through of Inverter Using Virtual Inertia Methods in Microgrid." International Journal of Engineering Research in Africa. Vol. 44. Trans Tech Publications Ltd, **2019**. [3].

E. Buraimoh F. K. Ariyo, M. O. Omoigui, and I. E. Davidson. "Investigation of Combined SVC and TCSC versus IPFC in Enhancing Power System Static Security." International Journal of Engineering Research in Africa, vol. 40, pp. 119-135. Trans Tech Publications, **2018**. [4]

E. Buraimoh and I. E. Davidson. "Modelling and Assessment of the Fault Ride-Through Capabilities of Grid Supporting Inverter-Based Microgrids" In 2020 Clemson University Power Systems Conference, South Carolina, USA, 10 - 13 Mar **2020**. [5].

E. Buraimoh and I. E. Davidson. "Modelling and Analysis of Standalone Inverter-Based Microgrids with Grid Supporting Voltage-Source Control under Changing Load" In 2020 In Proceeding of the IEEE PES/IAS PowerAfrica, Nairobi, Kenya, 20–23 August **2020**. [6]

E. Buraimoh and I. E. Davidson. "Overview of Fault Ride-Through Requirements for Photovoltaic Grid Integration, Design and Grid Code Compliance" In 2020 In Proceeding of 9th International Conference on Renewable Energy Research and Applications, Glasgow, United Kingdom 27-30 September **2020**.

E. Buraimoh and I. E. Davidson. "Comparative Analysis of the Fault Ride-Through Capabilities of the VSG Methods of Microgrid Inverter Control under Faults." In 2019 Southern African Universities Power Engineering Conference/Robotics and Mechatronics/Pattern Recognition Association of South Africa (SAUPEC/RobMech/PRASA), pp. 400-405. IEEE, Bloemfontein, South Africa. **2019**. [7].

E. Buraimoh and I. E. Davidson. "Development of an IGBT-Diode based Fault Current Limiter for Fault Ride-Through Enhancement in Microgrid Application". In Proceedings of the IEEE PES/IAS PowerAfrica, Abuja, Nigeria, 20–23 August **2019**. [8].

E. Buraimoh, F. K. Ariyo, and I. E. Davidson. "Power System Static Security Enhancement Through Interline Power Flow Controller." In 2018 IEEE PES/IAS PowerAfrica, pp. 330-335. IEEE, Cape Town, South Africa. **2018**. [9].

E. Buraimoh and I. E. Davidson. " Delayed Signal Cancellation Technique for Fault Ride-Through Control of a Grid-Supporting PV Inverter Microgrid," IEEE Access Journal, [submitted].

E. Buraimoh, I. E. Davidson, and F. Martinez-Rodrigo. " Decentralized Fast Delayed Signal Cancellation Secondary Control for Low Voltage Ride-Through Application in Grid Supporting Grid Feeding Microgrid.," Smart Grids Section of Frontiers in Energy Research [submitted].

DECLARATION

I hereby declare that this thesis is the candidate's original work; every cited or text has been appropriately referenced and has not been previously submitted in part or totality for another degree in this or any other University

Submitted by

_____ _____

E. Buraimoh Date

Student Number: 21854419

Approved for submission by

_____ _____

Supervisor: Professor I. E. Davidson Date

DEDICATION

This doctoral thesis is dedicated to family, mentors, friends, colleagues, teachers, and students who sacrificed their time and comfort, resources, freedom, social life, emotion, relationships, career, food, and desires for me.

ACKNOWLEDGEMENTS

"Let them give thanks to the LORD JESUS for his unfailing love and his wonderful deeds for mankind, for he satisfies the thirsty and fills the hungry with good things." –Psalm 107:8-9. I am grateful for the opportunity to complete another milestone. I express my sincere gratitude to Prof Innocent Ewean Davidson, my thesis supervisor and incredible mentor, for the tremendous support, mentorship, intuitive debates, endless inspiration, sponsorship, and enduring directives. The financial supports provided by the Research and Postgraduate Support Directorate and Prof I. E Davidson are much valued. I acknowledge the valuable suggestions, insights, and critical reviews provided by the anonymous external examiners and article reviewers to improve the quality of the thesis presentation.

My deepest gratitude to the International Education and Partnerships directorate and Erasmus + KA107 Project for the valuable opportunity that gave me the chance of the five-month-visiting research exchange program at the University of Valladolid, Spain. I cannot but thank Prof Fernando Martinez-Rodrigo, who served as my research host in Spain, for his scientific insights on my doctoral research. Sincere thanks are also expressed to Prof Santiago de Pablo and all his DEEPER research group members for graciously sharing the research information, support, and several useful recommendations.

Furthermore, I appreciate Dr. Funso Ariyo and my fellow Ph.D. students Abayomi Adebiyi and Jeremiah Adedeji for their necessary supports and assistance. Special thanks to all Smart Grid research center members, including Milna Joshi, Christophe Moma, Sindi Malanda, for words of encouragement and meaningful discussions regarding our various research investigations. Many thanks to the departmental secretary Mrs. Regina Naidoo and the Electrical Power Engineering Department's academic staff for a lovely atmosphere.

Lastly, I want to specially appreciate my parents Mr. Raimi Adetoye Buraimo and Mrs. Eunice Olusade Buraimo, my siblings Tope Kayode, Wumi Petrus-Nihi, Bimbo Oladeji, and Tunde Buraimo and their families for all their unqualified affection and love, patience, and words of inspiration.

LIST OF ABBREVIATIONS

AC	Alternating Current
AGC	Automatic Gain Control
AS/NZS	Australian/New Zealand Standard
DC	Direct Current
DER	Distributed Energy Resources
DG	Distributed Generators
dq	Direct-Quadrature
dq0	Park transform
DSC	Delayed Signal Cancellation
DVR	Dynamic Voltage Restorer
EPRI	Electric Power Research Institute
ESS	Energy Storage Systems
FACTS	Flexible Alternating Current Transmission System
FCL	Fault Current Limiter
FRT	Fault Ride-Through
f-V	Frequency-Voltage
HV	High Voltage
HVRT	High Voltage Ride-Through
IEC	International Electrotechnical Commission
IEEE	Institute of Electrical and Electronics Engineers
IGBT	Insulated-Gate Bipolar Transistor
IPP	Independent Power Producers
ISC	Short-Circuit Current
I-V	Current-Voltage
kVA	kilo Volt Ampere
kVAR	kilo Volt Ampere Reactive
kW	kilowatt
LPF	Low Pass Filter
LV	Low Voltage
LVRT	Low Voltage Ride-Through
MATLAB	Matrix Laboratory
MG	Microgrid
MPP	Maximum Power Point
MPPT	Maximum Power Point Tracking
MV	Medium Voltage

MW	Megawatt
NEMA	National Equipment Manufacturer Association in the United States of America
P&O	Perturbation and Observation
PCC	Point of Common Coupling
PF	Power Factor
PI	Proportional-Integral
PID	Proportional-Integral-Derivative
PLL	Phase Lock Loop
PMSG	Permanent Magnet Synchronous Generator
P–Q	Active-Power
Pu	Per Unit
PV	Photovoltaic
P-V	Power-Voltage
PWM	Pulse Width Modulation
P-ω	Active Power-Frequency
Q-E	Reactive Power-Volatge
R/X	Resistance to Impedance Ratio
RCC	Ripple Correlation Control
REE	Red Eléctrica de España
RES	Renewable Energy Sources
RMS	Root Mean Square
RPP	Renewable Power Plant
SAREGC	South African Renewable Energy Grid Code
SDBR	Series Dynamic Braking-Resistor
SSSC	Static Synchronous Series Compensator
STATCOM	Static Synchronous Compensator
SVC	Static VAR Compensator
TCSC	Thyristor Controlled Series Compensator
THD	Total Harmonic Distortion
UPQC	Unified Power Quality Conditioner
VOC	Open-Circuit Voltage
VSI	Voltage Source Inverter
WT	Wind Turbine
$\alpha\beta 0$	Clark transform

TABLE OF CONTENTS

ABSTRACT ii
LIST OF PUBLICATIONS iv
DECLARATION vi
DEDICATION vii
ACKNOWLEDGEMENTS viii
LIST OF ABBREVIATIONS ix
TABLE OF CONTENTS xi
LIST OF FIGURES xv
LIST OF TABLES xix
CHAPTER ONE 1
INTRODUCTION 1
1.1 Introduction to Microgrids 1
1.2 Study Background 3
1.3 Statement of Research Problem 6
1.4 Motivation for the Research 7
1.5 Aim and Objectives of the Research 8
1.5.1 Aim of the Research 8
1.5.2 Objectives of the Research 8
1.6 Scope of the Research 9
1.7 Research Contribution to knowledge 10
1.8 Organization of the Thesis 11
1.9 Publications 12
1.9.1 Journals 12
1.9.2 Conferences 12
CHAPTER TWO 13
LITERATURE REVIEW 13
2.1 Introduction 13
2.2 Microgrid Structure 13
2.2.1 Distributed Generation or Generators 14
2.2.2 Energy Storage Systems 15
2.2.3 Load 15
2.3 Microgrid Power Converters 15
2.4 Microgrid Operation Modes 17
2.4.1 Grid-Connected Mode 17
2.4.2 Island Mode 17
2.5 Hierarchical Control Structure 18

2.5.1 Primary Control Level 19
2.5.2 Secondary Control Level 19
2.5.3 Tertiary Control Level 20
2.6 Grid Integration of PV Energy System 21
2.6.1 Central Inverters 22
2.6.2 Module Inverters 22
2.6.3 Multi-String Inverter 22
2.7 Modelling of PV Arrays 23
2. 8 Maximum Power Point Tracking Control Algorithm 23
2.8.1 Perturbation and Observation 24
2.8.2 Hill Climbing 25
2.8.3 Incremental conductance 25
2.8.4 Conclusion on MPPT algorithms 27
2.9 Fault Ride-Through Requirement 27
2.10 The Fault Ride-Through Requirements and Ancillary Services. 28
2.10.1 Low Voltage and High Voltage Ride-Through 28
2.10.2 PV Generation FRT 29
2.11 Fault Ride-Through Enhancement 29
2.11.1 FRT Enhancement Strategies 29
2.11.2 Fault and Voltage Sag Detection 35
CHAPTER THREE 45
INVERTER-BASED MICROGRID DISCRETE-TIME MODEL 45
3.1 Introduction 45
3.2 Inverter Based Microgrid Control 45
3.2.1 Grid-Forming Inverter-Based Microgrid Topology 46
3.2.2 Grid-Feeding Inverter-Based Microgrid Topology 46
3.2.3 Grid-Supporting Inverter-Based Microgrid Models 47
3.3 Grid Synchronization and Control Model Simulation 48
3.3.1 Phase-Locked Loop 48
3.4 Control Simulation 52
3.4.1 Grid Forming Control Simulation 53
3.4.2 Grid Feeding Control Simulation 57
3.4.3 Grid Supporting Control Simulation 61
3.5 Control Response Validation 67
3.6 Conclusion 70
CHAPTER FOUR 71
INVERTER-BASED MICROGRID WITH PV DISCRETE-TIME MODEL 71

4.1 Introduction 71
4.2 Solar PV System Overview 71
4.3 Double Converter Modelling 72
4.3.1 DC-DC Conversion Phase and MPPT Control 72
4.3.2 DC-AC Inverter and Modified Grid-Supporting Control 75
4.4 Grid Supporting Control 78
4.5 System Simulation 81
4.6 Conclusion 88
CHAPTER FIVE 89
FAULT RIDE-THROUGH USING SECONDARY MICROGRID CONTROL 89
5.1 Introduction 89
5.2 Delayed Signal Cancellation Algorithm 90
5.3 Power Flow and Switched Reactor 99
5.3.1 Voltage Source Inverter and Grid Interactive Power Flow 99
5.3.2 Switched Inductance: Sizing and Switching 99
5.4 Reactive Power Referencing 104
5.5 Active Power Referencing and Fault Current Limitation 107
5.5.1 Inverter-Based Microgrid 107
5.5.2 Inverter-Based Microgrid with DC-DC Converter 108
5.6 Conclusion 112
CHAPTER SIX 115
FRT CONTROL IMPLEMENTATION IN INVERTER-BASED MICROGRID 115
6.1 Introduction 115
6.1.1 Model Parameters 115
6.1.2 Model Validation 117
6.2. Symmetrical Fault 118
6.2.1 Voltage 118
6.2.2 Current 120
6.2.3 Current and Voltage Harmonics 122
6.2.4 Power Generation and Load Delivery 123
6.3 Asymmetrical Fault 134
6.4 Conclusion 142
CHAPTER SEVEN 143
FRT CONTROL IMPLEMENTATION IN INVERTER-BASED MICROGRID WITH PV 143
7.1 Introduction 143
7.2. Fault 144
7.2.1 DC Side Analysis 144

7.2.2 Grid AC Side Analysis 152
7.3. Conclusion 164
CHAPTER EIGHT 166
CONCLUSION AND RECOMMENDATION 166
8.1 Conclusion 166
8.2 Recommendations and Future Works 168
REFERENCES 169
APPENDIX A: COUNTRIES' GRID CODE FAULT RIDE-THROUGH REQUIREMENT 187
A.1 Fault Ride-Through in Countries 187
A.2 High Voltage Ride-Through in Countries 191
A.3 Dynamic Grid Voltage Support in Countries 192
A.4 Spanish FRT Grid Code Requirements and specifics 193
A.5 Fault Ride-Through Requirements and Ancillary Services 194
A.6 Low Voltage and High Voltage Ride-Through 195
APPENDIX B: EXTRA EQUATIONS 196
B.1 Phase-Locked Loop Basic Model Equation 196
B.2 Phase-Locked Loop small-signal model 196

LIST OF FIGURES

Figure 1. 1: General structure of the microgrid 2
Figure 1. 2: The general structure of an inverter-based microgrid (a) PV inverter-based microgrid (b) WT inverter-based microgrid 2
Figure 1. 3: FRT/LVRT curves defined by Spanish, Danish, Chinese grid code [28] 4
Figure 1. 4: Spain and Denmark reactive power requirement under FRT operation mode 6
Figure 2. 1:Microgrid structure 14
Figure 2. 2:Microgrid hierarchical control structure 18
Figure 2. 3:Tertiary and secondary control block diagram 20
Figure 2. 4:I-V and P-V characteristics of the PV 24
Figure 2. 5:Basic perturbation and observation algorithm 24
Figure 2. 6:Incremental conductance algorithm 26
Figure 2. 7:FRT capability enhancement methods 30
Figure 2. 8:ESS strategy for FRT Enhancement of Inverter-Based System 31
Figure 2. 9:Brake chopper protection for FRT Enhancement of Inverter-Based System 31
Figure 2. 10:FRT enhancement with shunt connection of STATCOM 33
Figure 2. 11:FRT enhancement with shunt connection of SVC 33
Figure 2. 12:FRT enhancement with a series connection of FCL-FRT enhancement with a series connection of FCL 34
Figure 2. 13:The moving window's RMS voltage evaluation 39
Figure 2. 14:peak Voltage measurement sag detection method 40
Figure 2. 15: Synchronous Rotating Reference Frame Technique 40
Figure 2. 16:Phase shifting in a single-phase system 41
Figure 2. 17:Fast Fourier Transform Technique 42

Figure 3. 1: Schematics of the grid-forming inverter-based microgrid. 46
Figure 3. 2: Schematics of grid-feeding inverter-based microgrid 46
Figure 3. 3: Schematics of grid-supporting grid-feeding inverter-based microgrid 47
Figure 3. 4: Schematics of grid-supporting grid-forming inverter-based microgrid 48
Figure 3. 5: Block diagram of the Phase Lock Loop. 49
Figure 3. 6: Reference frame transformations 49
Figure 3.7: Grid-forming control structure model 54
Figure 3. 8: Voltage loop responses indicating current references i^*_d and i^*_q in grid forming .. 55
Figure 3. 9: Current loop responses and new voltage references u^*_d and u^*_q in grid forming ... 55
Figure 3. 10: Three-phase voltage and current of grid forming controlled microgrid 56
Figure 3. 11: Active and reactive power grid forming controlled microgrid 56
Figure 3. 12: Frequency of grid forming controlled microgrid 57
Figure 3. 13: Grid-feeding control structure model 58
Figure 3. 14: Power loop responses indicating current references direct-axis current i^*_d and quadrature-axis current i^*_q in grid feeding. 59
Figure 3. 15: Instantaneous active power P and reactive power Q in the grid feeding 59
Figure 3. 16: Current loop responses indicating new voltage references (u_d and u_q) in grid feeding 60
Figure 3. 17: Three-phase voltage and current of grid forming controlled microgrid 61
Figure 3. 18: Three-phase grid-supporting grid-feeding inverter-based microgrid control model operating as a current source 62
Figure 3. 19: Three-phase grid-supporting grid-forming inverter-based microgrid control model operating as a voltage source 62
Figure 3. 20: Virtual Impedance Model 64
Figure 3. 21: Root-mean-square voltages in the two grid supporting systems 66

Figure 3. 22: Active powers of the two grid supporting systems. 66
Figure 3. 23: Reactive powers of the two grid supporting systems. 66
Figure 3. 24: Angular frequencies of the two grid supporting systems. 67
Figure 3. 25:Reference and resultant active power in the grid feeding and grid supporting grid feeding systems 68
Figure 3. 26:Reference and resultant reactive power in the grid feeding and grid supporting grid feeding systems 68
Figure 3. 27:Reference and resultant active power in the grid forming and grid supporting grid forming systems 68
Figure 3. 28:Reference and resultant reactive power in the grid forming and grid supporting grid forming systems 69
Figure 3. 29:State variables for current source discrete-time state-space 69
Figure 3. 30:State variables for voltage source discrete-time state-space. 70

Figure 4. 1: Control structures of an inverter i DC-DC converter 72
Figure 4. 2: DC-DC converter schematic controlling a PV system 73
Figure 4. 3: Feedback loop model PV voltage control 75
Figure 4. 4: Modelling of the DC-link voltage loop applying power balance equation 77
Figure 4. 5:Incorporated Grid Supporting Control with Droop with DC-DC Converter 80
Figure 4. 6:The d-q current reference 82
Figure 4. 7: The d-q voltage reference 83
Figure 4. 8: Duty ratio d 83
Figure 4. 9: Voltage at the DC link and the PV terminals 84
Figure 4. 10: MPPT instant conductance V/I, incremental conductance, MPPT Error 84
Figure 4. 11: Generated P* reference, Calculated DC Power and AC Power Output 85
Figure 4. 12: PV Current, DC current and PV Diode Current 85
Figure 4. 13: Main grid Three-phase voltage waveforms 86
Figure 4. 14: Microgrid PCC Three-phase voltage waveforms 86
Figure 4. 15: AC output voltage waveform THD 87

Figure 5. 1: Proposed FRT control scheme 91
Figure 5. 2: Delayed Signal Cancellation Demonstration 93
Figure 5. 3: DSC sag detection compared to FFT, SRRF, PEAK and RMS methods 96
Figure 5. 4: DSC sag detection compared to FFT, SRRF, PEAK, and RMS at fault inception . 97
Figure 5. 5: DSC sag detection compared to FFT, SRRF, PEAK, and RMS at fault clearance . 97
Figure 5. 6: Power flow diagram between the inverter and the host grid 99
Figure 5. 7: Phasor illustrations for (a) maximum local load demand (b) no-load demand..... 100
Figure 5. 8: Grid voltage at inception and clearance of fault 102
Figure 5. 9: Pulses generated in all line 1 of the three-phase 103
Figure 5. 10: Pulses generated in all line 2 of the three-phase 103
Figure 5. 11: Pulses generated in all line 3 of the three-phase. 104
Figure 5. 12: Reactive power limit of inverter-based microgrid 106
Figure 5. 13:P−V curve for FRT and MPPT operations 109
Figure 5. 14: FRT operation control structure 111

Figure 6. 1: The topology of the MG examined 116
Figure 6. 2:Voltages in the grid and microgrid at grid voltage sag of 50% 118
Figure 6. 3:Voltages in the grid and microgrid at grid voltage sag of 60% 119
Figure 6. 4:Voltages in the grid and microgrid at grid voltage sag of 70% 119
Figure 6. 5:Current waveforms in the microgrid at grid voltage sag of 50% 121
Figure 6. 6:Current waveforms in the microgrid at grid voltage sag of 60% 121

Figure 6. 7:Current waveforms in the microgrid at grid voltage sag of 70%..... 122
Figure 6. 8:THD of voltage waveforms of the microgrid under 50% voltage sag..... 123
Figure 6. 9:THD of voltage waveforms of the microgrid under 60% voltage sag..... 123
Figure 6. 10:THD of voltage waveforms of the microgrid under 70% voltage sag..... 123
Figure 6. 11: Active power supplied by DER 1 under voltage sag of 50% 125
Figure 6. 12: Active power supplied by DER 2 under voltage sag of 50% 126
Figure 6. 13: Reactive power supplied by DER 1 under voltage sag of 50% 127
Figure 6. 14: Reactive Power supplied by DER 2 under voltage sag of 50%..... 129
Figure 6. 15: Active power supplied by DER 1 under voltage sag of 60% 130
Figure 6. 16: Active power supplied by DER 2 under voltage sag of 60% 130
Figure 6. 17: Active power supplied by DER 1 under voltage sag of 70% 131
Figure 6. 18: Active power supplied by DER 2 under voltage sag of 70% 131
Figure 6. 19: Reactive power supplied by DER 1 under voltage sag of 60%..... 131
Figure 6. 20: Reactive power supplied by DER 2 under voltage sag of 60%..... 132
Figure 6. 21: Reactive power supplied by DER 1 under voltage sag of 70%..... 132
Figure 6. 22: Reactive power supplied by DER 2 under voltage sag of 70%..... 132
Figure 6. 23: Active Power supply to local microgrid load under voltage sags..... 133
Figure 6. 24: Reactive Power supply to local microgrid load under voltage sags 133
Figure 6. 25:Grid and Microgrid voltages under L-G fault on the main grid 135
Figure 6. 26:Grid and Microgrid voltages under L-L-G fault on the main grid..... 135
Figure 6. 27:Grid and Microgrid voltages under L-L fault on the main grid..... 136
Figure 6. 28:Grid and microgrid current under L-G fault on the main grid..... 137
Figure 6. 29:Grid and microgrid current under L-L-G fault on the main grid..... 138
Figure 6. 30:Grid and microgrid current under L-L fault on the main grid 138
Figure 6. 31:Power supplied by DER 1 under L-G fault 139
Figure 6. 32:Power supplied by DER 2 under L-L-G fault..... 139
Figure 6. 33:Power supplied by DER 1 under L-L fault..... 139
Figure 6. 34:Power supplied by and DER 2 under L-L fault..... 140
Figure 6. 35:Power supplied to the local microgrid load under L-G fault..... 141
Figure 6. 36:Power supplied to the local microgrid load under L-L-G fault 141

Figure 7. 1:The examined topology of the double stage PV system used to form a microgrid with a local load..... 144
Figure 7. 2:PV voltage under 50% grid voltage sag 145
Figure 7. 3:DC link voltage under 50% grid voltage sag..... 145
Figure 7. 4:Average DC link current under 50% grid voltage sag..... 146
Figure 7. 5:PV voltage under 60% grid voltage sag 147
Figure 7. 6:DC link voltage under 60% grid voltage sag..... 147
Figure 7. 7:Average DC link current under 60% grid voltage sag..... 147
Figure 7. 8:PV voltage under 70% grid voltage sag 149
Figure 7. 9:DC link voltage under 70% grid voltage sag..... 149
Figure 7. 10:Average DC link current under 70% grid voltage sag..... 149
Figure 7. 11:Voltages in the grid and microgrid at grid voltage sag of 50% 152
Figure 7. 12:Voltages in the grid and microgrid at grid voltage sag of 60% 153
Figure 7. 13:Voltages in the grid and microgrid at grid voltage sag of 70% 153
Figure 7. 14:Current at the PCC 50% voltage sag 154
Figure 7. 15:Current at the PCC 60% voltage sag 155
Figure 7. 16:Current at the PCC 70% voltage sag 155
Figure 7. 17:THD at 50 % voltage sag with secondary control 156
Figure 7. 18:THD at 60 % voltage sag with secondary control 157
Figure 7. 19:Active Power supplied by PV under voltage sag of 50%..... 158

Figure 7. 20:Reactive Power supplied by PV under voltage sag of 50%..... 158
Figure 7. 21:Active Power supplied by PV under voltage sag of 60%..... 158
Figure 7. 22:Reactive Power supplied by PV under voltage sag of 60%..... 159
Figure 7. 23:Active Power supplied by PV under voltage sag of 70%..... 159
Figure 7. 24:Reactive Power supplied by PV under voltage sag of 70%..... 159
Figure 7. 25: Active power supply to local microgrid load under voltage sag of 50%..... 161
Figure 7. 26: Reactive power supply to local microgrid load under voltage sag of 50% 162
Figure 7. 27:Active power supply to local microgrid load under voltage sag of 60%..... 162
Figure 7. 28: Reactive power supply to local microgrid load under voltage sag of 60% 162
Figure 7. 29:Active power supply to local microgrid load under voltage sag of 70%..... 163
Figure 7. 30: Reactive power supply to local microgrid load under voltage sag of 70% 163
Figure 7. 31; The seamless switching operation based on P-V characteristics..... 164

LIST OF TABLES

Table 3. 1:Grid Implementation Parameters 52
Table 3. 2: PCC Transformer Parameters. 53
Table 3. 3:Grid Synchronization Parameters. 53

Table 4. 1: PV Simulation Parameters 81
Table 4. 2: PV Simulation Parameters 81
Table 4. 3: DC-DC Converter electrical parameters 82
Table 4. 4: MPPT and DC-DC converter control parameters 82
Table 4. 5: Eigenvalues of the developed model 87

Table 6. 1: Inverter electrical parameters 116
Table 6. 2: Inverter primary and secondary control parameters 117
Table 6. 3: Grid synchronization and parameters 117
Table 6. 4: Switched IGBT-diode inductance parameters 117
Table 6. 5: DER 1 Active Power P at Fault Inception under 50% voltage sag 125
Table 6. 6: DER 1 Active Power P at Fault Clearance under 50% voltage sag 126
Table 6. 7:DER 2 Active Power P at Fault Inception under 50% voltage sag 126
Table 6. 8:DER 2 Active Power P at Fault Clearance under 50% voltage sag 127
Table 6. 9: DER 1 Reactive Power Q at Fault Inception under 50% voltage sag 128
Table 6. 10:DER 2 Active Power P at Fault Clearance under 50% voltage sag 128
Table 6. 11:DER 2 Reactive Power Q at Fault Inception under 50% voltage sag 129
Table 6. 12:DER 2 Reactive Power Q at Fault Clearance under 50% voltage sag 130
Table 6. 13: Local Microgrid Load Delivery 134
Table 6. 14:Voltage unbalances measured under asymmetrical faults 136
Table 6. 15:Active Power Generation by the DERs within the microgrid 140
Table 6. 16:Reactive Power Generation by the DERs within the microgrid 140
Table 6. 17:Power supplied to the local microgrid load under L-L fault 141

CHAPTER ONE
INTRODUCTION

1.1 Introduction to Microgrids

The need to expand electricity access to people has played an essential role in global sustainable development's economic and technological growth. In this regard, in recent years, the distributed generators (DGs) / distributed energy resources (DERs) have become more relevant in supplementing conventional fossil energy resources for power generation [10]. The DG modules either run synchronically with the grid or independent of the grid as a microgrid [11]. Microgrids are DER controlled networks, including photovoltaic (PV) and Wind turbines (WT). Apart from DERs, microgrids also include energy storage systems (ESS) and local loads that can operate in grid-synchronous or standalone modes. A microgrid is an efficient source for economic, green, and sustainable energy for DER connection to the traditional grid [12]. The implementation of distributed generations (DGs) based on renewable energy sources (RESs), also known as DERs in modern electrical systems, has raised significant challenges such as bidirectional power flow in the distribution system, stochastic RES generation characteristics, and distinctive fault current properties. [1][13]. A microgrid is a low-voltage mini-grid; its concept is projected years back to aggregate RESs, energy storage systems (ESS), and loads to manage and control the DGs efficiently. Therefore, microgrids have acted as a prospective medium in which RESs are incorporated into the current distribution system with operational flexibility and controllability in different operating modes [14]. In recent times, power systems that generate electricity from RESs have increased their share of the total installed electricity generation capacity due to various advantages. Increased use of RESs has enabled the supply of clean, cheap, and low-cost energy in the last years. Since the 2010s, a limited amount of total reserve capacity can provide PV and WT systems energy. At this point, microgrids are the most reliable solution for incorporating RESs into a more extensive electricity network. Figure 1.1 provides an example of a microgrid [15], and further expanded in Figure 1.2 for both PV and WT based systems. Microgrids provide a promising solution for today's electrical energy problems based on reliable, safe, environment-friendly, and sustainable electric energy obtained from renewable energy sources. In microgrids, controllable voltage source inverters (VSI) interface different RESs such as PV, WT, batteries, fuel cells, and micro-turbines to improve control versatility and ensure high electrical power quality systems [16].

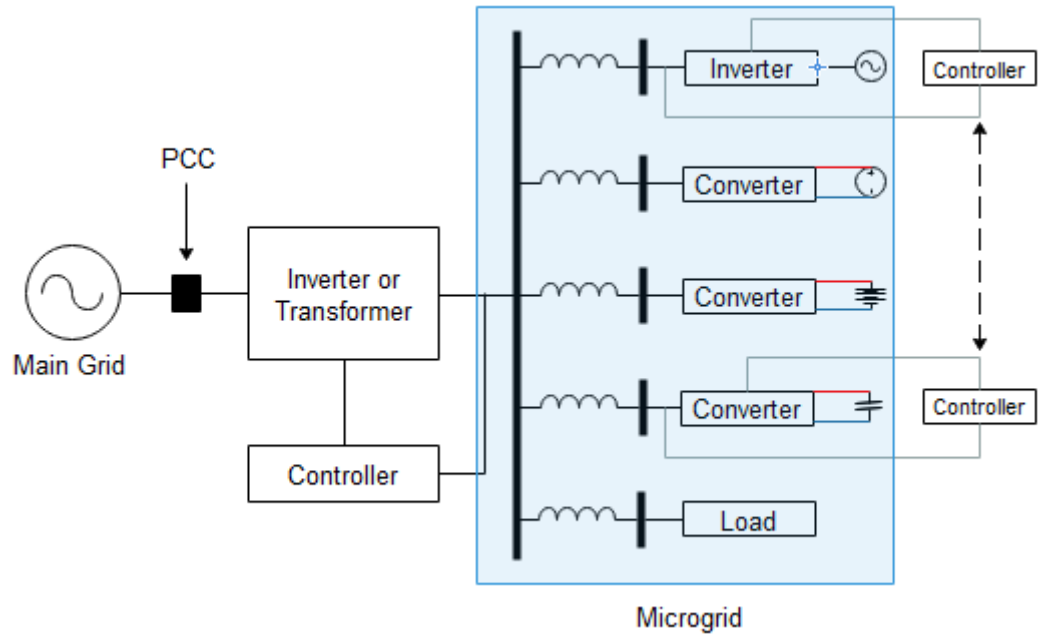

Figure 1. 1: General structure of the microgrid

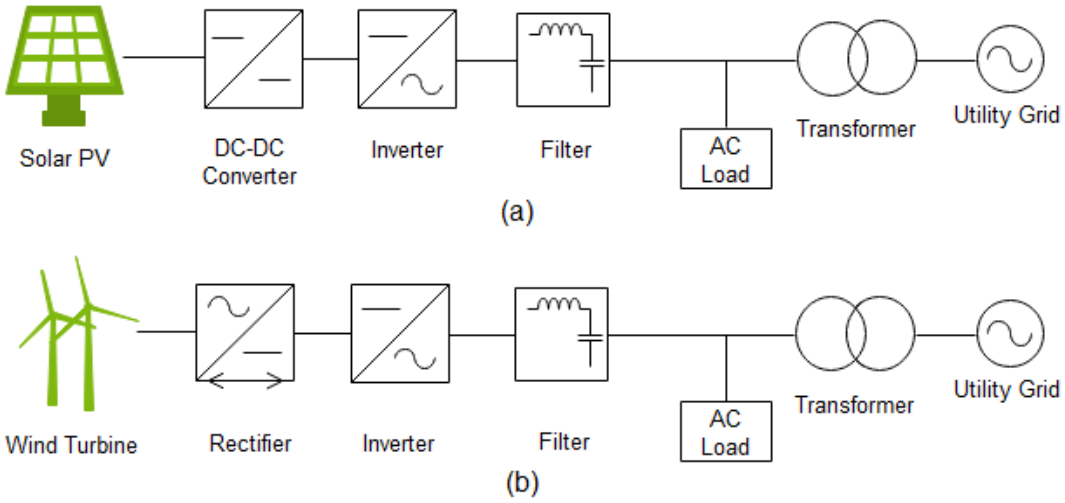

Figure 1. 2: The general structure of an inverter-based microgrid (a) PV inverter-based microgrid (b) WT inverter-based microgrid

The inverter interface isolates the DGs/DERs and the more extensive main grid electrically; nevertheless, it serves as an economic link to allow electrical energy transfer and ancillary services at the interface [17].

The rest of this chapter presents the study's background, statement of the research problem, motivation for the research, aim and objectives of the study, the study's scope, and research contribution to knowledge.

1.2 Study Background

Grid codes are standard requirements for grid-connected microgrids that demand specific critical rules for the control, set-up, and operation of microgrid schemes. Hitherto, the focus has been on the power quality demand at RES maximum power point. For example, the level of total harmonic distortion (THD) must be below 5 percent. However, with the increasing penetration of DERs aided by microgrids, emerging grid codes now require DERs to effectively participate in the sustenance of the overall system stability and reliability. For efficient DC to AC power conversion, the maintenance of the power conversion controllability is crucial.

Many problems are inherent between the microgrid and host utility grid due to the sensitivity of bidirectional power flow [14]. In voltage disruptions due to faults in the host system, studies conclude the instant switching from grid-connected mode to insulated mode [18]. Existing grid code requirements require the grid-connected inverter-based microgrids to stop energizing the microgrid loads in reaction to the main grid fault, especially voltage sags. Under the IEEE Std 929-2000 standard, low-voltage microgrids must be disengaged from the host grid before 120 cycles of voltage sag between 0.5 – 0.9 per unit. Consequently, when voltage drops occur, the DG / DER systems are required to detach from the grid and reconnect just at the time of fault or disturbance clearance. Therefore, ancillary services, including fault ride-through (FRT) supports, are not within microgrids' purview and are not necessarily required. The grid code standards are implemented to guarantee the utility maintenance workers' safety, safeguard the grid-connected equipment, and ensure general public safety, especially under low RES-based microgrid [19]. The isolation of low penetration of RES-based microgrid has no significant effect on the overall grid's operation and stability.

However, the requirements are different under high penetration of RES based microgrid in grid connection. As such, disconnecting high penetration of RES-based microgrid from the main grid has a significant consequence on the overall network's operation and stability. The microgrid's disengagement in response to disruptions or faults in the grid could have severe technical implications such as power outages, system instability, and voltage flickers [20]. In comparison, due to the increasing proliferation of grid-interactive and high-capacity microgrids, they are expected to deliver enormous amounts of power to the host grid while operating in grid-synchronous mode. This will mitigate the possible instability during a fault or voltage sag by ensuring the active transmission of power to local microgrid loads and support for reactive power to the host grid. This blocks high-capacity microgrid disconnection during grid failure or any disruption that may cause potential network instability [21]. With the increasing penetration of RE and rapid increase aggregation of PV panels, a substantial amount of power is generated and

contributed to the overall grid. Consequently, such a power generation's abrupt lockout would threaten the system's overall stability [20] [1].

Accordingly, grid codes are required to be revised with their respective specifications, given the increasing integration of RES, especially at active distribution systems. Previous works of literature [22][23] have demonstrated that RES based microgrids perform a critical responsibility in the overall system stability. Furthermore, microgrids, including photovoltaic schemes, may also be used to make available ancillary services to alleviate power electronics' technical challenges [24]. Various research is ongoing to ensure that microgrids, even at the low-voltage networks, can possess properties such as FRT or low voltage ride-through (LVRT) and inertia, just like what is obtainable in medium- voltage and high-voltage networks.

As a result, some developed countries have amended their respective grid codes to improve RES efficiency. In 2004, 2006, and 2008, Spain, Germany, and Denmark were among the first countries, respectively, that already issued the FRT requirements for DERs connected to the grid [25]. The Spanish, Danish, and Chinese code requirement is displayed in Figure 1.3 accordingly. Although these requirements are projected for the high-voltage network, they are valid for the low-voltage grid due to similar concepts [26] and increasing penetration at the low-voltage level. Voltage sags as a result of fault and other transient disturbances are severe challenging events in grid-connected systems. Because of power line short circuits, lightning strikes, and load dynamics, the grid-voltage magnitude can momentarily drop to a particular point, including zero levels. In such situations, large DER / DG systems' abrupt shutdown will trigger the collapse of power system distribution [27]. Henceforth, nowadays, it is obligatory for grid-synchronous DER/DG units to momentarily ride-through grid voltage sags. Simultaneously, the DER/DG units is expected to provide dynamic grid supports by contributing reactive power to help the grid withstand the transients.

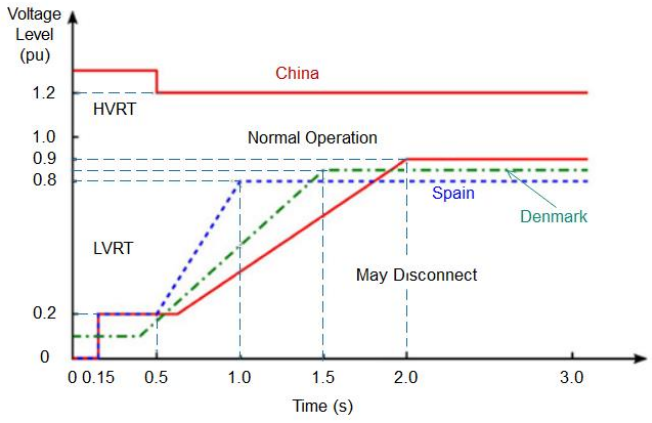

Figure 1. 3: FRT/LVRT curves defined by Spanish, Danish, Chinese grid code [28]

The national FRT specifications for Spain, Denmark, and China, in particular for medium and high-voltage distribution grid networks [9], [10], [16], are illustrated in Figure 1.3. In particular, when the grid-connected units are above the lines, they need to be connected to the main grid as an alternative to stopping power generation. Therefore, DER / DG systems will remain grid-connected if the voltage amplitude is above the lines. Nevertheless, in China, the voltage is also regulated, with DER / DG systems working in high voltage ride-through (HVRT) if the voltage magnitude is higher than the rated nominal value, nonetheless within limits [27]. It means that if the voltage profile is too high, HVRT is enabled. If the grid fails (voltage sags), grid-supporting schemes must resist disconnection and stay operational under fault duration. Simultaneously, some reactive power must also be provided to enhance grid resistance to PCC faults to avoid possible negative consequences.

In Germany, the DER/DG units connected to high-voltage and medium-voltage grids are expected to ride-through transient voltage sags and simultaneously offer reactive power support for prompt grid recovery [29]. Specific specifications for DER/DG units of over 6 kW nominal power have also been implemented in the Italian grid code.[30]. Additionally, Japan has increased the PV system's penetration, and the viability of fault rides for PV systems connected to single-phase LV grids has been tested in studies [31]. The challenges arising from the high DER / DG penetration, especially in PV systems, are envisaged and forecasted: thereby necessitating advanced control in combating these potential challenges. The network operators prioritized the discovery of solutions to ensure that distributed systems are consistently stable in operation and sustainable by using PV sources. Thus, existing grid code specifications are being continuously updated to permit an immense implementation of low voltage DER/DG systems based microgrids, especially PV with FRT capabilities [32].

Apart from FRT, the grid support, dynamic power control, and smart ancillary service provision are capabilities that future inverter-based microgrid systems are anticipated to have. Grid inverter-based microgrids are expected to possess all the abilities above alongside FRT. Consequently, to actualize this, the existing grid standards are being amended accordingly to enable FRT operation of low voltage microgrids, especially PV systems. The microgrid interfacing converter control must therefore also be advanced with these following requirements:

1. Dynamic grid support with FRT capability
2. Flexible power controllability with the non-MPPT operation
3. Control of reactive power while making optimal use of DER reactive power
4. Control of active power via the regulation of frequency
5. Further enhancing reliability and efficiency

Furthermore, the DER/DG units in a microgrid are expected to operate in their maximum active power point in a predetermined duration at a power factor of unity as soon as the grid-voltage recovers or fault clearance. Often, recurring voltage sags resulting from a fault or any other disturbance are inevitable, and these, therefore, pose a significant challenge to the power inverters of inverter-based microgrids. To ensure smooth operational changes (i.e., from maximum power point tracking point to a point suitable for fault ride-through operation and vice versa), inverter-based microgrid, traditional control methods must be improved given these strict and essential operating conditions. Furthermore, reactive power injection through interfacing inverters is considered in controller design, and thus, reactive power injection is permitted without exceeding the operational power limits. In such a way, the DER/DG systems of a microgrid, including PV systems, deliver dynamic supports to the grid.

The reactive power injection requirements during different degrees of depth in voltage sag in Spain and Denmark grids are revealed in Figure 1.4. As shown, the priority is given to the reactive current injection during fault ride-through operation, and in such a situation, the active power generation and delivery may be preserved or varied, however unnecessary. Considering the urgency and impart of prompt reactive power support, the voltage sags detection to ensure appropriate and suitable action under faults is critical.

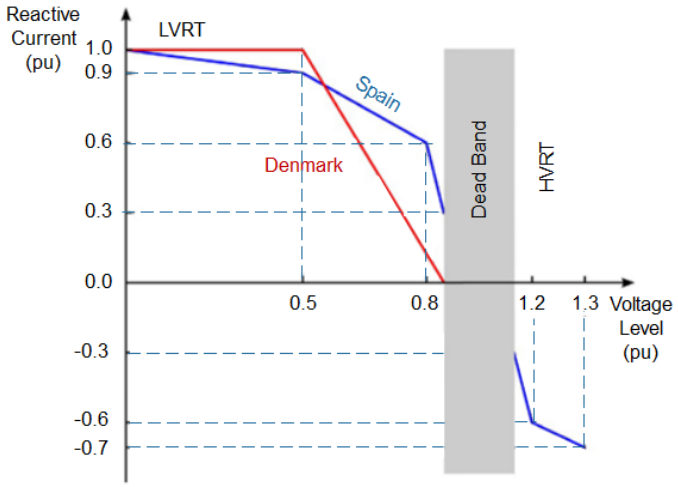

Figure 1. 4: Spain and Denmark reactive power requirement under FRT operation mode

1.3 Statement of Research Problem

The grid-connected microgrids' operating condition is critical, considering the increasing penetration of RES (PV and WT systems) and their large-scale integration into the traditional grid systems. The grid voltage drops immediately at the occurrence of fault or disturbance, and the depth of voltage sag, as a result, depends on the gravity of the fault. Hence, the interfacing inverter's current output rises to keep the injected active power constant to the grid. The inverter

current meets the upper limit as the grid voltage further drops intensively. Consequently, the injected active power to the grid falls. On the other hand, RES side converters (DC-DC for PV and AC-DC for WT) do not sense the voltage drop on the AC grid side, thereby generating active power into the DC link. Leading to a power imbalance between the RES incoming and outgoing powers and, by extension, the potential to damage DC link capacitors and voltage stresses on the power converter switches.

The various grid codes hitherto prescribe the disconnection of these RES to prevent any damage. However, with increased installed microgrid capacity and a substantial injection of power to the host grid, the disconnection of high capacity microgrids during grid fault or any other disturbance is avoided to forestall potential grid network instabilities. As a consequence of the fast-expanding DGs/DERs based on RESs, as stated earlier, nations have issued new grid codes with strict interconnection requirements, which stipulate that microgrids provide ancillary services to fulfill FRT requirement. FRT capability is among the problems of large-scale deployment of RES into the grid system that has not been thoroughly examined. Grid-connected RES, especially PV systems with adequately controlled interface converters, must inject power to the grid at acceptable quality. Similarly, the traditional grid systems where these renewable sources are connected as microgrids are often non-ideal sinusoidal voltage sources. Therefore, it is always challenging to maintain the required quality with constant amplitude and stable frequency.

The system operators stipulated the grid codes to specify the detailed responsibilities of various generating units and diverse loads under numerous circumstances. Several power quality occurrences in the grid, such as voltage sag, swell, transient/spike, harmonics frequency variation, flicker, and unbalance, may increase losses or even inexpedient to overall system stability, especially under transient faults. Thus, it is highly essential to device innovative control schemes for renewable energy-based microgrid systems under transient grid conditions for increased penetration and installed capacity of renewable energy sources in an acceptable and grid-friendly manner.

1.4 Motivation for the Research

The expected depletion of fossil fuels and the continued high energy demand for industrial and manufacturing industries in modern society were the main driving factors in searching for and creating regenerative and clean alternatives. The global green issue of reducing carbon dioxide emissions also needs to be addressed urgently [33][34]. The most economically applicate and widely adopted in today's global energy paradigms are hydroelectric, wind, and solar photovoltaic energy amongst various renewables. [35]. However, the grid code requirements for disconnection under fault, coupled with the inherent limitations of interfacing converters, hinder the largescale integration and exploitation of renewables [36][37]. Therefore, several attempts have been made

to increase the assimilation of various renewable energy sources into the traditional grid system. The employment of more energy systems is anticipated to solve the potential energy crisis. Nonetheless, these energy units' abilities to remain grid-connected under transient grid conditions and provide ancillary grid services are still challenges. In future renewable-dominated grids, such energy sources' disconnection can never be an option as the overall system's stability and reliability will be compromised. Consequently, there are lots of economic and technical benefits from proposing an innovative solution to complement the existing control of the interfacing power converters for grid-supporting renewable energy systems [1][3] [8].

1.5 Aim and Objectives of the Research

1.5.1 Aim of the Research

This research aims to develop a comprehensive hierarchical control structure with a unique secondary fault (low voltage) ride-through scheme for grid supporting inverter-based microgrids to fulfil the grid code requirement using delayed signal cancellation and stationary reference frame for the reactive power injection and fault current limitation.

1.5.2 Objectives of the Research

The objectives of this research are:

1. To develop time-domain models of DC-AC inverter-based microgrid to integrate ideal DC voltage source distributed energy resources with the ability to participate in grid frequency and voltage regulation.
2. To develop time-domain models of DC-AC inverter-based microgrid with a DC-DC converter and maximum power point tracking that integrate photovoltaic-based distributed energy resources with the ability to participate in grid frequency and voltage regulation.
3. To investigate grid fault impacts on the developed discrete-time models and propose a secondary level control scheme for fault ride-through enhancement using delayed signal cancellation in the stationary reference frame.
4. To evaluate the proposed microgrid secondary control's performance in mitigating AC voltage sags and AC overcurrent for efficient power delivery and a sustained grid connection of ideal DC voltage source distributed energy resources.
5. To evaluate the proposed microgrid secondary control's performance in mitigating AC voltage sags, AC overcurrent, and DC link overvoltage for efficient power delivery and sustained grid connection of photovoltaic-based distributed energy resources.

1.6 Scope of the Research

The modelling and emulation of this system through simulation are critical to investigating how the converter-based system responds to FRT/LVRT technical challenges, among other issues. This is valuable for our analysis, design, and verification. Thus, the time-domain models of grid supporting systems are developed from the typical grid feeding and grid forming systems. This is achieved by integrating the reactive power-grid voltage (Q-E) and active power-grid frequency (P-ω) droops into the control system of a typical grid-feeding and forming structures. Hence, the ability to partake in the grid voltage and frequency regulation via reactive power injection and active power generation is developed.

The reactive power injection is essential for the grid voltage restoration; hence, the secondary control incorporates a reactive power injection strategy. The negative and positive sequence components emerge in grid fault conditions. Consequently, the current references are accurately generated to ensure the FRT operation using the delayed signal cancellation (DSC) algorithm. Thus, the inverter-based microgrid models developed in this work explore the characteristic current reference generation approaches for grid-connected systems. The DSC provided a positive sequence and negative sequence for easy and prompt compensation at the hierarchical control structure's secondary control level.

This work focuses on implementing a hierarchical control with a fault ride-through capability, a smart method of control for eliminating the challenge of synchronization, management, and power quality of local microgrid load alongside. In the hierarchical scheme, the primary level has droop control alongside some subordinate loops. The hierarchical scheme's secondary level sets the references for the control's primary level, subject to the host grid condition's dynamics. The converter interface running in grid supporting mode can thus achieve fault ride-through through hierarchical controls while contributing to the main grid voltage and frequency regulation.

Due to the limitation imposed by a typical power inverter's complex power rating, this work similarly developed a fault current limiting system to regulate the active power generation during fault inversely proportional to the reactive power injection requirement to support the grid. Furthermore, the inverter-based microgrid with DC-DC Converter, such as grid-synchronous double stage PV, is required to inject excellent-grade power into the electricity grid by adequately regulating the interface DC-DC and DC-AC converters. However, FRT control is a bit difficult to achieve under this condition. Consequently, the proposed FRT strategy is significantly modified to accommodate a systematic change in operating point condition (MPPT) under fault to reduce the active power generation into the faulty grid based on the changing voltage sag depth.

Furthermore, the purpose of the FRT control scheme developed in this work is to prevent the grid-supporting microgrids from further inducing a short circuit current in the occurrence voltage sag, ultimately leading to the power generation loss. However, there is an insignificant fault current contribution from a small-scale DER / DG inverter-based system. However, the extensive PV grid integration, for instance, negatively impact overall grid stability during faults. Consequently, the inverter-based microgrid is controlled with the utmost flexibility to forestall shut down and subsequent disconnection of the inverter due to overcurrent protection activation.

This work focused on an inverter-based microgrid system with grid supporting capability. For instance, PV technologies are primarily power-electronic dependent for energy conversion compared to typical traditional power generators and wind turbine systems, which have rotating electrical mechanisms. Consequently, there is an absence of significant inertia in the inverter-based systems, especially in PV systems. On a positive note, the power electronic conversion systems facilitate swift control immediately; a fault is sensed in the grid, and this capability is exploited in this work. Thus, unwanted active power under fault is adequately controlled with the proposed FRT operation. Similarly, the change in operating point condition of the MPPT proposed for the inverter-based microgrid with DC-DC converter in this work is done with the assumption of uniform irradiation and temperature and that the system operates at MPP before fault occurrence.

1.7 Research Contribution to knowledge

The pointwise contribution of this work include

- This proposed scheme requires no mode switching and enables the PV system to ride through grid faults or transient disturbances. Incessant grid resynchronization after fault occurrence is avoided as in the seamless transition technique, thereby mitigating local load shedding. In the grid supporting model developed, no distinct control arrangements are required to ensure the transition from constant grid feeding (P–Q) to constant grid forming (ω–V) mode and vice versa.
- The proposed FRT control strategy in this work is integrated at the hierarchical control structure's secondary level. This interfaces with the primary control to achieve fault ride-through and dynamic grid supports using power references for the droop.
- A DSC algorithm is presented to detect the fault instantly in less than 0.1515ms to ensure reliability and prompt response. The DSC has a faster convergence time with improved separation of the positive and negative sequences realized. The voltage sag detection using DSC is utilized in injecting reactive power and limitation of the fault current, thus eliminating oscillations experienced in the power and the DC-link voltage.

- This study introduced an approach to limit the active power reference generated by the MPPT, which is applicable in a double-stage PV system. A specific control action is implemented to curtail the DC-source power generation and equip the interface converters with FRT capabilities to avoid activating the DC-link overvoltage protection scheme. This is achieved without shutting down the voltage boosting operation of the converter.

- The DC-DC and DC-AC converter's DC bus voltage is controlled during the sag cycle of the AC grid voltage. Thus, the solutions proposed in this study curtailed the usual momentous DC voltage increase in the DC bus under the transient process. The secondary level of control enhances the fulfillment of the emerging grid code FRT requirements while meeting local load requirements.

- Acceptable power quality for the local loads during fault duration is ensured by including an appropriately sized anti-parallel IGBT-diode switched inductance. It is noteworthy that as a result of a high *R/X* ratio in the low voltage distribution feeder line, injecting reactive power under faults may not substantially contribute to the recovery of voltage. Hence this work has been able to deploy an adequately sized anti-parallel IGBT-diode switched inductance at the PCC of the MG with the grid to reduce *R/X* ratio and effectively support the voltage under grid disturbance, provides protection, and alleviates the effects of fault, especially on the local sensitive loads of the microgrid. The traditional primary control is improved by the secondary control guiding power export and import in compliance with the grid code

- Consequently, a direct theoretical framework has been provided to determine the value of this switched inductance. Furthermore, this arrangement counteracts the effect of grid disturbances by limiting transient overcurrent throughout grid faults. This is enhanced by introducing a second control block that regulates the active power and reactive power exchange between the host grid and the microgrid in conformity with the stipulated utility grid standard

1.8 Organization of the Thesis

Chapter 1: Introduction
Chapter 2: Literature Review
Chapter 3: Inverter-Based Microgrid Discrete-Time Model
Chapter 4: Inverter-Based Microgrid with PV Discrete-Time Model
Chapter 5: Fault Ride-Through using Secondary Microgrid Control
Chapter 6: FRT Control Implementation in Inverter-Based Microgrid

Chapter 7: FRT Control Implementation in Inverter-Based Microgrid with PV
Chapter 8: Conclusion and Recommendation

1.9 Publications

The publications listed in this section are also materials forming part of this thesis with appearances in peer-reviewed accredited journals and conference proceedings.

1.9.1 Journals

The peer-reviewed journal articles emanating from this work are already listed in the "List of Publications," three published, one accepted, and one under revision.

1.9.2 Conferences

The peer-reviewed conference articles emanating from this work are already listed in the "List of Publications," seven published and three accepted.

1.10 Scholarships and Award

1. Durban University of Technology Doctoral Scholarship (Energy RFA) for 2018, 2019, and 2020.
2. Third Best Conference Paper Award at the 17th IEEE Clemson University Power Systems Conference, United States of America, March 2020

CHAPTER TWO
LITERATURE REVIEW

2.1 Introduction

Chapter two introduces the structure of microgrid generally, and the concept of an inverter-based microgrid is laid. The chapter also explains the primary level, secondary level, and tertiary level hierarchical control structure. Furthermore, the overview of MPPT control strategies and the need for change in its operating point condition is presented. The methods for limiting current through active power generation under fault for DC source inverter-based microgrids are presented. Alongside strategies for the reactive power injection are also presented. Furthermore, the chapter presented a review of similar works of literature. In conclusion, the work presented a review of similar works of literature

2.2 Microgrid Structure

A microgrid is the collection of DERs/DGs connected as an electrical island or synchronously operated with the grid to supply power to meet local and main grid load demands. The DER constitutes several renewable and non-renewable energy sources. A microgrid is a fragment of the overall grid system, consisting of aggregated DG/DER sources, interfacing converters, and resident microgrid loads, as shown in Figure 2.1. The DG source could have a prime mover mechanism, and the local load could be static, dynamic, or composite. A microgrid either operates independently or synchronously with the utility grid. The PCC connects microgrids to the rest of the utility grid. The energy transfer is expected to be smooth and not intermittent when switching from standalone to grid synchronous mode. [38][39]. Microgrid now represents an innovative concept by operating in low voltage (LV) distribution systems built on PV array generation, small-scale and medium-scale wind turbines, and other prime moving energy mechanisms.

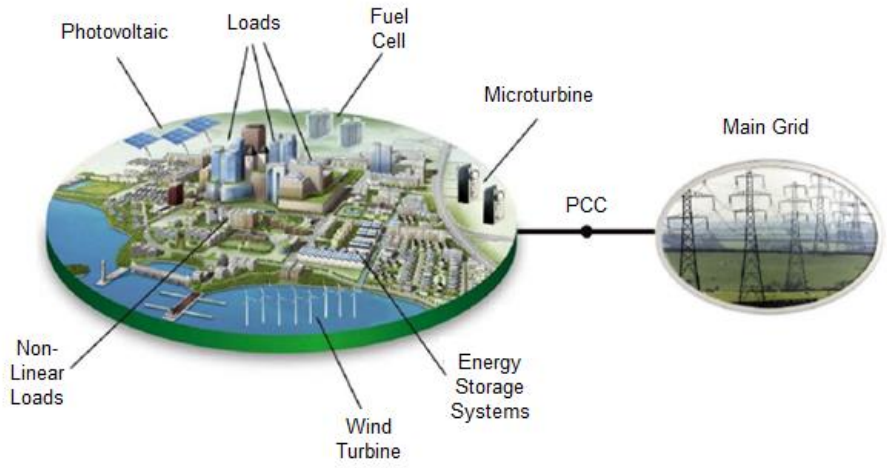

Figure 2. 1:Microgrid structure

The components of a typical microgrid are:

2.2.1 Distributed Generation or Generators

Microgrids exploit and utilize different air, water, wind, and biomass resources available within an electricity generation location. DG signifies small-scale energy production, typically less than 10 MW, to meet local needs [40][41]. The prime moving energy mechanism generates power from mechanical energy, and the mechanism is interfaced with the electric power system via converters. The DG sources are separated into two groups of non-renewable and renewable energy sources. The non-renewables are diesel engine generators and microturbines, while the renewables solar photovoltaic panels, fuel cells, wind turbines, geothermal, hydro turbines, and biomass.

2.2.1.1 Fuel Cell

A fuel cell is an electrochemical cell that transforms a fuel (hydrogen) and an oxidizing agent (oxygen) into electrical energy utilizing a couple of redox (electrochemical) reactions [42][43]. The by-products of this conversion are water and heat. Fuel cells yield ceaseless electricity provided oxygen and hydrogen are infused with power, usually between 5 kW and 250 kW. Fuel cells generate electricity and heat for homes under a near 100% system efficiency via the cogeneration process. A fuel cell stack's output voltage is typically lesser than the acceptable voltage range and depends on the current drawn. A DC-DC boost converter is, therefore, commonly utilized to improve and regulate the DC connection voltage.

2.2.3.2 Micro-Turbine

Micro-Turbines are 25 kW to 500 kW gas turbines from piston engine turbochargers, aircraft auxiliary power units, or small jet engines [44][45]. Hence they possess high speeds of between

40000 rpm to 120000 rpm. Micro-Turbines comprise a compressor, combustor, turbine, and electric generator on a single shaft or two split-shaft have two design forms. In single-shaft micro-turbines, the turbine and its generator both share a common shaft. The micro-turbine has a two or four-pole permanent magnet synchronous generator (PMSG) with an output voltage of up to 4,000 Hz frequency. Thus, appropriate power electronic converters are used to interface the PMSG to convert the relatively high frequency into 50/60 Hz system frequency.

2.2.3.3 Solar PV Array

A solar PV system converts sun radiations directly into electricity using solar photovoltaic cells of a P-Type-N-Type semiconductor diode visible to light. This diode comprises a thin silicon film with terminals. Charge carriers are created by the cells when light beams, and this causes the flow of current. The electric charge carriers' rate of production is contingent on the location of solar irradiance and the semiconductor's solar absorption capacity. Cells are stacked in both series and parallel connections to realize a single module. An array, therefore, consists of a string of several modules. Modules are wired in series and parallel into PV arrays that satisfy a wide range of electrical needs (wanted voltage and current).

2.2.2 Energy Storage Systems

The energy storage system (ESS) has a diverse role in microgrids; it improves the stability, power flow, power generation reliability, and power quality [46][47]. Some DGs/DERs, especially fuel cells, possess slow dynamic responses and cannot handle sudden changes in load. Furthermore, renewable power generations are contingent upon the instantaneous weather of the installation site. Therefore, ESS guarantees the immediate load demands are met, particularly in the grid-synchronous operating mode. Types of ESS include Flywheels, battery ESS, supercapacitors, or ultra-capacitors, and superconducting magnetic ESS.

2.2.3 Load

Loads on microgrids could be industrial, commercial, or residential. Depending on the type of service, such loads can be linear or non-linear loads, sensitive or insensitive loads, unbalanced or balanced loads. It is imperative to render precedence service to essential and sensitive loads in microgrid parlance and ensure supply reliability with enhanced power quality. Furthermore, reliable protection systems are put in place to mitigate the effects of harmonics and disturbances.

2.3 Microgrid Power Converters

Interfacing converters, i.e., AC-DC rectifiers, DC-AC inverters, and DC-DC converters, must convey the power generated from DER/DG sources to the host utility grid and local load if any. Most importantly, power inverters are typically used as interfaces to connect each source to the common bus in microgrids, allowing for parallel connection. The harmonic current content of the

system currents and microgrid is adequately compensated without external compensation devices [48]. All the interfaces collectively possess and exercise absolute control over the system's dynamics, especially under momentary conditions. Power electronic converters are finding increased use as the essential equipment to convert and control electrical power in the wide power range from milliwatts to gigawatts with power semiconductor devices. Nowadays, a larger percentage of all electricity generated is processed through power electronic interfaces [17]. Therefore, highly efficient, sustainable, reliable, and cost-effective power electronics systems are needed to reduce energy waste, improve power quality, and reduce power generation, power transmission/distribution, and end-user application costs. With increasing power densities, challenges related to the power electronic systems' quality have been more significant. Electronic converters are often used in microgrids to control the flow of power and convert it into a suitable DC or AC form.

Furthermore, power electronic converters possess no in-built inertia, contrasting synchronous generators' dynamic features. This dynamic feature enhances overall stability and static synchronization flexibility [49]. The droop control to emulate virtual inertias is realized within power converters' control schemes, which works similarly to synchronous generators to achieve better synchronization. This control helps attain stable reactive and active output power by monitoring and regulating the grid voltage and frequency. Therefore, the microgrid contributes to grid stability maintenance by sustaining the reactive power injection and active power generation. Typically, inverter interfaces are connected in a DG in parallel with appropriate power-sharing between them. Many control strategies have been proposed for achieving appropriate power-sharing (active and reactive), such as average current control, master-slave control, and circular-chain control. [50][51][52][53]. A decentralized control technique often used in parallel controlled inverters to prevent currents' circulation is a droop technique [54]. Droop control is commonly used in microgrids and relies on localized information to gain decentralized control; this makes it a more effective power-sharing technique than various high-bandwidth, network-based communication techniques [16][26].

The disconnection of interfacing power electronic converters during transients portends a grave threat to the microgrid and overall system stability and reliability. FRT capability requirements are needed for these converters to endure faults, make available short-circuit current, and remain grid-connected. Their control schemes can regulate transient responses to mimic the traditional synchronous generators, producing high short-circuit current naturally. However, the existing short-circuit support available is constrained by the power-electronic switch overload capacities [55].

2.4 Microgrid Operation Modes

The microgrid consists of a group of DERs/DGs and loads that can either operate synchronically with the main grid or operate autonomously in an islanded mode. DER/DG can operate as a voltage source or a current source with power electronic interfaces depending on the operation mode [56]. The converter interface is used because DGs' output voltage is often DC power, such as a solar system or fuel cell. Furthermore, some DG output AC power comes with variable frequencies, as in wind turbines. Lastly, some DG output AC power with a frequency is more significant than the network's frequency, as in microturbines. Reference [57] presents the development of an intelligent smart microgrid dynamic energy management system. The developed framework is introduced for evolving the smart energy management system online, which is capable of performing grid-connected and islanded operations

2.4.1 Grid-Connected Mode

The grid stipulates frequency and voltage references to the grid-tied converters. In the grid-connected mode, the main grid supports the voltage and frequency by imposing the supply standards [58]; thus, the DERs/DGs are only controlled to supply the power. In this mode, all power sources are linked side-by-side by the converter to supply stable loads and inject power into the main grid. Under grid-synchronous operation, the inverter systems operate in electrical tandem with the host grid as current sources. When the power electronic interface of a DG is functioning as a current source, at that moment, the goal is to generate power for local load and transfer excess into the host utility grid. [59]. The current source inverter operation is controlled to infuse specified active and reactive power via an effective reference control. The interfacing inverters are connected to the grid by a phase-locked loop (PLL) and generate both active and reactive grid power. Nevertheless, a microgrid lacks a grid system's dynamic support when under islanded operation [60][61].

2.4.2 Island Mode

RES determines the system frequency, voltage, and power flow control for an autonomous microgrid. The voltage and frequency are controlled in stand-alone operation using multi-loop control schemes [62][56][63]. A voltage source inverter is used when regulation of voltage and frequency is required, which is the case of a standalone mode of operation. Grid-connected converters can still be used for interfacing renewable energy sources and storage systems without a host grid. It is desirable to have purely inverter-based microgrids without a fossil fuel-based synchronous generator; hence, the interface inverters are utilized and regulated to generate frequency and voltage references. Therefore, under microgrid islanded mode, at least one of the interface inverters of the DERs should operate in voltage control mode, while one of the voltage control or current control modes could be selected in grid-connected conditions.

2.5 Hierarchical Control Structure

Innovative control structures are essential for achieving efficient microgrids [64]. Thus, the hierarchical control comprises primary, secondary, and tertiary control levels, as shown in Figure 2.2. The hierarchical structure is flexible and adaptable in microgrids' management to achieve a stable and dynamic performance with stiff economic consideration [64]. Thus, microgrids provide an operational framework and platform for effective DER integration.

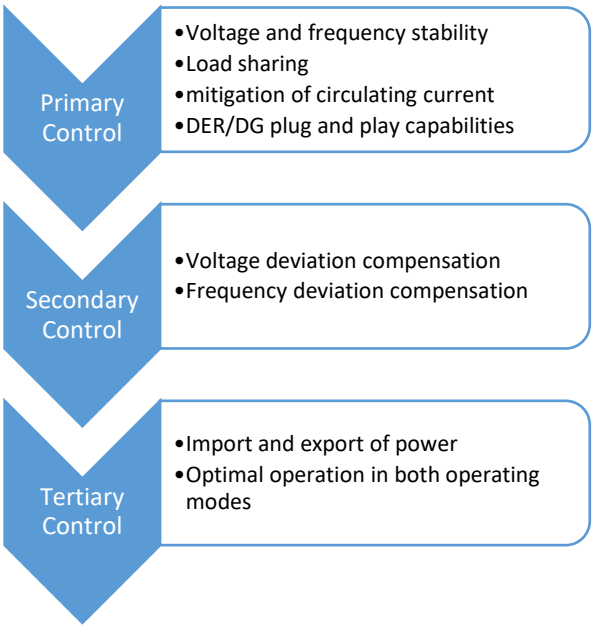

Figure 2. 2:Microgrid hierarchical control structure

The primary roles and requirements of the microgrid control scheme are [20][64]:

1. Frequency and voltage regulation in standalone and grid-synchronous operating conditions;
2. DG coordination and appropriate power-sharing;
3. Resynchronization to the host grid;
4. Power flow coordination of microgrid with the host grid;
5. Operational cost optimizing

The above-listed obligations are distinct impacts and time measures; consequently, hierarchical control assembly [65][66] to tackle respective obligations at distinct control levels is inevitable. The primary level control regulates the frequency and voltage stability of the microgrid after the islanding procedure. The running of power control sharing independently for the DERs with local loads is essential. Furthermore, effective sharing of power amongst DERs mitigates unwanted current circulation between interface inverters. This primary level is the major zero-level control

that contains DER inner current loop and outer voltage loop. The secondary control balances the frequency and voltage fluctuations generated by the primary control procedure. In due course, tertiary level regulates the optimal power export or inport interaction with the host grid [12], [13].

2.5.1 Primary Control Level

The primary control of an inverter-based microgrid in a hierarchical structure has two cardinal objectives of power-sharing, plug and play capabilities for the constituent DG sources; and circulating currents mitigation.

The microgrid is susceptible to frequency and voltage instability caused by power disparity between generation and consumption after islanding. Thus, the first objective is crucial. Similarly, the second objective is expected to be accomplished by adequate active power and reactive power sharing amongst DGs without communication links. Lastly, AC over-current and DC overvoltage are inevitable if circulating currents are not mitigated; thereby, damaging semiconductor switches and capacitors at the DC bus.

The DC-AC inverter control primarily consists of two linked inner and outer loops. The fast inner loop controls the current injection into the AC grid while the outer loop regulates the DC bus voltage [67]. The primary control establishes the point of reference for DG voltage and current control loops. The primary control is implemented as either current controlled or voltage controlled systems [17] [68]. In the current control operation, the active power and reactive power supply are controlled to specific stipulated references, as discussed in the subsequent chapters. Under the voltage source operation, the primary control stipulates the voltage reference through droop characteristics [69]. The inner loop ensures the quality of power delivery, harmonics limitation, over-current protection. The outer voltage or power loop balances the power flow through the DC-AC inverter by regulating the DC bus's voltage. The outer loop controller's architecture typically has deliberately slower dynamics to ensure stability [70].

2.5.2 Secondary Control Level

The secondary control is a centralized set-up equivalent to the synchronous generator’s automatic generation control, which tracks the instantaneous frequency and voltage and reinstates to respective rated standards. The level ensures that the system parameters fall inside the specified range while providing additional synchronization for either connection or disconnection of the utility grid's microgrid. Primary control has the tendencies to cause deviations in frequency even in a steady-state [64]. ESS mechanisms compensate for these deviations; however, ESSs cannot provide control load-frequency in long terms [71]. Therefore, the secondary control conveniently restores the frequency and voltage and compensates for the deviations [72][73].

Figure 2.3 shows how microgrid frequency and the DER terminal voltage are compared with the matching references ω^* and E^* in a hierarchical system's secondary control. Subsequently, the error signals are managed by respective controls given by Equation 2.1, where $k_{p\omega}$, $k_{i\omega}$, $k_{pE,}$ and k_{iE} are the respective controllers' parameters.

$$\begin{aligned}\delta\omega &= k_{p\omega}\left(\omega^* - \omega\right) + k_{i\omega}\int\left(\omega^* - \omega\right)dt + \Delta\omega_s \\ \delta E &= k_{pE}\left(E^* - E\right) + k_{iE}\int\left(E^* - E\right)dt\end{aligned} \tag{2.1}$$

The resultant signals δE and $\delta\omega$ are transmitted for voltage and frequency deviations compensation in the primary level control [64]. An additional term, $\Delta\omega$, is reflected in the frequency controller, as shown in Equation 2.1, to accelerate microgrid synchronization to a utility, and this is negligible in island operation. Conversely, a PLL tracks $\Delta\omega$ during grid synchronization [74], and the utility grid stipulates ω^* and E^* as given in Equation 2.1.

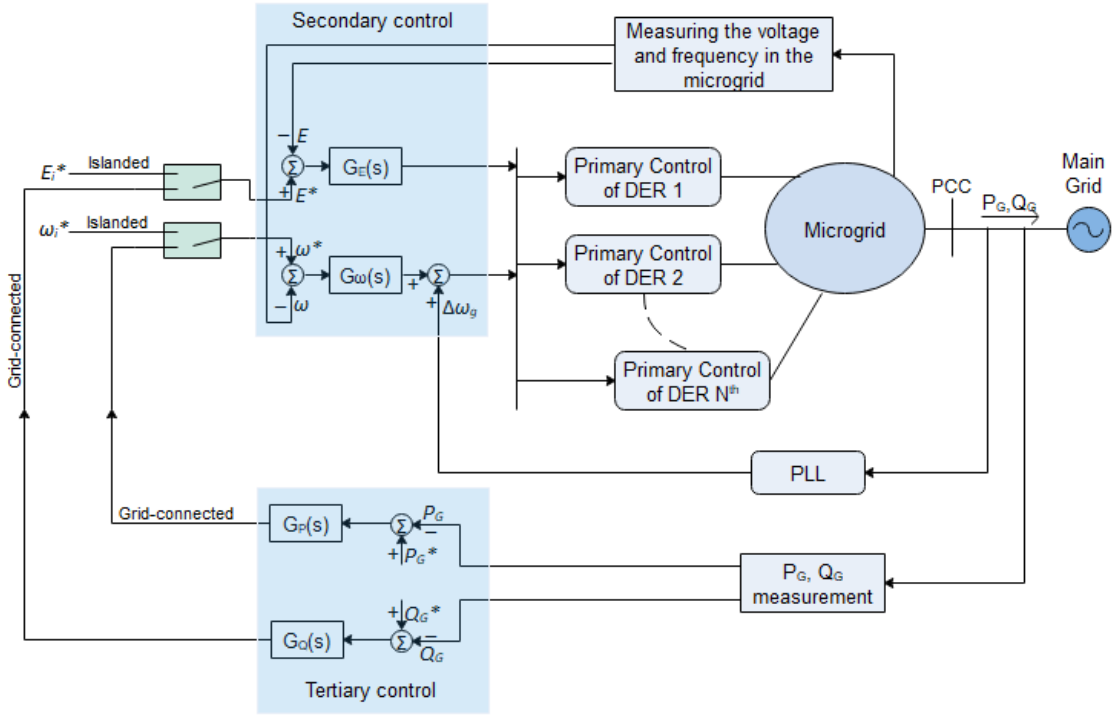

Figure 2. 3:Tertiary and secondary control block diagram

2.5.3 Tertiary Control Level

This control level is the uppermost layer in the hierarchical scheme, liable for improving the microgrid operation and power export/import. Power export/import capability involves microgrid interaction with the host utility and generates the set-points power (active and reactive) for the constituent DERs. The power flow management between the host and microgrid is realized by overseeing microgrid energy import and export in any case [56]. The control takes into cognizance the economic considerations for the optimal operation of the microgrid [75].

Figure 2.3 shows how the active output power P_G and reactive power generated Q_G of the microgrid are sampled for tertiary level control. These measured parameters are later matched with the respective references P^*_G and Q^*_G to achieve the frequency reference ω^* and voltage reference E^* based on Equation 2.2.

$$\begin{aligned} \omega^* &= k_p\left(P_G^* - P_G\right) + k_i \int \left(P_G^* - P_G\right)dt \\ E^* &= k_p\left(Q_G^* - Q_G\right) + k_i \int \left(Q_G^* - Q_G\right)dt \end{aligned} \tag{2.2}$$

where k_p and k_i are the parameters of the controllers. Frequency reference ω^* and voltage reference E^* are transmitted to the secondary level as input set-points.

2.6 Grid Integration of PV Energy System

Figure 1.2 (a) presents the topology of a PV grid-integrated system for energy conversion [76]. In transformer-less PV systems, step-up transformers are absent. There is a power electronic interface between PV panels and the grid since the PV panel voltage and current are incompatible with the grid voltage magnitude and frequency. The power electronic converter is a vital device for interfacing with control strategies due to the amplitude and frequency discrepancies between the source and grid. However, the power converters come with inherent challenges and produce harmonics that are tackled in practical applications [77].

High-order passive filters are primarily used to attenuate the harmonics injection from the converters sequel to high switching frequency [78] [79]. This has proved to be an efficient and smart solution. Moreover, transformer-less inverters are utilized to meet various demands, including high efficiency, relative portability, and cost-effectiveness. Consequently, advanced modulation strategies are designed to address the leakage current concerns [80][81][82].

Nevertheless, the power electronic interface system is essential in PV integration to the grid and, therefore, necessitates high-level control strategies to comply with strict grid stipulations. Various control scheme proposition and subsequent development largely depend on the power electronic converter's application and structure. In general, there are three approaches for optimal PV integration into the traditional grid system by modern technologies [76]. The various schemes identified in the literature [83][83] are given below

1. Module inverter
2. Multi string inverter
3. Central inverter

In all the schemes, the generation systems consist of paralleled strings or panels, with interface converters with the AC grid. The selection of suitable converters depends on voltage levels and power ratings.

In the substantial-scale PV grid integration, the power harvested is transported to a high voltage (HV) grid via LV/MV and MV/HV transformers. Large-scale grid-tied PV generation systems' main drawbacks are the long DC cables requirement and a common MPPT and panels mismatch. Long DC cables upsurge DC power loss aggregate while compromising the system's overall reliability due to its dependence on inverters' limited choices. These mismatches and common MPPT caused loss are considerably high when solar irradiance and temperature rapidly change. Therefore, the latest technologies require a more significant voltage up to 1000V at the DC link to minimize loss while posing new challenges and safety concerns.

2.6.1 Central Inverters

For example, central inverters used tens of kW of power up to several hundred kW power in residential or utility-scale systems to realize the less-significant loss and cheap costs, likewise to avoid complexity [84]. The connection of panels is made in series strings to meet the open-circuit voltage required in this application.

2.6.2 Module Inverters

In the module inverter, each PV panel is coupled to a converter, and then, the converter outputs are connected to increase the total power. Module inverter is deployed for small power uses [85]. The module inverters can be replaced straightforwardly in a plug-and-play fashion. However, the major drawback is the system inefficiency due to the mandatory high ratio for DC power transformation [85]. Nevertheless, this drawback is addressed by developing innovative DC power transformation schemes such as impedance-source inverters. Furthermore, DC-DC converters serving as power optimizers are used to condition the module's DC power output. Consequently, DC-AC inverters serving as grid interfaces are then be connected to these DC-DC converters to form a double-stage PV system. The module inverter is introduced [86], acting on each panel with a single MPPT.

2.6.3 Multi-String Inverter

Multi-String inverters are utilized in medium power applications. The boost converters are optional in a multi-string application. Transformers are usually deployed for more substantial power applications with a higher voltage of up to 1500V DC [87]. On the contrary, the multi-string system is efficient for small-power use because MPPT control is realized independently in each string [84]. This leads to improved aggregate power harvest from the PV, and also, strings are easily replaced in case of failures. Nevertheless, the series connection of PV

panels still causes mismatching issues. It combines the advantages of central and module inverter topologies. This setup is significantly efficient and versatile because various string is independently regulated. In commercial projects and operation, multi or single-string systems are employed to amass more substantial DC power from the PV system. Overall, system reliability is guaranteed as power injection is sustained even with the failure of one inverter.

It is important to note that large-scale PV power system structures with centre or string systems are implemented for grid integration to mitigate reliability challenges [88].

2.7 Modelling of PV Arrays

The PV cells and panels modelling is crucial for microgrid operation and simulation under different situations. This is critical to the development of appropriate control schemes to withstand fault or transient circumstances. Several works of literature [89] [90] [91] [92] [93], [94] and [95] have provided an adequate explanation of PV cells, current-voltage (I-V) characteristics, forward-bias and reverse-bias models, irradiance-dependent and temperature-dependent I-V characteristics, equations for diode current and thermal voltage and power-voltage (P-V) curve.

2. 8 Maximum Power Point Tracking Control Algorithm

The approaches for determining and sustaining the MPP process are numerous. The internal loop controls a reference or set-point for all the techniques, and the external loop updates the reference, defined through respective (unique) MPPT procedures [96]. Usually, MPPT procedures are implemented in the PV system controller design to continuously change the solar array impedance to keep the PV system running around the peak power point at different solar irradiance, temperature, and variable load conditions. [97]. Extremum-seeking control like perturbation and observation (P&O), hill climbing (HC), and incremental conductance (IC) techniques are intended to determine the limit of the power convex curve by changing the reference of the inner loop according to the power measured. The algorithms optimize the power generated by adjusting the voltage to ensure that the system operates in line with the P-V curve in Figure 2.4 at the "maximum power point" (or peak of the voltage). Figure 2.4 also reveals the maximum power point estimation from the open-circuit voltage V_{OC} and short circuit I_{SC}. The three most popular MPPT algorithms are listed accordingly in the literature:

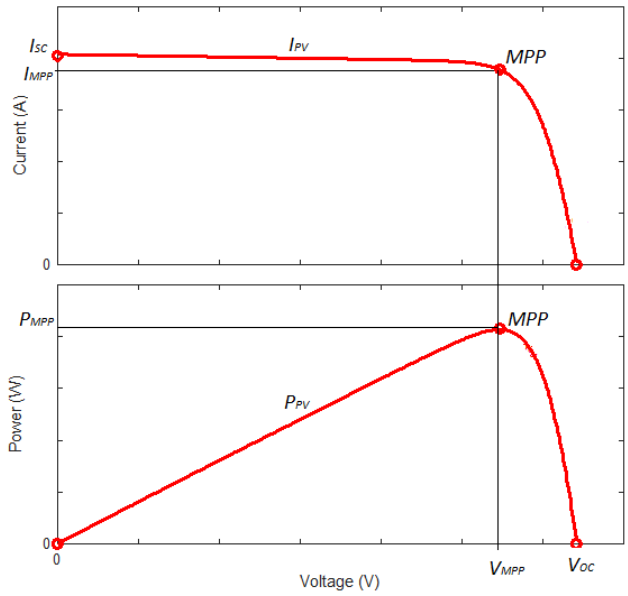

Figure 2. 4:I-V and P-V characteristics of the PV

2.8.1 Perturbation and Observation

The P&O procedure perturbs the voltage of operation in order to maximize output. Although this algorithm has several advanced and more optimized variants, as proposed in [98]. Figure 2.5 shows a fundamental perturbation and observation MPPT algorithm.

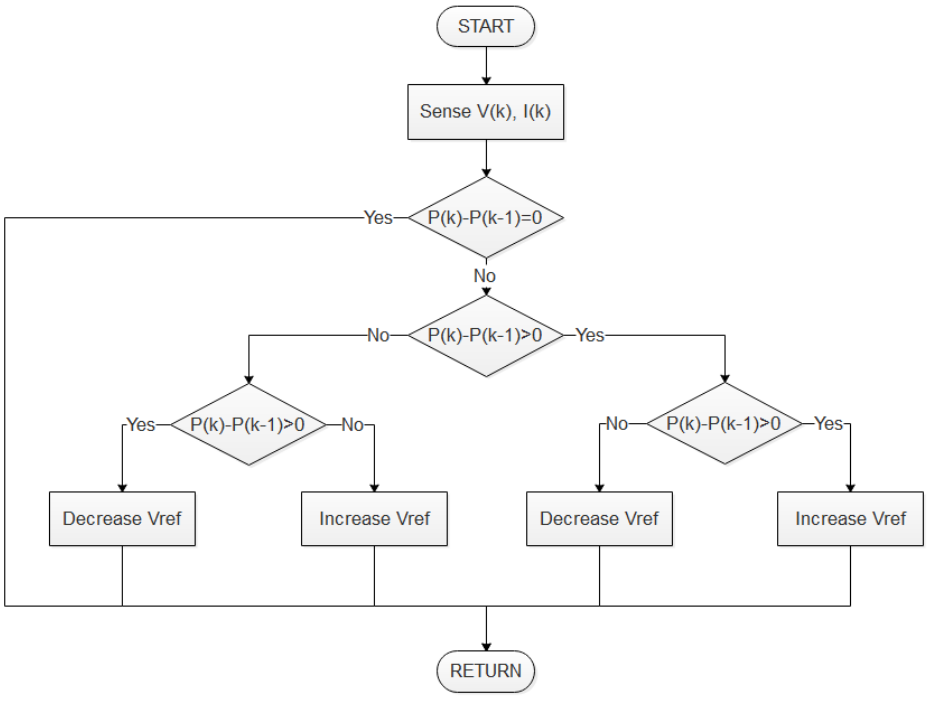

Figure 2. 5:Basic perturbation and observation algorithm

The P-V curve's careful observation shows that voltage increase and voltage decrease raises and reduces the power under the MPP left-hand-side operation and reduces and raises the power under MPP right-hand-side operation. Consequently, if the power rises, the successive

perturbation is sustained to capture the MPP, and the perturbation reverses in case of power drops. Two sensors measure the PV array voltage and current and compute power.

2.8.2 Hill Climbing

Hill climbing and perturbation and observation are sister methods, and therefore, they are alternative approaches with the same basics [99]. The Hill climbing technique implies a perturbation in the power converter duty ratio (cycle), while the perturbation and observation technique implies a perturbation in the PV array voltage of operation. The perturbation of the power converter's duty cycle perturbs the current and subsequently perturbs the voltage. Accordingly, the procedure is operational and applicable with average and instantaneous DC voltage and PV current with samples once in a switching cycle [100].

This procedure is continuous, and the system then oscillates about the MPP once attained to maintain MPP. The perturbation step size is reduced to minimize oscillation that could be experienced. However, the MPPT is slowed down by a smaller perturbation size, and therefore this adverse condition is solved by varying the perturbation extent, which diminishes as it approaches the MPP. In reference [100], the subsequent perturbation's extent is optimized using control based on fuzzy logic. Reference [101], proposed a double-level procedure offering swift tracking in level one and more precise tracking in level two. The estimation of the initial point close to the MPP is done by using a nonlinear equation that bypasses the first stage through comparison [102].

2.8.3 Incremental conductance

As presented in Figure 2.6, this algorithm compares incremental conductance in a PV system to instantaneous conductance. This raises or reduces the estimated voltage depending on the result until the MPP is attained. The technique, contrasting the hill climbing and perturbation and observation procedures, once MPP is reached, the voltage remains constant [99].

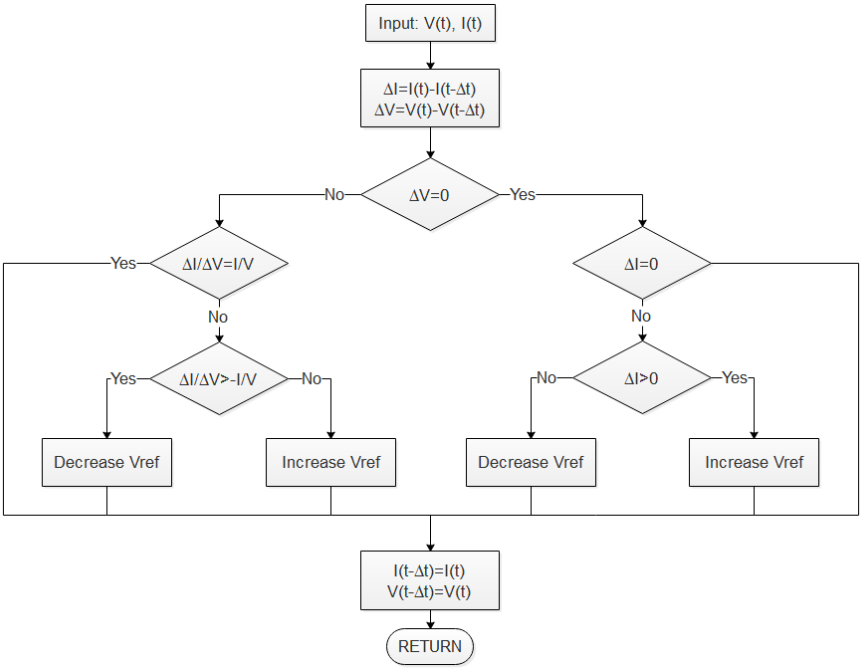

Figure 2. 6:Incremental conductance algorithm

The IC technique is based on the basis that the PV system's slope is zero on the maximum power point, as shown in Figure 2.4. The slope on the MPP's right is negative, while the slope is positive on the MPP's left, as given in the following equations.

$$\frac{dP}{dV} = 0, \text{ at maximum power point} \tag{2.3}$$

$$\frac{dP}{dV} > 0, \text{ left of maximum power point} \tag{2.4}$$

$$\frac{dP}{dV} < 0, \text{ right of maximum power point} \tag{2.5}$$

Since

$$\frac{dP}{dV} = \frac{d(IV)}{dV} = I + V\frac{dI}{dV} \approx I + V\frac{\Delta I}{\Delta V} \tag{2.6}$$

Consequently, Equations 2.3, 2.4, and 2.5 can be written as

$$\frac{\Delta I}{\Delta V} = -\frac{I}{V}, \quad \text{at maximum power point} \tag{2.7}$$

$$\frac{\Delta I}{\Delta V} > -\frac{I}{V}, \quad \text{left of maximum power point} \tag{2.8}$$

$$\frac{\Delta I}{\Delta V} < -\frac{I}{V}, \quad \text{right of maximum power point} \tag{2.9}$$

Therefore, the maximum power point is tracked by balancing instant conductance (I/V) with incremental conductance ($\Delta I/\Delta V$), in Figure 2.4. The reference voltage V^* is enforced for operation, and V^* is equivalent to V_{MPP} at the point of maximum power. The PV system activity

is sustained at the maximum power point when achieved. However, a shift in the current *I* is observed, and this implies that the PV array is still working.

The incremental extent defines how rapidly the system monitors the MPP. Quick monitoring may be accomplished with more significant incremental value, but the device does not function precisely at the point of maximum power but fluctuates around it, so a trade-off exists. In references [103][104], a strategy is suggested to put the PV operating point closer to the point of maximum power in the first stage and subsequently use the incremental conductance technique to monitor the MPP precisely in the second stage. The initial operating point is set by proper control of the power converter to balance the PV V_{OC}/I_{SC} with the load's internal resistance. In reviews [105][106], a linear function divides the I-V curve into two regions, one of which contains all the realistic maximum power points under changing atmospheric conditions. A less obvious but effective way to implement an incremental conductance method is to produce an error, which is a sum of instant and incremental conductance, as suggested in Equation 2.10 [99][105][106].

$$e = \frac{I}{V} + \frac{dI}{dV} \tag{2.10}$$

The error *e* drifts towards zero at the maximum power point considering Equation 2.10; thus, a proportional-integral control is employed in propelling *e* to zero.

2.8.4 Conclusion on MPPT algorithms

Other MPPT procedures and techniques include ripple correlation control (RCC), fractional short-circuit current [107], fractional open-circuit voltage [108][109], fuzzy logic control [110], fuzzy neural network [111], among several other methods. There is no consensus on the best MPPT method; thus, any technique that suits a particular application can be used. The essential criteria considered in MPPT development are implementation, sensors, multiple local maxima, costs, and applications. In power system applications generally, perturbation and observation, hill climbing, and incremental conductance are suitable [92].

2.9 Fault Ride-Through Requirement

The FRT provision ensures that every power plant's ability will stay linked under those limits during fault situations or low voltage [112]. E. ON and VE-T first suggested FRT specifications in 2003 German transmission operators. This condition is generally called FRT, and the voltage vs. time characteristics shown in Figure 1.3. The PV power plant should also deliver reactive power during voltage sags to improve the point of common coupling (PCC) voltage level until system stability is regained after its clearance. The disengagement of RESs beneath 80% of the rated voltage allows an unacceptable portion of the lost energy output. For example, the PV system method's FRT specifications have been introduced for low FRT demands in wind turbine

generations. They are revised in several countries as a consequence of increased efficiency and PV systems penetration levels. The overall FRT specifications of PV schemes concentrate on maintaining sustained grid-connection of DC-AC inverters without over-current generation but, in the meantime, offer dynamic reactive power support to aid grid recovery under different faulty conditions. Because of its benefits in voltage recovery and frequency stability, the FRT requirements are accepted and widely spread, ignoring the impacts of a high-penetration grid on transient stability.

2.10 The Fault Ride-Through Requirements and Ancillary Services.

The FRT ability is primarily reflected in the voltage-times chart that shows the required voltage disturbance capacity for a power generating sub-system due to failure to guarantee the systems' protection. The aim of using FRT is to avert loss of generation within the confinement of technical and non-technical feasibilities [113]. FRT's illustration is diverse across countries [114]. Units must remain connected to the grid at a given voltage irrespective of the grid conditions. Vilathgamuwa et al. [115] address its safety process and protection procedures in the event of a collapse in the main grid voltage.

The design of relays and some protective appliances rely heavily on low voltage ride-through requirements. A generation unit injects maximum reactive power during a fault without reaching the stipulated transient limit. Consequently, a system's FRT capability is enhanced in the face of different depths of voltage sags [18].

Symmetrical and asymmetrical disturbances have varying effects on the amplitude of three-phase voltage, and as a result, the impact on the FRT ability differs. Generally, the nature of the generating unit and its application and location all have a crucial effect on FRT analysis and applications. Lastly, the constituent generating units' grid resilience and dynamics significantly influence the draft of grid code guidelines on FRT. [113].

2.10.1 Low Voltage and High Voltage Ride-Through

The system operation needs to possess LVRT capabilities because of the high RES penetration level. The absence of automatic voltage regulation of a typical synchronous generator in RES based generating units has raised interest in WT and solar PV LVRT capability. Implementing this feature on wind turbines and solar PV is a fundamental challenge in sustaining a network connection [114] [116]. The operating cost compels the steady power generation during situations such as LVRT. The reactive current power injection standards under the grid fault for generating units are presented in this work. The switching high-capacity capacitors lead to voltage swell. Similarly, grid codes establish a new rule for faults causing an increase in voltage for power

generating systems, excluding synchronous generators [117]. Although this nature of fault rarely occurs, and capability, as prescribed by the grid code, is a high voltage ride-through (HVRT).

2.10.2 PV Generation FRT

Under high percentage penetration, the power system stability is significantly affected by the PV source's output during a fault. Consequently, the penetration level shall be taken into account in formulating FRT regulatory requirements. Emerging grid codes compel DERs to supply FRT ability and reactive power support ancillary services [1]. In certain grid codes, PV sources must possess FRT ability, just like other traditional power sources under the system’s fault condition. These requirements include prompt reversal to nominal active power generation and reactive power injection immediately after fault clearance. PV sources are expected to inject reactive power under fault conditions to mimic the synchronous generator excitation system's ability to tackle voltage sags. Furthermore, PV sources could remain grid-connected under zero percent voltage sags within a stipulated duration [118]. It is pertinent to note that PV sources must immediately resume pre-fault active power generation when system disturbance is cleared. PV inverters must have the appropriate capacities to meet these new requirements. Thus, an efficient control scheme/strategy is expected to be put in place for the solar PV-based systems.

2.11 Fault Ride-Through Enhancement

2.11.1 FRT Enhancement Strategies

Several strategies for FRT enhancement in grid-supporting inverter-based systems have been proposed in the literature and are summarized in Figure 2.7. The two primary categories of FRT enhancement approaches are extra device-based techniques and adjusted control-based techniques [119] [120].

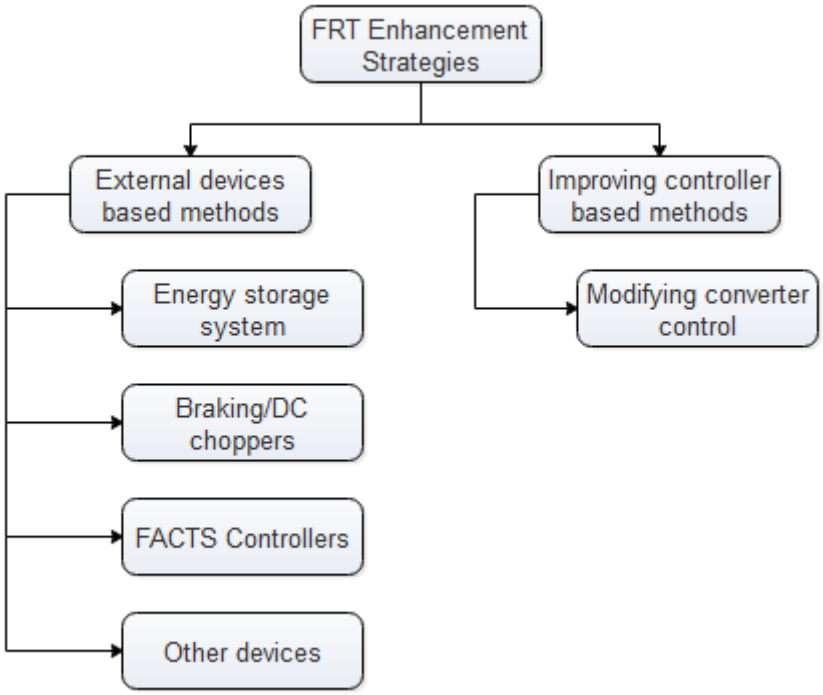

Figure 2. 7:FRT capability enhancement methods

2.11.1.1 External devices based methods

The FRT capabilities of microgrids have been enhanced through the deployment of external devices such as long-term and short-term ESSs, brake chopper, active crowbar system, flexible alternating current transmission system (FACTS) devices, dynamic voltage restorer (DVR), fault current limiters (FCLs) and Load Tap Changer.

2.11.1.1.1 Energy Storage Method

The ESSs consist of both short-term and long-term devices as battery ESS and supercapacitor ESS, respectively. The literature [121] [122] [123] proposes improving the FRT capacity using ESSs for grid-connected inverter-based systems, as presented in Figure 2.8. The ESSs are usually tied electrically to the DC-link via a DC-DC buck-booster [124].

The ESS absorbs surplus energy from the DC link when a DC overvoltage occurs; thus, AC grid fault. The DC-DC converter's duty cycle is altered in this period to reduce the power from the PV battery and, as a result, reduce DC link voltage. The ESS stored energy is released into the AC grid immediately after the grid fault is cleared, and thereby, the ESS enhances the FRT ability by regulating and guarding the DC side and DC-AC inverter from a high DC-link voltage. Furthermore, ESS implements the power oscillation suppression, peak shaving, and time-shifting [125] apart from improving the FRT.

However, ESS devices have high initial and servicing costs as the main disadvantages. Similarly, ESS also fluctuates DC parameters before and after a fault. While ESSs are used to suppress the DC link's excess energy and protect the DC-AC inverter by riding-through AC grid faults, the injection of reactive current to sustain the AC grid voltage is yet to be addressed.

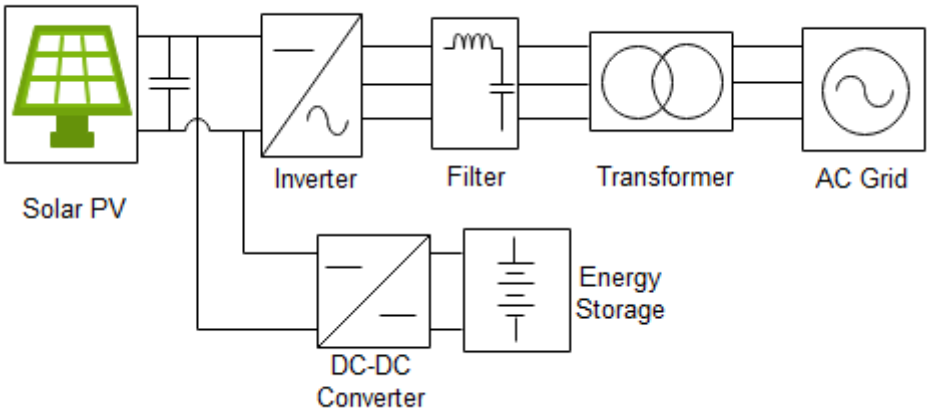

Figure 2. 8:ESS strategy for FRT Enhancement of Inverter-Based System

2.11.1.1.2 DC Braking chopper

As stated in the Statement of Research Problem, AC grid power and DC power imbalance when a fault occurs in the grid. Consequently, an over-voltage in the DC link is inevitable and thereby destroying the semiconductor switches. In literature, the braking chopper is proposed for both PV [126][127] and WT systems [128]. In the PV system, a brake chopper is installed the DC-link capacitor in parallel. In the WT system, an active crowbar (braking chopper) system for the PMSG system is installed at the DC-bus to dispel the excessive active power under faults [129][114]. DC Braking chopper comprises an IGBT switch with a series of power resistors, as presented in Figure 2.9. The gate signal G is equal to 1 where a fault is detected, and G equals 0 when there is no fault.

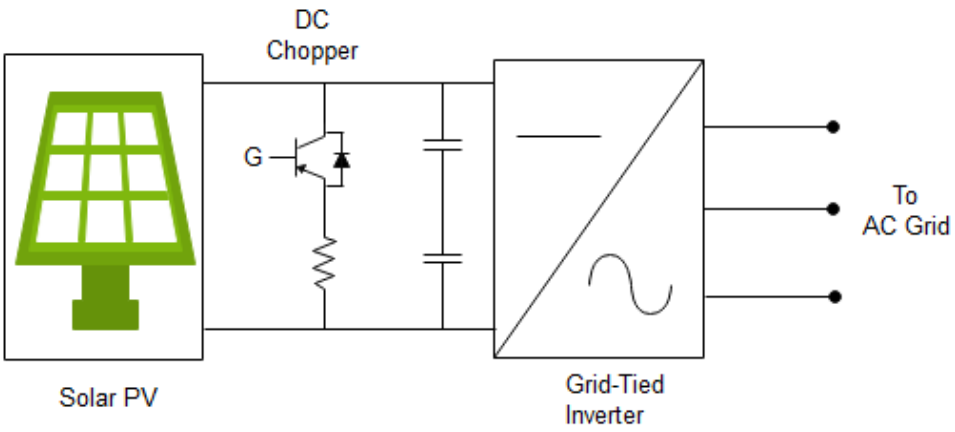

Figure 2. 9:Brake chopper protection for FRT Enhancement of Inverter-Based System

The braking chopper protects the DC-AC inverter from rising DC link voltage culminating in an overvoltage resulting from the AC grid fault. The gate pulses of the IGBT only trigger the chopper under fault. Hence, the power resistor absorbs the excess energy generated.

This braking chopper structure beneficial as a result of its low cost and simple control scheme. In references [126] [130], the DC-chopper and current limiters are utilized to absorb excess DC voltage and minimize extreme AC grid current to mitigate DC-link overvoltage and AC overcurrent problems, respectively, that can cause disconnection or inverter damage.

However, these braking choppers only dissipate power and possess no reactive power generation ability to support the AC grid voltage under fault. This is because all the generated power is dissipated at the expense of reactive power injection. As stated earlier in the previous paragraph, the braking chopper is combined with other devices such as Fault Current Limiter (FCL) to enhance performance. This, unfortunately, increases the overall cost.

2.11.1.1.3 FACTS Controllers

FACTS controllers are a valid alternative solution to ensure sustained grid connection of inverter-based systems under grid faults and to introduce reactive power as exigent. FACTS controllers are grouped into three categories based on grid connection; series, shunt, and hybrid. The FRT capabilities of both PV and WT systems have been enhanced in the literature. In WT especially, FACTS controllers in addition to FRT support, enhance voltage stability and provide reactive power supports. FACTS controller like static synchronous compensators (STATCOMs) [131], unified power quality conditioner (UPQCs) [132], static VAR compensator (SVC) [133], static synchronous series compensator (SSSC) [133], thyristor controlled series compensator (TCSC) [134] and dynamic voltage restorer (DVR) [135] have ended up playing immense roles in improving generating systems' FRT capabilities [136] [137]. For instance, STATCOM can improve the FRT of fixed speed wind turbines, and SSSC can be used in FRT capability enhancement control and voltage stabilization. During fault situations, series terminal voltage mitigation using DVR is done by injecting series voltage to the grid voltage at the PCC to retain steady DFIG stator voltage [138]. DVR uses a three-phase power converter tied through a transformer in series between WT and coupling points [139].

STATCOM’s reactive output power under the voltage dip is more-substantial compared to SVC. Figures 2.10 and 2.11 present STATCOM and SVC's shunt connection, respectively. Both devices can support the voltage recovery and inject reactive power, thereby increasing reactive power controllability for grid support to conform to grid code FRT stipulations. The coordination between the grid-connected inverter-based system and STATCOM has been proposed to deal with the suppression of grid fault's impact at the PCC. The traditional STATCOM is limited to only one capacitor-based storage with limited energy storage ability; however, reactive currents

are supplied to anticipate grid voltage recovery during faults or disturbances. Similarly, SVC injects reactive power to compensate for grid voltage sags, as discussed in [133].

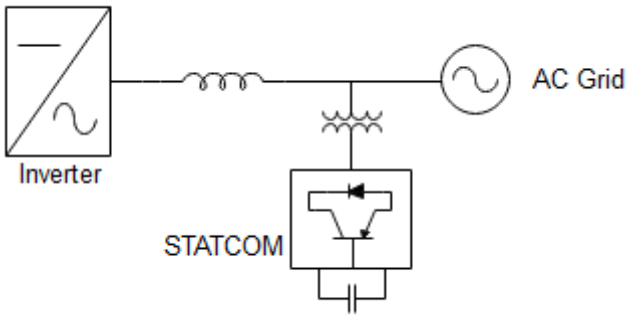

Figure 2. 10:FRT enhancement with shunt connection of STATCOM

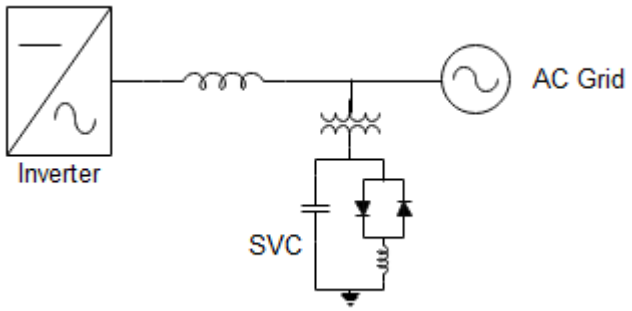

Figure 2. 11:FRT enhancement with shunt connection of SVC

These controllers are primarily utilized in compensating and injecting reactive power to boost the FRT capacity. DSTATCOM is a shunt compensation device generally used to solve power quality problems in distribution systems. The control strategy of the DSTATCOM plays a vital role in PCC voltage maintenance. Thus, [140] presents the application of a DSTATCOM to improve the power quality in a ship power system during and after pulse loads due to high energy demand. However, the system's entire cost and complexity are increased due to installing external FACTS hardware. For instance, installing devices such as DVR in the feeder line prevents the DC-AC inverter from sensing voltage drops in the AC grid. Furthermore, due to DVR's limited capacity, it is inappropriate for extreme AC grid voltage sag [141].

2.11.1.1.4 Fault Current and Voltage Limiters

Some external device methods are as well used in enhancing FRT capability in grid supporting inverter-based systems. These devices include fault current limiter (FCL), series dynamic braking power resistor (SDBR), and on-load electronic tap changer.

The FCL addresses the over-current when utilized between the microgrid and main grid as in reference [8][142] [143]. This shield the grid-tied inverter from the AC grid over-current and

thereby to improve the FRT under faults. The FCL decreases the excessive current at the DC-AC inverter's AC grid side under fault on the AC grid. Reference [144] proposed a dynamic current curtailment scheme applied in autonomous inverter microgrid in enhancing FRT and presented the effectiveness in limiting current and voltage. FCLs are utilized in reducing the contribution of the DGs to the fault's current level to enhance FRT [8]. References [145],[146] suggested different types of FCL and modified versions of FCL to enhance the microgrids, wind turbines, solar photovoltaic, and other DGs FRT capabilities. The FCL potential to enhance FRT is well established in the literature [147][148]. The FCL is located between microgrid and main network, and as such, FRT for all microgrid's DERs is commonly achieved [149].

The SDBRs are deployed in RES (PV and WT) systems to boost the FRT. The over-voltage concern is addressed by mitigating the excessive DC link voltage experienced under the AC grid fault. They are installed in series in-between the RES, and the grid coupling point is short-circuited in steady-state and activated under fault conditions, as presented in Figure 2.12.

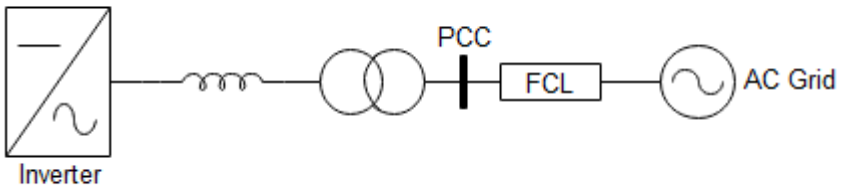

Figure 2. 12:FRT enhancement with a series connection of FCL-FRT enhancement with a series connection of FCL

The DC link voltage is in excess under faults, and subsequently, the SDBR dissipates excessive energy generated. This action prevents the DC-link voltage from accumulating sharply, thereby making SDBR address the power imbalance between DC and AC sides to improve FRT [19].

2.11.1.2 State of the art controller-based methods

Several strategies for FRT enhancement in grid-connected systems have been proposed in the literature; through the deployment of devices such as energy storage systems [121], brake chopper[126][127], active crowbar system, flexible alternating current transmission systems, dynamic voltage restorer (DVR), fault current limiters and load tap changer. All these external devices have enormous initial and servicing costs and introduce technical system complexities. For instance, energy storage causes fluctuations in the DC parameters before and after a fault. Thus, studies [28][150] have focused on developing modified, state-of-the-art strategies, and FRT is achieved with minimal cost and no extra devices. These are done with a view of improving host grid performance and fault recovery services. For instance, [151] presents a state of the art FRT techniques based on a low-pass notch phase-locked loop for smooth and swift transient responses

to sudden unbalanced grid conditions. Similarly, [152] proposed a strategy that supports the voltage by increasing the difference between positive-negative sequence voltages, thereby enhancing the grid-connected inverter system's stability and reliability. Furthermore, to attain a certain level of flexibility and robustness, [153] utilized a modulated pulse width modulation to control the stator phase voltage dynamic braking resistor for wind systems to mitigate grid fault types' impact. The control of single and double PV inverters is developed in [154] to resist disconnection during faults. The control proposed in [155] prevents active power generation and injects reactive power to support the grid. Nonlinear control for LVRT enhancement and post-fault recovery double stage PV system is proposed in [156]. A PV inverter control is presented in [157] which decouples active and reactive power, and seamlessly switch between the operating modes based on the state of the grid.

In the same way, many novel FRT management methods and schemes were suggested in [28][113][158]. Zamani et al. [150] recommend an inverter-interfaced RES regulating strategies to enhance the host grid's dynamic performance during disturbances and faults. In Kou and Wei [158], Some observations have been made regarding the specific grid code requirements for interconnection and operation of microgrids, which suggest LVRT functionality for microgrids and the provision of additional fault recovery services. A grid-connected microgrid is expected by these recommendations to ride through balanced and unbalanced sags in grid voltage, as expressed in the FRT voltage profile. Interruption, followed by a transition to autonomous operation, is only allowed if the fault persists [18].

A complementary controller for voltage is suggested in [159] for inverters-based DGs for the FRT control. This controller is expected to superimpose with numerous available voltage control schemes with minimum adjustments. These modifications, therefore, do not necessarily need to alter the initial configuration of these existing controllers. A hierarchical control has been proposed in the literature [65][160] towards realizing the numerous microgrid control and operation requirements. These propositions are with fundamental control goals, including voltage control, local power allocation among distributed energy units, frequency regulation, and power control (active and reactive) under synchronization with the host grid [16]. A rapid fault detection system plays a crucial role in enhancing the effects of these several strategies.

2.11.2 Fault and Voltage Sag Detection

Considering the urgency and impart of prompt reactive power support and active power limitation, the voltage sags detection to ensure appropriate and suitable action under faults is critical. The detection of voltage sag is crucial to the general performance of the FRT capability control during a fault in the grid in order to accurately and swiftly switch between operating

modes [161] [162]. Consequently, inbuilt fault detection schemes are put in place to disconnect grid-connected inverter-based systems during grid faults and avoid damage. As a result, several voltage-sag detection techniques, for instance, positive sequence technique [163], root means square (RMS) technique [164], peak value technique [165], the missing voltage method [161], and the wavelet transform technique [164] have been proposed. These techniques all have pros and cons with regards to detection speed, design complication, and effectiveness. Nevertheless, owing to the RMS technique design simplicity and insignificant complications, the detection technique is the most widely used. Topologies and control schemes of inverter-based microgrid must be designed and implemented to meet projected FRT requirements.

Towards fulfilling the fault ride-through requirements enacted by emerging grid codes for large-scale RES penetration in the traditional power grid system, the control schemes should take the following actions at the inception of grid voltage sag. [119]

1. Prompt and accurate fault detection to notify the system to effect a change from a normal operating mode to fault operating mode already put in place;
2. Protect the power electronic switched of the DC-AC inverter from AC grid overcurrent;
3. Protect the DC-link capacitor as well as the DC-AC inverter from the DC-link DC link overvoltage;
4. Generate and inject a commensurate reactive power to the depth of voltage sag in supporting grid voltage recovery,
5. Ensure sustained grid connection of the PV source to achieve overall system stability.

The DC source inverter-based microgrid, such as the PV system, must switch operating modes (steady-state to transient-state and vice versa) in complying with grid code FRT requirements. The FRT capability control's essence is to switch between these modes above immediately fault promptly is detected [161].

The voltage swells and sags are the short-term shift of the RMS value from the voltage's nominal value [166]. The voltage sags are distorted characteristics, reduction (less than 90%), and variation in RMS voltage outside the line voltage's normal range in a short duration (one-half cycle to specific seconds) caused by the internal or external power system fault. The magnitude and duration characterize a voltage sag or swell and maybe momentary or instantaneous, or temporary depending on their duration. The European Standard EN50160 [167] and IEEE Std 1159-1999 defined the duration and magnitude limits of systems' sag and swell. In the IEC terminology, the voltage sags or dips are among the dominant factors influencing the power supply quality [168]. The durations of momentary sag and temporary voltage sag are 'from

half cycles to 3 seconds' and 'from 3 seconds to 1 minute'. However, when the voltage sag is longer than one minute, it is called under-voltage [169].

The sags and swells are typically associated with systems' faults, starting current of large motor or heavy load starting, loads or switching, faulted line switching, lightning strokes, short circuits, and fast re-closing of circuit breakers. Thus, all these harm the system components and possess significant power quality disruptions, and they are critical challenges in transmission and distribution. Sag detection is the first essential step in sag compensation and fault ride-through operation. Thus, detection must be precise and swift to initiate the next crucial compensation and mitigation process, such as fault ride-through, power systems protection, and disconnection [166]. Precise and fast detection involves the identification and analysis of the dip or swell. [169]. Furthermore, the sag analysis and mitigation involve precise determining the sag or swell start and end [170]. Thus, the depth or magnitude, duration, and phase angle are essential parameters of sag. The duration is defined as the number of cycles during which the threshold value reduces the RMS value. The threshold is set at 90% of the nominal value.

Consequently, the detection of voltage sag is crucial to the general performance of the FRT capability control of a grid-supporting inverter-based microgrid during a fault in the grid. Therefore, a fast and accurate fault detection technique is technically recommended [162]. Inbuilt fault detection schemes are used to disconnect grid-connected inverter-based systems during grid faults and avoid damage to the DC sources. Conversely, the new FRT stipulations enforced by grid codes necessitate the inverter to stay grid-connected throughout the fault duration. The voltage sag or swell or dip detection is crucial to fault ride-through operation as it determines the dynamic performance of the fault ride-through enhancement device, tool, or strategy.

The voltage sag detection plays a vital role in sag compensation systems, protection, disconnection, and fault ride-through operation in which minimal delay time is required. There is no standardized procedure for detecting and evaluating the sag and swell; however, there are several literature techniques, but none is foremost in sag detection. As a result, several voltage-sag detection techniques, for instance, positive sequence technique [163], root means square (RMS) technique [164], synchronously rotating reference frame (SRRF), peak voltage value evaluation technique [165], the missing voltage method [161], and the wavelet transform technique [164]. These techniques all have pros and cons with regards to detection speed, design complication, and effectiveness. Nevertheless, owing to the RMS technique design simplicity and insignificant complications, the detection technique is the most widely used.

Most of these methods are based on transforming the AC signal into an equivalent DC signal, which provides ease of processing and analysis. Similarly, several detection methods express voltage sags in terms of RMS; however, the RMS method represents one cycle historical average

value, not an instantaneous value, which may lead to long detection time when voltage sag has occurred [170].

2.10.2.1 Root Mean Square Sag Detection Approach

Voltage measurement using the RMS value calculation is the most common tool. RMS values, continuously calculated for a moving window of the input voltage samples. This provides a convenient magnitude measurement, as expressed in the signal's energy content. A continuously moving window has N samples per cycle, Assuming the window contains N samples per cycle (or half cycle). The sag is detected after data for a window period has been processed. The RMS voltage is expressed as Equation 2.11. The resulting RMS value at N sampling instant "i" can be calculated by:

$$V^{rms}(i) = \sqrt{\frac{1}{N}\sum_{n=0}^{N-1} V^2(i)} \tag{2.11}$$

where, *N* is the number of the samples per cycle of the fundamental. *v(j)* is a jth sample of the recorded voltage waveform. V^{rms} is delayed relative to the phase voltage by N-1 sample points due to the N-sample window used.

The start and drop time of the sag is determined based on the predefined RMS voltage thresholds. The first point when Vrms falls below 0.9 pu is the start time. Search an interval with drops under 0.9 pu for at least half a period to find the end time. The recovery time is the first point in this interval. Because the RMS voltage moves to utilize a single-cycle window, the time the voltage starts or ceases, and the time that the voltage is below the defined threshold, it can be up to one cycle lag.

Figure 2.13 demonstrates a z-domain illustration for the RMS voltage magnitude evaluation using a moving window. The concept observes the shifts in voltage during the fault phenomenon as near as possible. The closer the fault event is displayed, the more RMS values are measured. The voltage drop is proportional to the sag level [171].

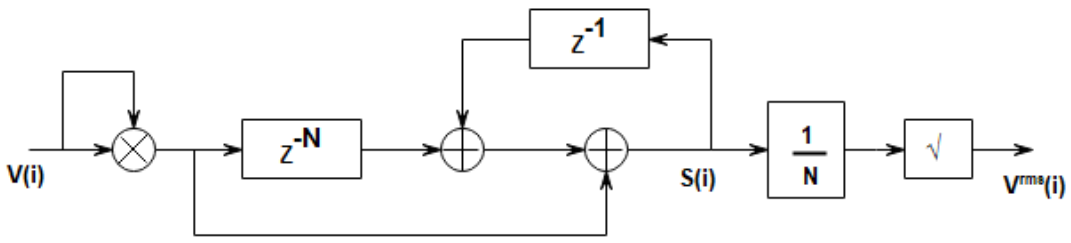

Figure 2. 13:The moving window's RMS voltage evaluation

According to the Equation 2.11 and Figure 2.13

$$s(i) = \sum_{n=0}^{N-1} V^2(i-n) \tag{2.12}$$

And

$$s(i-1) = \sum_{n=0}^{N-1} V^2(i-n-1) \tag{2.13}$$

Therefore, by subtracting Equation 2.13 from 2.12

$$s(i) - s(i-1) = \sum_{n=0}^{N-1} V^2(i-n) - \sum_{n=0}^{N-1} V^2(i-n-1) \tag{2.14}$$

Thus

$$s(i) - s(i-1) = V^2(i) - V^2(i-N) \tag{2.15}$$

Therefore

$$s(i) = V^2(i) - V^2(i-N) + s(i-1) \tag{2.16}$$

2.10.2.2 Peak value evaluation method

The peak voltage also enables the monitoring and detection of voltage sags. The input or sampled signal Vi(t) is given by Equation 2.17 where, Vm is the peak value of the input, and t is one half-cycle integer. The maximum of the absolute value over the preceding half-cycle is estimated in each of the samples.

$$V_i(t) = V_m \sin(\omega t) \tag{2.17}$$

If Vi(t) is shifted 90^o out of phase, therefore V'i (t) is obtained as Equation 2.18. Thus, the original signal Vi(t) and obtained V'i (t) form a pair of orthogonal functions.

$$V_i'(t) = V_m \sin(\omega t + 90^0) = V_m \cos(\omega t) \tag{2.18}$$

The orthogonal functions can be separately squared and multiplied by a multiplication factor k. Therefore, these resultant expressions are obtained and given as Equations 2.19 and 2.20. The multiplication factor k =1 for optimum performance of the square root circuit.

$$V_1(t) = kV_m^2 \sin^2(\omega t) \tag{2.19}$$

$$V_2(t) = kV_m^2 \cos^2(\omega t) \tag{2.20}$$

The orthogonal detector output voltage is equal to the peak (maximum) input voltage value due to the orthogonal pair concept. Hence, the obtained input peak is given in Equation 2.21.

$$V_{Peak} = \sqrt{V_1(t) + V_2(t)} \tag{2.21}$$

The process above measuring the peak value is shown in Figure 2.14. The line to neutral voltage is estimated, and the cosine equivalent of the voltage is determined by shifting the angle by 90°. The resultant voltage signals are squared and summed. The resultant's square root signifies the peak value used for the sag detected and analysed.

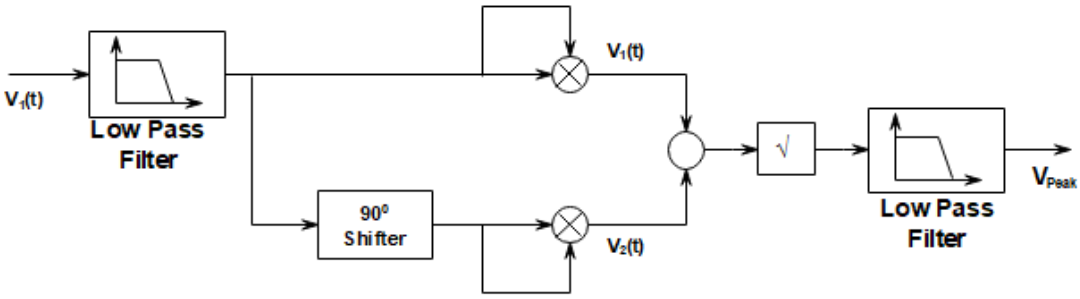

Figure 2. 14:peak Voltage measurement sag detection method

2.10.2.3 Synchronous Rotating Reference Frame (SRRF)

The SRRF voltage sag detection applies abc-dq transformation is estimate the equivalent dc quantities (d-q components proportional to the Vabc) of a three-phase system as shown in Figure 2.15 and expressed in Equation 2.22.

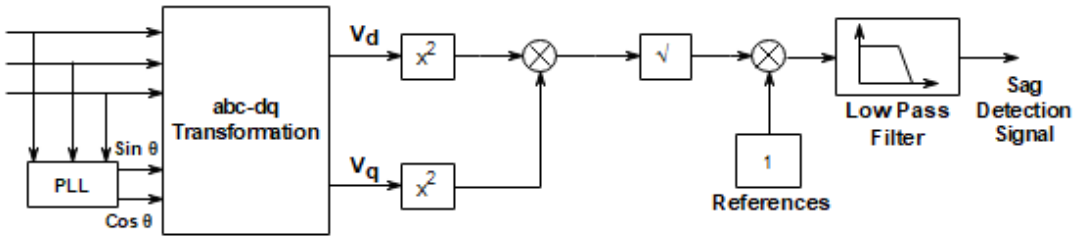

Figure 2. 15: Synchronous Rotating Reference Frame Technique

$$\begin{bmatrix} V_d \\ V_q \end{bmatrix} = \frac{2}{3}\begin{bmatrix} \cos(\omega t) & -\sin(\omega t) \\ \sin(\omega t) & \cos(\omega t) \end{bmatrix}\begin{bmatrix} 1 & -1/2 & -1/2 \\ 0 & \sqrt{3}/2 & -\sqrt{3}/2 \end{bmatrix}\begin{bmatrix} V_a \\ V_b \\ V_c \end{bmatrix} \quad (2.22)$$

The transformation involves both Clark and Park transformations. The SRRF voltage sag detection is also applicable in the single phase system with the phase shifting to achieve an orthogonal AC voltage. Consequently, the 90º phase shifting is similar to the peak detection method earlier discussed. Thus, the orthogonal AC voltage in stationary reference frame are given by Equation 2.23 and Figure 2.16:

$$\begin{aligned} V_\alpha &= V_{in} = V_m \sin(\omega t) \\ V_\beta &= \frac{V_{in}}{\omega} = \frac{V_m \sin(\omega t)}{\omega} = V_m \cos(\omega t) \end{aligned} \quad (2.23)$$

Where Vα and Vβ are the stationary reference frame equivalents of the single phase voltage Vin shifted.

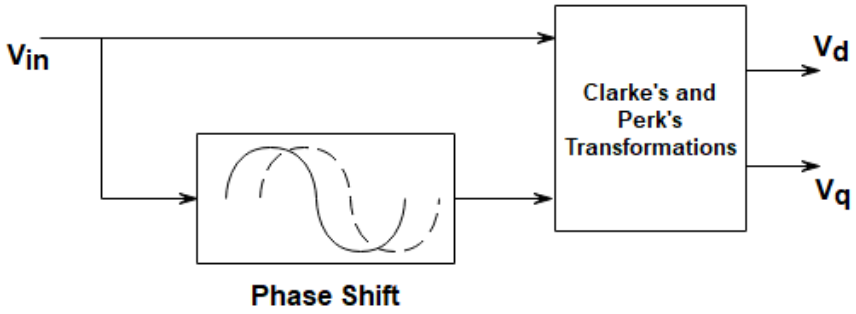

Figure 2. 16:Phase shifting in a single-phase system

The obtained DC voltage components V_d and V_q are then compared with the reference signal to generate the sag signal. Figure 2.15 recognizes the voltage sags of grid voltages, then V_{dq} voltage is calculated from V_d voltage and V_q voltage by using the following equation.

$$S_{dq} = \left|1 - \sqrt{V_d^2 + V_q^2}\right| \quad (2.24)$$

This detection method, with additional processing, minimizes the impact of point-on-wave. [166]. From Equation 2.24, V_{dq} varies with grid voltage magnitude, and the grid voltage variations (sag or swell) can be detected via the voltage value. However, in the event of an un-balance voltage sag (a single voltage and two-phase voltage sag) but not in the case of the balance voltage sag (three-phase voltages sag), this V_{dq} voltage must be filtered by a low-pass filter(LPF) to isolate a two to 100 Hz component (for 50-Hz distribution systems) due to this 100-Hz component. The proper cut-off frequency value of LPF, i.e., 50 Hz, is selected to remove the 100-Hz element.

Finally, the V_{dq} or V_{dq} filtered is compared with the dc comparator (that is to say, 0.9 pu). The comparator's output is a sag signal that initiates a fault ride-through process for voltage dip under fault. However, the use of low LPF cut-off frequencies results in a long detection time delay.

Figure 2.15 shows that squares' square root is obtained after converting the three-phase voltages into *d* and *q* elements. The value extracted is subtracted from a fixed value and is then filtered out with an LPF to remove the positive sequence part of voltage from the resulting element... However, this filter may delay phase or time; hence, the detection process response times are typically extended. A hysteresis comparator is supplied with a filter's output, which is the voltage sag/ swell measuring signal. This technique's significant disadvantage is that it uses three-phase voltage detection measurements and cannot detect the dip below a certain depth [166]. Similarly, a significant delay time is introduced through the low cut-off frequency of LPF, and this is poised to affect the compensation operation or fault ride through.

2.10.2.4 Fourier Transform (FT)

Another technique that can provide information about the grid voltage status is the Fourier Transform (FT), as shown in Figure 2.17. [166]. The magnitude and phase of each frequency variable of the supply can be precisely discovered by this method in the presence of harmonics. In order to avoid errors with the returned information about the fundamental element, previous methods effectively filter out harmonics other than the fundamental component. This process can lead to a temporary delay when the fundamental component phase changes are detected [172]. The RMS input voltage variance is calculated in FFT-based algorithms to evaluate the voltage sag. A discrete Fourier Transform (DFT) algorithm [173] is used to calculate the fundamental component's RMS value. Equation 2.5 is the Fourier series transform of the source voltage V(t).

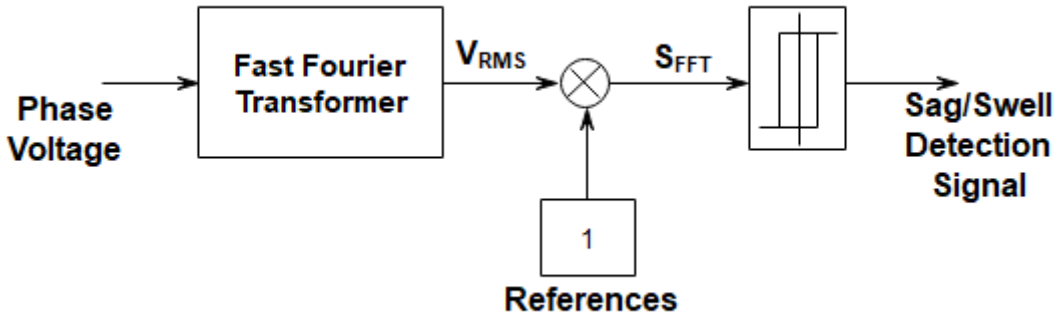

Figure 2. 17:Fast Fourier Transform Technique

$$v(t) = \frac{a_0}{2} + \sum_{n=0}^{\infty} a_n \cos n\omega_0 t + \sum_{n=0}^{\infty} b_n \sin n\omega_0 t \qquad (2.25)$$

for n = 1, the fundamental component a_1 and a_2 are evaluated by Equations 2.26 and 2.27 which separates the real and imaginary components

$$a_1 = \frac{2}{T}\int_0^T v(t)\cos\omega_0 t \cdot dt \tag{2.26}$$

$$b_1 = \frac{2}{T}\int_0^T v(t)\sin\omega_0 t \cdot dt \tag{2.27}$$

By applying discrete Fourier Transform (DFT) to the rectangular form, the Equations 2.28 and 2.29 are obtained.

$$a_1 = \frac{\sqrt{2}}{N}\sum_{i=0}^{N} v\left(t - i\frac{T}{N}\right)\cos\left(2\pi\frac{i}{N}\right) \tag{2.28}$$

$$b_1 = \frac{\sqrt{2}}{N}\sum_{i=0}^{N} v\left(t - i\frac{T}{N}\right)\sin\left(2\pi\frac{i}{N}\right) \tag{2.29}$$

The RMS value for the basic component can be determined as Equation 2.30 using the value of a_1 and b_1. Sag detection is derived from Equation 2.30.

$$S_{FFT} = \left|1 - \sqrt{a_1^2 + b_1^2}\right| \tag{2.30}$$

2.10.2.5 Proposed Delayed Signal Cancellation (DSC)

RMS approach prompts one fundamental period delay in the voltage variation detection ratio in the grid, which brings inaccurate estimation due to low-order harmonic distortion. Furthermore, in the peak voltage approach, the grid voltage's amplitude is the maximum of the sampled grid voltage within a particular time. Thus, this will significantly chomp half of the fundamental cycle in estimating the percentage grid voltage sag for the FRT procedure coupled with the fact that the low-order harmonic distortion prompts inaccurate sag/swell detection. The discrete FT technique extracts the voltage signals at various frequencies and computes their magnitudes, frequencies, and phase angles. However, just like the peak voltage technique, discrete FT consumes a minimum of one fundamental cycle to estimate the equivalent grid voltage accurately. Hence, under sag or swell in grid voltage, one fundamental cycle delay is prompted for precise sag detection. Under the balanced condition, the voltage magnitude in all the three phases of the three-phase system is relatively uniform, and the SRRF promptly and precisely estimate these magnitudes. However, this estimation is significantly inaccurate due to the low-frequency ripple appearance in the direct and quadrature components under unbalance or low-order harmonic distortion. Consequently, this is enhanced by inserting digital filters to smoothen these

components, but this cannot aid the accurate estimation of the equivalent magnitude per phase, thereby making this approach insufficient for FRT application [174]

A fault detection procedure built on a delayed signal cancellation (DSC) algorithm will be implemented to detect the fault instantly to achieve efficient and prompt responsiveness. The DSC algorithms will enhance the phase-locked loop concept with faster detection of the positive sequence and negative sequences, unlike Root Mean Square Sag Detection, Peak value evaluation, Synchronous Rotating Reference, and Fourier Transform. The DSC technique is efficient for faster convergence and detects faults within 0.1515ms under various unbalanced voltage conditions and will be evaluated in this work. The DSC will be used to determine the fault interval at which active and reactive power references are adjusted appropriately. This will enable a fault ride-through action to be taken to mitigate the fault's effect on the microgrid and resist the disconnection. The DSC will be appropriately applied to determine the extent of power curtailment, and dynamic grid voltage supports based on voltage grid voltage depth. Lastly, DSC is used to give adequate information for controlling the PCC voltage, ensuring quality power delivery to the microgrid loads irrespective of the transients on the main grid alongside the proposed switched reactor. The simulation study will be used to evaluate the proposed scheme's performance and effectiveness under the Spanish code's FRT requirements [1].

CHAPTER THREE
INVERTER-BASED MICROGRID DISCRETE-TIME MODEL

3.1 Introduction

Chapter three presents the modelling approach for inverter-based microgrids to operate both in grid forming and grid feeding modes, culminating in standalone and grid-connected operation modes for constituent inverters. This chapter also provided the theoretical framework for introducing active power-frequency and reactive power-voltage droops into the operation's grid feeding mode. This framework achieves a more advanced grid supporting mode of operation to participate in grid frequency and voltage regulations while running in a grid synchronous mode. In this chapter, time-domain models of grid supporting inverter-based microgrid systems are developed. Owing to the lack of sensitive communication interfaces between the parallel inverter[54] [175], the DER systems with droop control are widely used in the science community for coordination within an inverter microgrid [176]. Furthermore, numerous researches accomplished stable reactive power sharing using a faster-control loop that emulates the line impedance by implementing virtual output impedance in the droop control technique. However, in this chapter, droop control will serve as an interface between traditional primary control and the proposed secondary control to enhance the fault ride-through. The droops ensure that the systems participate in grid frequency and voltage regulation by active and reactive power control. Furthermore, in the case of a grid-supporting system operating as a voltage source (grid-supporting grid forming), a virtual impedance is incorporated into the droop system to suppress the fault current in the autonomous operation of the microgrid. The developed models provide accurate phase angle estimation, which is valid for power conditioning and secondary power references for effective fault ride-through. The simulation results for the different operation modes developed are presented to validate the developed models' function.

3.2 Inverter Based Microgrid Control

Different microgrids with a wide-ranging array of operation and control objectives, grid-forming, grid-feeding, and grid-supporting require sets of well-coordinated and designed control schemes to guarantee an efficient operation in a dynamic state [56][3]. The power-sharing, voltage/power, and current controllers locally regulate the inverter's output variables with high-performance bandwidth to ensure prompt response time in a dynamic state. In the hierarchical control architecture, these three different loops constitute the primary control level that provides microgrid stability.

The primary control's primary objective is to control the active power and reactive power interaction and export between DERs and host AC grid as voltage sources are controlled by the

current [177]. Consequently, it is imperative to develop grid-forming and grid-feeding systems models to understand the dynamics before transforming the models into a grid-supporting system for investigation purposes.

3.2.1 Grid-Forming Inverter-Based Microgrid Topology

The grid-forming inverter-based microgrid is signified as an ideal low-output voltage source which operates based on its own pre-set voltage reference E^* and frequency reference ω^* of the microgrid through a suitable control as presented in Figure 3.1

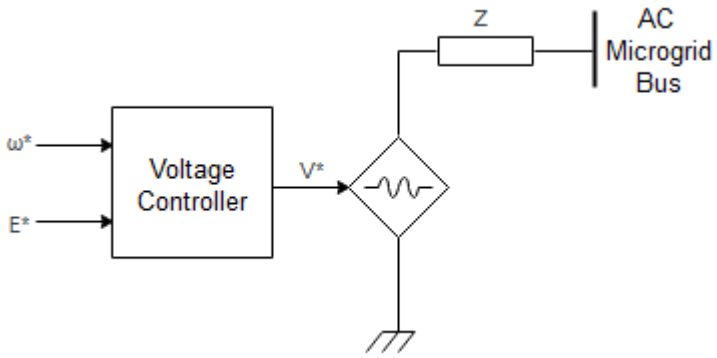

Figure 3. 1: Schematics of the grid-forming inverter-based microgrid.

3.2.2 Grid-Feeding Inverter-Based Microgrid Topology

The grid-feeding inverter-based microgrid is designed to deliver power to an operational grid as a controlled current source. They can be perceived as the ideal current source in parallel with high impedance to the grid. The basic structure of a grid-feeding inverter-based microgrid is presented in Figure 3.2

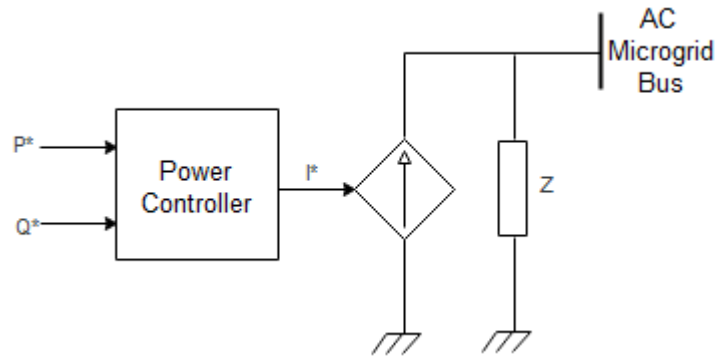

Figure 3. 2: Schematics of grid-feeding inverter-based microgrid

where P^* and Q^* respectively represent the active power and reactive power delivery. The current source is synchronized seamlessly with the grid voltage at the PCC, with the AC grid controls active power and reactive power precise exchange (import and export) with the host grid. In grid-

feeding inverter-based microgrid applications, the controlled source requires a grid source or synchronous generator to form the grid voltage references to operate. Thus, a grid-feeding inverter-based microgrid typically functions in a grid system with an energized source that sets the voltage and frequency references.

3.2.3 Grid-Supporting Inverter-Based Microgrid Models

A grid-supporting inverter-based microgrid control possesses a grid-feeding and grid-forming inverter-based microgrid control goals. The main goal is to deliver adequate active and reactive power values to regulate the grid voltage and frequency. The AC main grid is assumed to operate as an infinite bus at pre-set voltage and frequency, thereby accepting any amount of power generation.

3.2.3.1 Grid-Supporting Grid-Feeding Inverter-Based Microgrid Model

Furthermore, the grid-supporting grid-feeding inverter-based microgrid control is signified by an AC-controlled ideal current source parallel with a shunt impedance, as shown in Figure 3.3. Its implementation is similar to the grid feeding system operating as a controlled current source. Consequently, at least one grid forming unit is required for it to operate.

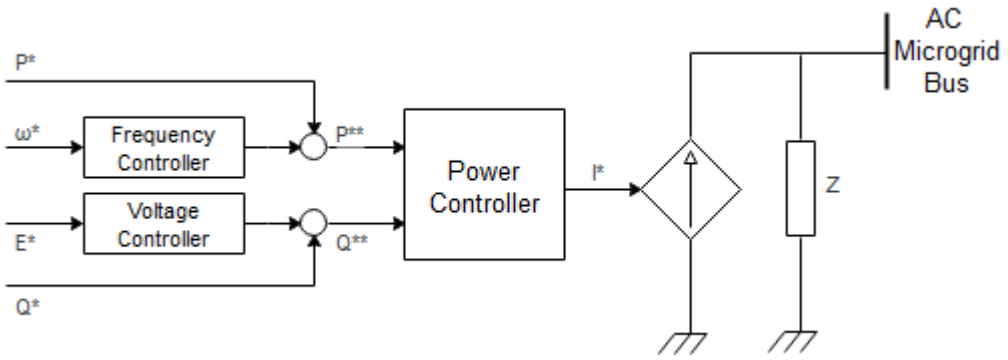

Figure 3. 3: Schematics of grid-supporting grid-feeding inverter-based microgrid

3.2.3.2 Grid-Supporting Grid-Forming Inverter-Based Microgrid Model

Finally, the grid-supporting grid-forming inverter-based microgrid control is signified as an AC voltage ideal source in series with a link impedance, as revealed in Figure 3.4. Unlike grid-supporting grid-feeding, grid-supporting grid-feeding is controlled as a voltage source with link impedance operating in both grid-connected and autonomous mode, as a synchronous generator does in a conventional grid.

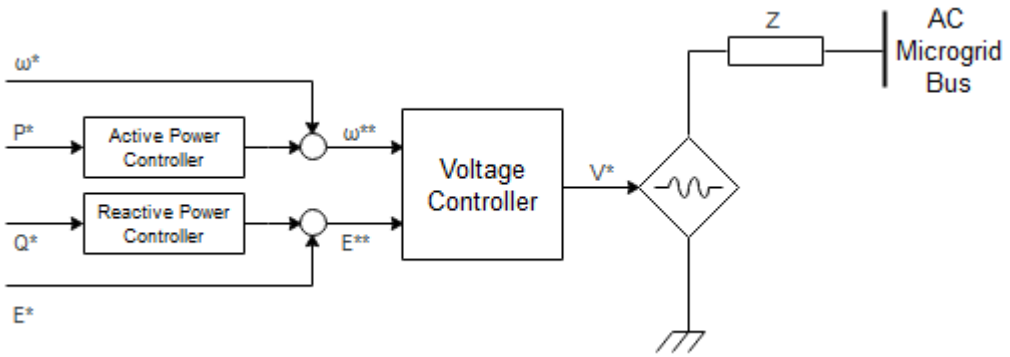

Figure 3. 4: Schematics of grid-supporting grid-forming inverter-based microgrid

The droop control is added to both grid-forming and grid feeding systems to form grid-supporting grid-forming and grid-supporting grid feeding systems, respectively. The droops add the capabilities to regulate their output current/voltage to keep the value of the grid frequency and voltage amplitude close to their rated values. However, the physical link impedance effect is commonly emulated within the grid-supporting grid-forming system's control loop to operate as a voltage source.

3.3 Grid Synchronization and Control Model Simulation

The AC grid voltage parameters, voltage magnitude, grid frequency, and phase angle of an inverter-based MG are essential to accurate and dynamic control of active power and reactive power injected. Thus, as stated earlier, a precise estimation of these parameters significantly affects the general inverter performance. Continuous parameter sampling and AC grid condition monitoring must also decide the appropriate and optimal operation mode dynamically. The inverter-based microgrid synchronization using PLL ensures appropriate response during normal and abnormal AC main grid conditions [56].

3.3.1 Phase-Locked Loop

Grid-connected systems are synchronized with the main grid with a three-phase Phase Lock Loop model. PLL is a closed-loop control system that uses an internal frequency oscillator to monitor a three-phase sinusoidal signal's frequency and phase. Figure 3.5 presents the internal illustration of PLL

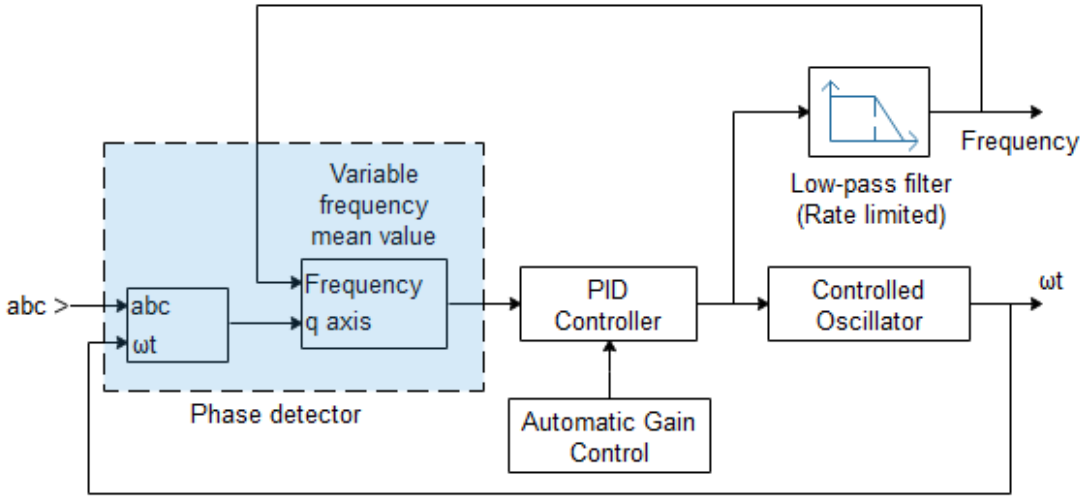

Figure 3. 5: Block diagram of the Phase Lock Loop.

The three-phase voltage input signal is Park transformed into a rotating frame *dq0* using an internal oscillator's angular velocity. The signal's quadrature axis is filtered using a Mean (Variable Frequency) block, proportional to the phase lag of *abc* signal and the rotating inner oscillator frame. With optional automatic gain control, a PID controller maintains the phase lag difference to zero by acting on a controlled oscillator. The PID output corresponds to the angular speed and is systematically processed and transformed to the equivalent mean frequency (Hz).

3.3.1.1 ABC-DQ0 Transformation

The *abc* to *dq0* model performs a Park transformation in a rotating reference frame, as shown in Figure 3.6.

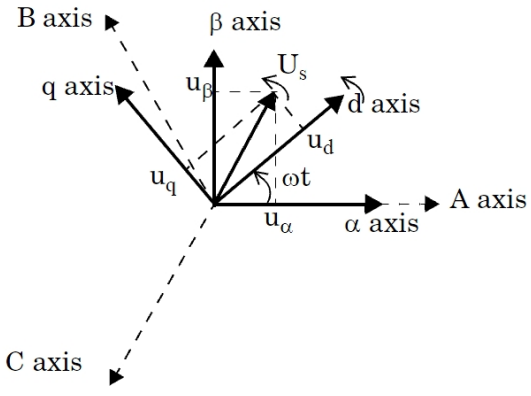

Figure 3. 6: Reference frame transformations

The *dq0* components of the AC grid voltage are deduced from the grid voltage V_{abc} signals by performing a Clarke transformation *abc* to *αβ0* in a static reference frame. Now an *αβ0* to *dq0* transformation in a rotating reference frame is performed such that there is $-\omega t$ rotation on the space vector equivalent of the voltage V_s, where V_s implies

$$V_s = v_\alpha + ju_\beta \tag{3.1}$$

The transformation of the *abc-to-dq0* depends on the alignment of the *dq* frame at *t=0*. The rotating frame's position is set by ωt (where ω represents the speed of ωt frame rotation). The following relations are obtained when the rotating frame is aligned with V_a axis:

$$V_s = v_d + ju_q = \left(v_\alpha + ju_\beta\right)\cdot e^{-j\omega t} = \frac{2}{3}\left(v_a + u_b \cdot e^{\frac{-j2\pi}{3}} + v_c \cdot e^{\frac{j2\pi}{3}}\right)\cdot e^{-j\omega t} \tag{3.2}$$

$$v_o = \frac{1}{3}\left(v_a + v_b + v_c\right) \tag{3.3}$$

$$\begin{bmatrix} v_d \\ v_q \\ v_o \end{bmatrix} = \frac{2}{3}\begin{bmatrix} \cos(\omega t) & \cos\left(\omega t - \frac{2\pi}{3}\right) & \cos\left(\omega t + \frac{2\pi}{3}\right) \\ -\sin(\omega t) & \sin\left(\omega t - \frac{2\pi}{3}\right) & \sin\left(\omega t + \frac{2\pi}{3}\right) \\ \frac{1}{2} & \frac{1}{2} & \frac{1}{2} \end{bmatrix}\begin{bmatrix} v_a \\ v_b \\ v_c \end{bmatrix} \tag{3.4}$$

The inverse transformation of equation 3.3 is given by equation 3.4, which is the exact values of each phase voltage

$$\begin{bmatrix} v_a \\ v_b \\ v_c \end{bmatrix} = \begin{bmatrix} \cos(\omega t) & -\sin(\omega t) & 1 \\ \cos\left(\omega t - \frac{2\pi}{3}\right) & -\sin\left(\omega t - \frac{2\pi}{3}\right) & 1 \\ \cos\left(\omega t + \frac{2\pi}{3}\right) & -\sin\left(\omega t + \frac{2\pi}{3}\right) & 1 \end{bmatrix}\begin{bmatrix} v_d \\ v_q \\ v_o \end{bmatrix} \tag{3.5}$$

3.3.1.2 Variable Frequency Mean Model

The Mean (Variable Frequency) model computes the mean value of the *q*-component of voltage v_q connected to the block's second input. The mean value of v_q is computed over an average running window of one cycle of the frequency f of the grid voltage signal:

$$Mean\left(v_q(t)\right) = \frac{1}{T}\int_{(t-T)}^{t} v_q(t)\cdot dt \tag{3.6}$$

where the period *T* is the inverse of frequency f. Furthermore, the initial mean output $v_q(t)$ is held constant to the specified initial value because the mean value is computed immediately after one cycle of simulation is completed

3.3.1.3 Automatic Gain Control

Automatic Gain Control is developed as a Positive Sequence detection system driven by the frequency *f* (Hz) and angular position *ωt* (radians) outputs of the overall PLL. The Positive-Sequence is modelled to compute the positive-sequence component (amplitude and phase) of the input AC grid voltage signal over a running window of one fundamental frequency cycle. The input *ωt* gives the reference frame required for the computation. The positive-sequence component of a three-phase voltage signal V_1 is computed as shown in equation 3.7

$$V_1 = \frac{1}{3}\left(V_a + a \cdot V_b + a^2 \cdot V_c\right) \tag{3.7}$$

where V_a, V_b, and V_c are the phasor equivalents of the three-phase AC grid voltage at the fundamental frequency. Furthermore, the complex operator *a* is specified as Equation 3.8 and are used in the three-phase voltage with a phase difference of 120^0 under a balanced condition.

$$a = e^{\frac{j2\pi}{3}} = 1\angle 120^0 \tag{3.8}$$

A Fourier analysis over one cycle of the fundamental input frequency is first applied to the three input signals *f*, *ωt,* and V_{abc} to evaluate the phasor values at the fundamental frequency. Subsequently, the transformation is applied to obtain a positive sequence.

3.3.1.4 PID Controller

The PID Controller output reflects the proportional, the integral, and the derivative of the input signal. The weights are the proportional, integral, and derivative gain parameters. The PID controller operates in one common implementation along the feedforward path of a feedback loop.

3.3.1.5 Controlled Oscillator

This oscillator is modelled as an integrator with modified inputs. The main input is the angular speed *ω* (radian per second) output of the PID Controller. The Integrator block outputs *ωt*, which is the integral equivalent of the input *ω* signal to time. In this work, the integrator is implemented as a one-state dynamic scheme presented in Equation 3.9.

$$\begin{cases} \dot{x}(t) = u(t) \\ y(t) = x(t) \end{cases}; \quad x(t_0) = x_0 \tag{3.9}$$

where *u* is the integrator input, *y* is the integrator output, *x* is the integrator state, and x_o is the initial state of x. The integrator's initial condition is defined as the algebraic difference between the integrator state and a constant (2π).

The integrator is modelled to self-readjust its state to the specified initial state based on an internally generated signal. This signal passed alongside a specified constant (2π) is passed through a Relational Operator, which performs the input's specified relational operation. The Relational operator has two input signals which output 'True' if the first input is greater than the second input.

3.3.1.6 Low pass filter

The PLL exhibits low-pass filtering attributes which detect the phase angle of the input voltage. Hence the error is attenuated using the second-order low pass filter model implemented in this work has the following transfer function in Equation 3.10.

$$H(s) = \frac{\omega_n^2}{s^2 + 2\xi\omega_n s + \omega_n^2} \tag{3.10}$$

where s is the Laplace operator, ω_n is natural frequency; $\omega_n = 2\pi f_n$ and ζ is the damping ratio

3.4 Control Simulation

The four systems' control implementations are done in MATLAB/SimPower environs using Tables 3.1, 3.2, and 3.3.

Table 3. 1:Grid Implementation Parameters

Parameters	Descriptions	Values
P^*	Microgrid active power reference	10 kW
Q^*	Microgrid reactive power reference	0 kVAr
P_L	Active power of the load	10 kW
Q_L	Reactive power of the load	5 kVAr
V_{abc}	Voltage (phase-phase)	400 V
V_{dc}	DC bus voltage	1100 V
f	Frequency	50 Hz
C_f	LC filter capacitance	2.31 μF
L_f	LC filter inductance	11 mH
ω_{cut}	Cut-off angular frequency	100π
E	Single-phase voltage reference	330 V
$K_{p\,I}$	proportional current loop gain	100
$K_{i\,I}$	integral current loop gain	1000
$K_{p\,V}$	proportional voltage loop gain	0.0125

$K_{i\,V}$	integral voltage loop gain	2
K_{PD}	Active power droop gain	20000
K_{QD}	Reactive power droop gain	437.4

Table 3. 2: PCC Transformer Parameters.

Parameters	Descriptions	Values
Pn	Nominal power	210 MVA
fn	Nominal frequency	50 Hz
V1-RMS	Voltage of winding 1	400 V
V2-RMS	Voltage of winding 2	11 kV
R_1/ R_2	Winding 1 and 2 resistance	0.27 pu
L_1/ L_2	Winding 1 and 2 inductance	0.08 pu
Rm	Magnetization resistance	500 pu
Lm	Magnetization inductance	500 pu

Table 3. 3:Grid Synchronization Parameters.

Parameters	Descriptions	Values
*P**	Microgrid active power reference	10 kW
*Q**	Microgrid reactive power reference	0 kVAr
P_L	Active power of the load	10 kW
Q_L	Reactive power of the load	5 kVAr
V_{abc}	Voltage (phase-phase)	400 V

3.4.1 Grid Forming Control Simulation

The grid-forming inverter-based microgrid presents a low-output impedance as voltage sources; consequently, an exceptional and precise synchronization scheme is put in place for parallel operation with other inverters with the same grid-forming control. The output impedances of each inverter determine their respective power-sharing when operated in parallel. The system operates steadily in island mode and stays disconnected from the host grid provided the operating conditions are within the specified technical limit. In the case of a grid failure, the grid voltage is generated by the inverter-based microgrid. The generated voltage in AC grid-forming inverter-based microgrid is utilized as a set-point for the rest of the grid-feeding inverter-based microgrids connected to it.

Grid-forming inverter-based microgrid stipulates and regulates the supply voltage and frequency to the AC loads. The primary structure of control comprises two cascaded control loops, as implemented in Figure 3.7.

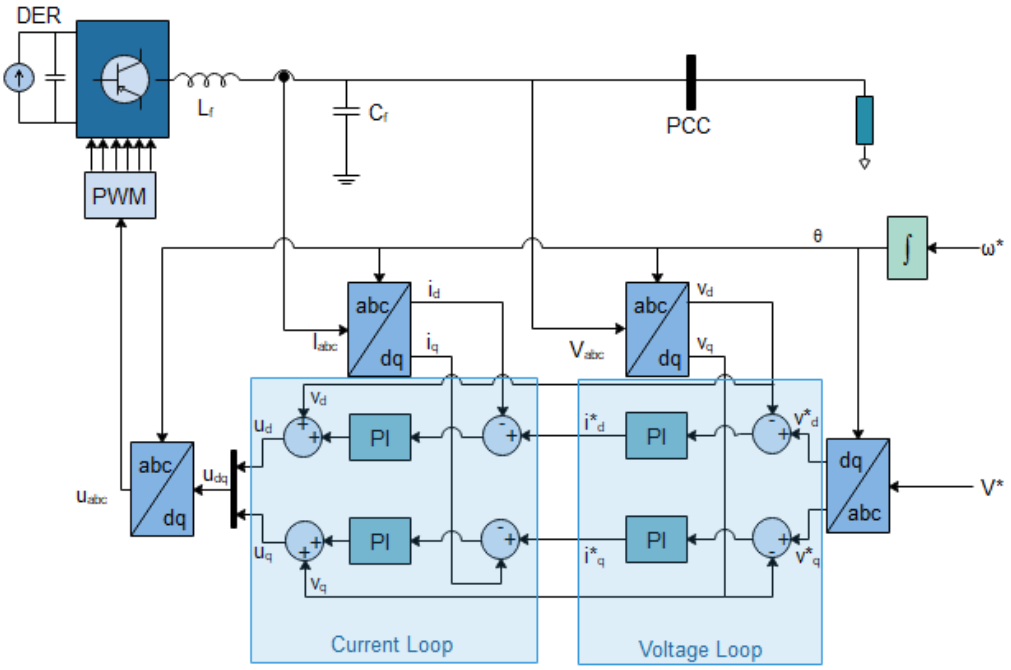

Figure 3.7: Grid-forming control structure model

Figure 3.7 shows how the grid-forming inverter-based microgrid control implementation is done in the *dq* reference frame. The control system inputs are E^* and ω^* of the voltage formed at the *PCC* by the inverter-based microgrid.

The outer loop is responsible for output voltage control; thus, the error between the measured and the reference voltage in this loop is the controller's input. The controller's output sets the reference current *I** for injection from the inverter to the grid. Notably, the voltage control loop of the grid-forming inverter-based microgrid is enabled only under island operating mode, where the microgrid is disconnected from the grid. The outer voltage control loop regulates the grid voltage to match its reference value *E**, as shown in equation 3.11

$$i_d^* = \left(k_{pv} + \frac{k_{iv}}{s}\right)\left[v_d^* - v_d\right] = \left(k_{pv}\left[1 + \frac{1}{T_{iv}s}\right]\right)\left[v_d^* - v_d\right]$$
$$i_q^* = \left(k_{pv} + \frac{k_{iv}}{s}\right)\left[v_q^* - v_q\right] = \left(k_{pv}\left[1 + \frac{1}{T_{iv}s}\right]\right)\left[v_q^* - v_q\right] \quad (3.11)$$

where the currents i^*_d and i^*_q are reference *d*-axis and *q*-axis current outputs of the *PI* controller, v^*_d and v^*_q are reference d-axis and q-axis voltages specified as reference value *E** and zero respectively. Furthermore, v_d and v_q are d-axis and q-axis values of the three-phase AC grid voltage under Park's transformation (*abc-dq*). Lastly, k_{pv} and k_{iv} are the proportional and integral

gains of the *PI* control. The voltage control loop's output responses indicating the d-q reference current are shown in Figure 3.8 with a settling time of less than 0.2 s.

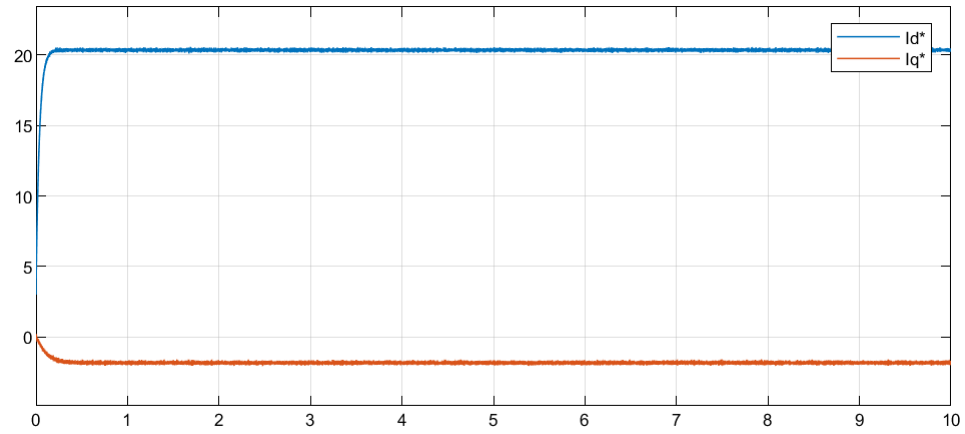

Figure 3. 8: Voltage loop responses indicating current references i^*_d and i^*_q in grid forming

Contrarily, the inner loop controls the inverter-based microgrid supply current and tracks the voltage loop (outer) reference current, as shown in Equation 3.12.

$$u_d = \left(k_{pi} + \frac{k_{ii}}{s}\right)\left[i_d^* - i_d\right] + v_d = \left(k_{pi}\left[1 + \frac{1}{T_{ii}s}\right]\right)\left[i_d^* - i_d\right] + v_d$$
$$u_q = \left(k_{pi} + \frac{k_{ii}}{s}\right)\left[i_q^* - i_q\right] + v_q = \left(k_{pi}\left[1 + \frac{1}{T_{ii}s}\right]\right)\left[i_q^* - i_q\right] + v_q \quad (3.12)$$

where u^*_d and u^*_q are reference *d*-axis and *q*-axis current outputs of the *PI* controller. Furthermore, i_d and i_q are d-axis and q-axis values of the three-phase AC grid current under Park's transformation (*abc-dq*). Lastly, k_{pi} and k_{ii} are the proportionate gain and integral gain of the *PI* control. The current control loop's output responses indicating the d-q reference voltage for the PWM are shown in Figure 3.9 with a settling time of less than 0.2 s.

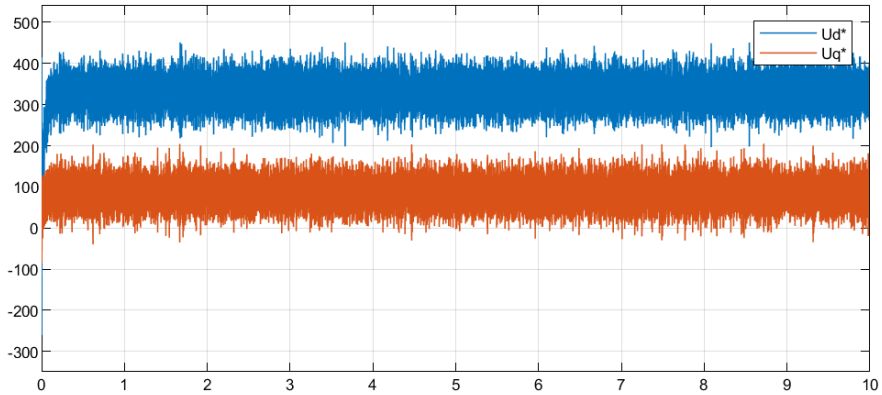

Figure 3. 9: Current loop responses indicating new voltage references u^*_d and u^*_q in grid forming

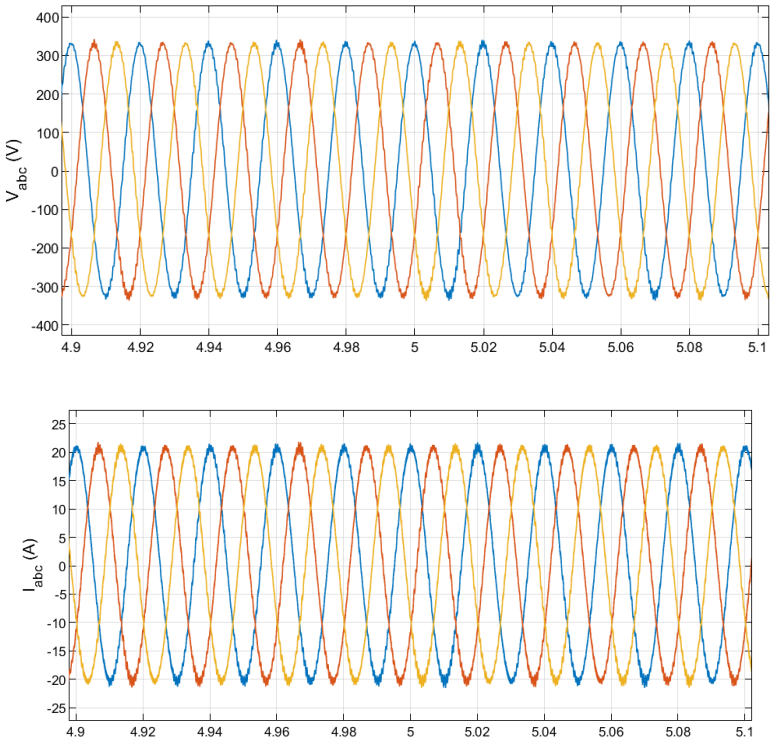

Figure 3. 10: Three-phase voltage and current of grid forming controlled microgrid

Therefore, the capacitor C_F is charged by the controlled current flowing through the inductor L_F to preserve the voltage output value near the reference stipulated for the voltage loop. The corresponding voltage and current measured at the coupling point are presented in Figure 3.10; grid forming controlled microgrid voltage and the current in each three-phase. Furthermore, the active power and reactive power grid forming controlled microgrid are shown in Figure 3.11. Figure 3.12 indicates the frequency regulation in the grid-forming system.

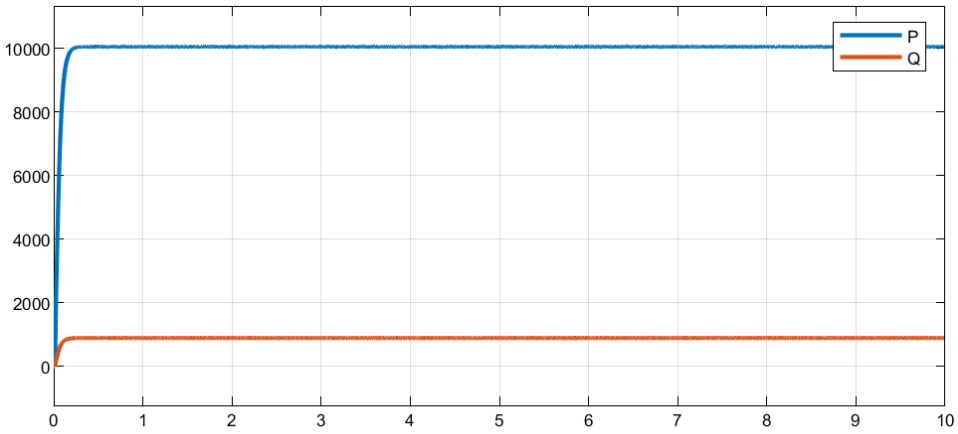

Figure 3. 11: Active and reactive power grid forming controlled microgrid

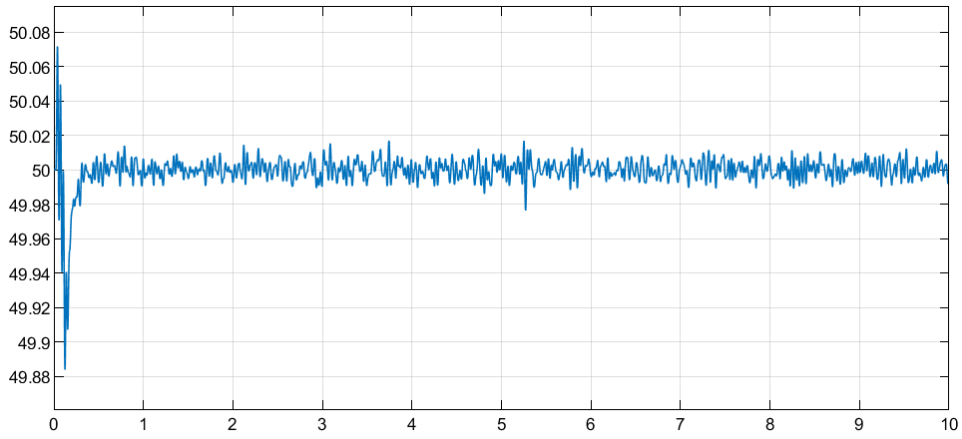

Figure 3. 12: Frequency of grid forming controlled microgrid

3.4.2 Grid Feeding Control Simulation

The grid-feeding inverter-based microgrids are implemented and controlled as current sources in shunt with a high output impedance. This control arrangement makes the inverter-based microgrid suitable for parallel operation and additional grid-feeding inverter-based microgrids in the grid-synchronous operating mode. Grid feeding control and operating mode are mostly utilized in grid-connected inverter interfaced DG systems, such as PV or wind power systems [178]. Grid-feeding inverter-based microgrids only operate in grid synchronous mode. If operated in a standalone island mode, there should be a grid-forming or grid-supporting inverter-based microgrid, or a local synchronous generator that sets the magnitude and frequency of voltage. Figure 3.13 demonstrates the controller implementation for an AC grid-feeding inverter-based microgrid.

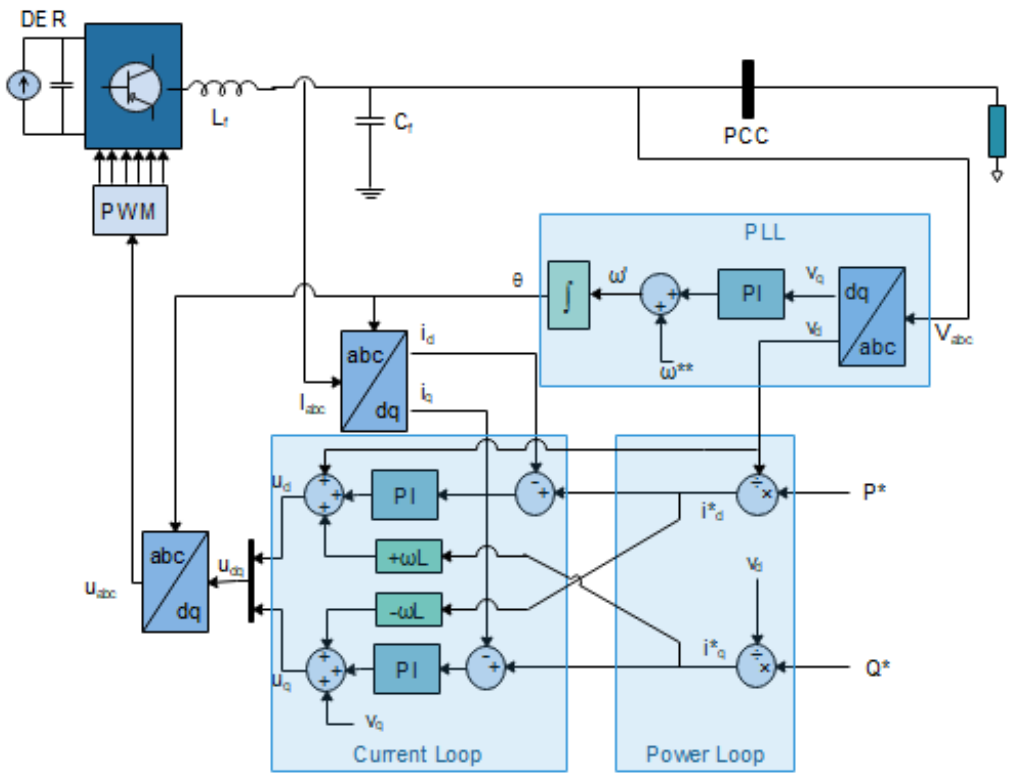

Figure 3. 13: Grid-feeding control structure model

Figure 3.13 demonstrates grid feeding control implementation in a direct-quadrature-based synchronous current control, with grid feed-forward voltage and the decoupling component used to boost the control output. The outer control loop determines the current reference in direct-quadrature, and these references are utilized in regulating grid power delivery. The calculated feed-forward signal provides this reference current from active power reference *P** and reactive power reference *Q**. The outer power control loop regulates the power injection by producing corresponding *q*-axis current i^*_q and *d*-axis current i^*_d outputs from the reactive power *Q** and new active power reference *P**, respectively, in line with the q-axis and d-axis component of the AC grid voltage as shown in

$$i_d^* = \frac{2}{3}\frac{P^*}{v_d}$$
$$i_q^* = -\frac{2}{3}\frac{Q^*}{v_d} \qquad (3.13)$$

The current reference responses (direct-axis current i^*_d and quadrature-axis current i^*_q outputs) of the power loop are shown Figure 3.14. A high-level controller such as MPPT control and plant controller sets the power reference values.

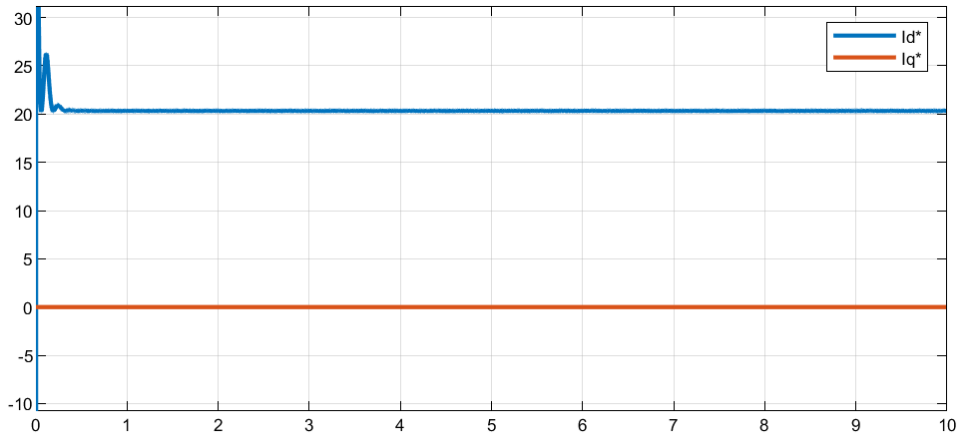

Figure 3. 14: Power loop responses indicating current references *direct*-axis current i^*_d and *quadrature*-axis current i^*_q in grid feeding.

The inner controller is a fast control loop for the current, which controls the current injection into the *AC* grid. The instantaneous values for both active power and reactive power are evaluated using

$$P = \frac{3}{2}\left(v_d i_d + v_q i_q\right)$$
$$Q = \frac{3}{2}\left(v_q i_d - v_d i_q\right) \tag{3.14}$$

Figure 3.15 shows the measured instantaneous active power P and reactive power Q in the system, aligning with the active power reference P^* = 10000 W and reactive power reference Q^* = 0 VAr.

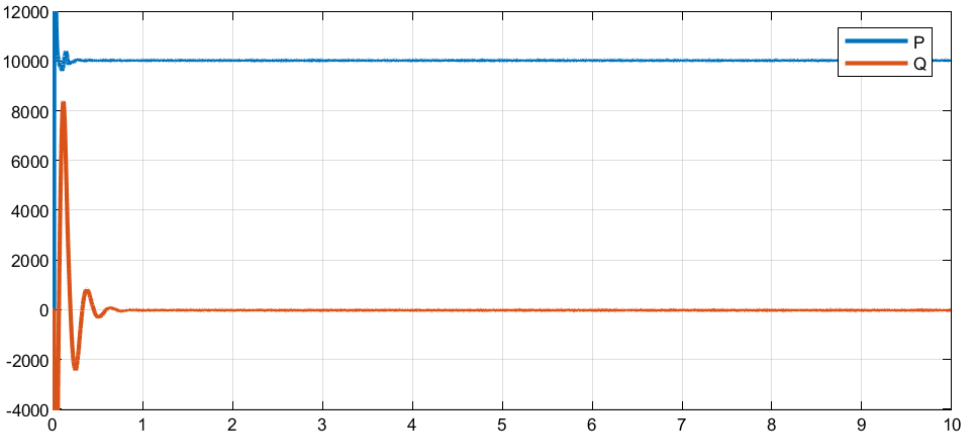

Figure 3. 15: Instantaneous active power P and reactive power Q in the grid feeding

The voltage/power and the current regulation loops simultaneously set the absolute reference for the voltage used as the inverter PWM input. According to the current references, i^*_d, and i^*_q, generated by the voltage control loop, the current control loop generates direct-quadrature-axis reference voltage (u_d and u_q) for the PWM. This control is performed using a PI controller, which expresses the controller output as in Equation 3.15.

$$u_d = \left(k_{pi} + \frac{k_{ii}}{s}\right)\left[i_d^* - i_d\right] + v_d + (\omega L)\times i_q^* = \left(k_{pi}\left[1 + \frac{1}{T_{ii}s}\right]\right)\left[i_d^* - i_d\right] + v_d + (\omega L)\times i_q^*$$
$$u_q = \left(k_{pi} + \frac{k_{ii}}{s}\right)\left[i_q^* - i_q\right] + v_q - (\omega L)\times i_d^* = \left(k_{pi}\left[1 + \frac{1}{T_{ii}s}\right]\right)\left[i_q^* - i_q\right] + v_q - (\omega L)\times i_d^* \quad (3.15)$$

Where k_{ii} and k_{pi} indicate integral and proportional gains, respectively, from the current control loop. The v_d and v_q elements of the voltage direct-quadrature axes imply feed-forward quantities while $+(\omega L)i^*_q$ and $-(\omega L)i^*_d$ are the quantities of cross-decoupling. Feed-forward and cross decoupled quantities are used to perform independent controls of the current d–q axis. Finally, the output filter inducer L is added in the cross-decoupling quantities. The current control loop's output responses indicating the d-q reference voltage for the PWM are shown in Figure 3.16.

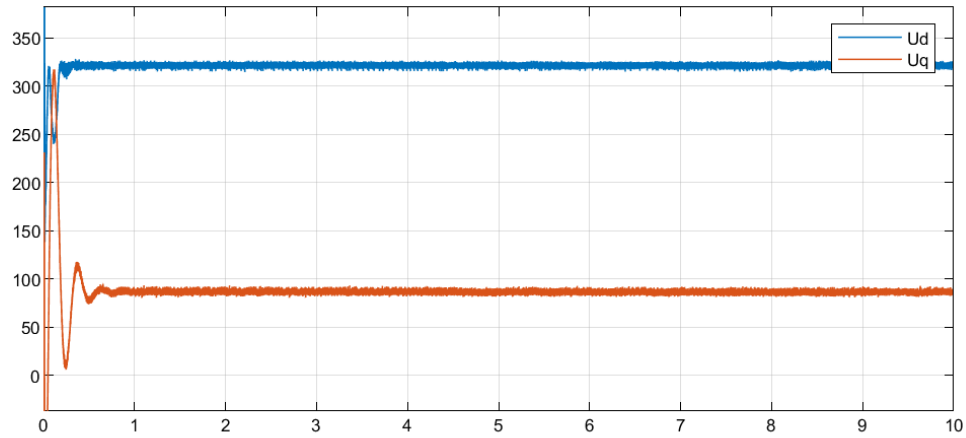

Figure 3. 16: Current loop responses indicating new voltage references (u_d and u_q) in grid feeding

The grid feeding system, PLL implementation is summarized thus: in the dq reference frame, the PLL generates the grid voltage angular position, which is regulated via the feedback loop driving the voltage quadrature component v_q to zero as shown in Equation 3.16

$$\theta' = \omega t = \int \omega' = \int\left(\omega^* + \left(k_p + \frac{k_i}{s}\right)\times v_q\right) \quad (3.16)$$

By the synchronization arrangement, ω' is the estimated frequency of the AC grid while the rated reference frequency ω^* signifies PLL's feed-forward, enhancing the phase estimation θ' dynamics, which is achieved by integration.

The corresponding current and voltage measured at the PCC is shown in Figure 3.17; grid feeding controlled microgrid voltage and the current in each three-phase

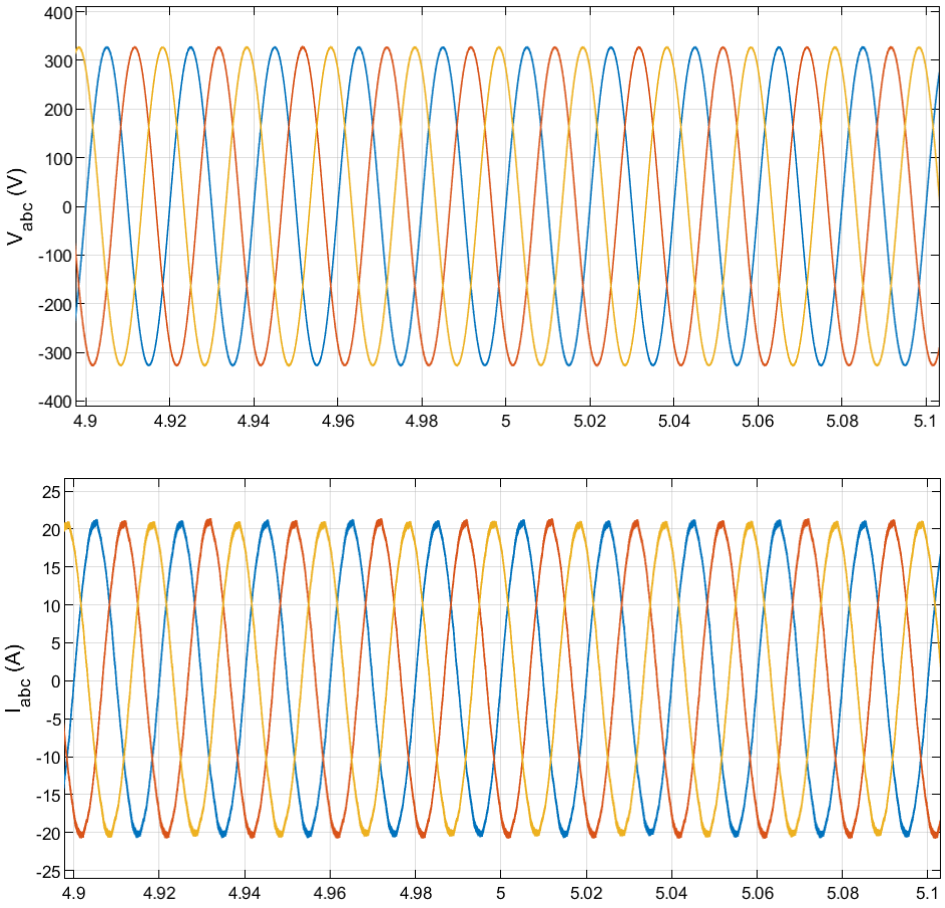

Figure 3. 17: Three-phase voltage and current of grid forming controlled microgrid

The grid feeding control can be made flexible by adding an intermediate control level to its primary control, as it will be implemented in the next section. This enables the system to participate in regulating the *AC* voltage magnitude and frequency of microgrid by changing the references of active power P^* and reactive power Q^* at an intermediate control level, and references set for the primary control [179].

3.4.3 Grid Supporting Control Simulation

The grid-supporting inverter-based microgrid fits the control and hardware topology of a typical three-phase voltage source inverter utilized in interfacing numerous *DER*s. It is intended to fill various roles and export power at any specified power factor when connected to weak grids, stiff grids, and a low-inertia *RES* dominated microgrid. Figures 3.18 and 3.19 are grid-supporting inverter systems whose output is connected to a stiff host grid.

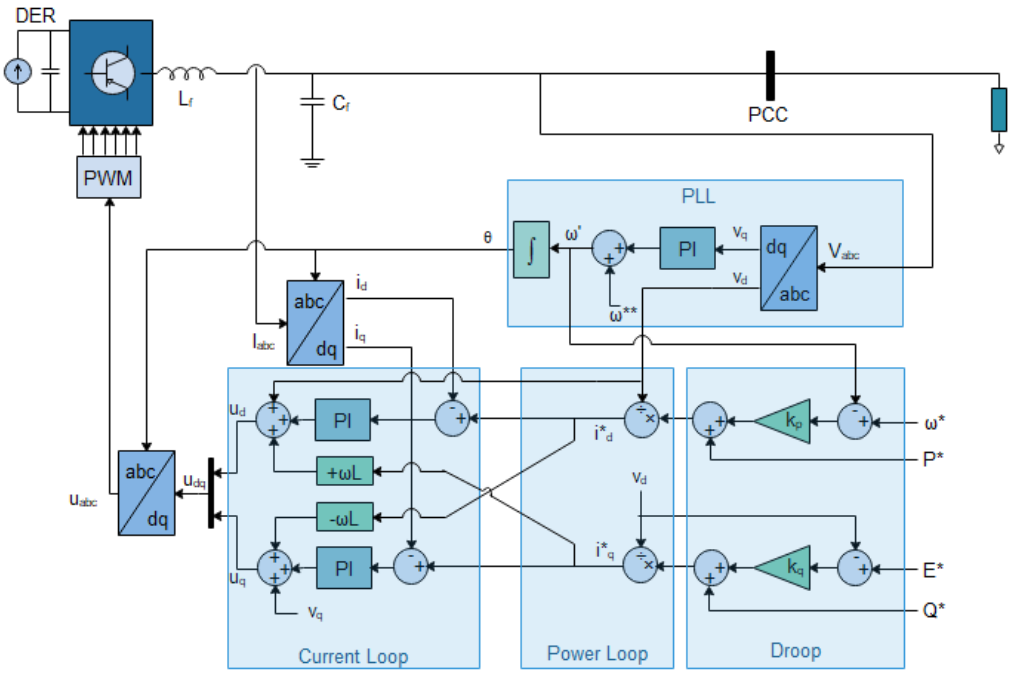

Figure 3. 18: Three-phase grid-supporting grid-feeding inverter-based microgrid control model operating as a current source

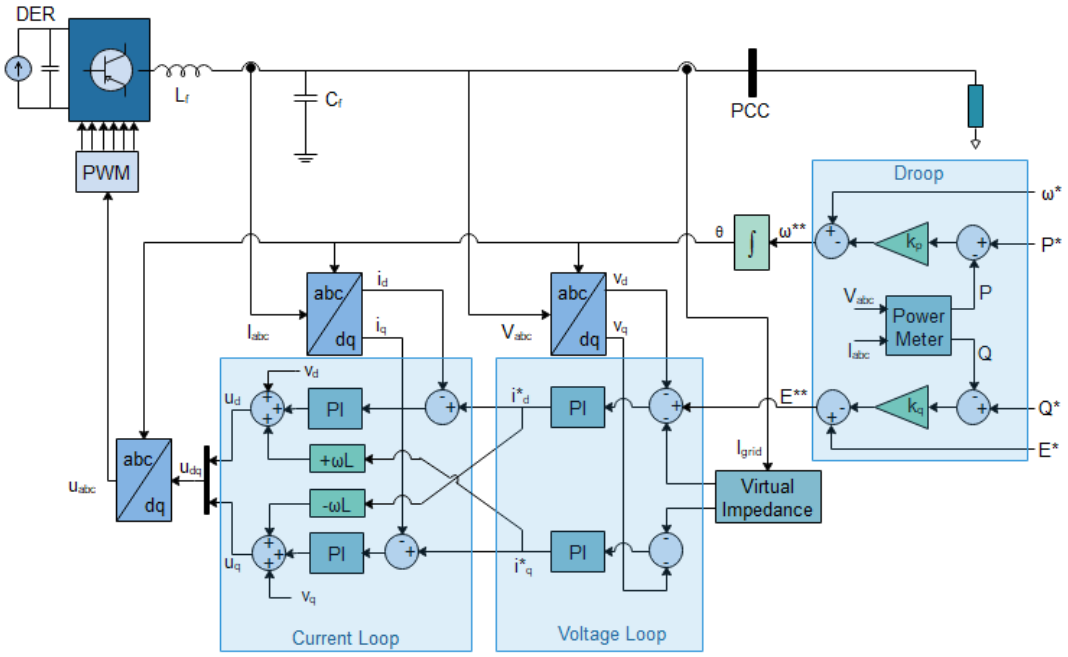

Figure 3. 19: Three-phase grid-supporting grid-forming inverter-based microgrid control model operating as a voltage source

The outer loop for grid-supporting grid-feeding operating as a current source specifies the current references corresponding to required or specified active power and reactive power references as already expressed in Equation 3.13. However, in the outer loop control for grid-supporting grid-forming operating as a voltage source, the voltage control loop uses the E^* and the output of the virtual impedance to generates the references currents (i^*_d and i^*_q) for the direct-quadrature axes components using the measured active power and reactive power as given in Equations 3.17 and

shown in Figure 3.19. This control is implemented with a PI control scheme such that the controller output is given by

$$\begin{aligned} i_d^* &= \left(k_{pv} + \frac{k_{iv}}{s}\right)\left[E^* - v_d - v_{dp-d}\right] = \left(k_{pv}\left[1 + \frac{1}{T_{iv}s}\right]\right)\left[E^* - v_d - v_{dp-d}\right] \\ i_q^* &= \left(k_{pv} + \frac{k_{iv}}{s}\right)\left[-v_q - v_{dp-q}\right] = \left(k_{pv}\left[1 + \frac{1}{T_{iv}s}\right]\right)\left[-v_q - v_{dp-q}\right] \end{aligned} \tag{3.17}$$

where k_{IV} and k_{PV} are the integral gain and proportional gain of the voltage PI control, respectively. The $v_{dp\text{-}d}$ and $v_{dp\text{-}q}$ the drop in voltage due to the grid or virtual impedance. The voltage drops in equation 3.18 in a resistive-inductive feeder line is expressed as

$$\begin{aligned} v_{dpd} &= Ri_d - \omega L i_q + L\frac{di_d}{dt} \\ v_{dpq} &= Ri_q - \omega L i_d + L\frac{di_q}{dt} \end{aligned} \tag{3.18}$$

Therefore, the virtual impedance is realized by subtracting the voltage drops in equation 3.18 from the stipulated voltage reference. The high-frequency influence of the current derivatives must be contained in this stationary reference frame application. Furthermore, a quasi-stationary method can be applied by ignoring the current derivatives while retaining the cross-coupling components, as in a steady-state response. However, in this work, a low-pass filter (*LPF*) is applied to the current derivatives, as in Equation 3.19, where ω_c is the cutoff frequency of the LPF. Detailed implementation of the virtual impedance is shown in Figure 3.20.

$$\begin{aligned} v_{dpd} &= Ri_d - \omega L i_q + \frac{\omega_c}{s+\omega_c} s L i_d \\ v_{dpq} &= Ri_q - \omega L i_d + \frac{\omega_c}{s+\omega_c} s L i_q \end{aligned} \tag{3.19}$$

This control loop regulates the active and reactive power to ensure the transfer of power from DC to the inverter's AC side. The voltage v_d is constant, and the active power is regulated by adjusting the current i_d. Similarly, the reactive power is regulated through the current i_q control.

The grid-supporting systems' inner loop controls the filter inductor current, following current references and removing cross-coupled terms caused by the reference frame transformation. This control implemented using a PI controller such that the controller output is similar to that grid feeding system expressed as in Equation 3.15

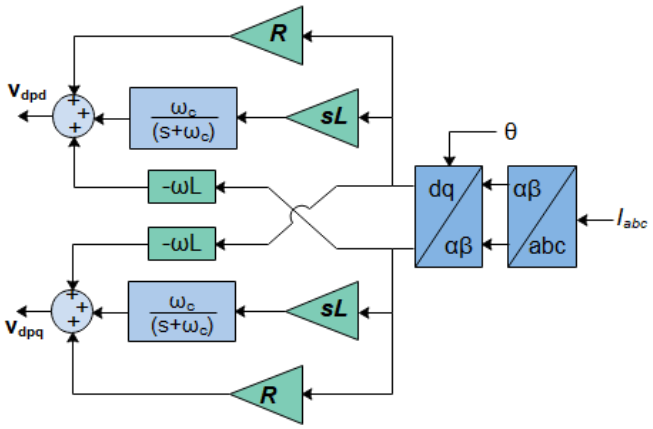

Figure 3. 20: Virtual Impedance Model

The entire system reference is the standard reference frame where each constituent generating unit's dynamics are transformed using the angular frequency ω. Subsequently, the decoupling of the active and reactive power is done through Park transformation (*abc-dq*).

Therefore, an AC grid-supporting system is either regulated as a current source with parallel impedance or a voltage source with link impedance. Both control modes' primary goal is to actively contribute to AC grid voltage magnitude E^* and frequency ω^* regulation via droop control. The droop controls provide a frequency and voltage control platform by regulating active power and reactive power grid delivery. A droop control scheme implements the effective distribution and allocation of required power among the inverter-based DERs of a given microgrid. Droop emulates the frequency and voltage regulation of a typical synchronous generator at the inverter output. Inverters' parallel-connection improves overall performance and reliability in microgrids, even with a constituent parallel inverter's failure [180] [181]. The droop controls have generally been recognized as the most efficient power-sharing scheme due to flexibility and lack of significant communication networks between parallel-connected inverters [54] [182].

In Figure 3.18, the inverter-based microgrid is controlled as a current source, with the primary goal of regulating the frequency and voltage magnitude of both the main grid and microgrid and ensure steady delivery of power to the local load. The grid codes governing the grid connection of wind turbines, for instance, stipulate that a percentage of the generated power be exported to the main grid strictly for a regulation [19]. The droop equations present the delivered power influence on AC grid voltage and frequency. The droop characteristics expression of both frequency and voltage related to the active power and reactive power are given as Equation 3.20 for the grid-supporting system operating as a current source.

$$P^{**} = P^{*} + k_p\left(\omega^{*} - \omega\right)$$
$$Q^{**} = Q^{*} + k_q\left(E^{*} - v_d\right) \tag{3.20}$$

where k_p and k_q are the coefficients of the frequency and voltage droops of the inverter, respectively. Similarly, P^* and Q^* are active and reactive power references, respectively. Furthermore, the new references generated by the droop for active power and reactive power are signified by P^{**} and Q^{**}, respectively. Also, ω^* signifies the set-point frequency while E^* is the voltage's rated set-point amplitude.

The inverter-based microgrid is controlled to emulate an AC voltage source in Figure 3.19, connected via a linkage impedance to the grid, as in the synchronous generator structure. The active and reactive power that the inverter-based microgrid provides is dependent on the AC grid voltage. The emulated voltage source with virtual impedance emulated in the current control promotes participation in the grid frequency and voltage magnitude regulations in both grid-synchronous and islanded operating modes without the need to connect any grid forming inverter in the microgrid. This grid-supporting system operates in parallel in a microgrid with flexible power-sharing without the communication links. The droop characteristics in Equation 3.21 are implemented alongside virtual output impedance control, which dynamically modifies the operating parameters per exigencies [54]. The droop characteristics equations of both frequency and voltage related to the active power and reactive power are written as Equation 3.21 for the grid-supporting system operating as a voltage source.

$$\omega^{**} = \omega^{*} - k_p\left(P^{*} - P\right)$$
$$E^{**} = E^{*} - k_q\left(Q^{*} - Q\right) \tag{3.21}$$

where P and Q are the measured active power and reactive power being generated and injected into the main grid from the frequency droop gain, the frequency is determined and integrated to set the phase. The new references generated by the droop for frequency and voltage are signified by ω^{**} and E^{**}. Therefore, the dynamic features and inertia characteristics of conventional generators are mimicked with incorporated negative feedback. Similarly, with a voltage droop gain, the voltage magnitude is determined, equivalent to a *d*-axis output voltage reference. In other words, the control ensures the magnitude reference of the output voltage is in line with the *d*-axis voltage component of the reference frame, while zero voltage *q*-axis component reference is maintained [58] [175].

Figures 3.21 shows the root-mean-square equivalent of the three-phase voltage in the developed grid supporting systems.

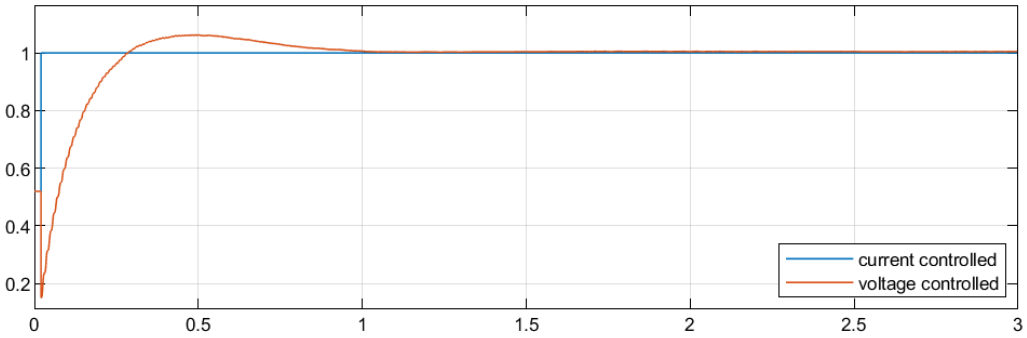

Figure 3. 21: Root-mean-square voltages in the two grid supporting systems

Figure 3.22 shows the active power generation in the grid supporting systems, and Figure 3.23 shows reactive power injection in the two systems (current-controlled and voltage-controlled). The angular frequency estimation is shown in Figure 3.24 indicating the rate of change of the sinusoidal wave of the voltages in the two systems

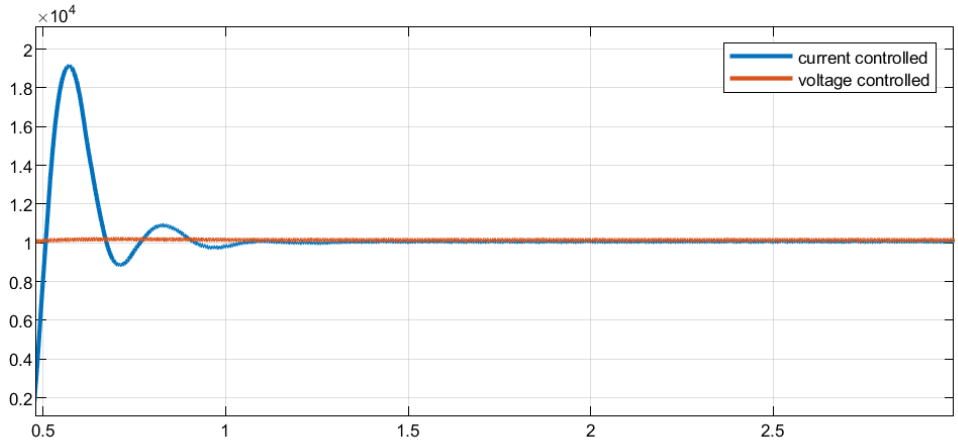

Figure 3. 22: Active powers of the two grid supporting systems.

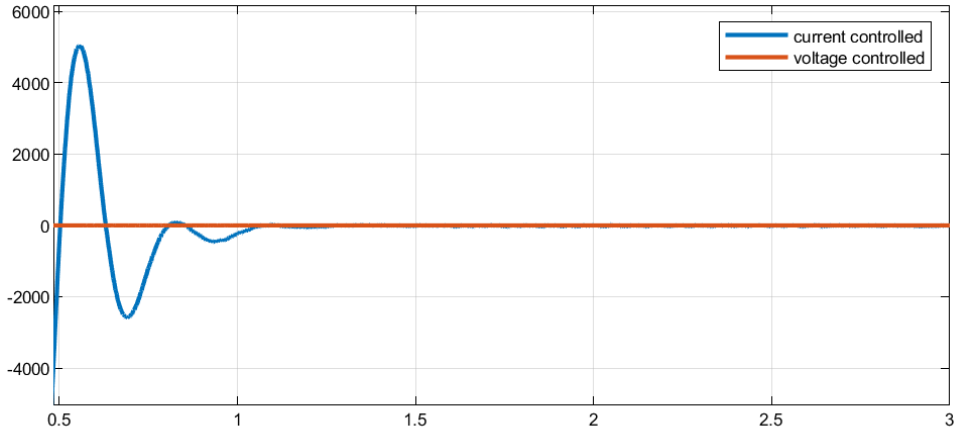

Figure 3. 23: Reactive powers of the two grid supporting systems.

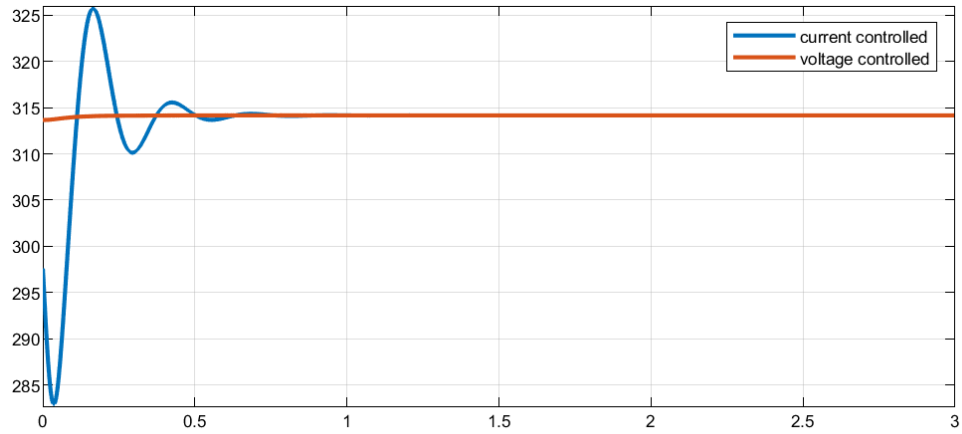

Figure 3. 24: Angular frequencies of the two grid supporting systems.

In grid-supporting inverter-based microgrids, the droop regulation techniques are implemented to control the active power and reactive power grid exchange to maintain the grid voltage magnitude and frequency within specified limits. The droop control principle is derived from a typical synchronous generator's self-regulating ability and support provided under grid-connection. This involves curtailing the active power delivered under frequency upsurge and reducing the reactive power injected under the AC grid's voltage amplitude surges.

3.5 Control Response Validation

The models (grid feeding, grid forming, grid-supporting grid-feeding, and grid-supporting grid-feeding) control systems are validated using controllers' responses in Figures 3.25, 3.26, 3.27, and 3.28. Figures 3.25 and 3.26, 3.27, 3.28 show the power reference changes' responses and the load dynamics in the developed inverter-based systems. The responses are swift and lack substantial overshoot under the changing operating points. The response of the inverter-based systems is a crucial performance condition that must be satisfied. The active and reactive power references dictate the grid feeding (Grid F) and grid-supporting grid-feeding (GSG F) systems' dynamics. Thus, the active power reference is stepped up to 20 kW from the 10 kW initial value and subsequently stepped down to 5 kW. Due to the coupling between reactive power and active power, the change in power reference and load dynamics are performed under different simulations. The reactive power is stepped down from the initial 2 kVAr to 0.2 kVAr and subsequently stepped up to 1.5 kVAr

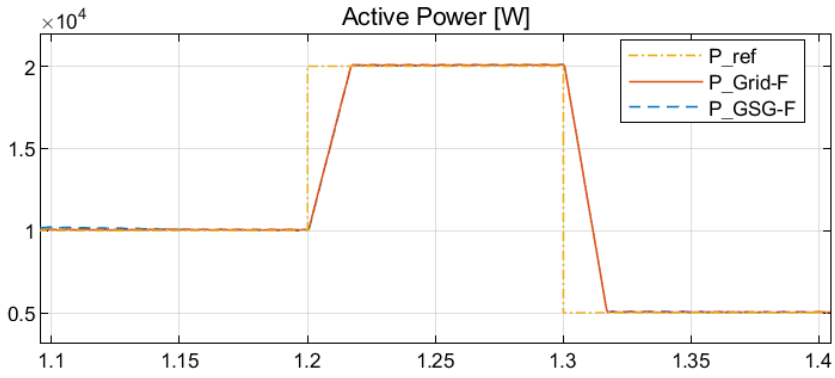

Figure 3. 25:Reference and resultant active power in the grid feeding and grid supporting grid feeding systems

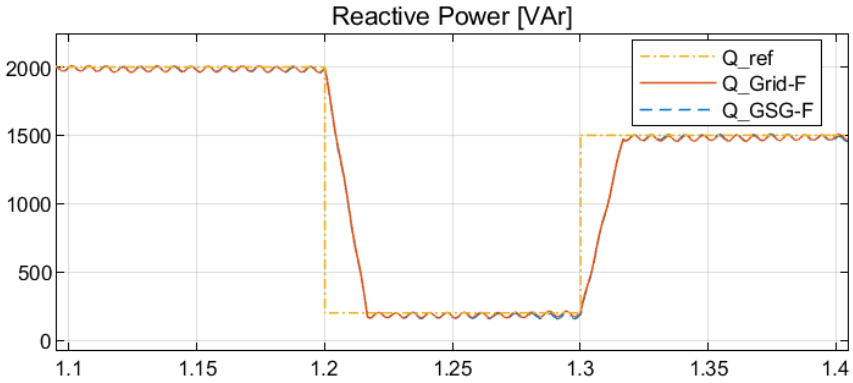

Figure 3. 26:Reference and resultant reactive power in the grid feeding and grid supporting grid feeding systems

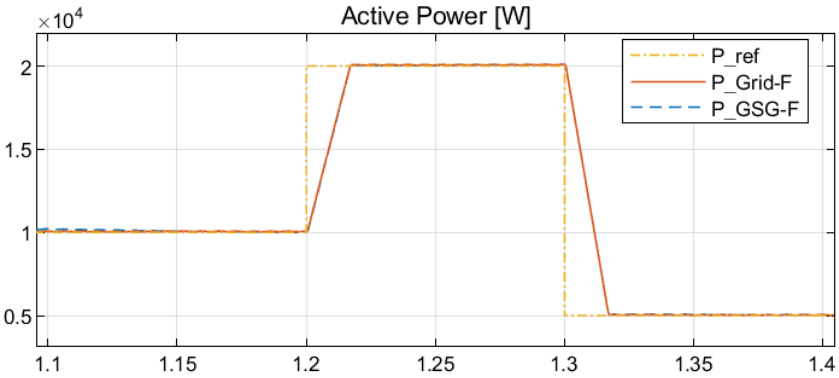

Figure 3. 27:Reference and resultant active power in the grid forming and grid supporting grid forming systems

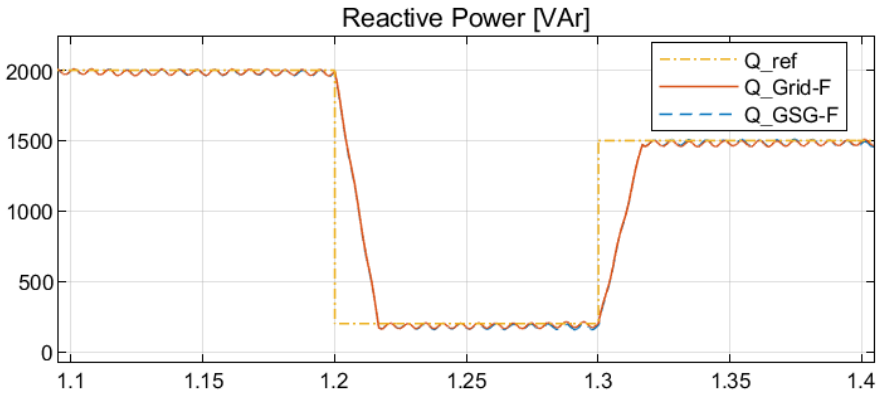

Figure 3. 28:Reference and resultant reactive power in the grid forming and grid supporting grid forming systems

Similarly, the changing load conditions stipulate the grid forming systems' dynamics and grid supporting grid forming; hence, the load active and reactive powers are stepped up and down from the initial values, using a dynamic load model. The initial load value of 1kW is applied at 0.995037 leading power factor, which is stepped up to 1.5 kW and subsequently stepped up to 0.5 kW. The resulting output active and reactive powers for the grid forming (Grid-F) and the grid-supporting grid-forming inverter-based microgrids are shown in Figures 3.27 and 3.28. Furthermore, the grid supporting schemes' effectiveness is verified through an equivalent State-Space model of the system obtained from power analysis using Control System Toolbox™ as presented in Figures 3.29 and 3.30

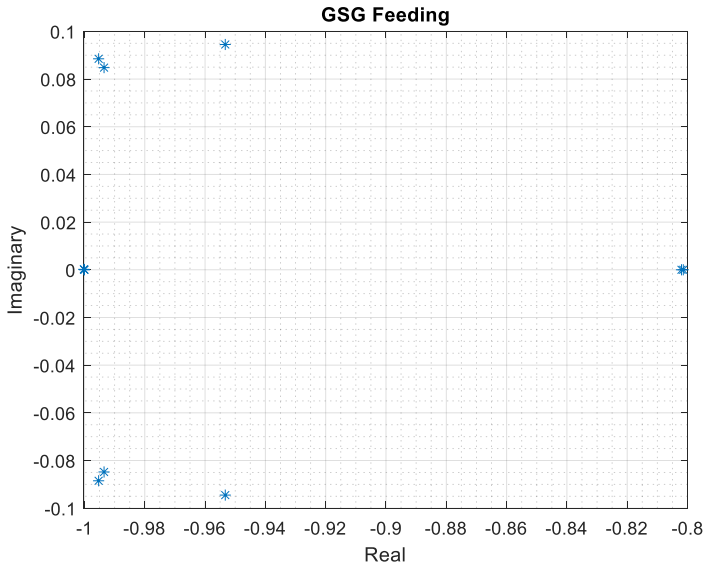

Figure 3. 29:State variables for current source discrete-time state-space

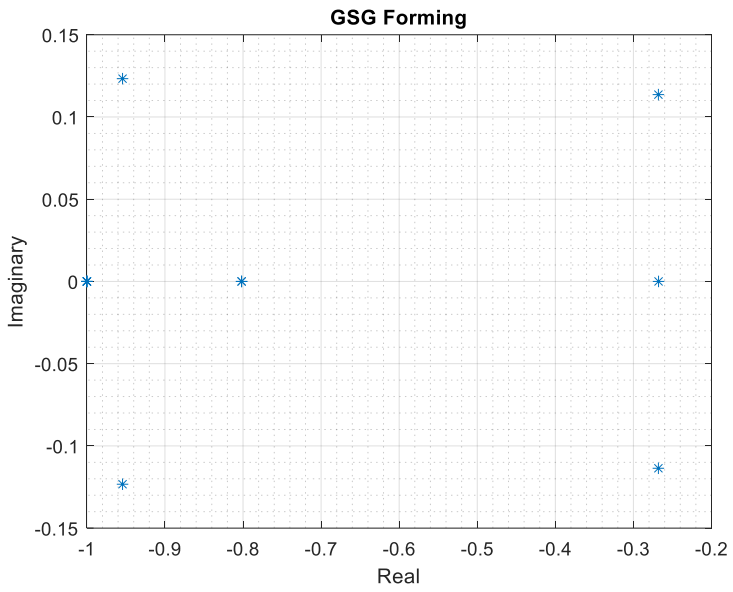

Figure 3. 30:State variables for voltage source discrete-time state-space.

The discrete-time state-space models equivalent to the proposed systems are developed using Control System Toolbox™ power analysis. The analysis has a sampling time of 4 milliseconds for both the current source-model and voltage source-model of the grid-supporting system. The equivalent matrices A, B, C, and D of the current source-model (GSG Feeding) are 11 by 11, 11 by 11, 18 by 11, and 18 by 11 state dimensions, respectively. The equivalent matrices A, B, C, and D of the voltage source-model (GSG Forming) are 11 by 11, 11 by 8, 18 by 11, and 18 by 8 state dimensions, respectively. The complex eigenvalues obtained from the matrix A in the two models are presented in Figures 3.29 and 3.30, showing state variable stability.

3.6 Conclusion

The design and control of power converters required for DC-AC conversions are critical to enhancing durability, reliability, and efficiency. The interfacing power converters are crucial for the power conditioning for efficient load management and the integration of renewable energy sources. The DC-AC conversion phase synchronizes the renewable system to the primary grid and efficiently transfers DC generated power into the AC grid. In this chapter, an inverter-based microgrid with an ideal DC voltage source is assumed to develop the grid forming and grid feeding systems' time-domain model to operate as grid supporting schemes. Hence the grid-supporting system can participate in the frequency and voltage regulation of the grid system. The modelling and emulation of this system through simulation are critical to investigating how the converter-based system responds to FRT/LVRT technical challenges, among other issues. This is valuable for our analysis, design, and verification.

CHAPTER FOUR
INVERTER-BASED MICROGRID WITH PV DISCRETE-TIME MODEL

4.1 Introduction

The switch-model power electronic inverters are deployed as the central technology in enabling integrating intermittent DC power into the traditional AC grids. Various DER architectures have been designed depending on many attributes, including the installed system's size and application. The reliability of the power electronic interface inverters is critical in all these architectures. Recent studies [183] demonstrate enhanced operation of power electronic interface inverters can be reached by optimum modelling and selection of the control parameters. The DC-DC converter is necessary to help interface a DC DG source, especially PV panels, to extra maximum power and stabilize the DC-link. A typical case of this is a double stage PV system with MPPT control for the DC-DC converter and a slightly modified control for the DC-AC inverter already established in chapter three. Consequently, this chapter introduces the unique concept of integrating active power-frequency and reactive power-voltage droops for a PV system to dynamically support the grid by participating in the frequency and voltage regulation. Lastly, this chapter presented the results of simulations to validate the models developed.

This chapter is an extension of the previous chapter in which a DC-DC boost converter is added to an inverter-based microgrid in grid supporting mode. This reflects real DC source DER/DG dynamics, especially a double-stage Solar Photovoltaic system. As countries worldwide drive towards increasing RES use, especially in grid-synchronous operating conditions. Furthermore, the global capital and installation cost of PV panels continuously declines. However, for proper integration of the PV system, the power conversion unit is inevitable. Consequently, the design and control of power converters required for DC-DC and DC-AC conversions are critical to enhancing durability, reliability, and efficiency [89]. This chapter does not focus on the modelling of the *PV* power system as there are several studies on that [184][185][186]. However, the control scheme for an inverter-based microgrid used with a DC-DC converter is modelled in this chapter. Similarly, the control implementation of a grid-supporting system for a *PV* source is used with the droop, and a DC-DC converter is developed.

4.2 Solar PV System Overview

PV modules are a significant part of an entire PV system [89], and the PV cells play a critical role in the photovoltaic effect; consequently, PV cells are essential for overall PV system reliability and efficiency [187]. Furthermore, the interfacing power converters are as important too for the power conditioning for efficient load management. The PV source with the interfacing power conversion system is shown in Figure 4.1. The power conversion is staged into two sections; the

DC-DC conversion phase and the DC-AC conversion phase. The latter synchronizes with the renewable system with the main grid and efficiently transfers DC generated power into the AC grid. The former regulates the PV source extract maximum power irrespective of the environmental condition affecting the PV source power generation. There exist a DC-link between these two conversion phases with a capacitor, C_{DC}, while the DC-AC inverter interfaces the entire system to the three-phase AC grid.

The modeling and emulation of this system through simulation are critical to investigating how the inverter-based microgrid responds to FRT/LVRT technical challenges, among other issues. This is valuable for our analysis, design, and verification. Consequently, the inverter-based microgrid with DC-DC converter discrete-time models is developed.

4.3 Double Converter Modelling

The DC-DC conversion phase has an MPPT control to ensure operation at *MPP* for maximum power extraction, and the DC-AC inverter phase efficiently delivers the extracted power to the AC grid [70]. Furthermore, the PV source current and voltage are typically mismatched to the AC grid voltage magnitude and frequency due to the inherent intermittencies; hence, the power electronic-based interfaces are inevitable. Consequently, to ensure a reliable, secure, and efficient energy conversion from PV systems, the power electronic converters' design, control, and operation should be carefully considered.

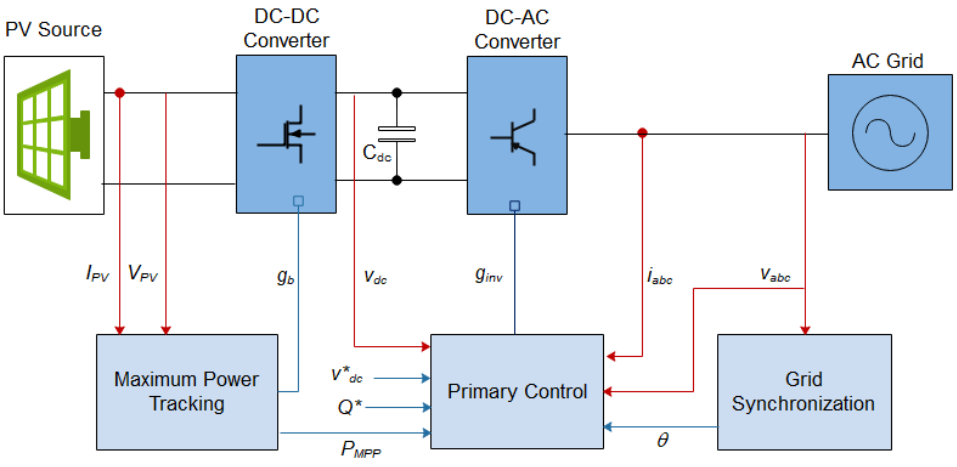

Figure 4. 1: Control structures of an inverter in an Inverter-Based Microgrid with DC-DC converter

4.3.1 DC-DC Conversion Phase and MPPT Control

A DC-DC converter converts a source of direct current (DC) from one voltage level to another. The primary purpose of the MPPT scheme is to ensure the PV modules at the input of this phase operates for maximum power extraction. The DC-link serves as the output to the DC-DC

conversion and input to DC-AC conversion phases. The extracted power is from the first phase is delivered to the input of the second phase.

4.3.1.1 DC-DC Converter System

The DC-DC converter rating strongly depends on the probable PV module voltage range and the DC-AC inverter's required input. A comparatively high DC link voltage is required (up to1000V) in a grid-connected DC-AC inverter. The converter either operates in a boost or a buck mode. The boost mode is activated to step up the nominal voltage when lower than this required reference, while the buck is triggered to limit the voltage when higher than the required DC-AC inverter voltage. The DC-DC converter in Figure 4.2 operates in a boost mode and comprises an IGBT block G that implements a semiconductor device controlled by the gate signal. An inductor L and a semiconductor diode S are connected to the IGBT block. Two capacitors C_{PV} and C_{DC} are connected to the input and output of the DC-DC converter, respectively.

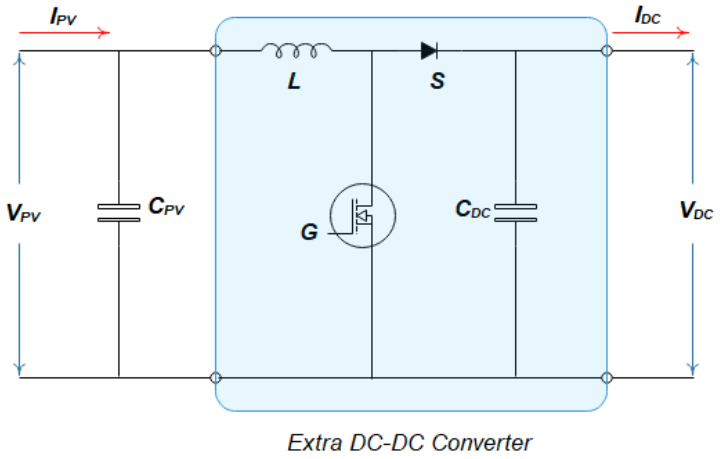

Figure 4. 2: DC-DC converter schematic controlling a *PV* system

A PWM signal controls the IGBT block by 'on' and 'off' switching over a particular period. The IGBT turns on when the collector-emitter voltage is positive and more significant than the internal source voltage, and a positive signal is applied to the gate input. However, the IGBT switches off when the collector-emitter voltage is positive, and a zero signal is applied at the input gate. The duty cycle *d* falls within the range of 0 and 1 under the switching cycle period. The duty cycle *d* controls the voltage ratio between the input voltage V_{PV} of the PV and output voltage V_{dc} of the DC link as Equation 4.1 [188].

$$V_{dc} = \frac{1}{1-d} V_{PV} \tag{4.1}$$

The individual circuit components in Figure 4.2 are assembled to model and simulate the boost converter, and the IGBT is switched on and off by a preferred duty cycle. A large capacitor keeps the output voltage steady in simulation.

4.3.1.2 Maximum Power Point Tracking (MPPT)

MPPT control algorithms are required for maximum power extraction considering the intermittency caused by irradiance, temperature, and shading. Several MPPT control algorithms are already implemented to achieve optimum system performance. The algorithm senses PV module current and voltage to evaluate duty ratio *d* for the converter. The PWM signal controller then generated for the gate driver to, therefore, control the IGBT.

The short-circuit current I_{SC} and the open-circuit voltage V_{OC} are specified in the current-voltage (*I-V*) curve and power-voltage (*P-V*) curve of a characteristic of the PV module, as shown in Figure 2.4. The corresponding MPP's PV current I_{MPP}, voltage V_{MPP}, and power P_{MPP} of *PV* power P_{PV} are also specified. Consequently, the MPPT algorithm's output can take any control variable; voltage, current, power, and duty cycle at the maximum power point, as shown in the *I-V* and *P-V* characteristics of the PV presented in Chapter Two.

These electric features are contingent on temperature, and solar irradiance sensed on the *PV* cells. The *MPP* current increases proportionally when the solar irradiance increases, as reported in chapter two. The MPP voltage decreases when the cell temperature increases, which reduces output power even under similar irradiance. The MPP varies with the temperature and irradiance change throughout the day. MPPT tracks and operate the PV modules at the MPP regardless of temperature and irradiance variations. Consequently, the MPPT control follows the *MPP* to maintain the optimal output power.

4.3.1.2.1 Incremental Conductance MPPT with Integrator

This work implemented the extremum-seeking MPPT called incremental conductance (IC) already given in chapter two. The already established technique matches incremental conductance with instantaneous conductance and reduces or increases the voltage depending on the result until the MPP is attained. The voltage remains constant once MPP is reached, unlike the perturb and observation procedure. The IC algorithm regulates the modeled DC-DC converter in attaining MPP. The technique is based on the slope observation and interpretation, as is a zero slope at the *MPP* ($dP_{PV}/dV_{PV}=0$). Furthermore, a positive slope ($dP_{PV}/dV_{PV}=+ve$) on the MPP's left and a negative slope ($dP_{PV}/dV_{PV}=-ve$) on the right. Note that ($P_{PV}=V_{PV}I_{PV}$).

4.3.1.2.2 Boost Converter Inner-Loop Control

The converter's inner control loop regulates the converter to the specified reference, and MPPT algorithms technically set the reference. This control regulates the converter voltage input to achieve the desired voltage output. Figure 4.3 shows how the boost converter is implemented, and the V_{PV} input voltage in Equation 4.1 is re-expressed as Equation 4.2. Thus, feedback control is applied in attaining the anticipated input PV voltage. In the feedback loop model of Figure 4.3, the converter voltage is sampled back to the controller via a summing block to extract the error. Subsequently, the controller generates the appropriate duty cycle, attenuating the error to preserve the input voltage at a specified reference.

In an inverter-based microgrid with a DC-DC converter for PV grid integration, the V_{PV} is regulated by the duty ratio. A feed-forward scheme is effected to enhance the DC-bus voltage dynamics based on the postulation that there is no conversion loss from DC to AC. Consequently, the PV's DC side power is equivalent to AC side power transmitted to the AC grid, as shown in Equation 4.3. Thus, since quadrature-axis component voltage V_q is forced to zero value by the PLL's PI controller, the estimated direct-axis current component as a function PV variable is obtained as Equation 4.4 [189].

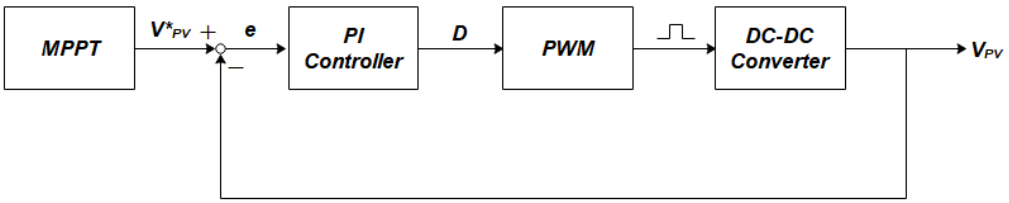

Figure 4. 3: Feedback loop model PV voltage control

$$V_{PV} = V_{dc}(1-d) \tag{4.2}$$

$$I_{PV}V_{PV} = v_d i_d + v_q i_q \tag{4.3}$$

$$i_d^{\approx} = \frac{I_{PV}V_{PV}}{v_d} \tag{4.4}$$

4.3.2 DC-AC Inverter and Modified Grid-Supporting Control

DC-AC inverter transforms input DC power into output AC power. In an inverter-based microgrid with a boost converter, the grid-tied inverter's purpose is to synchronize with the AC grid frequency and transfer the available PV power to the network. The voltage of the DC-link shall be greater than the magnitude of the grid-voltage. The inverter controller is crucial to effectively

deliver DC power from the PV to the AC network and provide high-level grid interaction functionality. The PLL of the controller synchronizes the AC grid voltage to the inverter output. The primary control supplies a corresponding duty cycle to the pulse width modulator. The IGBT-Diode switches are then operated by the modulator-generated signals to produce appropriate output waveforms.

The control of grid-connected inverter-based microgrid with DC-DC converter should meet specific fundamental demands; MPPT and high-quality power injection, low THD voltage, and current waveforms. Consequently, just like an ordinary inverter-based microgrid, the primary controller is sectioned into two cascading control loops: outer power or voltage and inner current. Figure 4.1 presents an AC-DC inverter's primary control scheme in an Inverter-Based Microgrid with DC-DC Converter systems with the introduction of droop control, where G_{INV} and G_B are inverter gate and converter signals, correspondingly. The outer loop produces the reference current for the inner control loop, and then the current control loop regulates the currents and, by extension, power injected.

In an ordinary inverter-based microgrid with an ideal voltage source, the dynamics of optimizing the power extraction and controlling the power fed into the grid are assumed to be done by the inverter. The inverter-based microgrid with DC-DC converter structure does, however, decouple the dynamics.

4.3.2.1 Outer Control Loop

A capacitor with a substantial capacity is installed at the DC-link to balance DC side power with AC side power in an inverter system with a DC-DC converter. It is essential to regulate and smoothen the DC input power before transmission into the AC side via the inverter. The amount of injected power determines the AC grid current peak. Therefore, the active power is controlled by regulating the capacitor DC link voltage, as implemented in Figure 4.4. For the PV source to remain grid-connected, the outer loop control maintains constant DC link voltage. However, the DC-link voltage is relatively more significant than the AC grid voltage's magnitude to guarantee an appropriate injection of power to the AC side. The power at the DC side is given by Equation 4.5. Similarly, the active power injected into the AC grid is given by Equation 4.6. Following power balance while assuming negligible DC-AC inverter power loss, the input power (DC side) is equivalent to the output power (AC power) as given by Equation 4.7. The d-axis voltage V_d equals the phase voltage amplitude E, and the q-axis voltage V_q equals zero when the V_d is aligned with the AC grid voltage. $G_{dc}(s)$ is obtained as the transfer function representing the DC-link voltage plant, thus using Equation 4.8 to linearize the small-signal analysis Equation 4.7. Therefore, $V_{dc}(s)$ is expressed as Equation 4.9. Consequently, a PI controller $G_{DC\text{-}PI}(s)$ is implemented in regulating the voltage at the DC-link in generating a corresponding direct-axis

reference current i^*_{dc} as Equation 4.10. Thus, $G_{CL}(s)$ represents a closed-loop for the direct-axis current control representing the DC-link voltage control loop. The power balance Equation 4.7 can be re-expressed as shown in Equation 4.11, to implement $v_d=E$ and $v_q=0$ to reflect the direct-axis voltage component's alignment with the AC grid voltage. Consequently, the voltage at the DC-link is given as Equation 4.12. Accordingly, the $G_{dc}(s)$ in the previous model in Equation 4.8 is decomposed and modelled as shown in Figure 4.4.

$$P_{dc} = v_{dc} i_{dc} - v_{dc} C_{dc} \frac{dv_{dc}}{dt} \tag{4.5}$$

$$P_{ac} = \frac{3}{2}\left(v_d i_d + v_q i_q\right) \tag{4.6}$$

$$v_{dc} i_{dc} - v_{dc} C_{dc} \frac{dv_{dc}}{dt} = \frac{3}{2}\left(v_d i_d + v_q i_q\right) \tag{4.7}$$

$$G_{dc}(s) = \frac{v_{dc}(s)}{i_d(s)} = \frac{3E}{2\left[I_{dc} - sC_{dc}V_{dc}\right]} \tag{4.8}$$

$$v_{dc}(s) = i_d(s) G_{dc}(s) = i_d(s) \frac{3E}{2\left[I_{dc} - sC_{dc}V_{dc}\right]} \tag{4.9}$$

$$i^*_{dc} = \left[v_{dc} - v^*_{dc}\right] G_{dc-PI}(s) \tag{4.10}$$

$$C_{dc} \frac{dv_{dc}}{dt} = i_{dc} - \frac{3E}{2v_{dc}} i_d \tag{4.11}$$

$$v_{dc}(s) = \frac{1}{C_{dc}s}\left[i_{dc}(s) - \frac{3E}{2v_{dc}} i_d(s) \right] \tag{4.12}$$

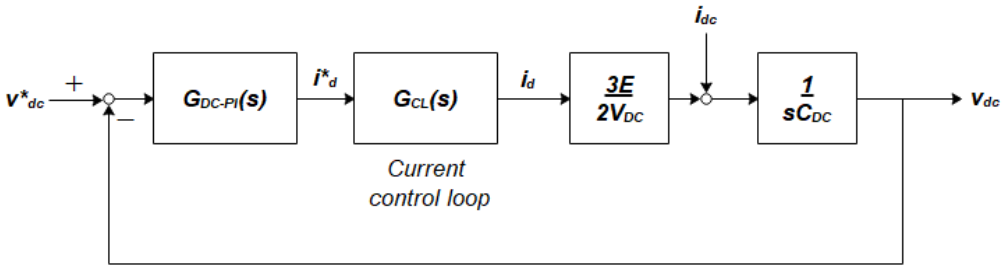

Figure 4. 4: Modelling of the DC-link voltage loop applying power balance equation

Subsequently, *PI* controllers are applied to DC-link voltage plant transfer function $G_{DC}(s)$, and this results in Equation 4.13 where $k_{p\text{-}dc}$ and $k_{i\text{-}dc}$ are the proportional and integral gains while $T_{i\text{-}dc}$ is the time constant of the integral gain. Similarly, the current control closed-loop is calculated as in Chapter 3 and as represented by the PI controller given in Equation 4.14 where $k_{p\text{-}cl}$ and $k_{i\text{-}cl}$ are the proportional and integral gains while $T_{i\text{-}cl}$ is the time constant of the integral gain. Hence, the

overall DC voltage open-loop control is modelled as Equation 4.15 from Figure 4.4 and Equations 4.13 and 4.14.

$$G_{dc-PI}(s) = k_{p-dc} + \frac{k_{i-dc}}{s} = k_{p-dc}\left[1 + \frac{1}{T_{i-dc}s}\right] \tag{4.13}$$

$$G_{CL}(s) = k_{p-cl} + \frac{k_{i-cl}}{s} = k_{p-cl}\left[1 + \frac{1}{T_{i-cl}s}\right] \tag{4.14}$$

$$\begin{aligned} G_T(s) &= \frac{3E}{2V_{dc}} \times \frac{k_{p-dc}s + k_{i-dc}}{s} \times \frac{k_{p-cl}s + k_{i-cl}}{s} \\ &= \frac{3E}{2V_{dc}} \times \frac{k_{p-dc}\left(1 + T_{i-dc}s\right)}{T_{i-dc}s} \times \frac{k_{p-cl}\left(1 + T_{i-cl}s\right)}{T_{i-cl}s} \end{aligned} \tag{4.15}$$

Furthermore, the active power available related to the reference *d*-axis current estimated by Equation 4.10 and relation to the active power reference is drawn from Equation 3.14 in Chapter 3, when the $v_q=0$. However, the *q*-axis outer loop control for the reference current is consistent with the approach already presented in Chapter 3.

4.3.2.2 Inner Current Loop Control

The presence of a DC-DC converter with a regulated DC-link voltage introduces dynamics into the control. The direct-axis and quadrature-axis components are equivalent to *DC* quantities of the DC-link of the DC-AC inverter. Similarly, as in Chapter 3, the *PI* controllers are used to regulate the grid current, in line with the required active and reactive power, via the direct-axis and quadrature-axis output current components. Conversely, the direct-axis and quadrature-axis components are linked and, therefore, causing slight complications in their independent control system. Similarly, the AC grid voltage also influences the dynamics of the control system. Consequently, the *dq* references of the output voltage are improved by subtracting feed-forward *dq* voltage and decoupling components as in Equation 3.15. Consequently, the *dq* output currents injected into the grid are decoupled in line with the desired modulation signal after applying the Laplace Transform to derive the s-domain equivalent.

4.4 Grid Supporting Control

The circuit and control diagram of the developed time-domain models of DC-AC inverter-based microgrid with a DC-DC converter and maximum power point tracking that integrate photovoltaic-based distributed energy resources is shown in Figure 4.5. To achieve the second objective and ensure that the system in Figure 4.5 possesses the ability to participate in grid

frequency and voltage regulation, the droop control implemented in Chapter 3 is introduced between the DC link voltage control outer loop and the inner current control.

The objective here is to implement an active power control and reactive power control based on droop control to fit the overall control scheme of an inverter-based microgrid with a DC-DC converter. This applies to the PV system. The control is based on the output power regulation at a lesser value to MPPT extracted power P_{mpp} per the grid frequency and voltage variation, as shown in Equation 3.20. The variance of ω from ω^* is exploited in regulating the output power. Typically, P_{mpp} is estimated with MPPT control.

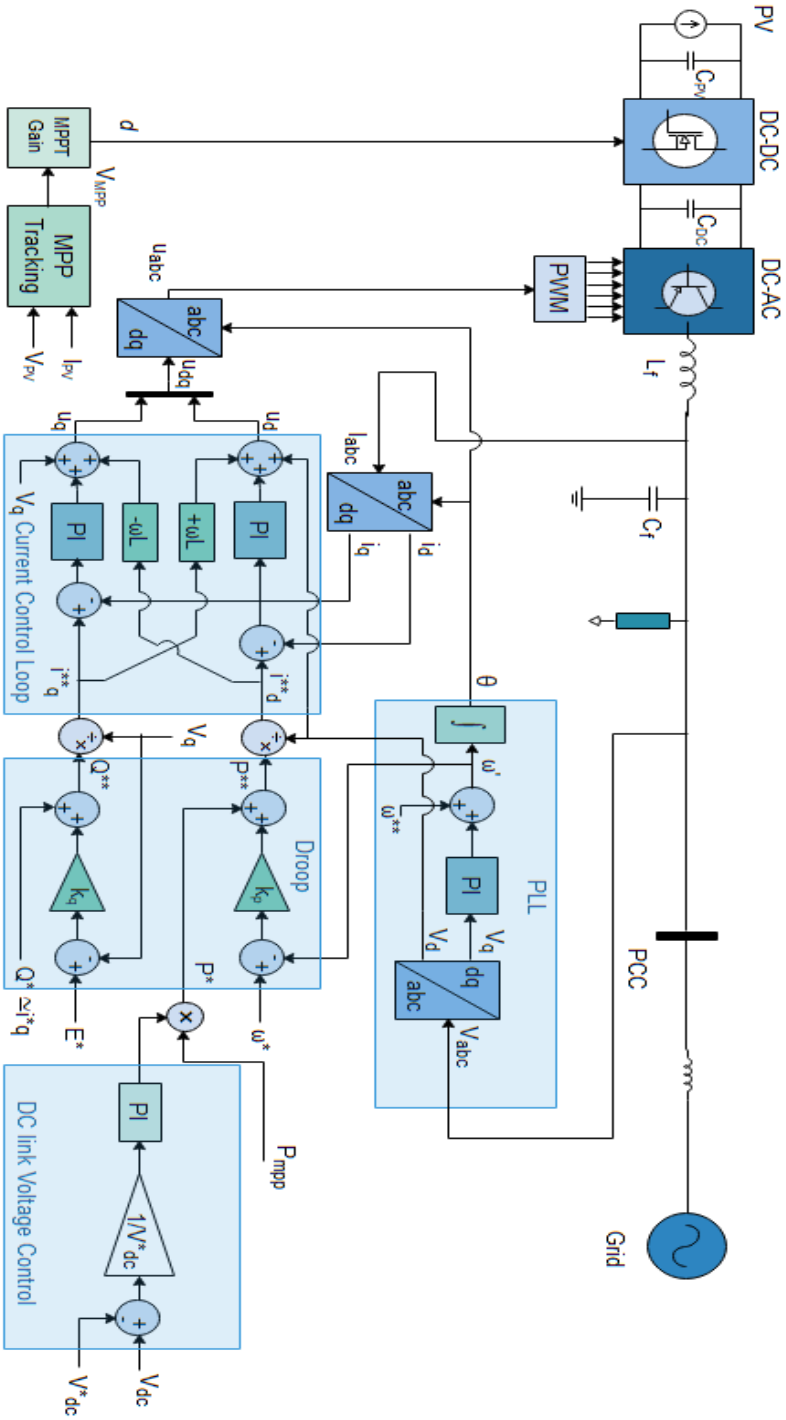

Figure 4. 5:Incorporated Grid Supporting Control with Droop for Inverter Based Microgrid with DC-DC Converter

The inverter's active power output is determined using *P-ω* droop control, mimicking synchronous generators' inertial response, while the reactive power output of the voltage source inverter is determined using *Q-E* droop.

4.5 System Simulation

The parameters of implementation used in the model simulation are given in Tables 4.1, 4.2, 4.3, and 4.4. Also, to validate the model developed, the irradiance is varied, as shown in Table 4.3.

Table 4. 1: PV Simulation Parameters

Parameters	Descriptions	Values
P_{MPP}	PV system maximum power	20 kW
Q^*	PV reactive power reference	0 kVAr
P_L	Active power of the load	10 kW
Q_L	Reactive power of the load	5 kVAr
E_e	Maximum irradiance	1000 W/m^2
T_e	Temperature	25^0 C
V^*_{dc}	Reference DC link voltage	1000 V
E	AC single phase voltage amplitude	330 V
C_{DC}	DC link capacitor	2400 μF
C_{PV}	PV side capacitor	10 μF
L	DC link inductor	5 mH
C_f	LC filter capacitance	2.31 μF
L_f	LC filter inductance	11 mH
$K_{p\ cl}$	proportional current control loop gain	0.3
$K_{i\ cl}$	integral current control loop gain	20
$K_{p\ dc}$	proportional DC link voltage loop gain	7
$K_{i\ dc}$	integral DC link voltage loop gain	800
P_L	Active power of the load	10 kW
Q_L	Reactive power of the load	0.5 kVAr

Table 4. 2: PV Simulation Parameters

Time (seconds)	Irradiance (W/m^2)
0-2	1000
2-4	800
4-6	500
6-8	700
8-10	600

Table 4. 3: DC-DC Converter electrical parameters

Parameters	Descriptions	Values
L	Series inductance	5 mH
R	Series resistance	0.0005 Ω
C_{PV}	Input DC link capacitor	10 µF
R_S	Diode internal resistance	10 mΩ

Table 4. 4: MPPT and DC-DC converter control parameters

Parameters	Descriptions	Values
$K_{p\ MPPT}$	Regulator P gain	5
$K_{i\ MPPT}$	Regulator I gain	1
f_{PWM}	DC-DC converter PWM switching frequency	20 kHz

The grid operates at the 11 kV phase to phase RMS voltage, and a 400/11000 V step-up transformer is installed between the grid and the microgrid. The DC-AC inverter control fed the extracted DC power properly into the AC grid. This is realized using two loop current control. The outer loop is a controller for DC-link voltage. This loop, otherwise known as the power loop, is designed to produce the *dq* references for current used by the internal current loop control in Figure 4.6. The inner loop generates the reference *dq* voltage used as the PWM input, as shown in Figure 4.7.

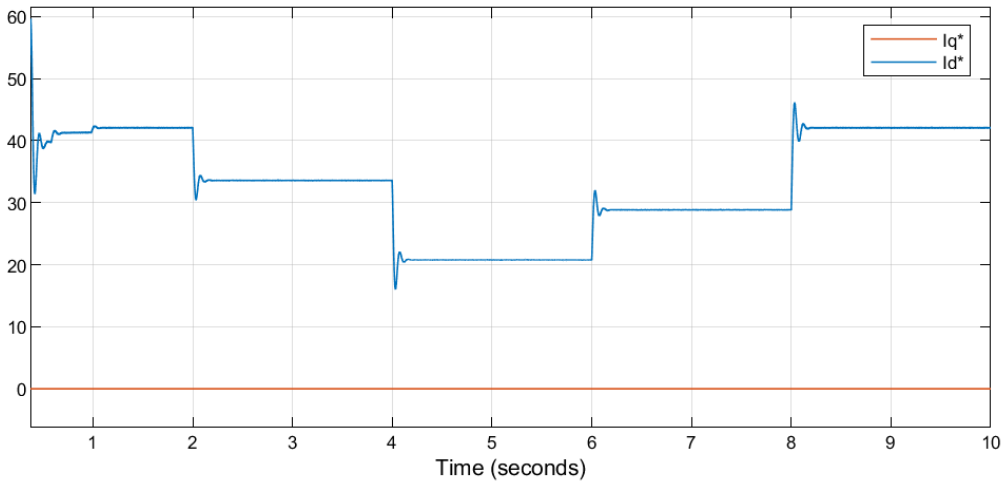

Figure 4. 6:The d-q current reference

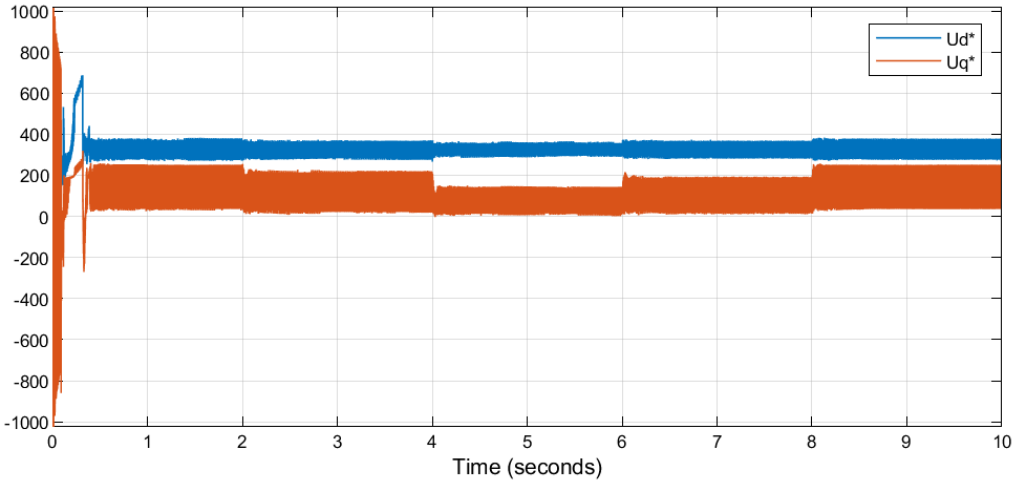

Figure 4. 7: The d-q voltage reference

The output of the MPPT here is the duty cycle *d* as presented in Figure 4.8. The PV voltage V_{PV} shown in Figure 4.9 is regulated by the duty cycle d of the converter. The MPPT controller supplies the corresponding *d*, which is the PWM input for the DC-DC converter. The DC-DC converter switches are then operated by the PWM signals to produce the output's proper waveforms.

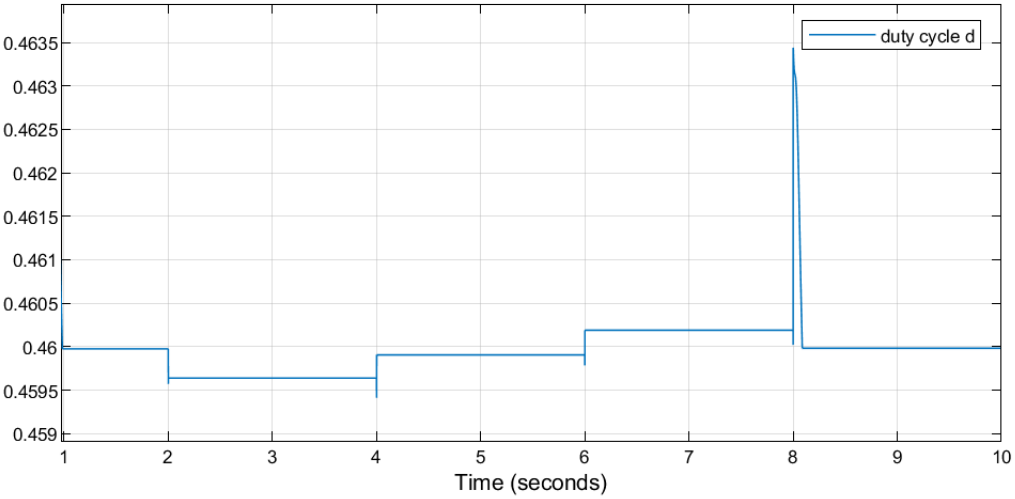

Figure 4. 8: Duty ratio *d*

The DC link voltage V_{DC} in Figure 4.9 steadily fluctuates within a range, and it is moderately constant at 1000 V, mainly when the system attained a steady-state operation at 0.5 seconds. V_{DC} is constant with respect to the PWM 5000 Hz switching frequency, which is equivalent to a period of 0.0002 seconds. Therefore, the duty cycle *d* switching the IGBT is fine-tuned to regulate the input V_{PV} as shown in Figure 4.9. Thus, in Figure 4.8, the duty cycle is precisely tuned to operate at the PV arrays' MPP voltage V_{MPP}. The constant output voltage V_{DC} in Figure 4.9 serves as the inverter's input. Therefore, an inverse proportion relationship exists between the duty cycle and voltage V_{PV}. Hence, rising *d* reduces the voltage input, and reducing *d* raises the voltage input. Thus, feedback control has been applied to attain the preferred voltage input V_{PV}, as presented.

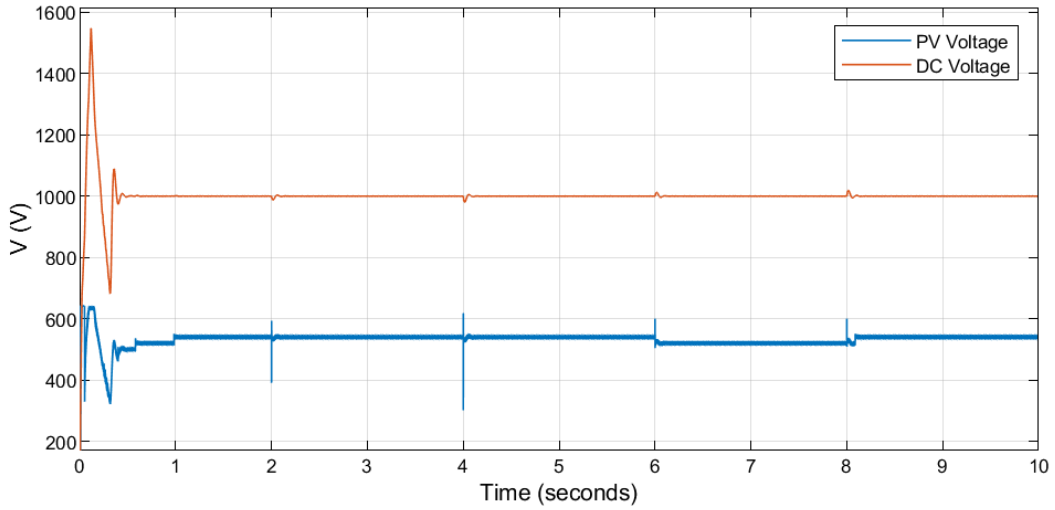

Figure 4. 9: Voltage at the DC link and the PV terminals

The MPPT algorithm regulates the DC-DC converter activities, which ensures that the PV strings operate at MPP. Hence the incremental conductance equation in Chapter 2 is given in Figure 4.10. The MPP is monitored by relating instant conductance (I/V) with incremental conductance (ΔI/ΔV). In other words, the MPPT ensures that the PV system works at a reference voltage V^* such that the MPPT is only attained when the $V^*=V_{MPP}$.

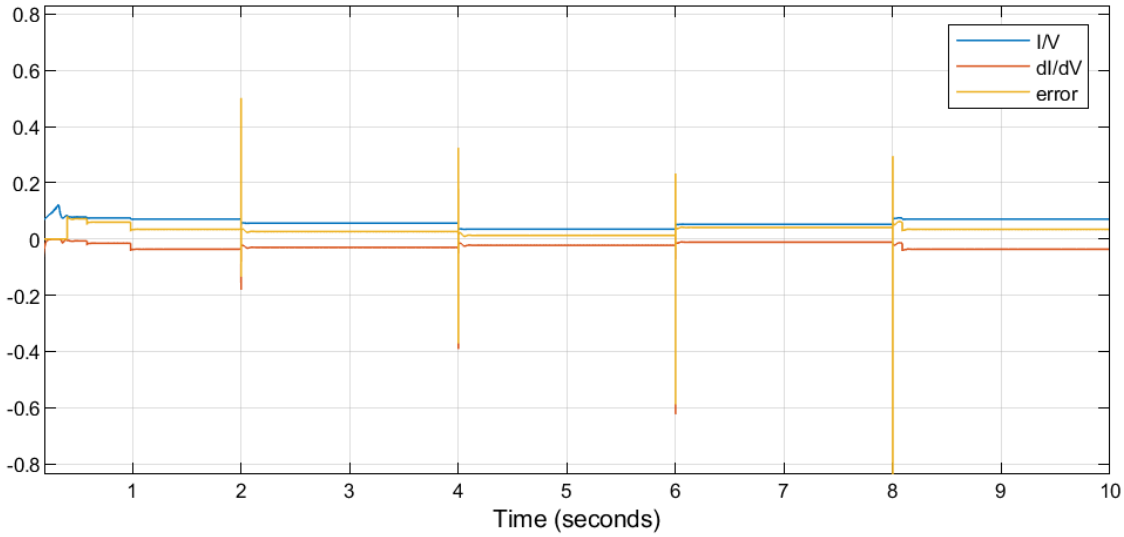

Figure 4. 10: MPPT instant conductance V/I, incremental conductance, MPPT Error

In the overall conversion scheme, the DC-DC converter model regulates the maximum power extraction from the PV modules to the DC link while the DC-AC inverter model actively transmits power synchronously to the AC grid. The maximum power P^* generated by the droop's output is given in Figure 4.11, which indicates the reference to the voltage/power control.

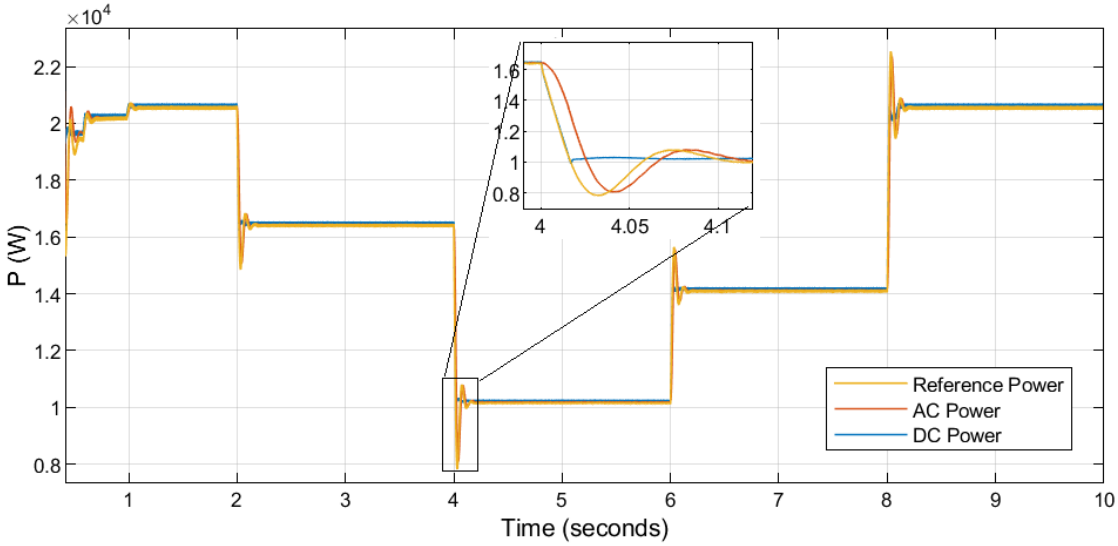

Figure 4. 11: Generated *P** reference, Calculated DC Power and AC Power Output

The modelled DC-DC converter accepts reference power *P** as input. The converter processes the power and transmits it into another DC voltage level in the DC link as output. This output power of the DC-DC serves as the input to the DC-AC as given in Figure 4.11 as calculated DC power. Similarly, this is responsible for the different current values for the PV arrays and DC links, as shown in Figure 4.12. Similarly, the current through the diode is reported in Figure 4.12.

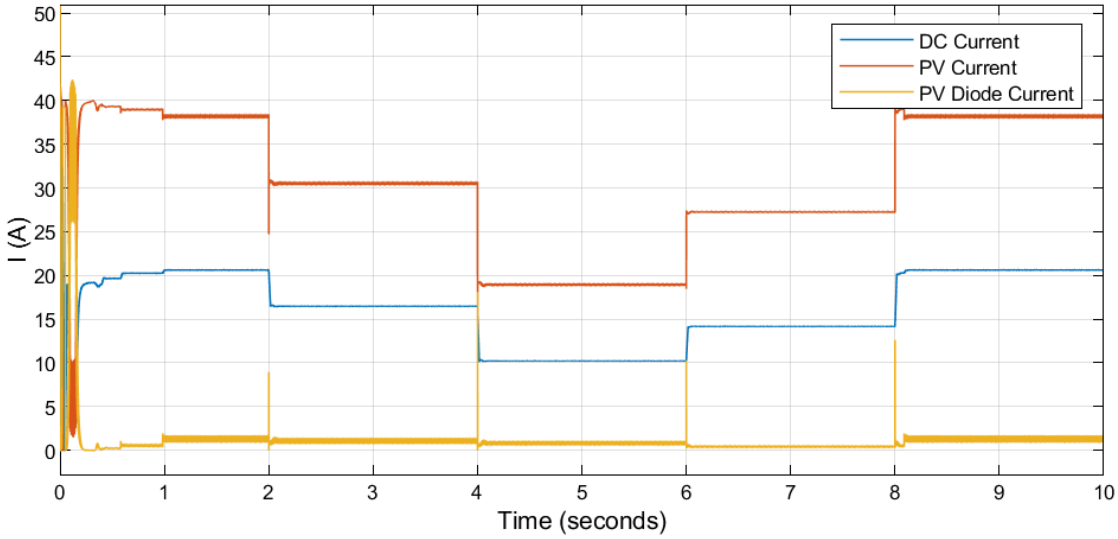

Figure 4. 12: PV Current, DC current and PV Diode Current

The MPP changed accordingly with a varying irradiance at a constant temperature of 25 ^{0}C, as shown in Table 4.3. Thus, the control followed the maximum power point and maintained the optimum operational output for PV power using MPPT control. This, therefore, validates that MPPT algorithms and control track and run the PV system at the maximum power point, notwithstanding fluctuations in environmental circumstances. The corresponding power output injected to the AC grid system is, therefore, revealed in Figure 4.11.

The DC-AC inverter transforms input DC power into output AC power. In an inverter-based microgrid with a DC-DC converter, the inverter's purpose is to synchronize with the AC grid frequency and voltage while transferring the available PV power to the network. The converter optimized generated power, and the inverter injected the DC equivalent power efficiently into the system at the AC side. The control developed focuses on controlling Power. Stable and effective control is needed to optimize the generated power and transmit power efficiently to the low-noise and low THD AC power grid. The main grid voltages at the PCC and within the main network are shown in Figures 4.13. The microgrid voltages at the PCC and within the main network are shown in Figures 4.14.

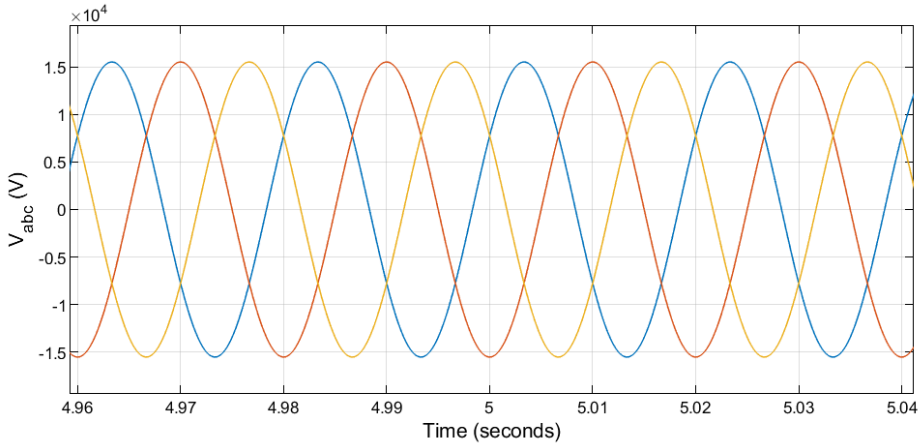

Figure 4. 13: Main grid Three-phase voltage waveforms

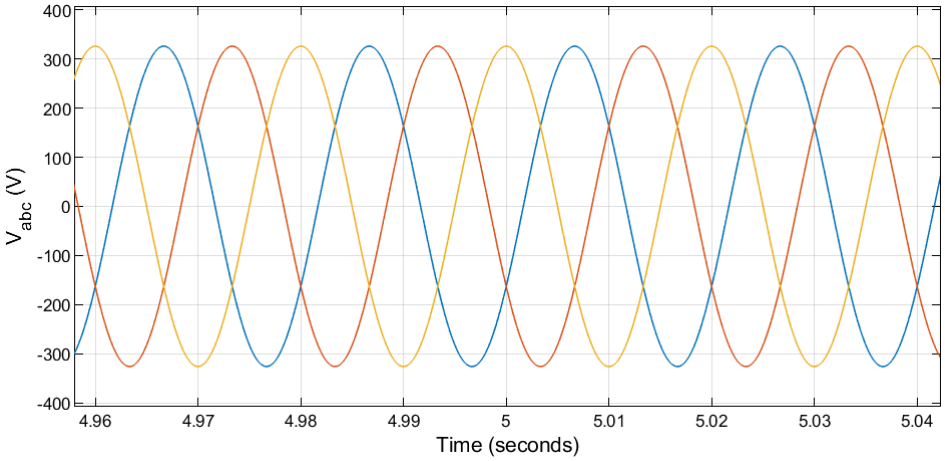

Figure 4. 14: Microgrid PCC Three-phase voltage waveforms

Similarly, the THD of the voltage at the PCC is given in Figure 4.15. The less THD measurement in the three phases' waveforms further proves that the developed model fulfils one of the requirements for a grid-supporting operation [190]. Figure 4.15 signifies the quality of power injected into the main grid and local microgrid load.

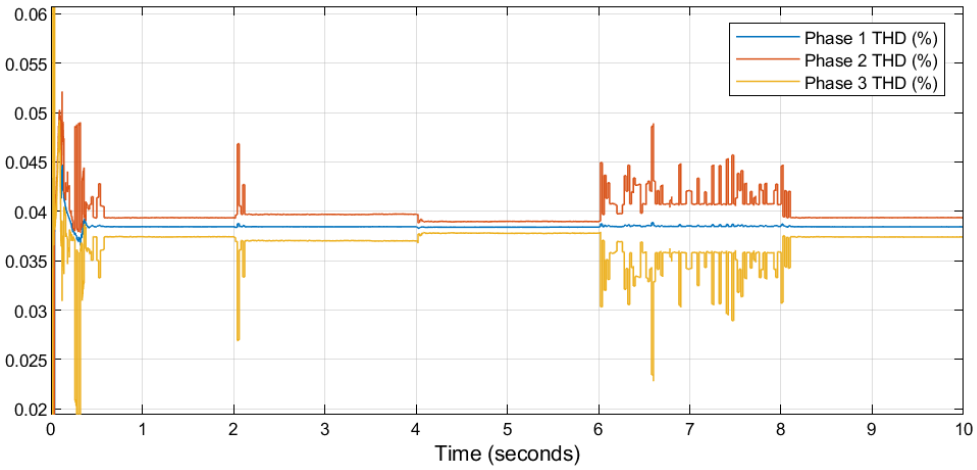

Figure 4. 15: AC output voltage waveform THD

In the three-phase grid-connected inverter-based microgrid, the grid-voltage V_{abc} and the current I_{abc} are two AC variables used for the control. In summary, the results of the inverter AC output model are given by these parameters.

The Control System Toolbox™ power analysis is utilized in computing the equivalent state-space model of the system's electrical models built with Simscape™. The customary A, B, C, D matrices of the discrete-time state-space system are therefore evaluated. Thus, the system realized 26 states-by- 26 states state-space A matrix. 26 states-by- 13 input state-space B matrix. 72 output-by- 26 states state-space C matrix. 72 output-by- 13 input state-space D matrix. The Lambda λ = eig(A) returns a column vector containing the square matrix A's eigenvalues. The two systems' eigenvalues are given in Table 4.5, and the plot is given in Figure 4.16.

Table 4. 5: Eigenvalues of the developed model

Mode	**Model**	**Mode**	**Model**
λ_1	-0.6256 + 0.0000i	λ_{14}	-0.9863 + 0.0000i
λ_2	-0.4110 + 0.0000i	λ_{15}	-0.9863 + 0.0000i
λ_3	-0.4110 + 0.0000i	λ_{16}	-1.0000 + 0.0000i
λ_4	-0.2678 + 0.0000i	λ_{17}	-0.9999 + 0.0000i
λ_5	-0.9991 + 0.0000i	λ_{18}	-0.9999 + 0.0000i
λ_6	-0.9743 + 0.1131i	λ_{19}	-1.0000 + 0.0000i
λ_7	-0.9743 - 0.1131i	λ_{20}	-1.0000 + 0.0000i
λ_8	-0.9743 + 0.1131i	λ_{21}	-1.0000 + 0.0000i
λ_9	-0.9743 - 0.1131i	λ_{22}	-1.0000 + 0.0000i
λ_{10}	-0.8018 + 0.0000i	λ_{23}	-1.0000 + 0.0000i
λ_{11}	-0.8018 + 0.0000i	λ_{24}	-1.0000 + 0.0000i
λ_{12}	-0.9512 + 0.0000i	λ_{25}	-1.0000 + 0.0000i

λ_{13}	-0.9863 + 0.0000i	λ_{26}	-1.0000 + 0.0000i

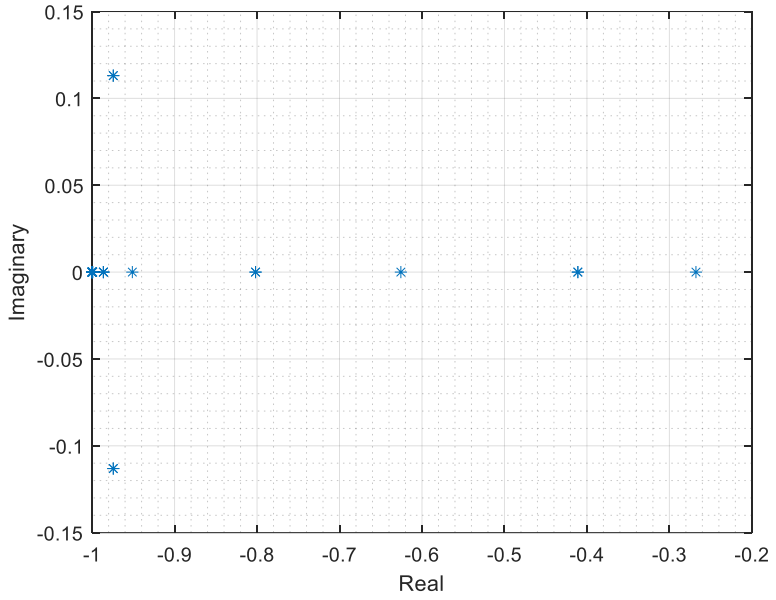

Fig. 14. Eigenvalues of the State-Space equivalent of the system

4.6 Conclusion

The objective here is to implement an active power control and reactive power control based on droop control to fit the overall control scheme of an inverter-based microgrid with a DC-DC converter. This is typical of the PV system operating in the grid-supporting mode for voltage and frequency regulations and has been applied to the grid supporting mode. The control is based on the output power regulation at a lesser value to MPPT extracted power P_{mpp} per the grid frequency and voltage variation as shown. The drop is implemented between the outer DC link voltage control and the iner loop current control without compromising the grid-connected PV system's design and effectiveness. The variance of ω from $\omega*$ is exploited in regulating the output power. Typically, P_{mpp} is estimated with MPPT control. The inverter's active power output is determined using P-ω droop control, mimicking synchronous generators' inertial response, while the reactive power output of the voltage source inverter is determined using Q-E droop.

CHAPTER FIVE
FAULT RIDE-THROUGH USING SECONDARY MICROGRID CONTROL

5.1 Introduction

Chapter five presents the proposed FRT approach of this work, which is implemented at the hierarchical control structure's secondary level. Similarly, the fault detection scheme: delayed signal cancelation algorithm, which extracts the positive sequence and negative sequence components, is also presented. The sequence detection is used for adequate compensations at the secondary level to provide accurate references for the primary level of control to mitigate voltage sag effect because of faults or transients in the main grid. Similarly, to mitigate the effect of severe grid fault on the sensitive microgrid load and maximum reactive power injection into the grid during a fault, power flow analysis is conducted between the grid and the microgrid.

Consequently, a theoretical framework for the determination of the capacity of an IGBT switched inductance is presented. The reactive power referencing approach for FRT used to support the grid voltage is also presented against the methods already discussed in chapter two. Furthermore, the current limitation approach is presented by setting the active power reference to comparable to the depth of the grid voltage drop while considering the inverter complex power rating to avoid the inverter limit protection scheme's activation. Lastly, the active power referencing in an inverter-based microgrid with a DC-DC converter is a little bit cumbersome; consequently, this chapter introduces a unique method of changing the operating limit of the MPPT control of the DC-DC converter. The approach introduced can shift the operating point from MPP mode to FRT mode, and vice versa; the grid fault is immediately cleared.

This chapter proposes a secondary control for the fault ride-through of an inverter-based microgrid. The inverter-based microgrids' time-domain models have already been developed in Chapter 3 (with an ideal DC source) and Chapter 4 (with a PV source). This chapter proposes a delayed signal cancellation algorithm for fault detection and changing the system's operating point to fulfill the fault ride-through and provide dynamic voltage supports. The time-domain models already developed cannot ride-through grid fault without the proposed secondary control. The fast and accurate detection of fault is crucial to the secondary FRT control proposed. Similarly, the appropriate injection and generation of power under normal and fault conditions is essential.

Faults are typically unbalanced, and in asymmetrical situations (phase to ground and line to line), the grid codes are less stringent than strict regulations placed under the symmetrical (three-phase) fault. Nevertheless, other restrictions are imposed, including a prohibition on the grid absorption of both active and reactive power in the event of a fault as stipulated in the Spanish P.O.12.3 regulation [191][192]. Therefore, the grid imbalance can be eliminated promptly alongside

current limitations by suppressing grid active power absorption and supporting grid voltage recovery by contributing an adequate reactive current.

The Spanish grid code guidelines[28][193] are used to establish the FRT's secondary control in this thesis. These government-issued documents stipulate that grid-connected DGs should ride-through a drop in grid voltage of at least 0.2 pu lasting 500 milliseconds. However, when the voltage drops versus time are outside the FRT curve, these DERs can disconnect from the grid. Also, DERs are required to inject a specified quantity of reactive power defined by the reactive power support capability to support the voltage sag, as shown in Figure 1.4 of Chapter 1. Nonetheless, during the voltage drop beyond 90%, an insignificant amount of reactive power support is expected to be injected. The Spanish grid code essentially specifies a certain amount of reactive current/power (per unit) injection based on the percentage drop in voltage.

5.2 Delayed Signal Cancellation Algorithm

In order to avoid exceeding the limit, the PCC voltage magnitude control is set up to buffer and prevent exceeding the grid code maximum specified and required voltage range (0.9–1.1 pu). The values of its symmetrical components are obtained to implement an effective unbalanced grid voltage compensation. The delayed signal cancellation (DSC) is implemented, following Figure 5.1 to detect the presence of symmetrical components and obtain their values accordingly. A time of 5ms is used for the grid frequency of 50 Hz. This is calculated by $N_d=fs/(4f_1)$, where fs is the sampling frequency, and f_1 is the fundamental frequency, which is 50 Hz grid frequency in our study case

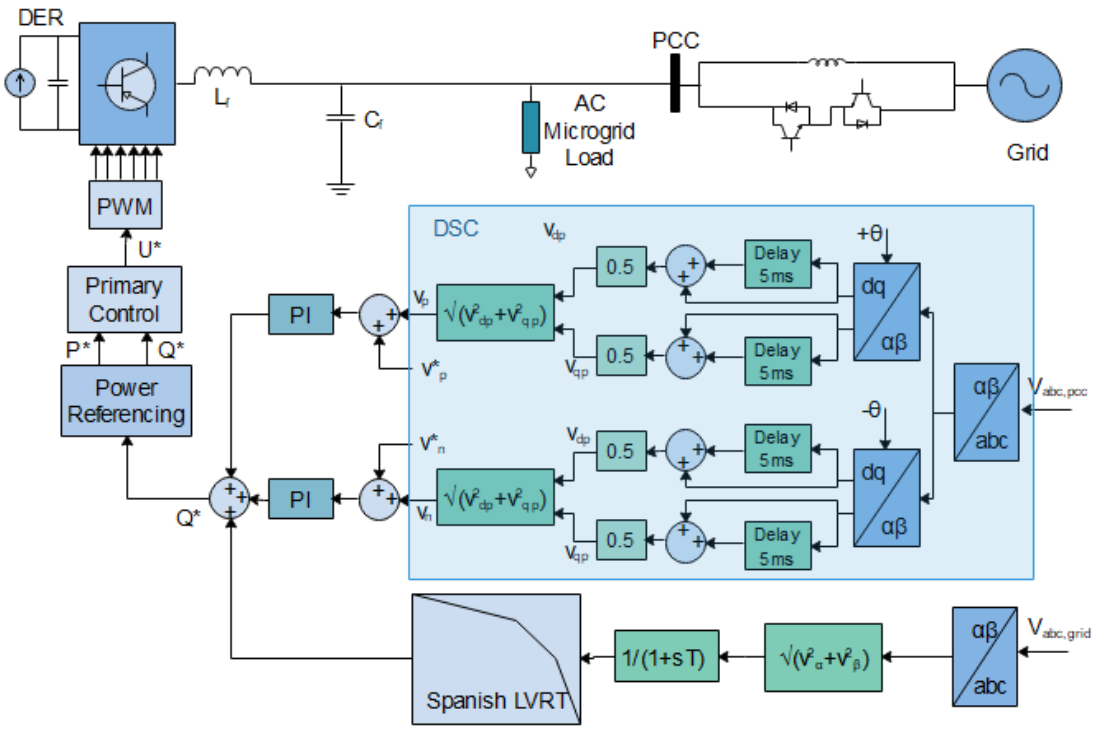

Figure 5. 1: Proposed FRT control scheme

The DSC algorithm is centred on the three-phase voltage measurement and subsequent decomposition into their commensurate symmetrical components [194]. In the stationary reference frame, the voltages measured in phase are primarily indicated using the Clarke (*abc-*$\propto\beta$) transformation.

$$\begin{bmatrix} v_\alpha \\ v_\beta \end{bmatrix} = \begin{bmatrix} 1 & 0 & 0 \\ 0 & \frac{\sqrt{3}}{3} & -\frac{\sqrt{3}}{3} \end{bmatrix} \cdot \begin{bmatrix} v_a \\ v_b \\ v_c \end{bmatrix} \tag{5.1}$$

In line with the resultant stationary reference frame above, two opposite rotations are executed using the host grid voltage's phasor measured angle (θ and $-\theta$). This angle θ matches the same provided at the output of the phase-locked loop. The positive component implies

$$\begin{bmatrix} v_\alpha^p \\ v_\beta^p \end{bmatrix} = \begin{bmatrix} \cos\theta & \sin\theta \\ -\sin\theta & \cos\theta \end{bmatrix} \cdot \begin{bmatrix} v_\alpha \\ v_\beta \end{bmatrix} \tag{5.2}$$

The negative component implies

$$\begin{bmatrix} v_\alpha^n \\ v_\beta^n \end{bmatrix} = \begin{bmatrix} \cos\theta & -\sin\theta \\ \sin\theta & \cos\theta \end{bmatrix} \cdot \begin{bmatrix} v_\alpha \\ v_\beta \end{bmatrix} \tag{5.3}$$

The values obtained for $v_{\alpha\beta}^{p}$and $v_{\alpha\beta}^{n}$ are subsequently kept for half a period in two independent data buffers. Lastly, the positive component and negative component final samples are obtained and immediately kept in the two buffers at a time equivalent to half a period. The components and their additions are expressed in Equations 5.4 and 5.5. The second term samples in Equations 5.4 and 5.5 are equal to the components of the first term, and, however, a fourth duration is shifted, and this change is expressed by multiple of the second terms. The negative and positive sequence components of voltage and current signals need to be obtained for the LVRT application. The positive-sequence component $v_{\alpha\beta}^{p}$and negative-sequence components $v_{\alpha\beta}^{n}$ are separated by traditional DSC techniques described in the literature using Equations 5.4 and 5.5. This accurate sequence separation process involves a delay of the signal within a quarter of the fundamental frequency.

$$v_{\alpha\beta}^{p} = \frac{1}{2}\left[v_{\alpha\beta}(t) - jv_{\alpha\beta}\left(t - \frac{f_s}{4 \cdot f_g} \right) \right] \tag{5.4}$$

$$v_{\alpha\beta}^{n} = \frac{1}{2}\left[v_{\alpha\beta}(t) + jv_{\alpha\beta}\left(t - \frac{f_s}{4 \cdot f_g} \right) \right] \tag{5.5}$$

The traditional DSC algorithm demonstrated in the Figure 5.2(a), where two components t_1 and t_2 of $v_{\alpha\beta}(t)$ are rotated counter-clock wisely. Subsequently, in Figure 5.2(b), the fundamental delay cycle $v_{\alpha\beta}(t - f_s/4 \cdot f_g)$ is applied respectively to extract components t_1. Consequently, this adds a phase shift delay of $-\pi$ to the component t_1. Hence, a phase shift delay of -2π is added to the component t_2. Therefore, the backward rotation clock wisely will compensate by the addition of $+\pi$ to the two components' phases. Consequently, t_1 is rotated back to its initial position. Thus, the component t_1 is doubled in length, and t_2 is reduced to zero with the superimposition of Figures 5.2 (a) and (b). The resultant is, therefore, shown in Figure 5.2 (c).

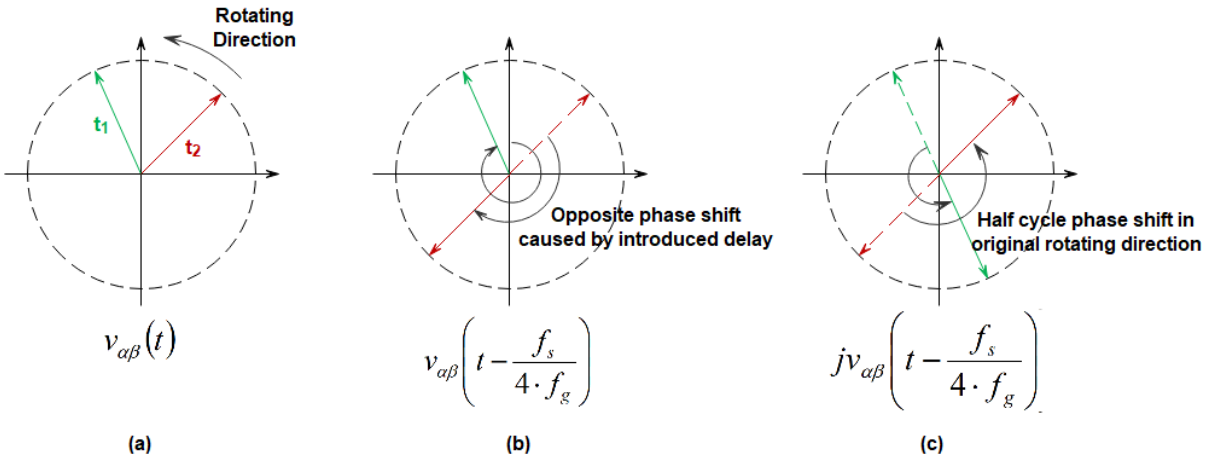

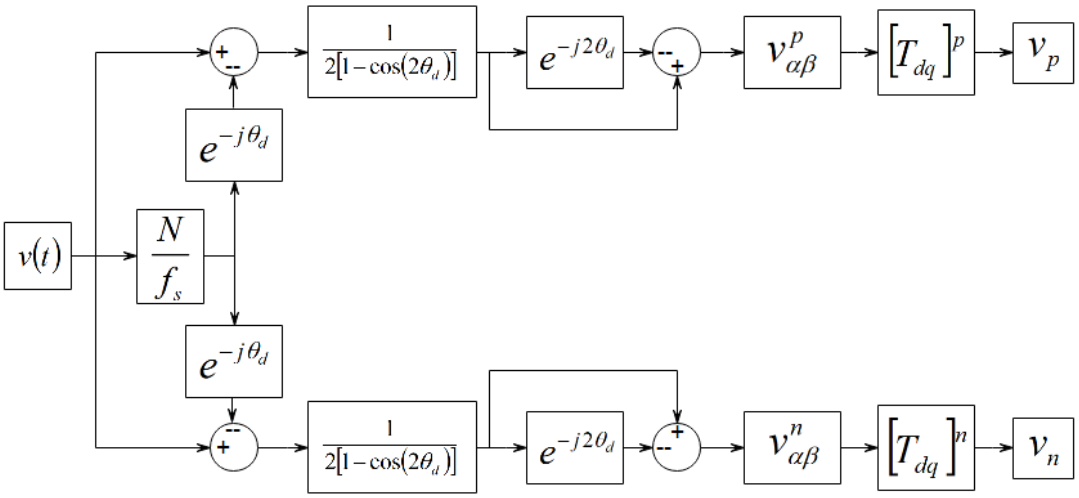

(d)

Figure 5. 2: Delayed Signal Cancellation Demonstration

The fast DSC implemented in this work is different from conventional DSC used in [195] with the substantial delay (5ms for 50Hz) incurred as a result of using $v_{\alpha\beta}^{p}$and $v_{\alpha\beta}^{n}$, which is a significant weakness. Similarly the ration $f_s/4 \cdot f_g$ must be an integer, which is not realistic in actual implementation. Furthermore, a further drawback of $v_{\alpha\beta}^{p}$and $v_{\alpha\beta}^{n}$ is that the vector $v_{\alpha\beta}\left(t - f_s/4 \cdot f_g\right)$ will require a relatively high memory. The Fast DSC implemented for sequence components separation has a reduced settling time.

The voltage vector $v_{\alpha\beta}$consists of both positive and negative components as expanded by:

$$v_{\alpha\beta} = v_{\alpha\beta}^{p} + v_{\alpha\beta}^{n} \tag{5.6}$$

Such that

$$v_{\alpha\beta} = v_{\alpha} e^{j\omega t + \phi_1} + v_{\beta} e^{-j\omega t + \phi_2} \tag{5.7}$$

Where $\phi_1$and ϕ_2 are chosen as random angles depicting negligible phase shifts. Thus, Equations 5.4 and 5.5 can be expanded as a result of Equation 5.7.

$$v_{\alpha\beta}^{p} = \frac{1}{2}\left[v_{\alpha\beta}(t) - \frac{j}{\omega} \cdot \frac{\partial v_{\alpha\beta}(t)}{\partial t} \right] \tag{5.8}$$

$$v_{\alpha\beta}^{n} = \frac{1}{2}\left[v_{\alpha\beta}(t) + \frac{j}{\omega} \cdot \frac{\partial v_{\alpha\beta}(t)}{\partial t} \right] \tag{5.9}$$

Hence, the filtered version of the $v_{\alpha\beta}(t)$is expressed as $v(t)$where

$$v = v_{\alpha\beta}(\omega t) - e^{-j\theta_d} v_{\alpha\beta}(\omega t - \theta_d) \tag{5.10}$$

Where θ_d is the delay angle expressed as in Equation 5.11

$$\theta_d = \frac{2\pi f_s}{N \cdot f_g} \tag{5.11}$$

The voltage vector v is derived by applying Equations 5.6 and 5.7 to Equation 5.10 as expressed in Equation 5.12

$$v = v_{\alpha\beta}^{p} e^{j\omega t} + v_{\alpha\beta}^{n} e^{-j\omega t} - e^{j\theta_d}\left[v_{\alpha\beta}^{p} e^{j(\omega t - \theta_d)} + v_{\alpha\beta}^{n} e^{-j(\omega t - \theta_d)}\right] \tag{5.12}$$

Hence the negative sequence component is canceled out in Equation 5.12 as further expressed in Equation 5.13.

$$v_{\alpha\beta}^{p} = \frac{v}{\left[1 - e^{-j2\theta_d}\right]} = \frac{1}{2}\left[\frac{\left[v_{\alpha\beta}(\omega t) - e^{-j\theta_d} v_{\alpha\beta}(\omega t - \theta_d)\right]\left(1 - e^{j2\theta_d}\right)}{1 - \cos(2\theta_d)}\right] \tag{5.13}$$

Therefore the negative component canceled out is expressed by Equation 5.14

$$v_{\alpha\beta}^{n} = \frac{1}{2}\left[\frac{\left[v_{\alpha\beta}(\omega t) - e^{j\theta_d} v_{\alpha\beta}(\omega t - \theta_d)\right]\left(1 - e^{-j2\theta_d}\right)}{1 - \cos(2\theta_d)}\right] \tag{5.14}$$

The positive and negative sequence components are similar to that of traditional DSC provided the delay angle in Equations 5.13 and 5.14 approaches zero, as expressed in Equation 5.11.

Hence a time delay of f_s/N seconds, which corresponds to the θ_d as given in Equation 5.11 is realized. Thus at the exact delay angle $\theta_d = \pi/2$, the output of the traditional DSC is achieved. However, the delay can be made greater than 5ms with noise when the .

Suppose

$$\begin{aligned} a &= v_\alpha - v_\alpha^{\theta_d}\cos\theta_d - v_\beta^{\theta_d}\sin\theta_d \\ b &= v_\beta - v_\beta^{\theta_d}\cos\theta_d + v_\alpha^{\theta_d}\sin\theta_d \\ c &= v_\alpha - v_\alpha^{\theta_d}\cos\theta_d + v_\beta^{\theta_d}\sin\theta_d \\ d &= v_\beta - v_\beta^{\theta_d}\cos\theta_d - v_\alpha^{\theta_d}\sin\theta_d \end{aligned} \tag{5.15}$$

Therefore the sequence component estimates in the stationary reference frame are given as

$$v_\alpha^{p} = \frac{1}{2}\left[\frac{a - a\cos(2\theta_d) + b\sin(2\theta_d)}{1 - \cos(2\theta_d)}\right] \tag{5.16}$$

$$v_{\beta}^{p} = \frac{1}{2}\left[\frac{b - b\cos(2\theta_d) - a\sin(2\theta_d)}{1 - \cos(2\theta_d)}\right] \tag{5.17}$$

$$v_{\alpha}^{p} = \frac{1}{2}\left[\frac{c - c\cos(2\theta_d) + d\sin(2\theta_d)}{1 - \cos(2\theta_d)}\right] \tag{5.18}$$

$$v_{\alpha}^{p} = \frac{1}{2}\left[\frac{d - d\cos(2\theta_d) - c\sin(2\theta_d)}{1 - \cos(2\theta_d)}\right] \tag{5.19}$$

This the proposed fast DSC is deployed for the secondary control is given in Figure 5.2(d). Therefore a transformation from *αβ0* stationary reference frame to *dq0* rotating reference frame is performed using

$$v_{\alpha} + jv_{\beta} = (v_d + jv_q)e^{j\omega t} \tag{5.20}$$

The positive and negative component voltage-independent control is done in conformity with their respective sequence references is expressed in Equation 5.21.

$$\Delta Q = \left(k_{pp} + \frac{k_{pp}}{sT_{ip}}\right)\left[v_p^* - v_p\right] + \left(k_{pn} + \frac{k_{pn}}{sT_{in}}\right)\left[v_n^* - v_n\right] \tag{5.21}$$

where k_{pp} and k_{pn} are the PI control's proportional gains for the positive sequence while k_{ip} and k_{in} are the integral gains in the negative sequence. In this work, the grid supporting is required to aid grid voltage recovery by the reactive power injection, especially during faults in the grid. Furthermore, this injection will, in turn, contribute to the overall stability and reliability of the system. The mandatory reactive power injection (dynamic grid support) in meeting the grid code requirements is summarized in Equationgiven in subsection 5.4, according to the Spanish network code [1]. Consequently, the required reactive current injection under fault in the AC grid is guided by subsection 5.4. Once the PCC voltage sequence components are obtained in direct-quadrature coordinates when grid failure occurs using Equation 5.21 as broken down into Equations 5.22 and 5.23, the two PCC voltage-independent control systems restore normal sequence references. Positive sequence control aims to bring the PCC voltage's positive sequence level back to its rated value. In this case, therefore, the error is used to regulate the reactive power Q_p injected into the grid while considering the electronic power switch thresholds. Likewise, the PCC voltage's negative sequence regulation restores the quadrature portion to zero normal condition references. This balances and buffers the further unbalance in PCC voltage introduced by reactive power injection into the grid.

The monitoring of grid voltage is crucial to the FRT operation of grid-supporting systems. The DSC algorithm accurately tracks the grid voltage level and promptly activates immediately fault is detected. The DSC detects the grid restoration after fault clearance, and the system switches back to the normal MPPT operating condition, as shown in Figure 5.3, compared with the other fast Fourier transform, synchronous rotating techniques reference frame, peak, and root mean square (RMS) technique. The dynamic grid-supporting regulation is primarily linked to prompt reactive power injection control. The responses of the detection schemes and the proposed DSC at the inception of fault and fault clearance are presented in Figures 5.4 and 5.5, respectively.

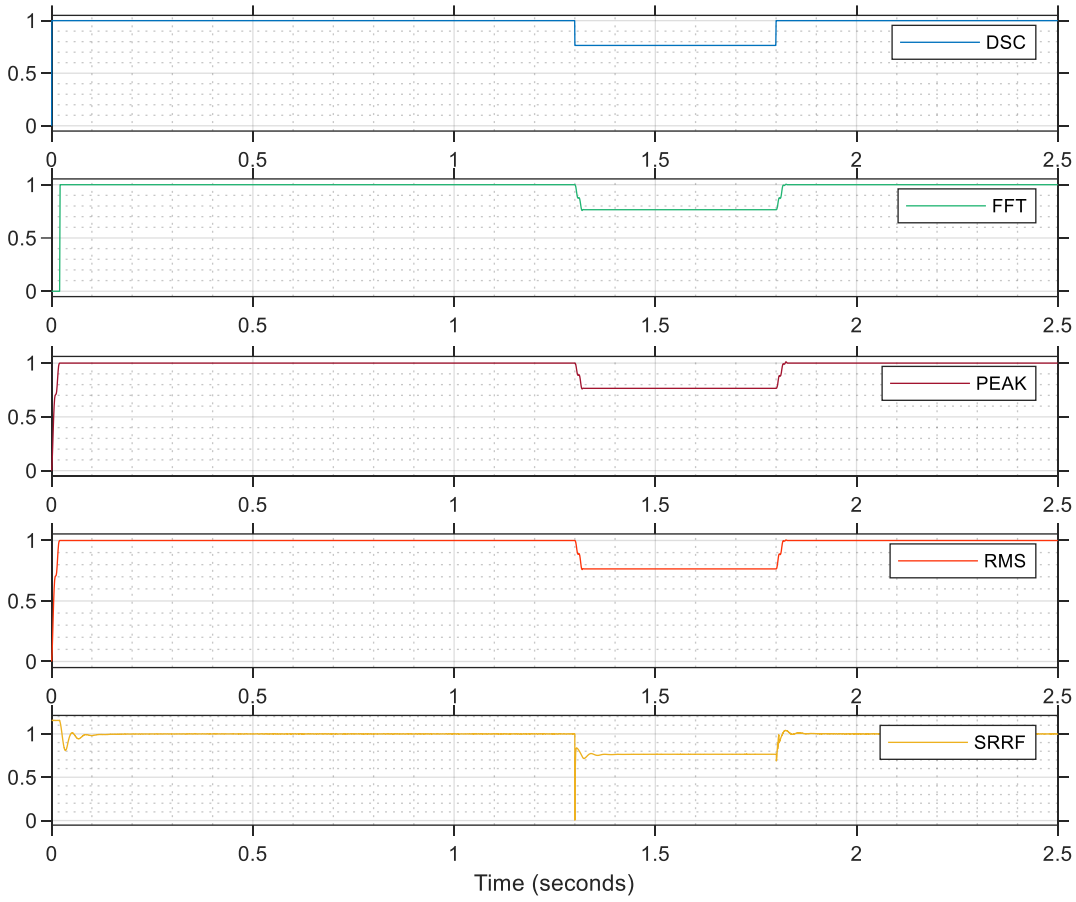

Figure 5. 3: DSC sag detection compared to FFT, SRRF, PEAK and RMS methods

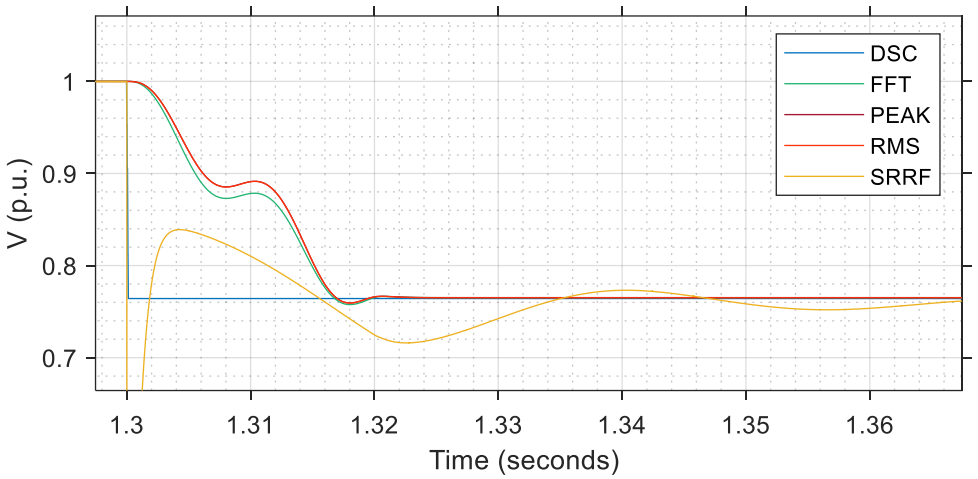

Figure 5. 4: DSC sag detection compared to FFT, SRRF, PEAK, and RMS methods at fault inception

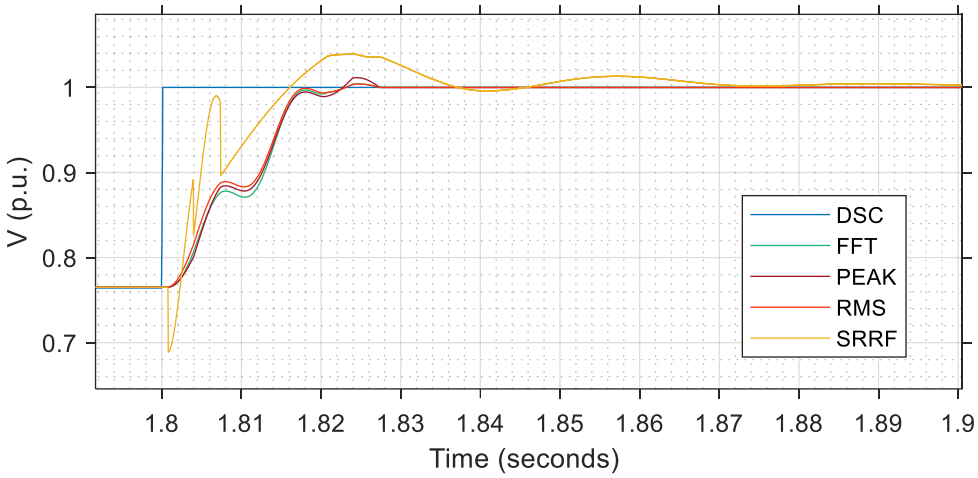

Figure 5. 5: DSC sag detection compared to FFT, SRRF, PEAK, and RMS methods at fault clearance

At the inception of fault, the time taken for the various techniques to reach the voltage sag's actual depth is given in Table 5.1. Similarly, the time taken for these methods to recover to the nominal system voltage value is also shown in Table 5.1. The DSC method showed superior performance in early detection of fault and the quality of value signal evaluation at the fault instance. SRRF method also displayed a faster detection in a way similar to DSC; however, the sag detection went beyond the actual system sag, and the overshoot is experienced with a longer settling time of 0.0699 seconds after the fault instance and 0.071 seconds after fault clearance. Also, the FFT, PEAK, and RMS methods have similar performance with a significant delay in identifying the fault inception and fault clearance.

Table 5. 1: Sag Detection

Techniques	Detection Time of Fault Inception (seconds)	Detection Time of Fault Clearance (seconds)
DSC	1.3001522	1.80015210
FFT	1.3167960	1.82308800
PEAK	1.3169960	1.82274000
RMS	1.3169840	1.82309200
SRRF	1.3012721	1.81606000

The microgrid voltage at the local load point of connection with the PCC is controlled by the control scheme using the DSC to independently adjust both positive and negative components in conformity with their respective sequence references. Thus, the DERs and local sensitive loads' microgrid voltage is enhanced with respect to the voltage sag experienced in the main grid. Therefore, active power is uninterruptedly delivered to the microgrid sensitive load while delivering ancillary voltage support service to the main grid. The independent controls of the voltage at the point of common coupling of the microgrid to the main grid are expressed in Equations 5.22 and 5.23.

$$Q_p = \left(k_{pp} + \frac{k_{ip}}{s} \right) \left[v_p^* - \sqrt{v_{dp}^2 + v_{qp}^2} \right] = \left(k_{pp} + \frac{k_{pp}}{sT_{ip}} \right) \left[v_p^* - \sqrt{v_{dp}^2 + v_{qp}^2} \right] \tag{5.22}$$

$$Q_n = \left(k_{pn} + \frac{k_{in}}{s} \right) \left[v_n^* - \sqrt{v_{dn}^2 + v_{qn}^2} \right] = \left(k_{pn} + \frac{k_{pn}}{sT_{in}} \right) \left[v_n^* - \sqrt{v_{dn}^2 + v_{qn}^2} \right] \tag{5.23}$$

where k_{pp} and k_{pn} are the PI control's proportional gains for the positive sequence while k_{ip} and k_{in} are the integral gains in the negative sequence. The aggregate reactive power injection from the microgrid through the PCC to the utility grid for ride-through and reactive power support implies Equation 5.24 using Figure 5.1.

$$\Delta Q = Q_p + Q_n + Q_{req} \tag{5.24}$$

where Q_p and Q_n are the reactive powers obtained from the PCC voltage's independent control as earlier given in Equations 5.22 and 5.23. Q_{req} is estimated using the Spanish grid code LVRT requirement based on the depth of voltage sag, as shown in Figure 5.1.

5.3 Power Flow and Switched Reactor

5.3.1 Voltage Source Inverter and Grid Interactive Power Flow

In inverter grid supporting mode, there is power interaction with the host grid, which involves power exchange. The equivalent power flow diagram between the inverter-based microgrid and the host grid is shown in Figure 5.6, where V_i signifies the VSI voltage, and V_g represents the grid voltage. Similarly, the inverter's inherent impedances and its filter circuit are lumped together as Z_i while the grid impedance is represented as Z_g. The load current and impedance are signified by I_L and Z_L, respectively. These impedances above are typically inductive owing to the significant output inductance of the VSI. Nevertheless, this inverter impedance can be significantly influenced by the type of control strategy employed [197], and grid impedance is highly resistive in low-voltage distribution feeder lines [198]. Similarly, the impedance (resistance and inductive reactance) of the grid is significantly present and taken into consideration in microgrids located at a long distance away far from the host grid. Consequently, this work puts into consideration the line impedance of the grid. In line with the grid codes' stipulation, only reactive current is injected all through the period of voltage sag. Consequently, the resulting compensating voltage is relatively in phase with the grid voltage.

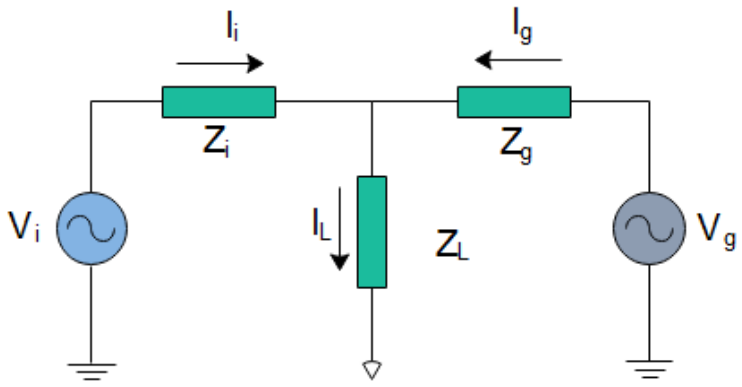

Figure 5. 6: Power flow diagram between the inverter and the host grid

5.3.2 Switched Inductance: Sizing and Switching

A microgrid is to ensure the required uninterrupted supply of quality power to the local sensitive loads besides fulfilling the FRT requirement of reactive power support in the event of disturbance on the main grid. In this work, this is ensured by ascertaining that all the sections in the microgrid are supplied with a constant voltage at a regular frequency. The proposed DSC scheme in Figure 5.1 shows this requirement's implementation through an additional reactive power injection for dynamic grid voltage support. The VSI injects a significantly high amount of reactive power in supporting the utility grid and sustains microgrid load voltages since the grid impedance is usually low [199]. However, the secondary control based LVRT schemes is significantly limited in

voltage sag compensation. A PCC voltage moderation scheme based on PI control using the DSC positive and negative is introduced to tackle this problem. Furthermore, under a strong (stiff) main grid connection, independent control of the point of common coupling voltage and, by extension, microgrid voltage is not sufficient for good power quality since the host grid imposes the voltage. Thus, control strategies may not effectively restore the network voltage, especially at the PCC [200],[201]. Hence, a switched inductance is inserted in the PCC series to the main network during a voltage disturbance to increase the network impedance to regulate the microgrid voltage independently irrespective of the host grid condition. Thus, sustaining the PCC voltage at the rated magnitude.

The appropriate sizing and switching of this inductance ensure sustained microgrid voltage irrespective of a host grid disturbance. The inductance size is estimated with the voltage sag in the worst-case scenario, which must be compensated at PCC. It also depends on the expected current flow through the inductance under voltage sag. The balance between microgrid generated power (active and reactive) and the local load consumption determines the current flow (magnitude and phase angle) through the inductance during grid disturbance. In this work's proposed strategy, the total microgrid generated active power is commensurate with the rated local load capacity to limit the current flow's amplitude into the main grid during the grid fault. However, excess active power may still be supplied to the main grid due to varying load demand, affecting the inductance size.

Two scenarios are created for the investigation to estimate the required size of the inductance.

1. The local load's active power demand is presumed to be the maximum installed capacity and equivalent to the total active power generated by the DGs/DERs in the first scenario. Furthermore, only reactive power is injected through the series inductances. Figure 5.7 (a) reveals the phasor illustrations analogous to the first scenario.

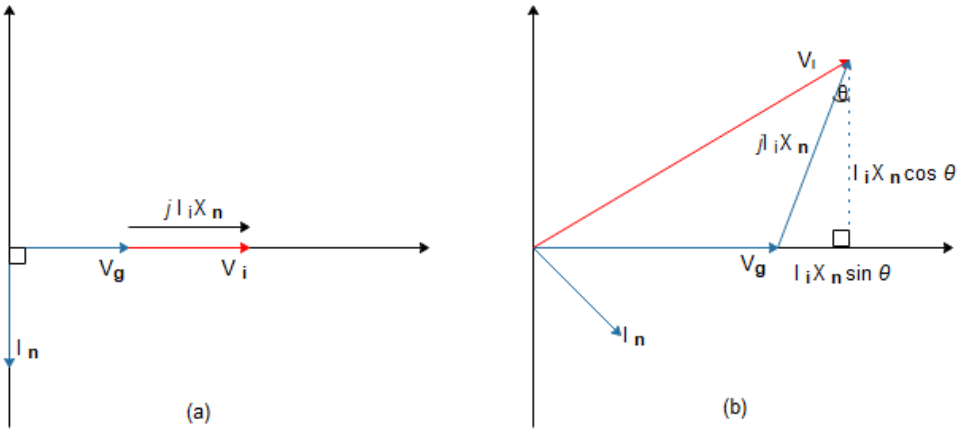

Figure 5. 7: Phasor illustrations for (a) maximum local load demand (b) no-load demand

2. The power demand from the local load is presumed to be zero, and the aggregate DERs' active power generation is exported to the main grid in the second scenario. Figure 5.7 (b) reveals the phasor illustrations analogous to the second scenario.

Any of these two methods can be used in calculating the value of the switched inductance, but from the phasor diagram, it is evident that the series inductance capacity in the second case is larger. Consequently, the second case's switched inductor capacity is appropriate for implementing the FRT control used in this work.

The load demand is assumed to be zero, and the rated load power is assumed generated and supplied to the host grid to estimate the required value for the series inductance. This estimation's phasor diagram is presented in Figure 5.7, where V_g represents the host grid's phase voltage. Similarly, X_n signifies needed switched inductive reactance while I_n indicates current flow. The inverter-based microgrid voltage is therefore given by

$$V_i^2 = \left(I_n X_n \cos\theta\right)^2 + \left(V_g + I_n X_n \sin\theta\right)^2 \tag{5.25}$$

Consequently, the value of the series inductance is determined by solving the quadratic equation generated by making the X_n the subject of the formula in Equation 5.25. It is therefore given as

$$X_n^2 + \left[\frac{2V_g \sin\theta}{I_n}\right] X_n + \left[\frac{V_g^2 - V_i^2}{I_n^2}\right] = 0 \tag{5.26}$$

Since I_n is the current flow through the inductance X_n, the angle θ is calculated from

$$\theta = \cos^{-1}\left[\frac{P_{rated}}{S_{\max}}\right] = \cos^{-1}\left[\frac{I_d}{\sqrt{I_d^2 + I_q^2}}\right] \tag{5.27}$$

where P_{rated} is the rated active power moved to the main grid, which corresponds to the d-axis component of the nominal current of DER. Under this scenario, as the load demand is zero, the active power transmitted to the grid is equivalent to the combined active power generation of the DERs.

In typical low voltage distribution lines, the resistive component (R) is high [56],[202], and therefore the R/X ratio is considerably reduced with the series incorporation of a comparatively sizable inductance. Hence, an extra inductance may cause a depreciation in voltage regulation, particularly within the microgrid. Therefore, the inductance is only inserted during a main grid voltage disturbance by the anti-parallel IGBT-diode switches' operation in Figure 5.1. The fault detection detects a fault condition or disturbance leading to voltage sag at the grid. This simultaneously generates alternating pulses for the switching on of the anti-parallel switches and

uses the delay signal cancellation in detecting fault. Then the switching pulses are off once a fault is detected, and the voltage sag is observed in 0.1515 ms as shown in Figures 5.8, 5.9, 5.10 and 5.11.

Under substantial L-L-L-G fault at the time of 1.3 seconds, as shown in Figures 5.8 with a 50% sag in the grid voltage, the fault is cleared on 1.8 seconds. The corresponding product of the output of the delayed signal cancellation and the driving a pulse generator is used to generate positive and negative cycles pulses to switch the anti-parallel IGBTs. Ordinarily, the Pulse Generator generates square wave pulses at regular intervals in which waveform parameters, such as the amplitude, phase delays, and pulse duration, determine the pulse output. These pulses generated are canceled out by multiplying them with the DSC output in Figure 5.3. Consequently, Figures 5.9, 5.10, and 5.11 show the pulses generated in the three-phase system with all the faults detected in less than 0.1515 ms. The corresponding sag detection is shown for the pulses generated in each phase to control the IGBT-diode switches. These show that the fault is detected within 0.1515 ms in all phases to activate the FRT scheme and the inductor's switching. These pulses activate the IGBT-diode-based switch's switching operation and adequately change the switching control system's operating mode at fault inception and fault clearing instants.

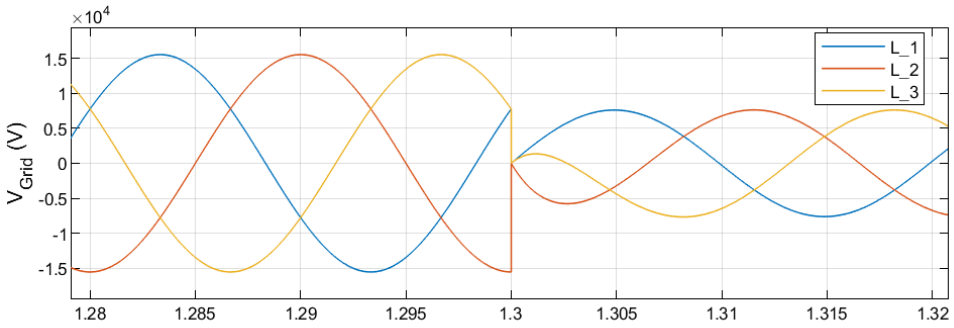

(a)

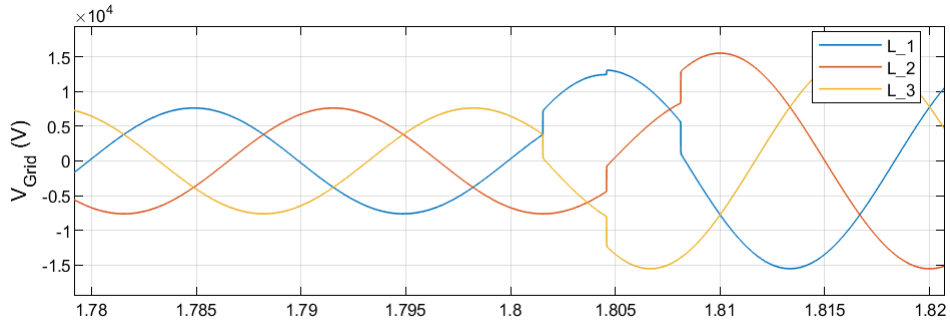

(b)

Figure 5. 8: Grid voltage (a) at the inception of the fault and (b) clearance of fault

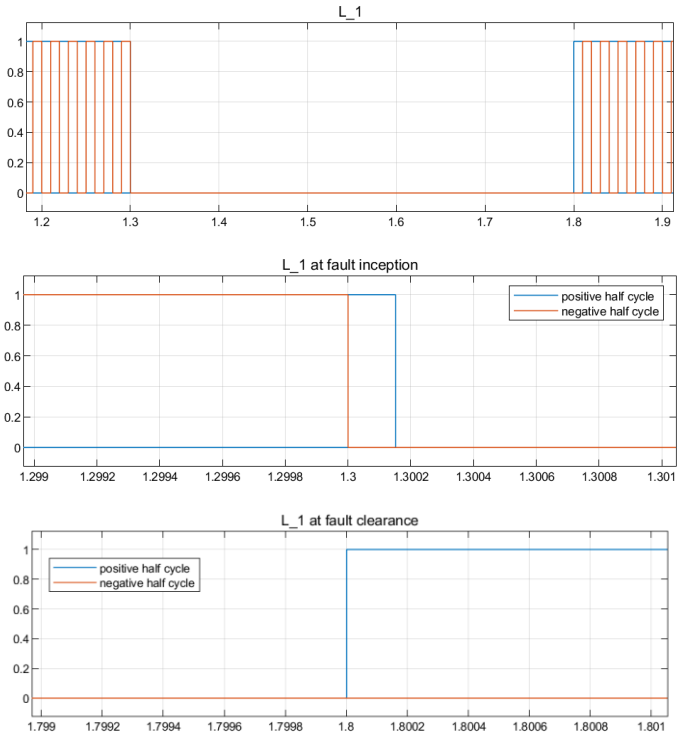

Figure 5. 9: Pulses generated in all line 1 of the three-phase

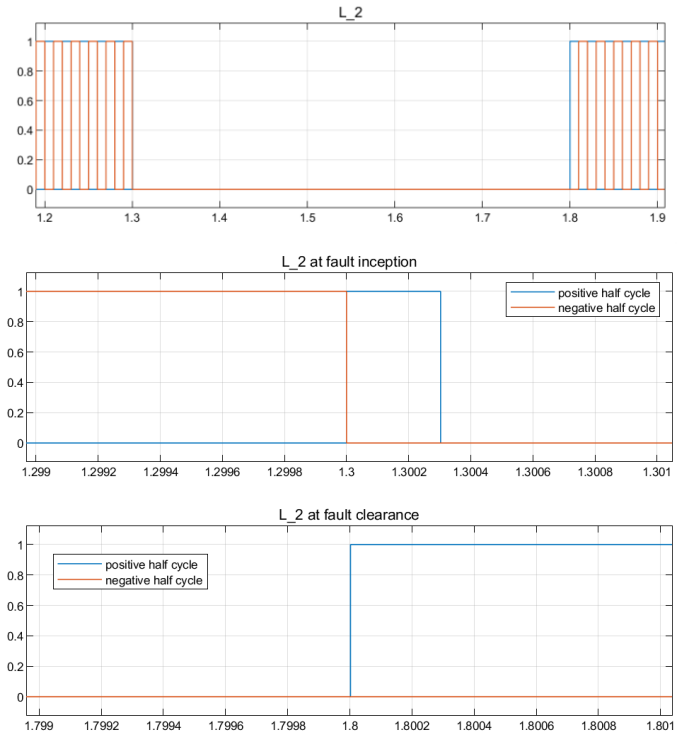

Figure 5. 10: Pulses generated in all line 2 of the three-phase

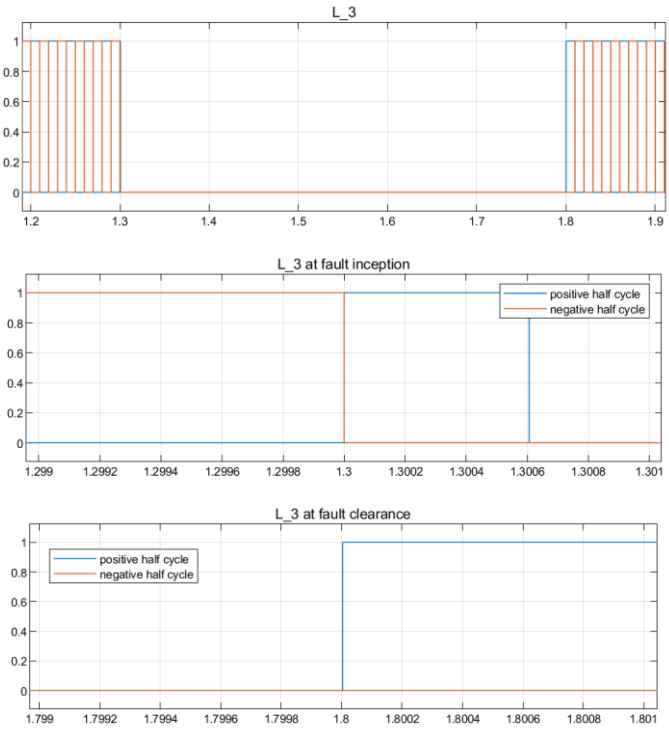

Figure 5. 11: Pulses generated in all line 3 of the three-phase.

5.4 Reactive Power Referencing

In this work, the grid supporting is required to aid grid voltage recovery by the reactive power injection, especially during faults in the grid. Furthermore, this injection will, in turn, contribute to the overall stability and reliability of the system. The mandatory reactive power injection (dynamic grid support) in meeting the grid code requirements, as earlier illustrated in Chapter Two, is summarized in Equation 5.14, according to the Spanish network code [1] [30]. Consequently, the required reactive current injection under fault in the AC grid is guided by

$$Q_{ref} = \begin{cases} \left(\frac{93}{70} - \frac{6}{7} \cdot V_{gN}\right) Q_N & V_{gN} \le 0.5 \\ \left(\frac{57}{100} - 6 \cdot V_{gN}\right) \cdot Q_N, & 0.9 \ge V_{gN} > 0.5, \\ \left(1 - \frac{1}{5} \cdot V_{gN}\right) \cdot Q_N, & V_{gN} > 0.9 \end{cases} \tag{5.28}$$

VgN indicates the rated grid voltage at the nominal value. The reactive power refers to the inverter's rated reactive current. The reactive power reference Q_{ref} refers to the reactive current required to be injected from a Microgrid. The reactive current's needed reference signal is generated per the grid's voltage sag depth through the proposed secondary control loop. When this voltage drops below 0.9 of the nominal value, the secondary control scheme will instantly start reactive current/power support, as shown in Equation 5.14. Reactive power / current injection is systematically regulated to ensure that voltage above 0.9 of the nominal value is restored,

instead of precisely 0.9 V_{gN}. To improve overall reliability, productivity, and safety, immediate detection of faults in systems is crucial; hence the Clarke transformation of the measured grid voltage is done using Equation 5.1 and shown in Figure 5.1. The magnitude is conditioned and subsequently monitored using a first-order low pass filter. In essence, this prevents accidental activation of the anti-parallel IGBT-diode switching arrangement for the inductance. As shown in the pulse generation results in Figures 5.9, 5.10, and 5.11, fault occurrence and clearance are detected within 0.1515 seconds.

The presence of disturbance within the host grid, thereby leading to voltage sag or swell, causes the reactive power reference to be evaluated based on Equation 5.29, where Q^* represents the reference of the inverter's reactive power before voltage sag and dynamic change ΔQ is dictated based on Equation 5.28. By the control strategy proposed, the reactive power needed is commensurate to the percentage voltage drop depth. Consequently, the active power and the reactive power generated from the DER and injected through the inverter must be realistic such that it conforms to the complex power equation and prevents inverter overloading. The grid codes stipulate grid reactive power support by all connected generating units; however, it is also essential to ensure a continuous supply of active power to the microgrid sensitive load irrespective of grid conditions. Thus, the reactive power injection control is implemented in the proposed strategy as an FRT solution by generating active power $P*$ and reactive power $Q*$ references for the primary control to supply a current reference for the grid and load. The reference $P*$ for active power is accurately tracked at the maximum power P_{MPP}, ($P* = P_{MPP}$) and $Q* = 0$ *VAr* under grid normal operating mode at the unity power factor. However, the reference $Q*$ is generated to inject reactive power under fault with respect to the grid code stipulations. The support requirement ensures that the injection is comparable to the depth of the voltage sag [1] as depicted in Equation 5.16.

$$Q_{new}^{*} = Q_{ref} + \Delta Q \tag{5.29}$$

$$k = \frac{1}{\left(V_g^{*} - V_g\right)} \cdot \frac{\left(I_q - I_q^{*}\right)}{I_N} \quad \text{where } I_q < 1 \tag{5.30}$$

where V^*_g is the grid's initial voltage before grid disturbance in p.u, V_g is the instantaneous voltage in the nominal rating percentage during voltage fault, while I^*_q is the initial reactive current prior to a disturbance in the grid. The inverter-based microgrids are expected to operate at the unity power factor at maximum power. Hence, there is no reactive power injection until voltage sag, which implies that $I^*_q = 0$ at $V^*_g = 1$ *p.u*. The grid codes also require that k be greater than 2 p.u (20% of the nominal grid voltage) for a sufficiently minimal reactive current injection [203]. For instance, a minimum reactive current I_q (30 % of the nominal current) is injected into the grid

once the grid voltage level decreases to 90 % of the nominal voltage. Equation 5.16 above further shows that complete reactive power injection between 90 to 100% of the nominal current is allowed under a serious voltage fault of less than 0.5 per unit in which the active power injection is disabled. However, the extent to which reactive power is injected is constrained by the complex power limit S_{max} of the inverter, as shown in Figure 5.12. This constraint is considered in designing the proposed FRT strategy. Hence, the preventing of DC-AC converter trip-off because of over-current protection.

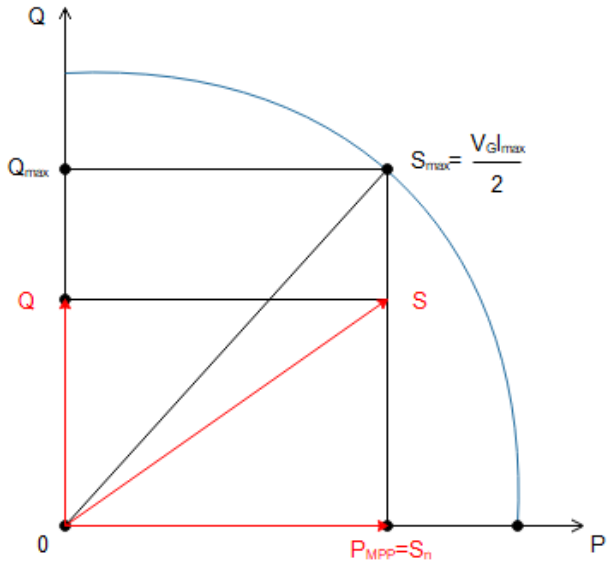

Figure 5. 12: Reactive power limit of inverter-based microgrid

The emerging grid codes require microgrid systems to provide reactive power under grid faults. Hence the constraints imposed by Figure 5.5 are summarized as Equation 5.17 in which $k \geq 2\ p.u.$ is specified in Equation 5.29. The amplitude of the current I_g^{max} expected to be injected into the grid is given in Equation 5.32 as it relates the active current I_d, reactive current, and maximum allowable current level I_{max} of the inverter. This work proposes a constant peak current control. Therefore, the inverter's overcurrent tripping during the voltage faults is avoided when the injected current peak is maintained constant. Consequently, the grid current peak is set as Equation 5.32. Considering the need for reactive current (power) injection as shown in Equation 5.28 of reactive power injection by grid code, the current of the AC grid in the direct-quadrature reference equivalent is given by Equations 5.33 and 5.34 subjects to their respective conditions.

$$\begin{cases} I_q = I_N, & 0 \leq V_g < \left(1 - \dfrac{1}{k}\right) \\ I_q = k\left(1 - V_g\right) i_N, & \left(1 - \dfrac{1}{k}\right) \leq V_g < 0.9 \end{cases} \tag{5.31}$$

$$I_g^{\max} = nI_N \tag{5.32}$$

$$\left.\begin{aligned} I_q &= \left[k\left(1-v_g\right)\right]I_N \\ I_d &= \sqrt{\left[n^2 - k^2\left(1-v_g\right)^2\right]}I_N \end{aligned}\right\} \qquad \left(1-\frac{1}{k}\right) \le v_g < 0.9 \tag{5.33}$$

$$\left.\begin{aligned} I_q &= I_N \\ I_d &= \sqrt{\left[n^2 - 1\right]}I_N \end{aligned}\right\} \qquad v_g \le \left(1-\frac{1}{k}\right) \tag{5.34}$$

The maximum value of n is $I_{max}/I_{N,}$ and therefore, the inverter-based sub-system is not disconnected from the main grid during the FRT process. Consequently, this constraint is consequently considered in developing the FRT scheme and operation of the inverter-based microgrid.

5.5 Active Power Referencing and Fault Current Limitation

5.5.1 Inverter-Based Microgrid

In a grid supporting inverter without a local load, the active power set-point is zero under fault for effectively limiting the active current magnitude and jack up the reactive current within the apparent power limit. This, by extension, limits the fault current observed at the PCC. However, under normal operating conditions, maximum power point tracking (MPPT) output imposes the active power reference instantaneously at a 100 percent power factor.

Therefore, due to the reactive power (current) injection, the active power (current) injection is limited. Thus, the reference P^* for the inverter's active power is computed using Equations 5.35. Thus, the complex power limit is taken into consideration, such that under no circumstance is this power exceeded. Therefore, the reference active power P^* is only maintained when there is no reactive power injection.

$$P^* = \begin{cases} \sqrt{\left(S_{\max}^*\right)^2 - \left(Q_{new}^*\right)^2} & if \quad \sqrt{\left(P^*\right)^2 + \left(Q_{new}^*\right)^2} > S_{rated} \\ P^* & else \end{cases} \tag{5.35}$$

P^* signifies the inverter's active power reference before voltage sag, and Srated represents the maximum tolerance. The active reference limit triggers and S^*_{max} represent the manufacturer's inverter maximum complex power. The maximum complex power confines the references of active power and reactive power within its value, as shown in Equation 5.35.

5.5.2 Inverter-Based Microgrid with DC-DC Converter

The monitoring of grid voltage is crucial to the FRT operation of the grid-supporting systems. The DSC algorithm accurately tracks the grid voltage level and promptly activates, immediately a fault is detected, as shown in Figure 5.3. The reference current generated at any point in time, especially under the FRT operation, does not comprise the inverter system protections for both overvoltage and overcurrent by incessant triggering. The DSC detects the grid restoration after fault clearance, and the system switches back to the normal MPPT operating condition. However, if the duration of fault exceeds the stipulations of the FRT curve, the system is then permitted to disconnect

The dynamic grid-supporting regulation of inverter-based microgrid with DC-DC converter under faults is primarily linked to reactive power injection control. The droop control enabled simultaneous active and reactive power injection frequency-active power, and the voltage-reactive power droop relationship. The droop is further enhanced using the switched inductance proposed in section 5.3.2 to reduce the *R/X* ratio of the feeder line between the grid and the microgrid and maximize the injection of reactive current (power) to support the AC grid voltage under fault.

The references of active current (power) and reactive current (power) are fixed by control goals and grid transient conditions. Before a fault, the dynamic power reference $P^*=P_{MPP}$ is governed by the MPPT procedure at the unity PF. As soon as the DSC detects the fault, the active and reactive power references are recomputed. Typically, in direct-quadrature equivalent for the three-phase grid parameters, *P* and *Q* are computed as Equation 5.36. The corresponding direct-quadrature grid currents are given in Equation 5.37. The reference grid current, according to Equation 5.37 and with $V^2_d + V^2_q = V^2_{gN}$, as the active current (power) and reactive current (power) are required to be modified under FRT mode as Equation 5.38. Thus, the current reference I^*_g is the direct-quadrature equivalent of the three-phase AC grid current, and $G_P(s)$ and $G_Q(s)$ are the *P* and *Q*, proportional-integral controller.

$$\begin{aligned} P &= \frac{3}{2}\left(v_d i_d + v_q i_q\right) \\ Q &= \frac{3}{2}\left(v_q i_d - v_d i_q\right) \end{aligned} \tag{5.36}$$

$$\begin{bmatrix} i_d \\ i_q \end{bmatrix} = \frac{2}{3\left(v_d^2 + v_q^2\right)} \begin{bmatrix} v_d & v_q \\ v_q & -v_d \end{bmatrix} \begin{bmatrix} P \\ Q \end{bmatrix} \tag{5.37}$$

$$i_g^* = i_d^* = \frac{2}{3\left(v_d^2 + v_q^2\right)}\begin{bmatrix} v_d & v_q \end{bmatrix}\begin{bmatrix} G_P(s)\left(P^* - P\right) \\ G_Q(s)\left(Q^* - Q\right) \end{bmatrix} \tag{5.38}$$

Chapter Two previously stated that the microgrids or DGs are permitted to feed-in the active power during the voltage sags, although limited to the grid according to grid code stipulation. For this purpose, a grid-connected inverter-based microgrid with a DC-DC converter injects minimal power to the network under the voltage sag period relative to the pre-fault condition capacity while sidestepping DC-link overvoltage as will be presented under this section. Figure 5.11 shows the $P-V$ characteristics of a solar PV, where P_{MPP} and V_{MPP} represent the MPP power and voltage, which is assumed to be the MPP's pre-fault values.

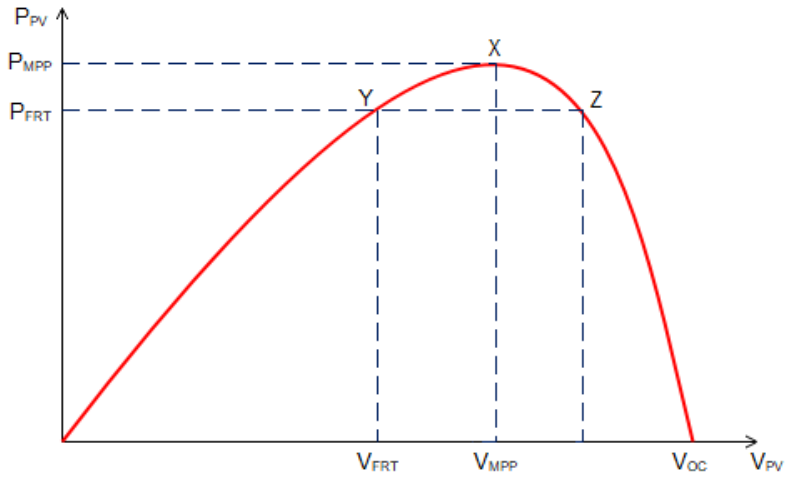

Figure 5. 13:P−V curve for FRT and MPPT operations

During normal MPP operating mode, the DC-DC converter is controlled by the MPPT through the duty ratio (cycle) to extract maximum power. In contrast, the DC-AC inverter controls the DC-link voltage to regulate active power injection to the AC side. However, certain adjustments are applied to limit this active power injection under grid voltage sag caused by faults. In this work, the proposed technique matches the DC generated power with the AC grid injected to preserve a moderately constant DC-link voltage. In this work, the DC and AC power balance is maintained at a value other than zero. As a result, the AC grid receives a simultaneous injection of active power and reactive power. Hitherto, the DC-DC converter is completely isolated to remove the possibility of active power injection under voltage sag, thereby limiting fault current.

The DC-DC converter's goal under the proposed method is no longer to enforce MPP operations but to control the power generated by the PV to match the instantaneous permissible active power. The converter is regulated to determine the optimal V_{PV} value that attains power balance. The point should, therefore, shift from point *X* in Figure 5.11 to lower points of control, i.e., either point *Y* or point *Z*. This thesis dissertation describes and analyzes moving the operating point from *X* to *Y*. Thus, a negative voltage value ΔV_{PV} is added to the pre-fault V_{MPP} value, as follows in

Equation 5.39. The strategy proposed will enable the controller to achieve FRT using the current reference directly derived from the active power and reactive power references, according to Equation 5.38. The linear droop is used in determining the voltage value $\Delta V_{PV.}$ This droop relationship implements the FRT, which involves curve-programmed active power decrease during the FRT operation. Hence, the characteristic linear droop relationship between PV voltage and PV power, according to Figure 5.11, is approached by Equation 5.40. In Equation 5.40, k_{PV} is the constant P-V droop factor, and this relationship is irradiance- and temperature-dependent. However, the PV system is assumed to be operating at the MPPT before grid faults occurrence.

$$V_{FRT} = V_{MPP} - \Delta V_{PV} \tag{5.39}$$

$$V_{PV} \approx V_{MPP} + k_{PV}\left(P_{PV} - P_{MPP}\right) \tag{5.40}$$

The FRT strategy requires that the grid voltage drop depth be proportional to the level of regulated active power injection into the AC grid to inject reactive power to support the AC grid voltage drop. Consequently, this work proposes another droop based correlation of the active power generated and the grid voltage given in Equation 2.41. In Equation 2.41, V_G is the grid voltage magnitude, P_G is the grid injected active power, k_d shows the relationship's droop coefficient, and V^*_G reference and P^*_G reference are the corresponding initial rated standards for grid voltage and active power just before transients.

In a lossless DC-AC conversion system, the MPPT extracted power is equal to the injected AC power. Consequently, Equation 5.42 is presented based on no loss. Thus, applying the relation in Equation 5.42 to Equation 5.40 and 5.41 and combining the two equations yields Equation 5.43, indicating an inverse proportionality between the voltage grid changes and PV voltage changes.

$$V_G - V_G^* = -k_d\left(P_G - P_G^*\right) \tag{5.41}$$

$$P_{PV} = P_G \tag{5.42}$$

$$k_d\left(V_{PV} - V_{MPP}\right) = -k_{PV}\left(V_G - V_{MPP}\right) \tag{5.43}$$

Hence, under normal grid conditions with nominal grid voltage, the PV voltage is maintained at maximum power point voltage. However, the PV voltage is systematically adjusted by Equation 5.43 under fault. This occurs consequently upon grid voltage drop lower than the nominal voltage. Consequently, a smooth switch is ensured between MPP and FRT operating modes and vice versa. The FRT voltage for the PV is dependent on the depth of the grid voltage sag, as shown in Equation 5.44, where the ratio $k_{PV} : k_d$ is the proportional control gain. Hence voltage value ΔV_{PV} is given as Equation 5.45.

$$V_{FRT} = V_{MPP} - \frac{k_{PV}}{k_d}\left(V_G - V_G^*\right) \tag{5.44}$$

$$\Delta V_{PV} = \frac{k_{PV}}{k_d}\left(V_G - V_G^*\right) \tag{5.45}$$

Therefore, as depicted in Equation 5.45, the FRT scheme's implementation is depicted in Figure 5.14, with the maximum power point tracking control gain.

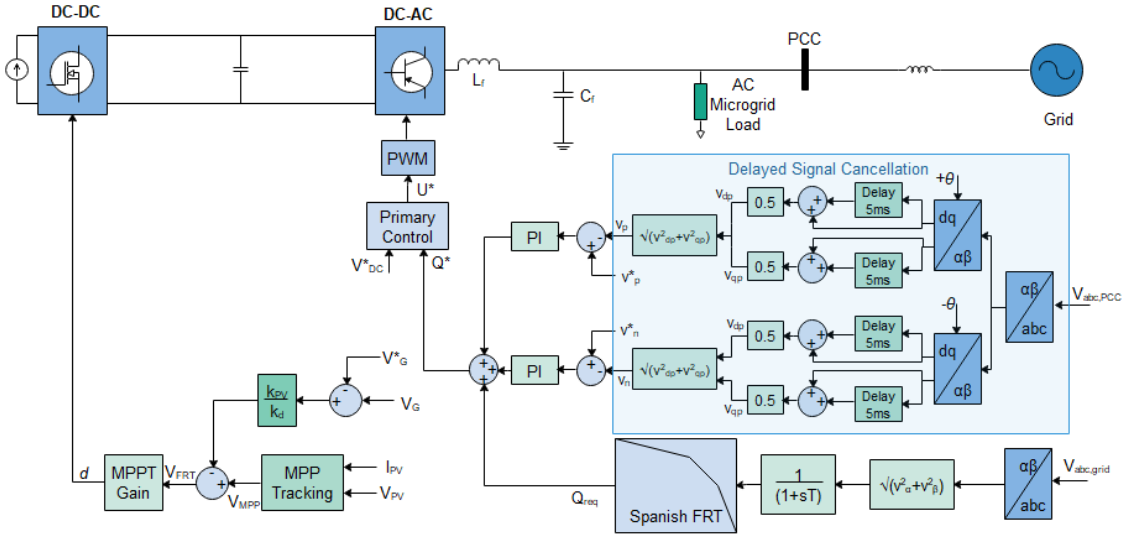

Figure 5. 14: FRT operation control structure

This work has proposed an FRT controller, which adds dynamic variation to the traditional control schemes of an inverter-based microgrid with a DC-DC converter. Thus, it is an optimistic approach to the fault ride-through and AC grid fault control of the double-stage PV in grid-supporting mode.

5.5.2.1 Operating Point Justification

There are two operating points (*Y* and *Z*) for the FRT operation in Figure 5.6. Point *Y*, below V_{MPP}, is found in the lower-voltage area, in which a change in PV power with respect to the change in *PV* voltage (dP_{PV}/dV_{PV}) is small; while at the other point *Z*, dP_{PV}/dV_{PV} is large. Any of the operating points above is feasible for FRT operation, though, with different steady-state performance. Shifting the operating mode to *Z* for FRT will cause a larger variation in power to voltage as compared to shifting the operating mode to *Y*. Consequently, the FRT operating point is proposed to be shifted to point *Y* with positive control gain *k*. A voltage sag caused by a grid's fault reduces the PV-side voltage reference to a value V_{FRT} as depicted in Equation 5.44. Similarly, the duty cycle *d* will increase due to a reduction in V_{PV} in Equation 4.1 of Chapter 4 in order to keep V_{DC} relatively constant while achieving FRT.

5.5.2.2 Droop Ratio Design

The ratio k_{PV}/k_d is strongly influenced by the PV inherent features which in turn are environment-dependent. Similarly, the ratio is affected by the link impedance between the microgrid and grid as it determines the extent to which the impact of the grid fault is felt at the PCC. Specifically, the ratio is given as

$$k_{PV} = \frac{V_{MPP}}{P_{MPP}} \tag{5.46}$$

This assumes that the PV operates at MPP under constant temperature and uniform irradiance before the fault occurrence. Consequently, substituting Equation 5.46 into Equation 5.44 results in Equation 5.47, and it is implemented according to Figure 5.7

$$V_{FRT} = V_{MPP} - \frac{V_{MPP}}{P_{MPP}}\left[\frac{k_{PV}}{k_d}\left(V_G - V_G^*\right)\right] \tag{5.47}$$

5.6 Conclusion

The secondary control developed involves the active power and reactive power reference calculation to decide the amount to generate and inject. The injected reactive power must comply with the required reactive currents based on the percentage voltage drop as stipulated in the emerging grid codes under different voltage sags caused by faults. Simultaneously, the DC side overvoltage and AC side overcurrent are mitigated by the active power decrease and current amplitude curtailment strategies in compliance with the complex/apparent power ratings.

The delayed signal cancellation algorithms allow for separating the sequence components for dual control at the PCC of the negative-sequence and positive-sequence components during a disturbance in the main grid. Hence, the reactive power is injected into the main grid in accordance with the grid code requirement under both balanced and unbalanced grid conditions. The developed scheme guarantees inverter protection by ensuring that the current does not exceed the inverter current rating under grid fault conditions. Thus, the inverter-based microgrids operate in two non-switching modes of steady-state and transient FRT. Under steady-state operation for the inverter system with DC-DC converter, it is assumed that the steady-state operation is at MPP before and after fault clearance. Once the fault is detected using a delayed signal cancelation algorithm, the inverter switches to the transient FRT mode to address the issues mentioned above in compliance with the grid codes.

This developed FRT control approach will be implemented in an inverter-based microgrid and evaluated under voltage sag grid conditions for an ideal DC source and real DC source (double stage PV system) inverter-based microgrid in Chapters 6 and 7. In real and ideal DC source inverter-based microgrids, some additional loops were implemented to control the DC-AC inverter to allow the entire PV set-up to accurately ride-through any disturbances. Furthermore, in the case of a real DC source, these control adjustments are put in place to efficiently integrate the DC-DC converter and current limit control for the voltage at the DC-link and reactive current injection.

The case of a real DC source (double stage PV system) is a little bit complicated. During a voltage sag occasioned by fault, if no control measures are taken to regulate the MPPT control of the DC-DC converter, the power from the real DC source (PV arrays) remains generated. As such, the DC voltage continues to rise and can reach the extreme limit. In grid fault conditions, therefore, the system is not self-protected. Different control measures must be put in place to reduce the DC source's power and equip the converters with FRT capabilities. A simple method for protecting DC-link against overvoltage is switching off the DC-DC converter if the DC link voltage exceeds a limit. Furthermore, a hysteresis controller reconnects the DC-DC converter after the fault clearance, and the DC voltage falls within a safe range. In the solutions proposed in [154].

In the case of an inverter-based microgrid with a DC-DC converter such as a double-stage PV system, three different ways have been proposed in the literature [204] to limit the DC voltage during a fault in the grid. The first technique involves short-circuiting the DC source (e.g., PV array) by turning the DC-DC converter switch ON during the entire voltage sag cycle. Furthermore, the second approach involves leaving the DC source open by switching OFF the switch of the DC-DC converter; Then; another solution is to adjust the converter's MPPT control to inject a reduced amount of power from the PV source compared to the pre-fault maximum power working conditions. Consequently, in all the reviewed literature above, the MPPT control or the DC-DC converter is deactivated under the AC grid fault. In the technique proposed in this work, the MPPT is not disconnected, but rather, the MPP operating point is shifted to a lesser power level by decreasing the operating reference voltage to prevent DC overvoltage.

Lastly, the appropriate sizing and switching of this inductance ensure sustained microgrid voltage irrespective of a host grid disturbance. The inductance size is estimated with the voltage sag in the worst-case scenario, which must be compensated at PCC. It also depends on the expected current flow through the inductance under voltage sag. The balance between microgrid generated power (active and reactive) and the local load consumption determines the current flow (magnitude and phase angle) through the inductance during grid disturbance. In this work's

proposed strategy, the total microgrid generated active power is commensurate with the rated local load capacity to limit the current flow's amplitude into the main grid during the grid fault. However, excess active power may still be supplied to the main grid due to varying load demand, affecting the inductance size.

CHAPTER SIX
FRT CONTROL IMPLEMENTATION IN INVERTER-BASED MICROGRID

6.1 Introduction

Control schemes and topologies for the grid-supporting microgrid need to be designed and implemented to meet projected FRT requirements. This research aims to develop a secondary control scheme for enhancing a droop controlled grid supporting inverter-based microgrids using delayed signal cancellation and stationary frame control for reactive power injection and fault current limitation. The secondary FRT control stipulates set-points for primary control. The primary control consists of the droop, power, and current loops to fulfil various operation and control specifications in a microgrid. These two levels form a hierarchical control system, and the strategy does not require a mode switch. Resynchronization of microgrids as proposed in a seamless transition method [205]–[206] after fault clearance is avoided, and shedding of local loads is prevented. The active power and reactive power are regulated in a grid supporting network to meet local demand requirements, and the surplus microgrid power is distributed concurrently to the main grid. Active power and reactive power are governed by regulation of frequency and voltage, respectively so that local power-sharing among constituent inverters is not compromised in any way.

Chapter 6 evaluates the FRT approach proposed in chapter 5 on a grid supporting the inverter-based microgrid model already developed in chapter 3. The grid code FRT compliance of the system is therefore evaluated based on the grid voltage, microgrid PCC voltage, current output waveforms of the DERs, THD of DER voltage and current, active power generation and reactive power injection, and active power delivery to the local microgrid sensitive load in both symmetrical and asymmetrical grid conditions.

6.1.1 Model Parameters

This FRT approach's effectiveness is investigated on a grid-connected microgrid system consisting of two DERs and local load, as depicted in Figure 6.1. Various faults are simulated on the main grid and are switched on at time t = 1.3 s and assumed to be automatically cleared at t = 1.8 s. The common types of power system faults are the triple-phase to ground (L-L-L-G), double line to ground (L-L-G), single line to ground (L-G), and line-to-line faults (L-L). These faults lead to different degrees and types of voltage sag within the grid and grid supporting microgrids at the PCC. In simulating the grid faults, the fault resistances of 0.7 Ω, 0.5 Ω, and 0.3 Ω are used to produce 70%, 60%, and 50% voltage sags at constant ground resistance of 0.001 Ω and snubber resistance of 1000 Ω.

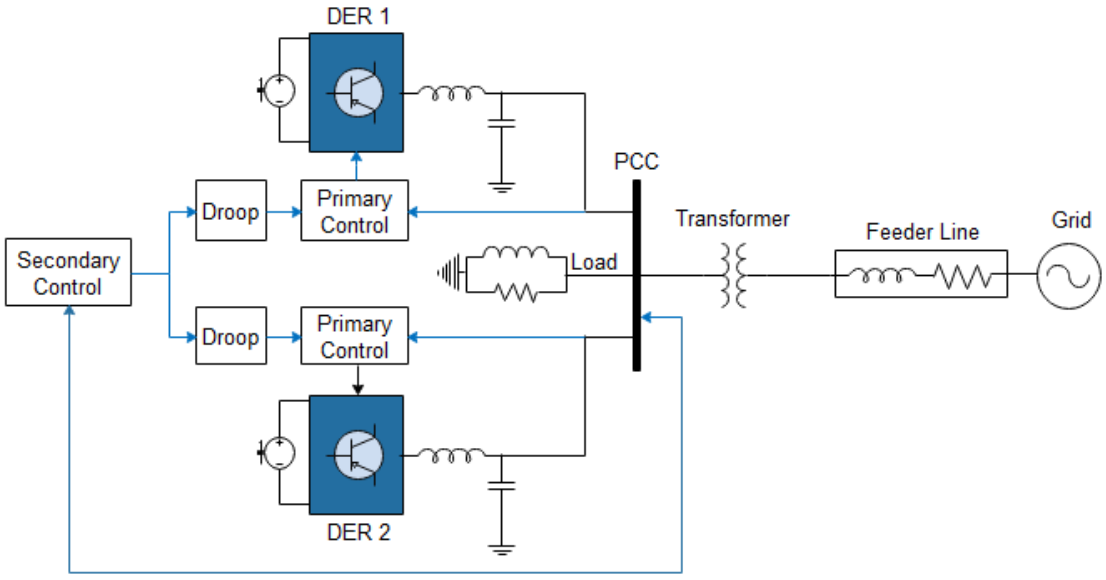

Figure 6. 1: The topology of the MG examined

The simulations are performed in MATLAB/Simulink/SimPower software. Two inverter-based distributed energy resources, DER 1 and DER 2 are used to form microgrid energy sources. DERs 1 and 2 feed a local microgrid load of 10 kW with a power factor of 0.90. The excess power generated in the microgrid by these DERs is distributed into the main utility grid, while the DERs also participate in the frequency and voltage regulations through their respective droops in the primary control. Installed at the PCC is a step-up transformer of 0.400/11 kV phase to phase RMS through which the excess generation is supplied to the host grid. The other parameters used in the simulations are shown in Tables 6.1, 6.2, 6.3, and 6.4.

Table 6. 1: Inverter electrical parameters

Parameters	**Descriptions**	**Values**
kVA_1	DER 1 rated power	12 kVA
kVA_2	DER 2 rated power	6 kVA
V_{abc}	Voltage (phase-phase)	400 V
V_{dc}	DC bus voltage	1100 V
f	Frequency	50 Hz
C	LC filter capacitance	2.31 µF
L	LC filter inductance	11 mH

Table 6. 2: Inverter primary and secondary control parameters

Parameters	Descriptions	Values
ω_{cut}	Cut-off angular frequency	100π
E	Single-phase voltage reference	330 V
$K_{p\ PCC+-}$	Positive sequence and negative sequence P gain	0.0125
$K_{i\ PCC+-}$	Positive sequence and negative sequence I gain	2

Table 6. 3: Grid synchronization and parameters

Parameters	Descriptions	Values
f_{min}	PLL minimum frequency	45 Hz
$K_{p\ PLL}$	Regulator P gain	180
$K_{i\ PLL}$	Regulator I gain	3200
$K_{d\ PLL}$	Regulator D gain	1

Table 6. 4: Switched IGBT-diode inductance parameters

Parameters	Descriptions	Values
L_r	Reactor inductance	0.005
R_{on}	Switch internal resistance	0.001
R_s	Switch snubber resistance	0.00001

6.1.2 Model Validation

The DER inverters are modelled in detailed states. The selection of control parameters is determined by the SimScape closed-loop auto-tuner, which computes a linearized approximation of the nonlinear dynamic system models. The model's responses are similar to the responses shown in Figures 3.25 and 3.26 while considering the inner power/voltage control loop dynamics, current control loop, and detailed model parameters. The modelled grid-supporting systems' power setpoints are changed in three steps at times 1.0 s and 1.5 s. These values are 4 kVA, 12 kVA, and 20 kVA at the unity power factor to validate the inverter's response and portray a typical grid supporting system. The corresponding dynamic responses in active power, voltage, current, and frequency are observed to validate the detailed model used in the simulation. The voltage stability is maintained despite the increasing current drawn due to an increase in load. Similarly, the active power increases with the growing load with slight deviations in the frequency at the step increase in power. The strategy implemented in the simulations can be deployed for low

voltage ride-through of a solar PV based grid-connected microgrids. It can be used for the interface FRT control of large scale grid-connected battery energy storage systems.

6.2. Symmetrical Fault

6.2.1 Voltage

For balanced voltage sag, the main grid fault, triple-phase to the ground, simulates the voltage sag of 50% in evaluating the proposed strategy. The extent of the voltage sag on the main grid is shown in Figures 6.2, 6.3, and 6.4, which prompts a corresponding rise in the current amplitude.

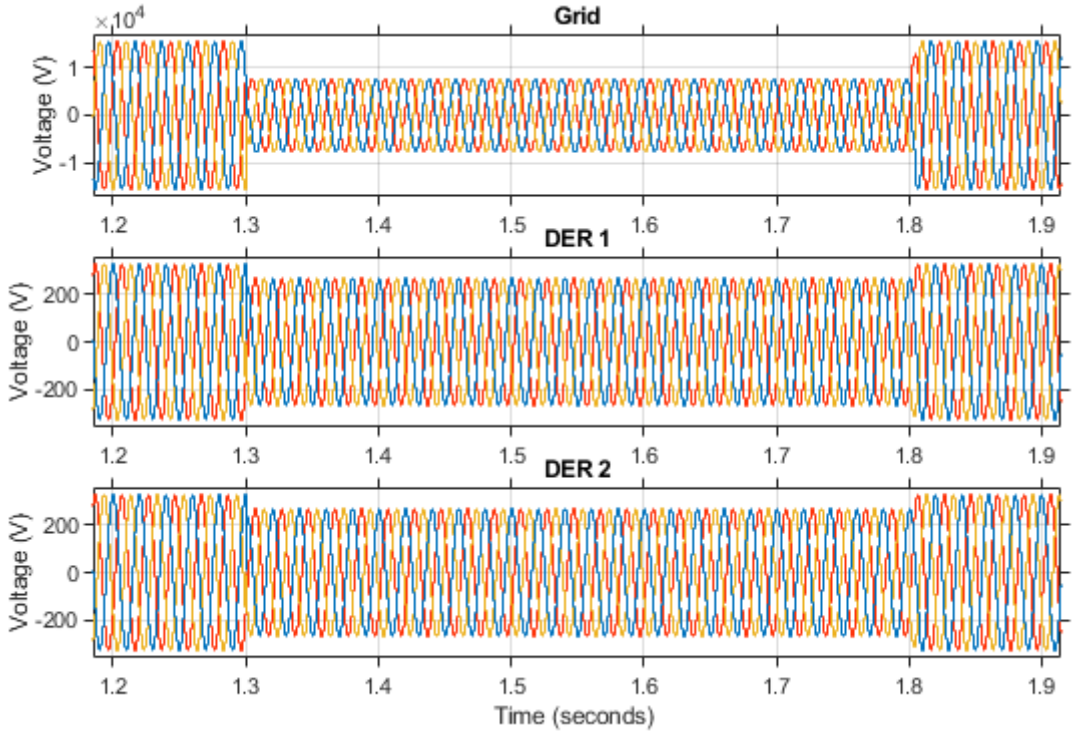

Figure 6. 2:Voltages in the grid and microgrid at grid voltage sag of 50% produced by L-L-L-G fault

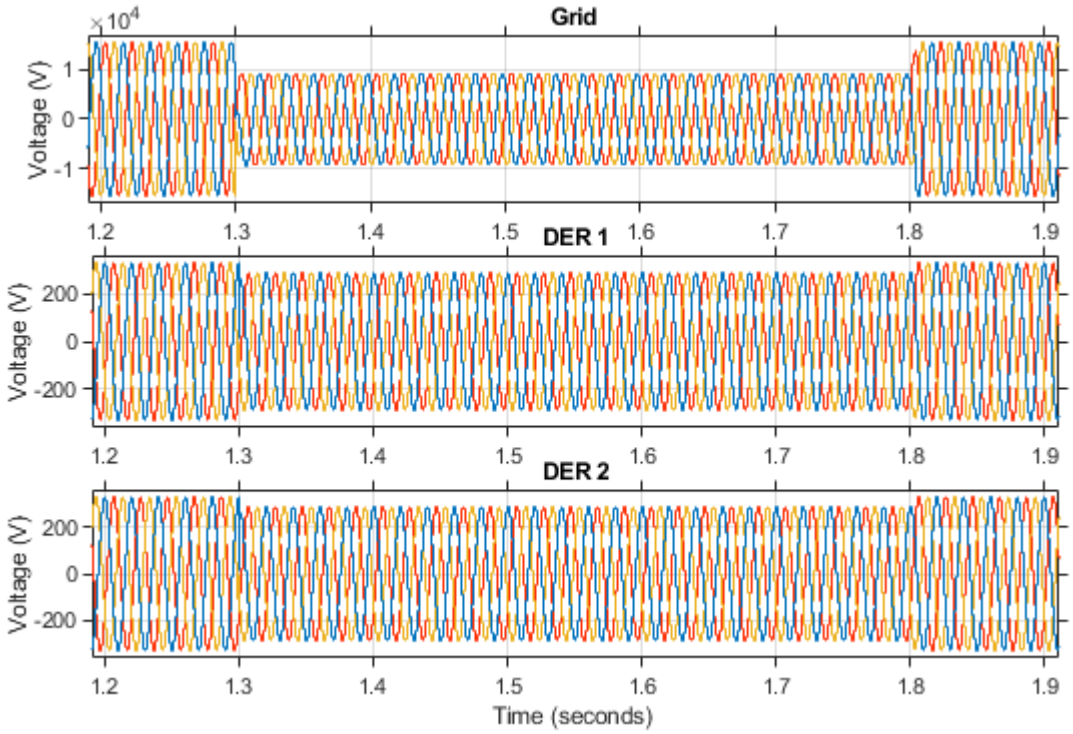

Figure 6. 3:Voltages in the grid and microgrid at grid voltage sag of 60% produced by L-L-L-G fault

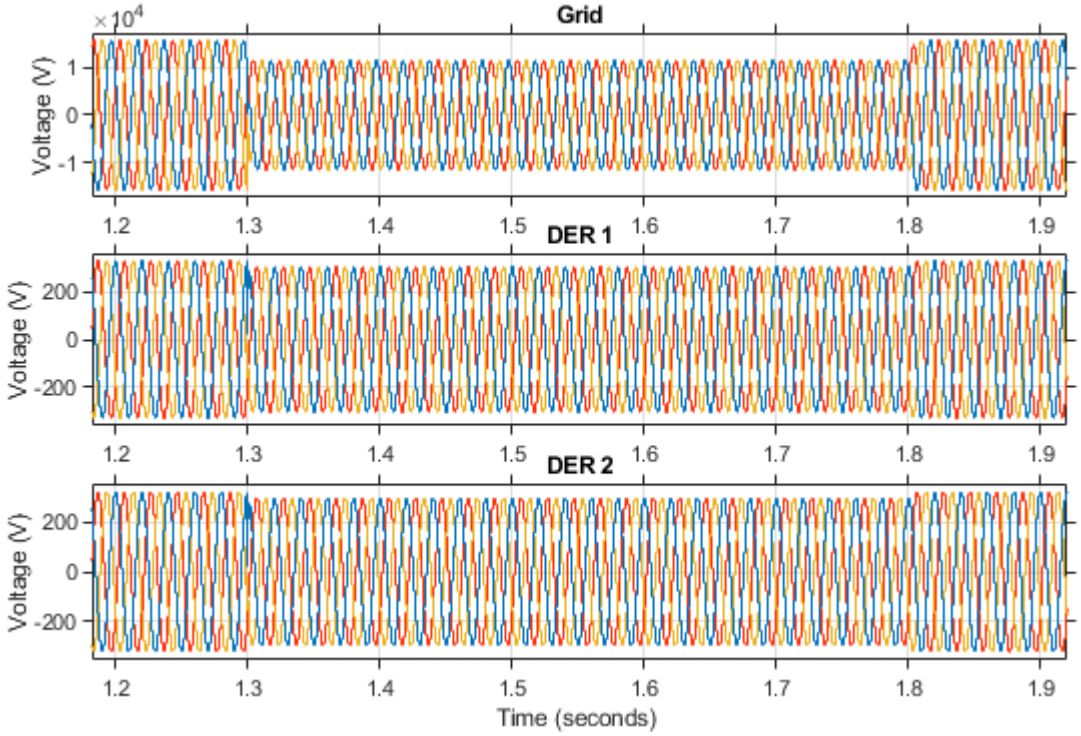

Figure 6. 4:Voltages in the grid and microgrid at grid voltage sag of 70% produced by L-L-L-G fault

The prompt current amplitude limitation is provided by the secondary power reference embedded in the secondary control's FRT scheme in each of the DER, as shown in Figure 5.1 and depicted by Equations 5.21. The active and reactive current references are changed instantaneously at fault

inception. Similarly, these references are properly restored immediately fault condition is over with appropriate tuning of the k_p and k_i gains of the proportional-integral controllers. Thus, Figures 6.2, 6.3, and 6.4 reveal a smooth transition from pre-fault to a fault and, subsequently, from fault to post-fault condition. Therefore, DERs' LC filter's output current is appropriately limited, as shown in Figure 6.5, 6.6, and 6.7. Consequently, 50%, 60%, and 70% voltage sag percentages observed at the PCC to the grid are improved to 81.69%, 87.34%, and 92.19% in the microgrid.

The voltage sag on the main utility is detected at the PCC at 0.1515 ms, less than half of the first cycle of fault occurrence. This implies that the fault is detected in 1.3001515 s as shown in the positive half cycle and 1.300 on the negative half cycle dot. Consequently, the FRT scheme fault mode operation is activated with simultaneous switching of the IGBT-diode switched reactor in series with all the phases for balanced transient conditions and series with only the affected phase in unbalanced conditions. The grid voltages for all the balanced voltage sag conditions resulting in 50%, 60%, and 70% voltage sag are shown in Figures 6.2, 6.3, and 6.4.

The FRT schemes for DERs of the microgrid ensured that the microgrid voltage is compensated for the microgrid's effective running irrespective of the main grid transient condition. The DER microgrid voltage is improved to 81.69%, 87.34%, 92.19% under 50%, 60%, and 70% sag measured at the PCC as shown in Figures 6.2, 6.3, and 6.4, respectively.

6.2.2 Current

The fault current limiting ability of this secondary control with an appropriate selection of the PI controller gains, the DER 1, and DER 2 contribute to the main grid voltage reactive power support based on their kVA ratings. Figures 6.5, 6.6, and 6.7present the output current waveforms of the DERs on 50%, 60%, and 70% voltage sag at the PCC. The DER output currents are appropriately limited, and no significant distortion is observed in the signals of DER output voltage and current. Thus, it is clear that the inverter currents are appropriately limited in the first cycle after fault inception at 1.3 s, as shown in Figures 6.2, 6.3, and 6.4 and Figures 6.5, 6.6, and 6.7. The delay of 0.00016 after the fault for the activation of the proposed control is short and insignificant. However, overcurrent produced between 1.30000 and 1.30016 s cannot damage the inverter semiconductor switches. Furthermore, grid faults technically appear across the filter capacitor, and the transient current overshoot at fault inception vanishes almost instantaneously and is therefore ignored. It must be noted that the current overshoot at the instance of transient disturbance is completely attenuated whenever the VSI based DER is tied to an electrically weak grid far from the inverter installation.

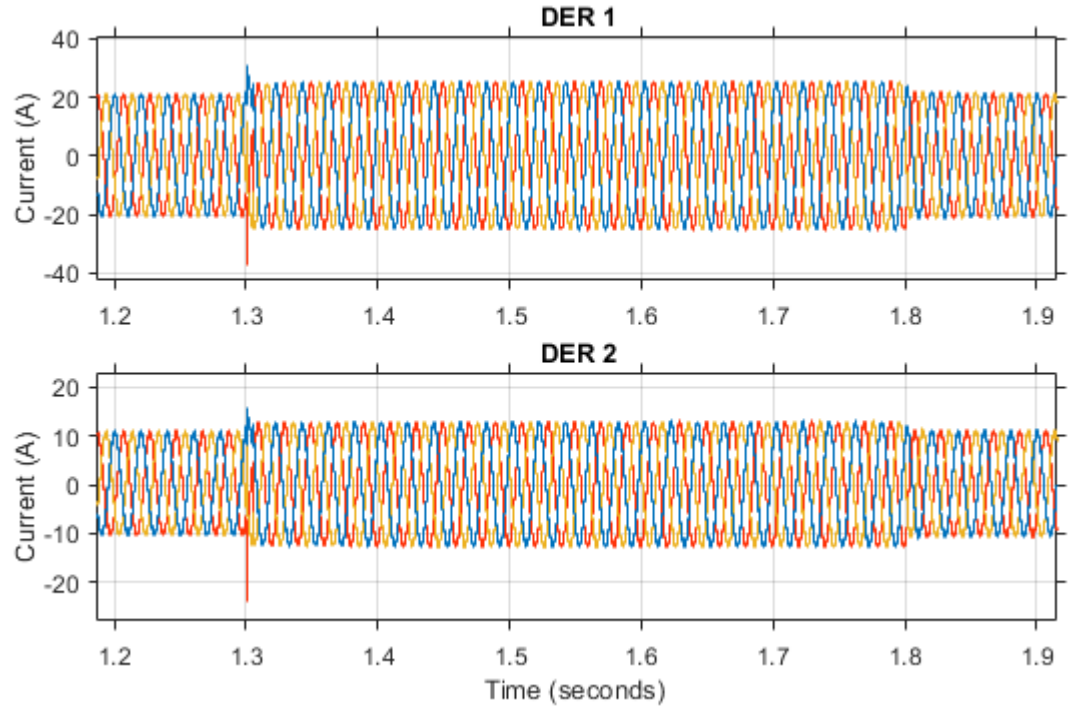

Figure 6. 5:Current waveforms in the microgrid at grid voltage sag of 50% produced by L-L-L-G fault

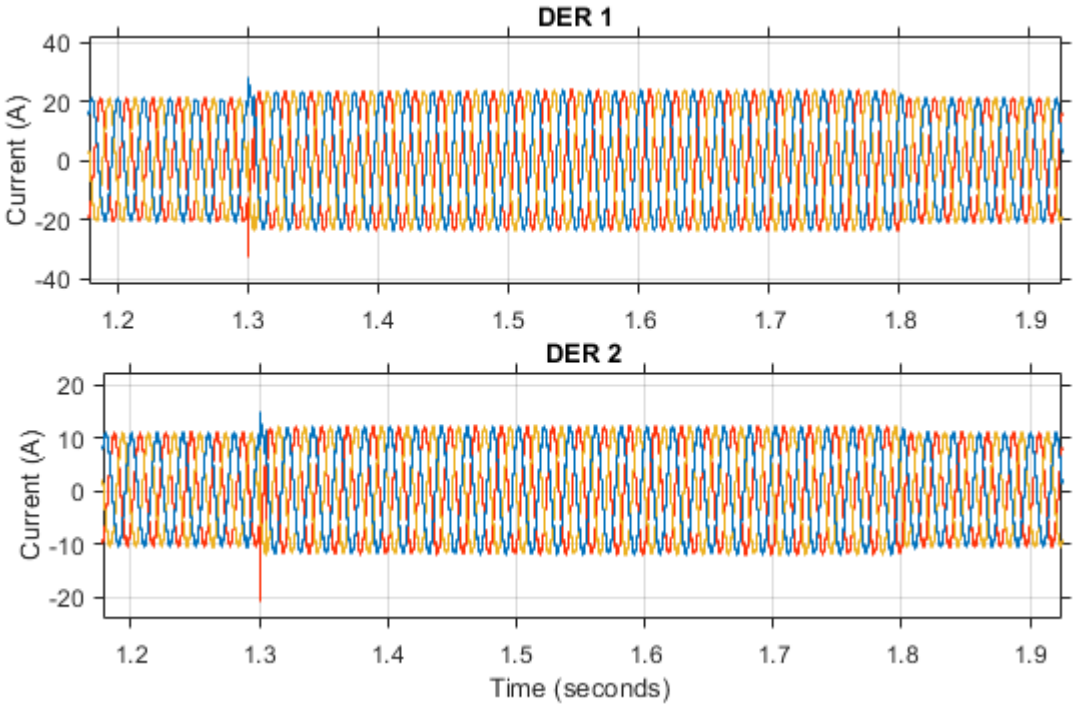

Figure 6. 6:Current waveforms in the microgrid at grid voltage sag of 60% produced by L-L-L-G fault

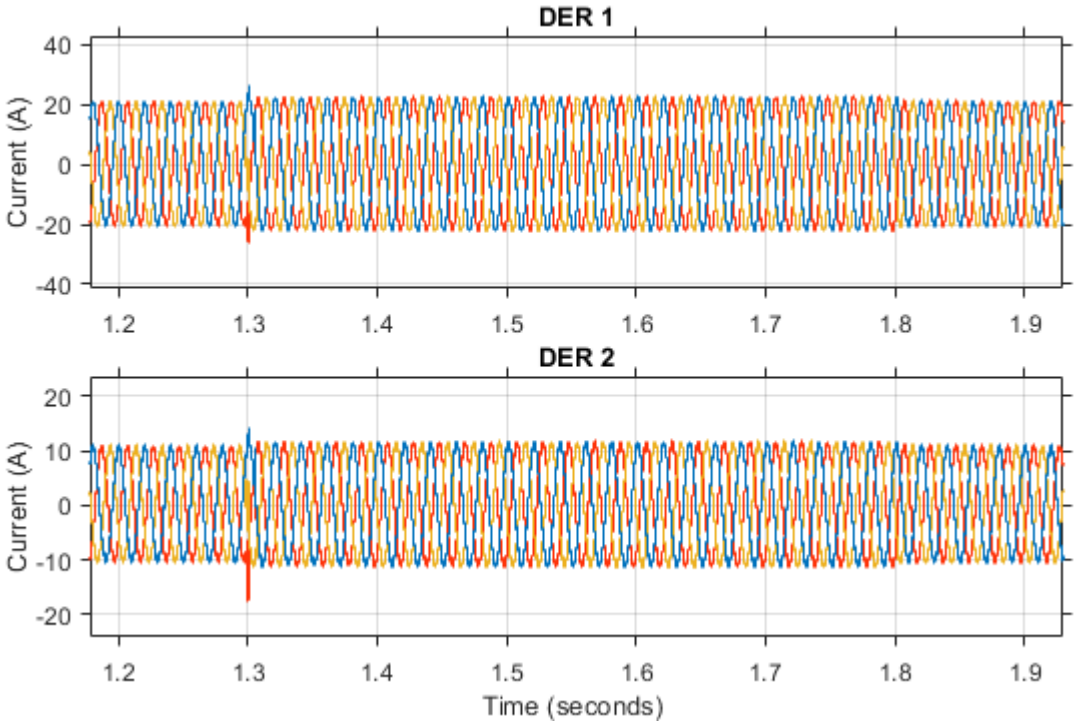

Figure 6. 7:Current waveforms in the microgrid at grid voltage sag of 70% produced by L-L-L-G fault

6.2.3 Current and Voltage Harmonics

Following the EN50160 standard, the THD of output voltage waveforms of any generating unit must not exceed 8% [207]. Consequently, the THDs (before, during, and after fault clearance for various fault types causing 70%, 60%, and 50% voltage sags) of DER voltage signals and output current waveforms are revealed in Figures 6.8. 6.9 and 6.10. The THD is measured using a fast Fourier transformation analysis in MATLAB. As signified in the DER voltages' low THDs and output current, the excellent signal quality indicates the FRT scheme's efficient performance in this work.

The microgrid voltages, as observed, demonstrate high-quality waveforms, output DER voltage, and current. The voltage harmonics are relatively negligible with reference to the current harmonics. The low THD recorded indicates a significant power factor, high efficiency, and a small peak current. This reveals this proposed FRT strategy's effectiveness at the secondary control and conformity with the IEC 61000-3-2 standard [208]. The THD of the collective microgrid voltage is reported in Figures 6.8. 6.9 and 6.10.

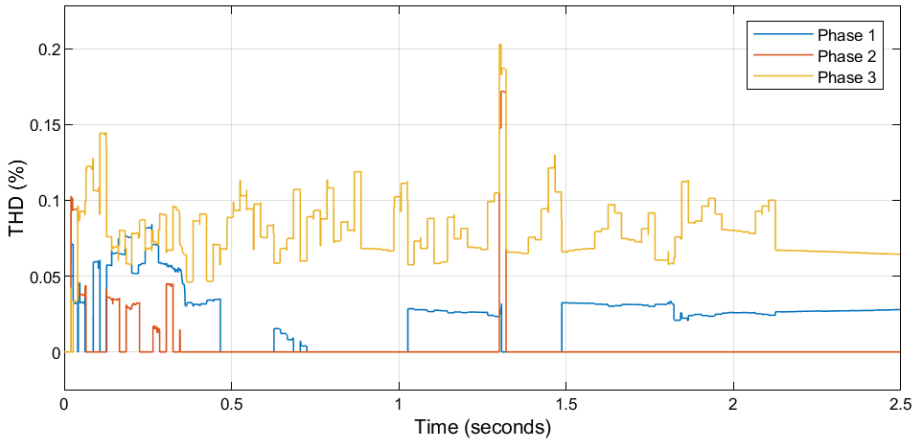

Figure 6. 8:THD of voltage waveforms of the microgrid under 50% voltage sag

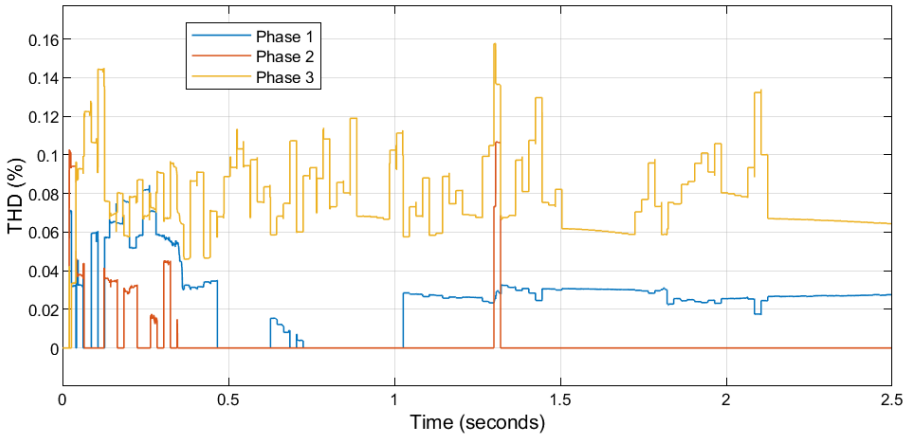

Figure 6. 9:THD of voltage waveforms of the microgrid under 60% voltage sag

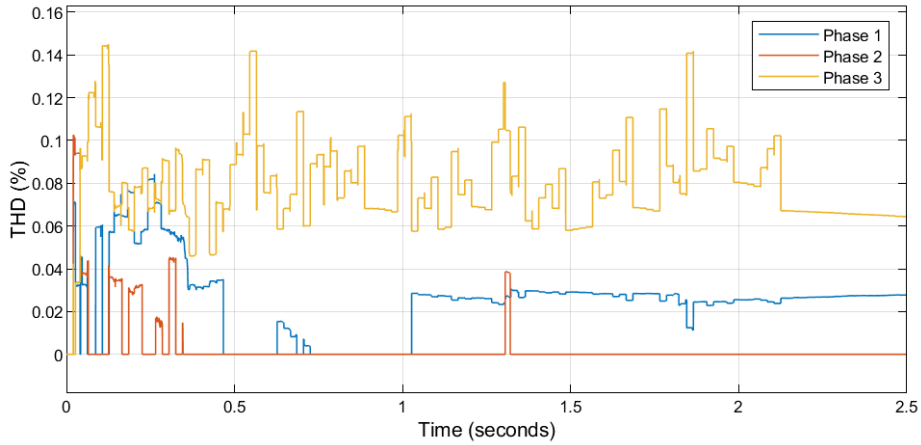

Figure 6. 10:THD of voltage waveforms of the microgrid under 70% voltage sag

6.2.4 Power Generation and Load Delivery

In compliance with the grid codes, the FRT control arrangements ensure a commensurate reactive power in supporting grid voltage sag, thereby effecting DERs ride through disturbances. Consequently, the changeover from grid synchronous to the islanded mode of operation is avoided. The microgrid voltage is kept within the range of operation (0.9–1.1 Spanish grid code) to guarantee continuous delivery of active power to the sensitive local microgrid loads as shown

in Figures 6.11, 6.12, 6.13, 6.14, 6.15, 6.16, 6.17, 6.18, 6.19, 6.20, 6.21 and 6.22. The increase in the reactive power requirement limits the inverter active power reference generation to conform to the FRT scheme's complex power limit and VSI ratings. This controller performance is further enhanced with an IGBT-diode switched AC reactor to improve the voltage and prevent the transient overcurrent in the microgrid during the grid fault. This ensures a continuous supply of the microgrid's local sensitive load while meeting FRT's grid code requirement. Similarly, the active power injection from the microgrid to the main grid is limited to maximize reactive power generation in supporting voltage sags (0.85–0.9 pu), moderate voltage sags (0.5–0.849 pu), and critical grid voltage sags (less than 0.5 pu).

Under the fault period, the increased reactive power generation ensures that the microgrid voltage is regulated to an acceptable magnitude. The fault clearance is immediately effected at the time t = 1.8 s; the FRT scheme senses the rise in main grid voltage to an acceptable range of 0.90–1.10 at the PCC. Thus, the reactive power injection is reduced based on the degree of voltage rise. The active power limitations under the various depth of voltage sags are presented in Figures 6.11, 6.12, 6.15, 6.16, 6.17, and 6.18. Similarly, Figures 6.13, 6.14, 6.19, 6.20, 6.21, and 6.22 show the increase in reactive power injected and a steep proportional decline in active power. The implementation of this FRT control with the DSC algorithms tracks the main grid disturbance using the voltage sag sensed at the PCC. Furthermore, DSC use at secondary control is compared and evaluated compared to FFT, RMS, and SRRF methods under the same sag level. The FRT strategy limits active and reactive references in both DERs as required to cause microgrid voltage improvement without significant distortion to the DER output current and voltage waveforms.

The analysis of Figures 6.11, 6.12, 6.13, and 6.14 are presented in Tables 6.5, 6.6, 6.7, 6.8, 6.9, 6.10, 6.11, and 6.12. The proposed DSC algorithm provides the best response at fault inception and clearance.

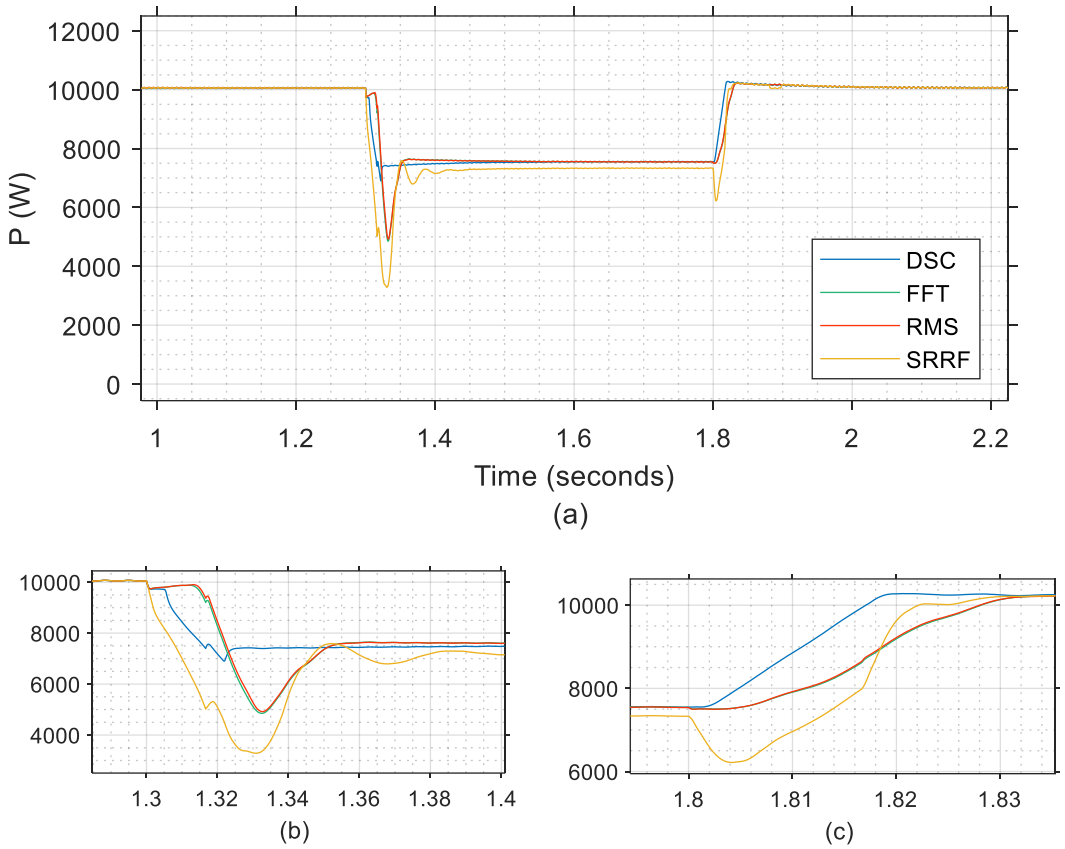

Figure 6. 11: Active power supplied by DER 1 under voltage sag of 50% produced by L-L-L-G fault

Table 6. 5: DER 1 Active Power P at Fault Inception under 50% voltage sag

	Active Power P (kW)			
Time (s)	**Proposed DSC Secondary Control**	**FFT Secondary Control**	**RMS Secondary Control**	**SRRF Secondary Control**
1.30	10.06	10.06	10.06	10.06
1.31	7.441	7.631	7.620	7.141
1.32	7.181	8.266	8.452	5.093
1.33	7.417	5.121	5.276	3.300
1.34	7.416	6.079	6.120	5.559
1.35	7.437	7.356	7.358	7.527
1.36	7.441	7.631	7.620	7.141
1.37	7.461	7.635	7.631	6.816
1.38	7.461	7.613	7.612	7.193
1.39	7.481	7.620	7.617	7.278
1.40	7.480	7.606	7.597	7.149

Table 6. 6: DER 1 Active Power P at Fault Clearance under 50% voltage sag

	Active Power P (kW)			
Time (s)	**Proposed DSC Secondary Control**	**FFT Secondary Control**	**RMS Secondary Control**	**SRRF Secondary Control**
1.80	7.549	7.544	7.539	7.330
1.81	8.853	7.908	7.920	6.961
1.82	10.270	9.625	9.220	9.625
1.83	10.250	10.130	10.140	10.210
1.84	10.230	10.200	10.200	10.210
1.85	10.210	10.200	10.200	10.210
1.86	10.200	10.170	10.170	10.170

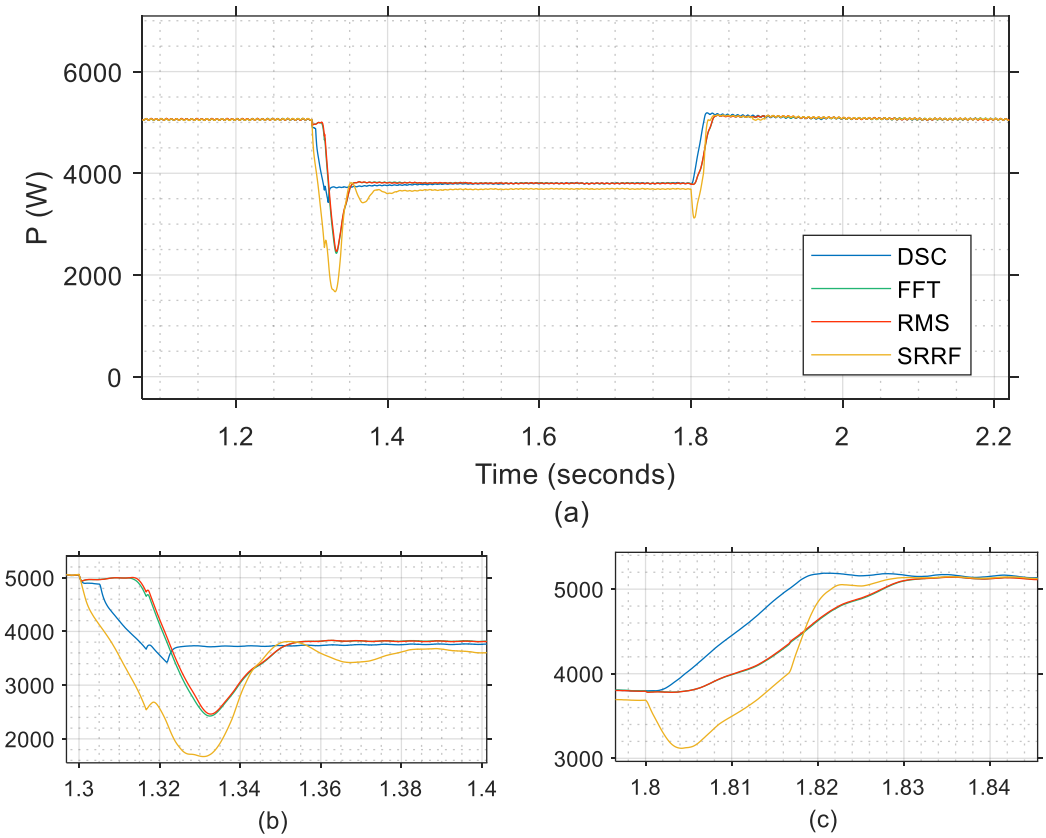

Figure 6. 12: Active power supplied by DER 2 under voltage sag of 50% produced by L-L-L-G fault

Table 6. 7:DER 2 Active Power P at Fault Inception under 50% voltage sag

	Active Power P (kW)			
Time (s)	**Proposed DSC Secondary Control**	**FFT Secondary Control**	**RMS Secondary Control**	**SRRF Secondary Control**
1.30	5.056	5.056	5.058	5.062
1.31	4.997	4.997	4.997	3.538
1.32	3.729	2.566	2.645	1.679
1.33	3.729	2.566	2.645	1.679
1.34	3.722	3.039	3.061	2.800
1.35	3.737	3.686	3.689	3.786
1.36	3.737	3.819	3.819	3.593

1.37	3.755	3.823	3.826	3.433
1.38	3.753	3.819	3.814	3.617
1.39	3.765	3.825	3.820	3.671
1.40	3.760	3.815	3.810	3.601

Table 6. 8:DER 2 Active Power P at Fault Clearance under 50% voltage sag

	Active Power P (kW)			
Time (s)	**Proposed DSC Secondary Control**	**FFT Secondary Control**	**RMS Secondary Control**	**SRRF Secondary Control**
1.80	3.797	3.798	3.794	3.687
1.81	4.452	3.988	3.992	3.496
1.82	4.452	3.988	3.992	3.496
1.83	5.167	5.097	5.100	5.136
1.84	5.151	5.125	5.123	5.132
1.85	5.145	5.129	5.124	5.136
1.86	5.140	5.113	5.110	5.118

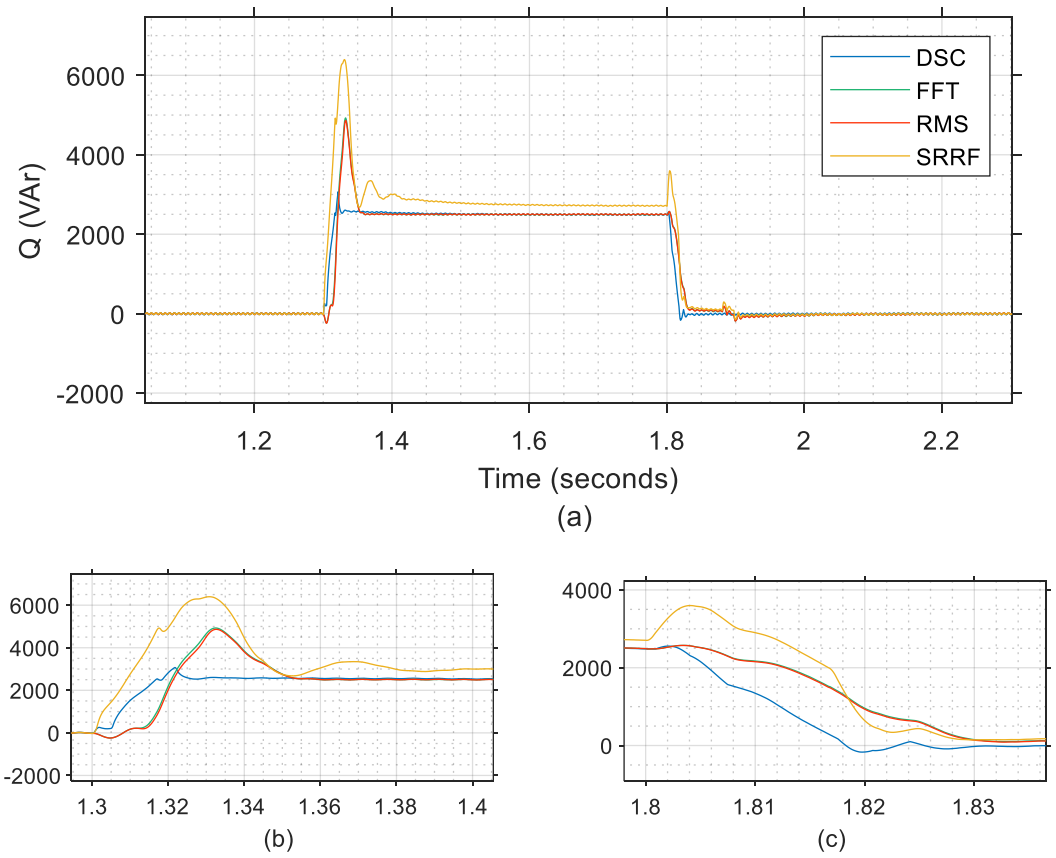

Figure 6. 13: Reactive power supplied by DER 1 under voltage sag of 50% produced by L-L-L-G fault

Table 6. 9: DER 1 Reactive Power Q at Fault Inception under 50% voltage sag

	Reactive Power Q (VAr)			
Time (s)	**Proposed DSC Secondary Control**	**FFT Secondary Control**	**RMS Secondary Control**	**SRRF Secondary Control**
1.30	256.90	-85.6	-90.90	633.8
1.31	1508.8	171.2	170.9	2755.10
1.32	2822.7	2195.7	2017.5	4945.20
1.33	2579.8	4657.1	4510.7	6382.3
1.34	2562	3847.8	3805.1	4459.0
1.35	2575.8	2762.1	2748.4	2749.6
1.36	2558.7	2502	2504.0	3048.8
1.37	2552.4	2501.5	2498.8	3346.8
1.38	2549.8	2500.9	2498.7	2984.6
1.39	2556.5	2506.4	2512.4	2915.9
1.40	2556.5	2506.4	2512.4	2915.9

Table 6. 10:DER 2 Active Power P at Fault Clearance under 50% voltage sag

	Reactive Power Q (VAr)			
Time (s)	**Proposed DSC Secondary Control**	**FFT Secondary Control**	**RMS Secondary Control**	**SRRF Secondary Control**
1.80	2485.1	2492.8	2491.6	2706.7
1.81	1343.7	2171.5	2155.0	2901.1
1.82	-160.9	959.0	933.8	639.3
1.83	-24.5	151.9	137.7	144.1
1.84	-43.3	78.4	70.6	126.6
1.85	-0.60	86.5	91.4	135.5
1.86	-30.2	64.0	72.0	100.6

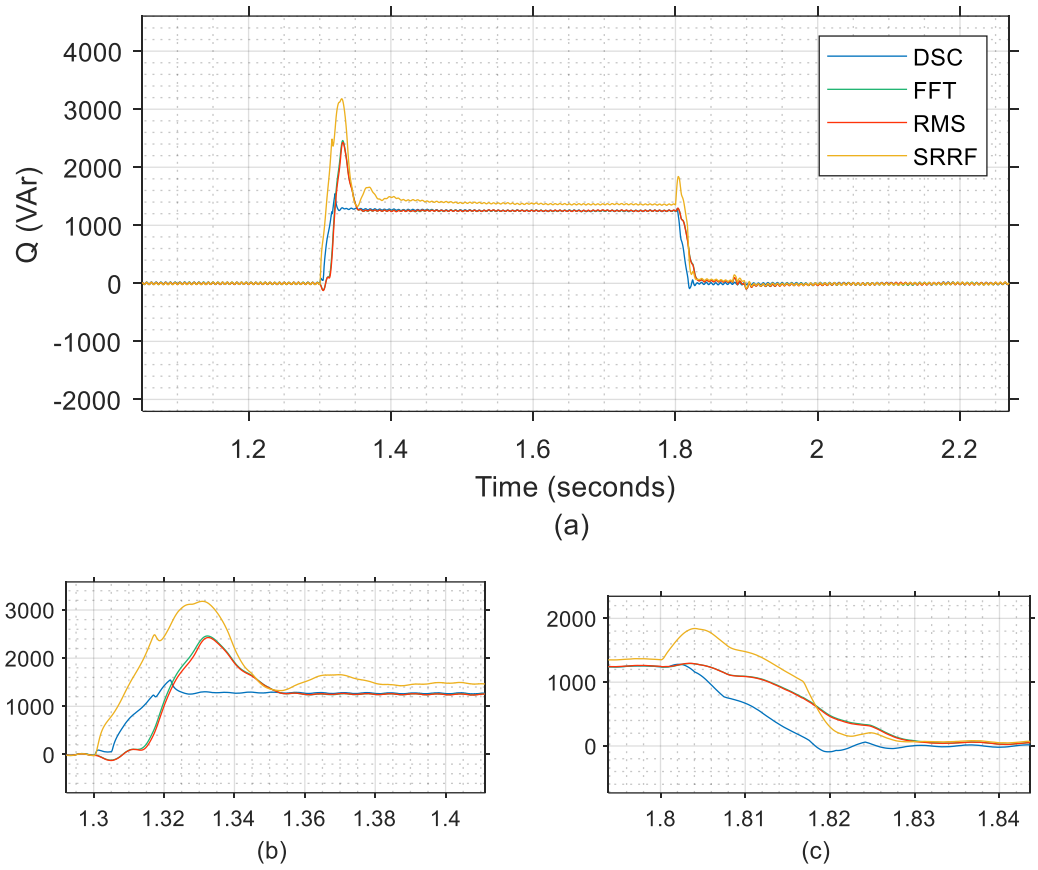

Figure 6. 14: Reactive Power supplied by DER 2 under voltage sag of 50% produced by L-L-L-G fault

Table 6. 11:DER 2 Reactive Power Q at Fault Inception under 50% voltage sag

	Reactive Power Q (VAr)			
Time (s)	**Proposed DSC Secondary Control**	**FFT Secondary Control**	**RMS Secondary Control**	**SRRF Secondary Control**
1.30	3.9	7.4	1.2	0.9
1.31	736.3	87.2	82.8	1444.2
1.32	1424.8	1100.2	1006.5	2444.7
1.33	1288.4	2330.6	2254.0	3169.5
1.34	1274.4	1916.9	1898.9	2209.0
1.35	1291.1	1380.5	1374.8	1362.8
1.36	1271.7	1246.9	1248.4	1509.2
1.37	1279.8	1257.5	1264.7	1655.7
1.38	1267.3	1247.5	1246.5	1478.9
1.39	1275.6	1257.0	1257.8	1450.9
1.40	1264.9	1244.0	1242.3	1482.5

Table 6. 12:DER 2 Reactive Power Q at Fault Clearance under 50% voltage sag

	Reactive Power Q (VAr)			
Time (s)	**Proposed DSC Secondary Control**	**FFT Secondary Control**	**RMS Secondary Control**	**SRRF Secondary Control**
1.80	1241.4	1243.9	1248.4	1352.7
1.81	670.0	1091.9	1088.9	1478.8
1.82	-90.1	478.7	463.2	298.5
1.83	6.6	82.3	71.8	67.6
1.84	-19.3	28.9	28.0	50.9
1.85	13.0	51.5	49.1	69.9
1.86	-25.5	30.0	27.2	43.7

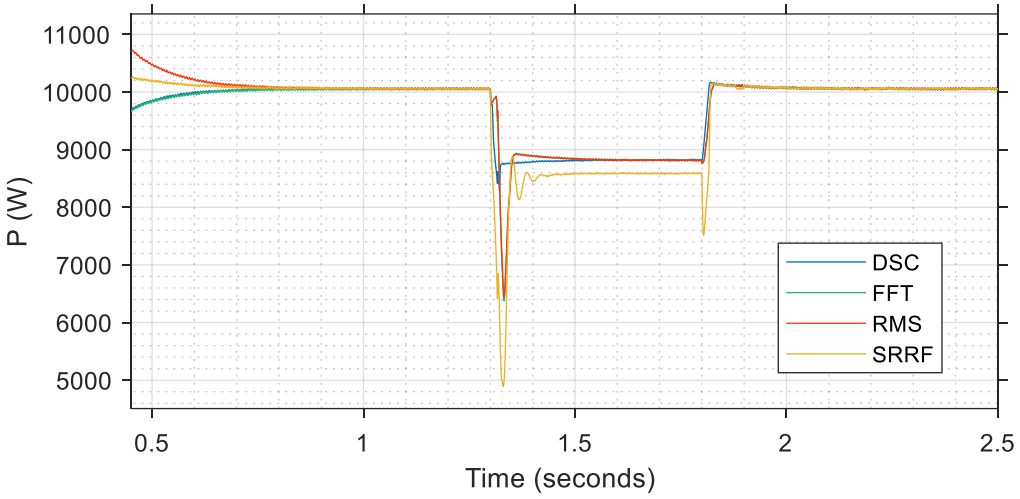

Figure 6. 15: Active power supplied by DER 1 under voltage sag of 60%

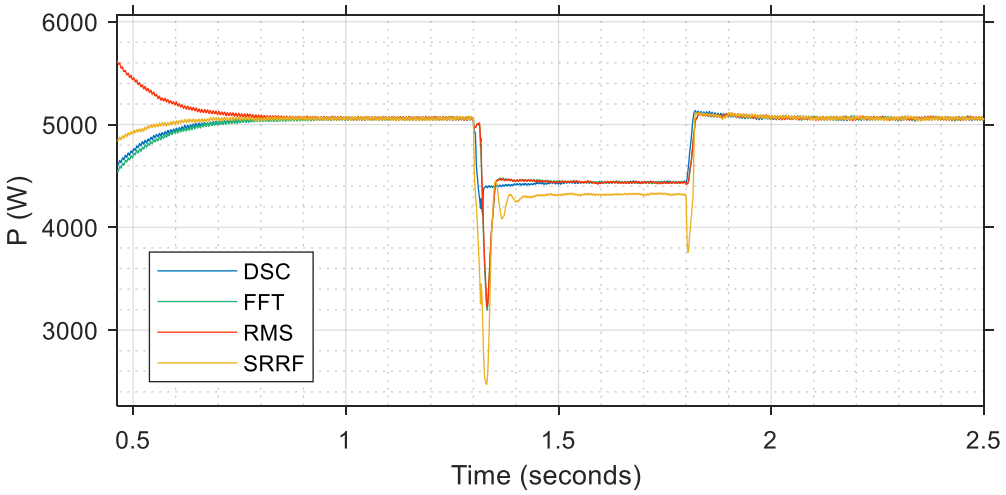

Figure 6. 16: Active power supplied by DER 2 under voltage sag of 60%

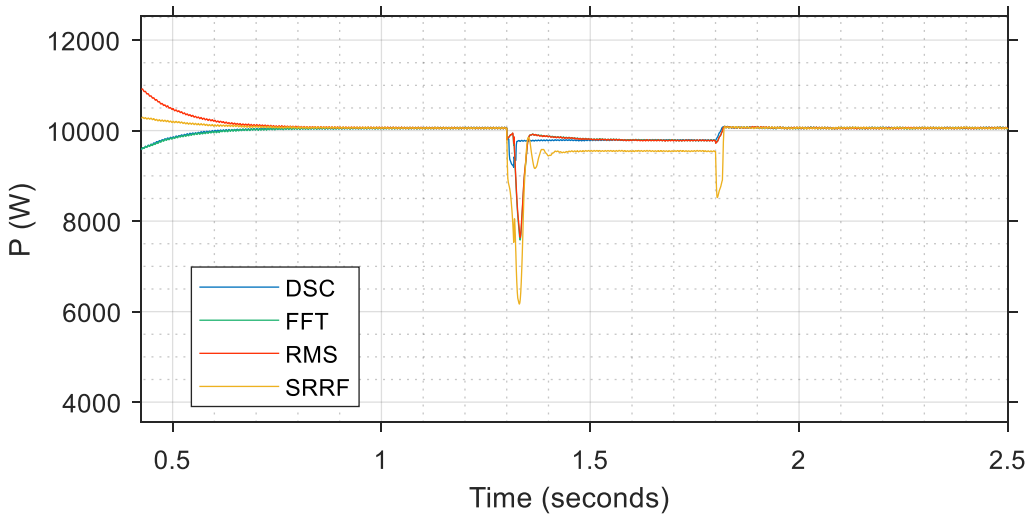

Figure 6. 17: Active power supplied by DER 1 under voltage sag of 70%

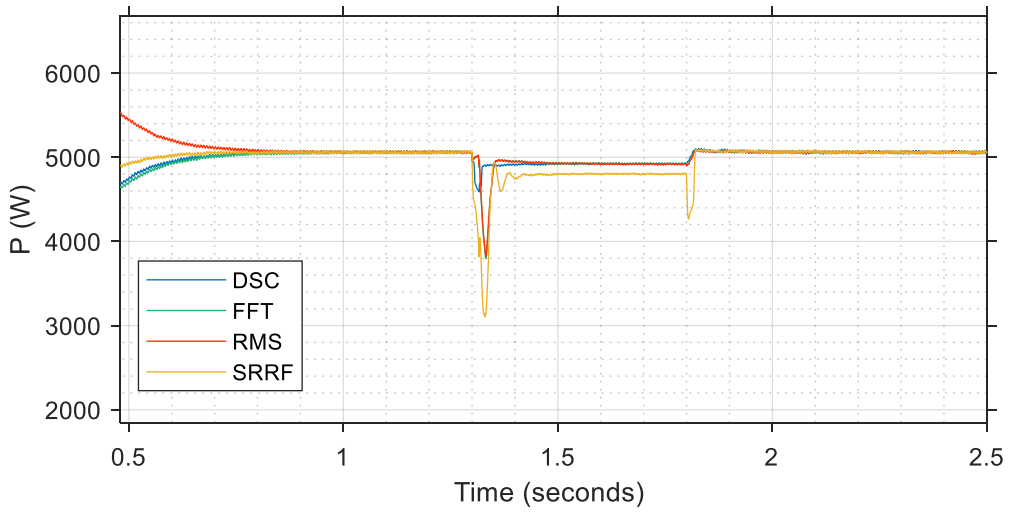

Figure 6. 18: Active power supplied by DER 2 under voltage sag of 70%

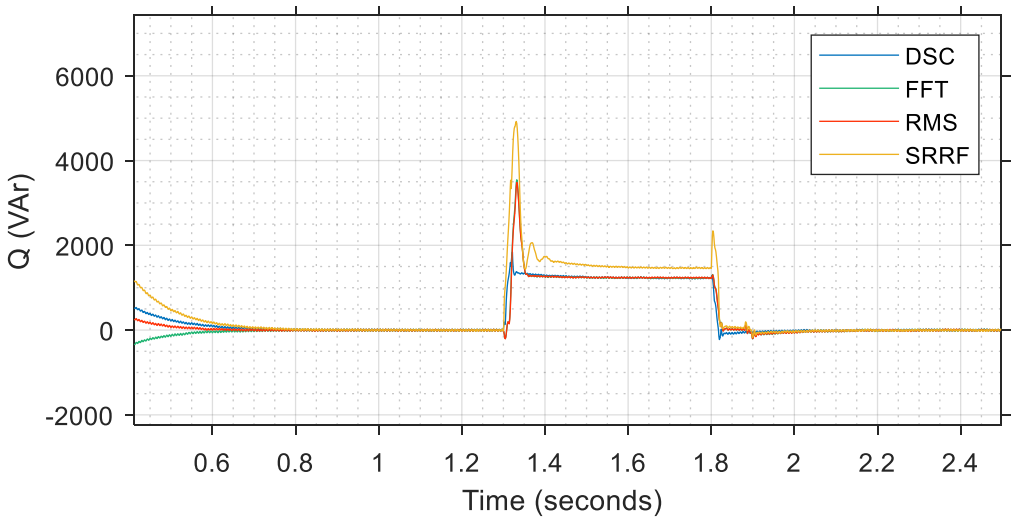

Figure 6. 19: Reactive power supplied by DER 1 under voltage sag of 60%

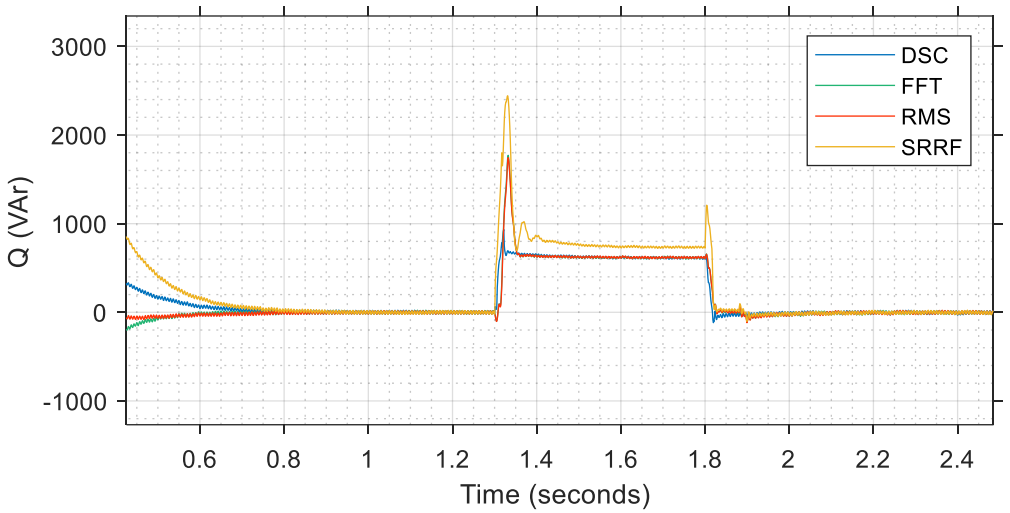

Figure 6. 20: Reactive power supplied by DER 2 under voltage sag of 60%

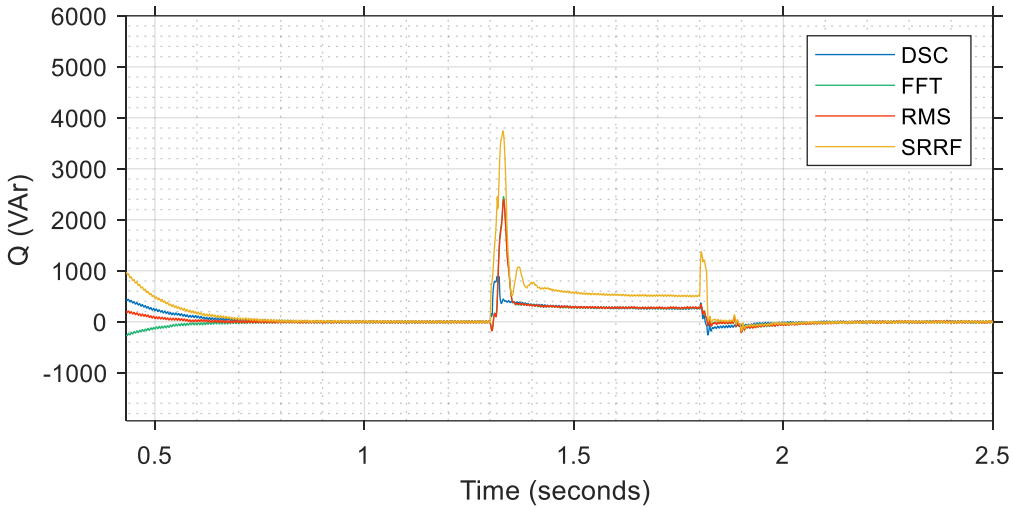

Figure 6. 21: Reactive power supplied by DER 1 under voltage sag of 70%

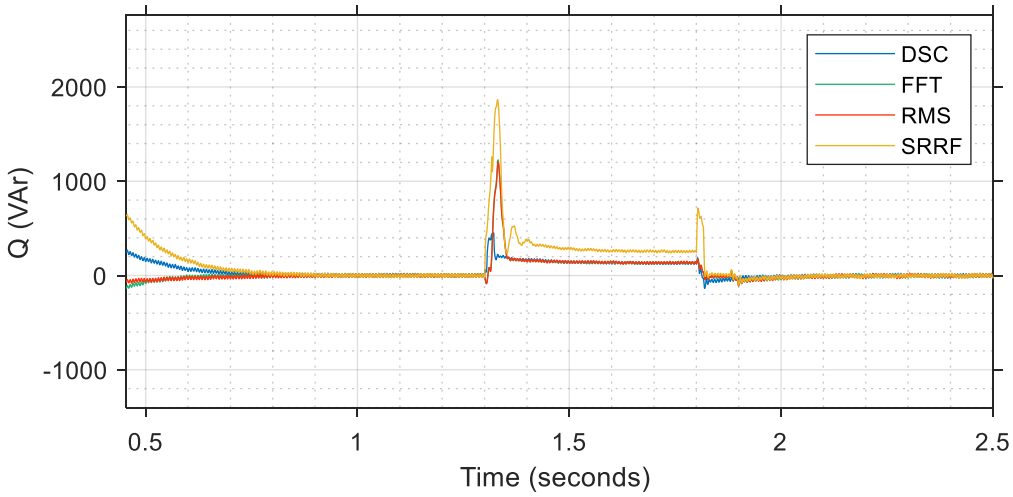

Figure 6. 22: Reactive power supplied by DER 2 under voltage sag of 70%

The aggregate active power supply by DERs is limited as a result of voltage sag occasioned by grid fault. The DERs are controlled to inject an active power amount that meets the local load demand and reduces the active power injection into the faulted main utility grid. Throughout

voltage sags, the decreased grid voltage magnitude and the 'off' switching of the IGBT-diode AC reactor limit active power transmitted to the grid. The amplitude of fault current is limited, and the microgrid voltage is improved for the transfer of active power to the local load. For excessive voltage sag, generated active power is limited to the rated value of the local load. Any time there is an excess generation, the surplus is supplied to the faulted grid. However, in the acute incidence of grid voltage sag to the tune of 20% or less, no active power can be generated for the local microgrid load and main grid load. Consequently, DER reactive power generation is maximized in supporting the host grid's voltage in compliance with Spanish grid codes.

The local load's active power consumption under different voltage sag depths is presented in Figures 6.23 and 6.24. Table 6.13 provides the active and reactive power drop experienced under 50%, 60%, and 70% depths of voltage sags

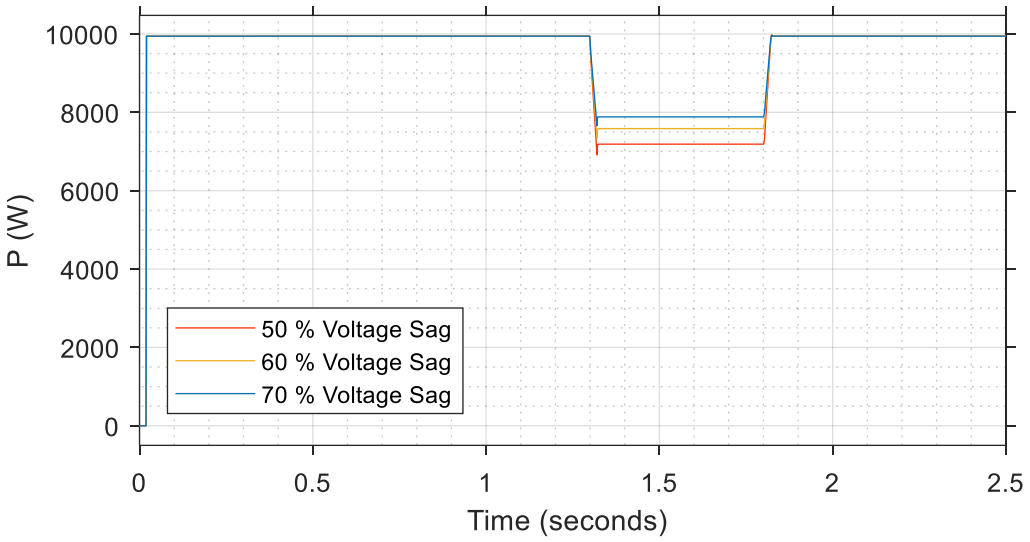

Figure 6. 23: Active Power supply to local microgrid load under voltage sags

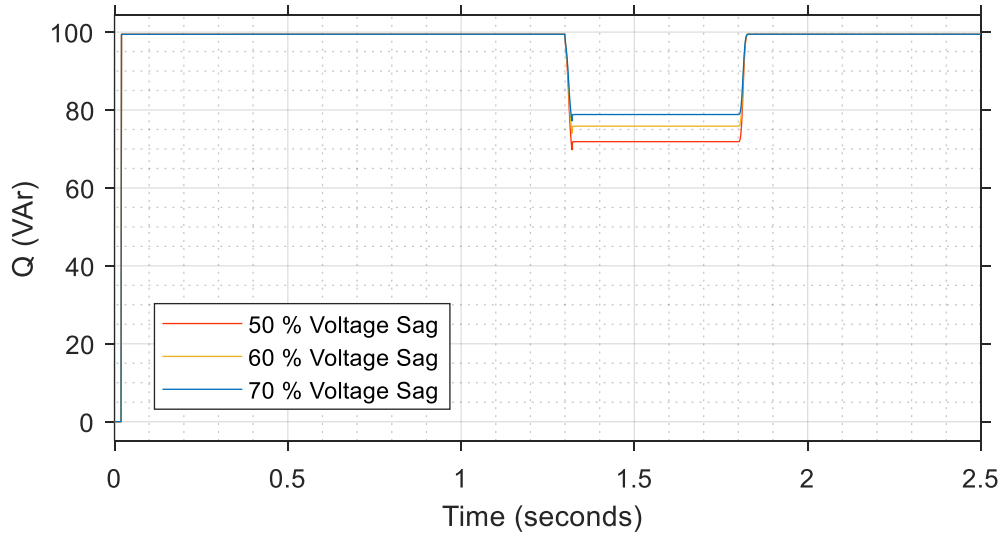

Figure 6. 24: Reactive Power supply to local microgrid load under voltage sags

Table 6. 13: Local Microgrid Load Delivery

	50% Voltage Sag		60% Voltage Sag		70% Voltage Sag	
Time (s)	**P (kW)**	**Q (VAr)**	**P (kW)**	**Q (VAr)**	**P (kW)**	**Q (VAr)**
1.30	9.944	99.4	9.944	99.4	9.944	99.4
1.31	8.292	84.2	8.515	86.3	8.687	87.9
1.32	6.916	69.8	7.338	74.0	7.659	77.2
1.33	7.188	71.9	7.585	75.8	7.884	78.8
1.80	7.188	71.9	7.585	75.9	7.884	78.8
1.81	8.274	75.5	8.527	80.8	8.714	83.2
1.82	9.650	96.7	9.705	97.2	9.743	97.5
1.83	9.944	99.5	9.944	99.5	9.944	99.5
1.84	9.944	99.4	9.944	99.4	9.944	99.4

6.3 Asymmetrical Fault

Single phase-to-ground faults are the most common in typical distribution systems [209][210]. The other asymmetrical faults include the line to line and double line to ground. The efficacy of the proposed control strategy is also tested under the unbalanced grid conditions listed above. This unbalanced fault is simulated in Line 1 between t = 1.30 and t = 1.80. Under a single L-G fault, the grid voltage and DER voltage and current are shown in Figures 6.19 and 6.20. Under an L-L-G fault, the grid voltage and DER voltage and current are shown in Figures 6.21 and 6.22. Under an L-L fault, the grid voltage and DER voltage and current are shown in Figures 6.23 and 6.24.

No significant distortion appears in the DER 1 and 2 output voltage waveform and current waveform. The FRT control with the IGBT switched AC reactor effectively compensated for the unbalance sags in voltage magnitude. The three-phase voltage within the microgrid as indicated by the DER 1 and DER 2 appear with relatively balanced values compared to the grid voltage unbalance.

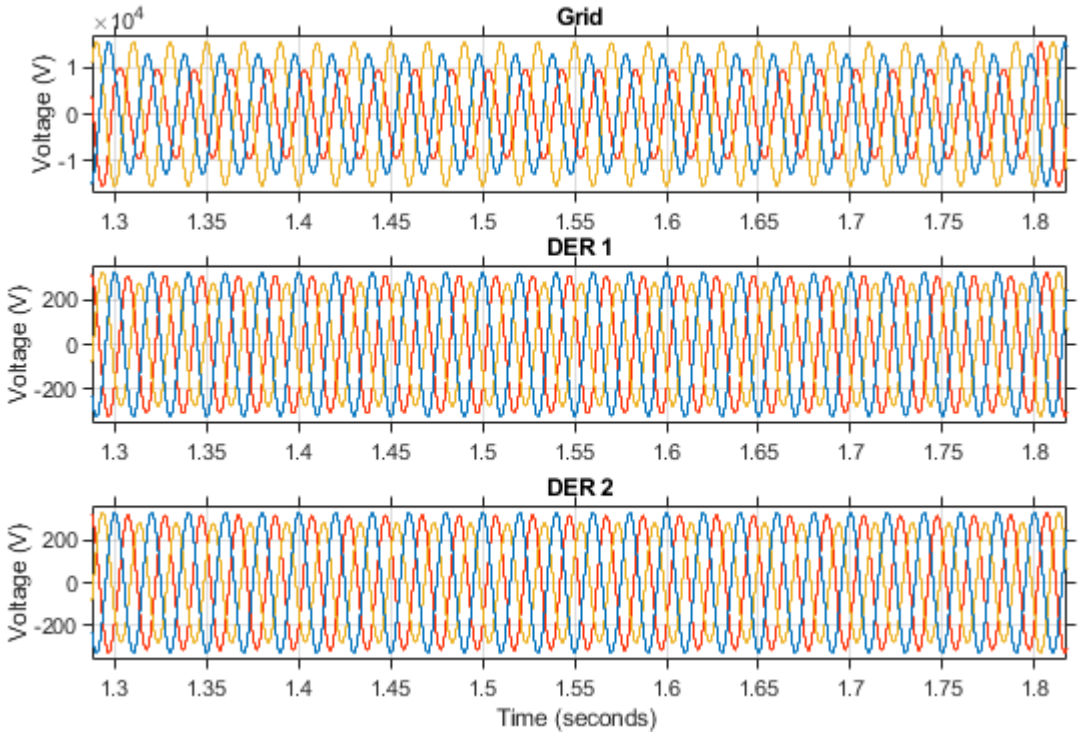

Figure 6. 25:Grid and Microgrid voltages under L-G fault on the main grid

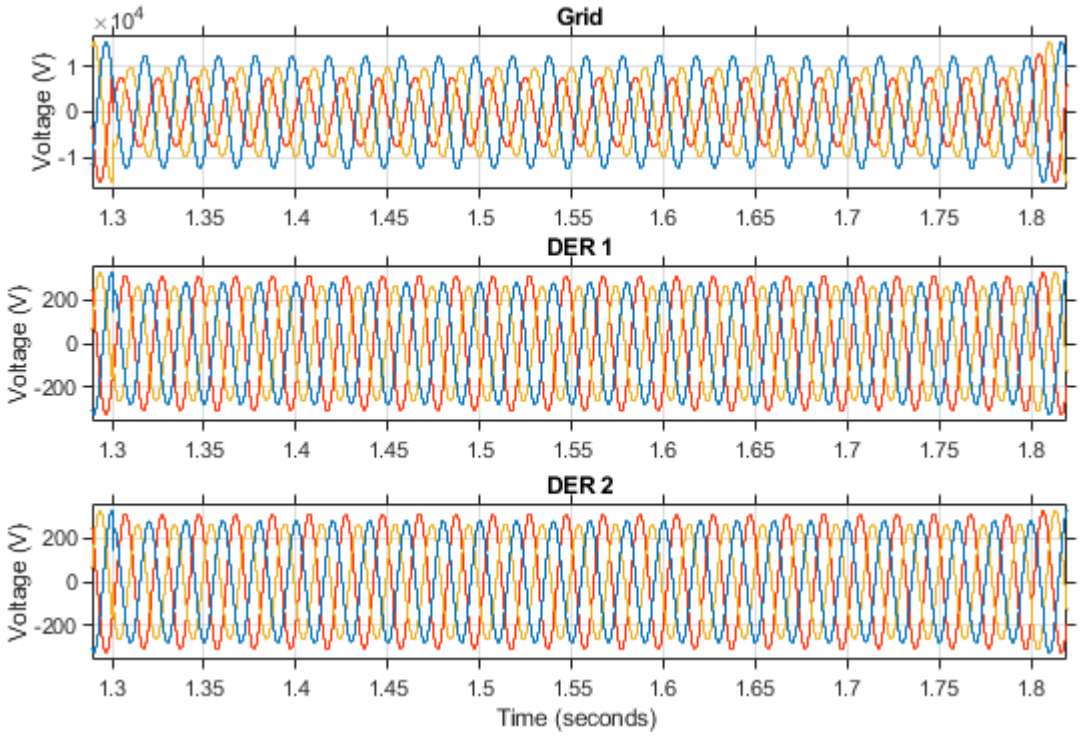

Figure 6. 26:Grid and Microgrid voltages under L-L-G fault on the main grid

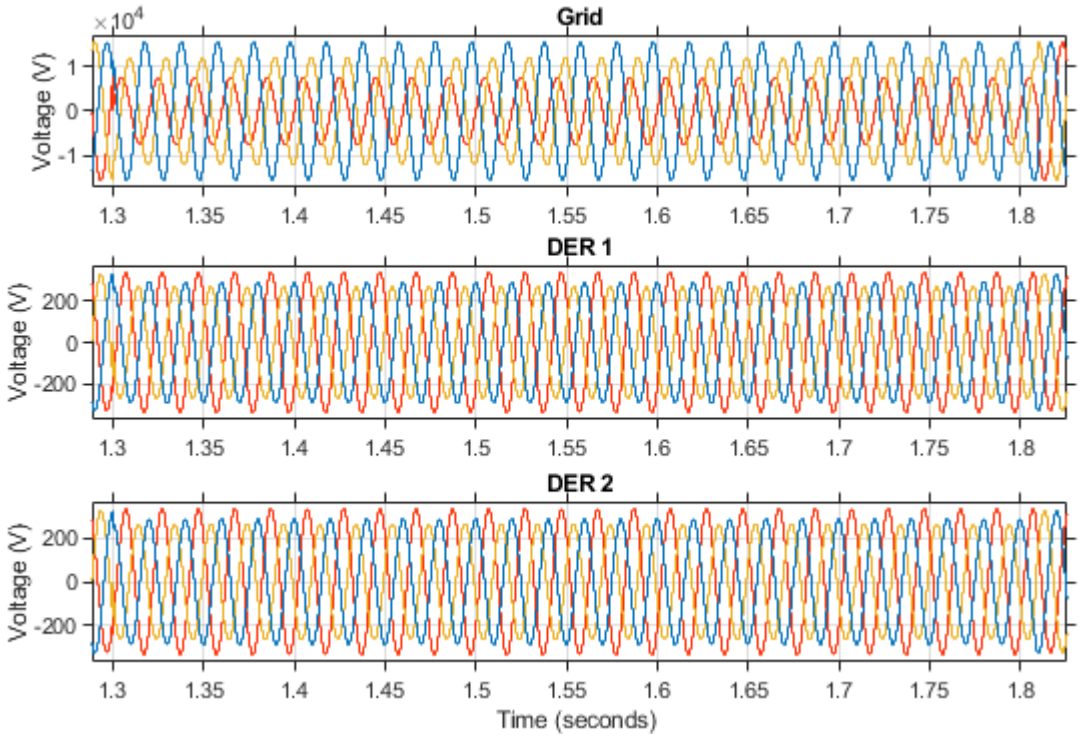

Figure 6. 27:Grid and Microgrid voltages under L-L fault on the main grid

During an unbalanced transient leading to an unbalanced voltage sag within the grid, the PCC's voltage unbalances are evaluated from the phase to phase voltages V_{ab}, V_{bc}, and V_{ca}. Applying NEMA (National Equipment Manufacturer Association in the United States of America) voltage unbalance definition is given as the ratio of maximum deviation from the mean phase to phase voltage to mean of phase to phase voltages, the unbalance within the grid under L-G fault is calculated. Similarly, the unbalance calculated for other types of asymmetrical faults is given in Table 6.14. The proposed control actively compensated the unbalance in line to line voltages by reducing the unbalance to relatively negligible percentages.

Table 6. 14:Voltage unbalances measured under asymmetrical faults

Fault Type	**Voltage Unbalance**	
	Grid	**Microgrid**
L-G	24.14%	4.44%
L-L-G	24.31%	7.13%
L-L	35.36%	12.20%

Similar to the case of balanced voltage sag occasioned by a symmetrical transient disturbance on the main grid, Figures 6.19–6.33 further affirm the effectiveness of the proposed FRT secondary control in riding through faults, compensating unbalance voltage sag and improving microgrid voltage, limiting the amplitude of current, and ensuring local load power demand are met. Irrespective of the main grid unbalance condition, the microgrid voltage balance is relatively maintained within the limit. Currents are limited to ensure uninterruptible supply to the local load before exporting excess generation to the main grid.

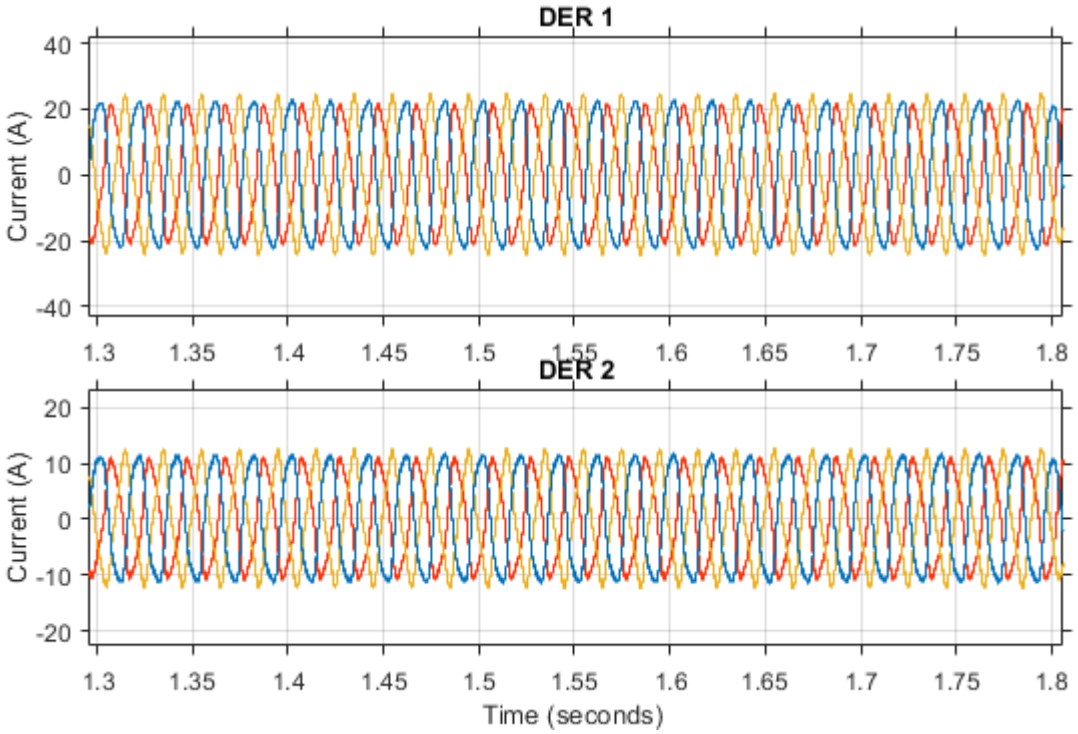

Figure 6. 28:Grid and microgrid current under L-G fault on the main grid

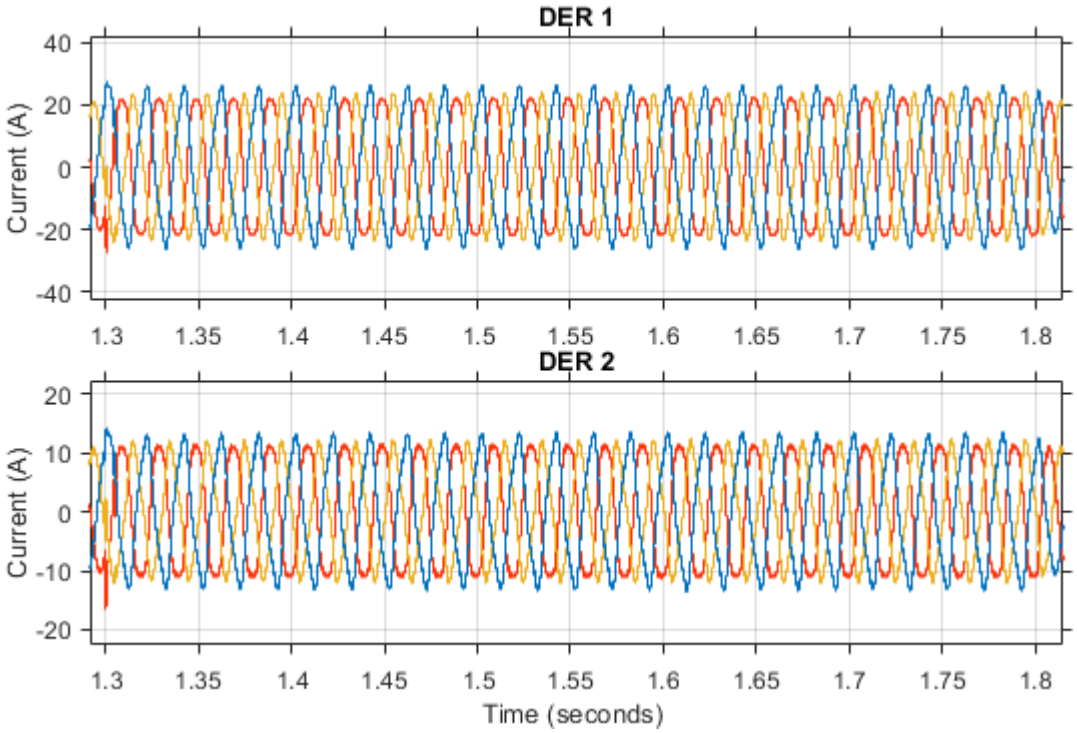

Figure 6. 29:Grid and microgrid current under L-L-G fault on the main grid

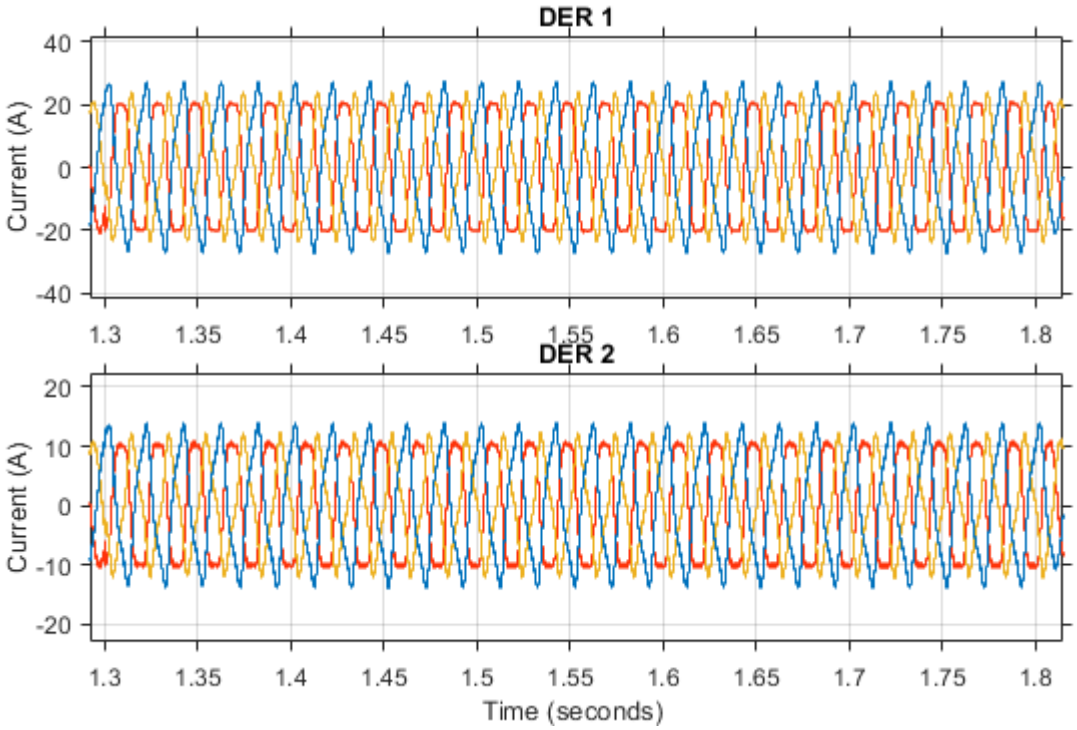

Figure 6. 30:Grid and microgrid current under L-L fault on the main grid

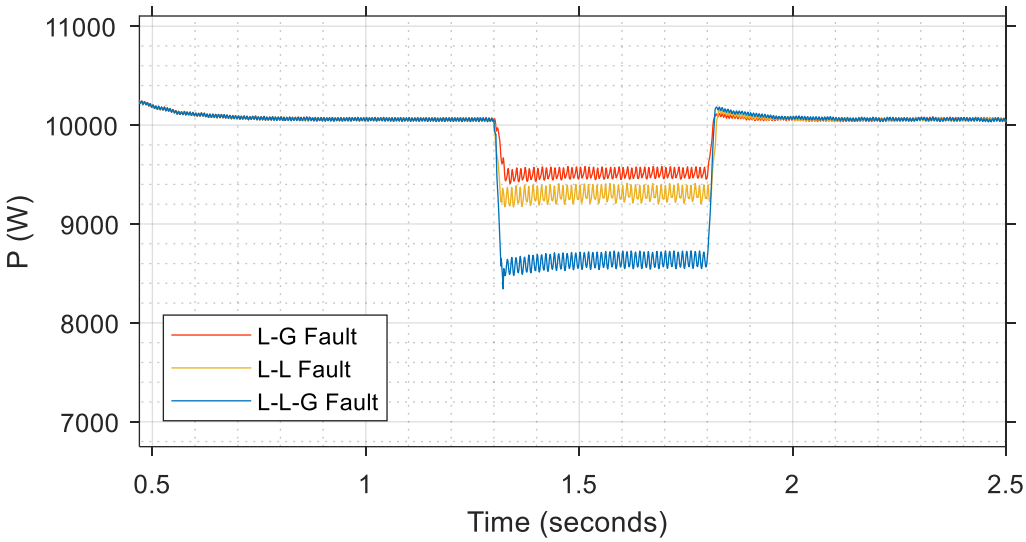

Figure 6. 31:Power supplied by DER 1 under L-G fault

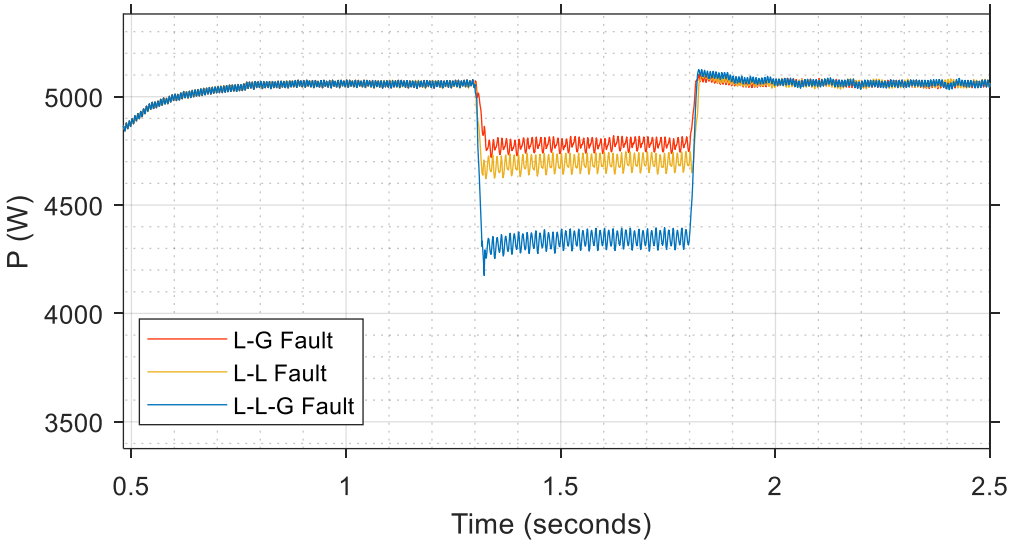

Figure 6. 32:Power supplied by DER 2 under L-L-G fault

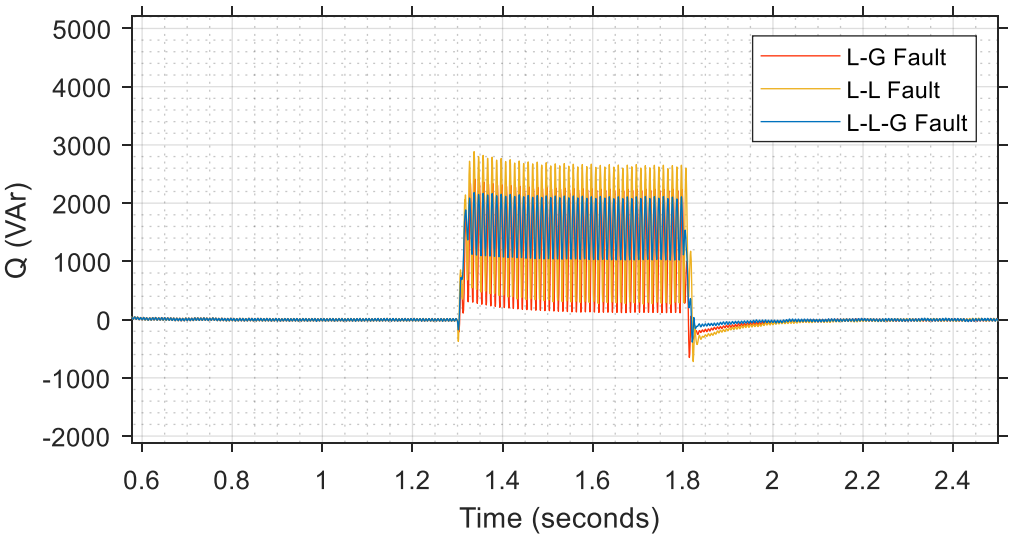

Figure 6. 33:Power supplied by DER 1 under L-L fault

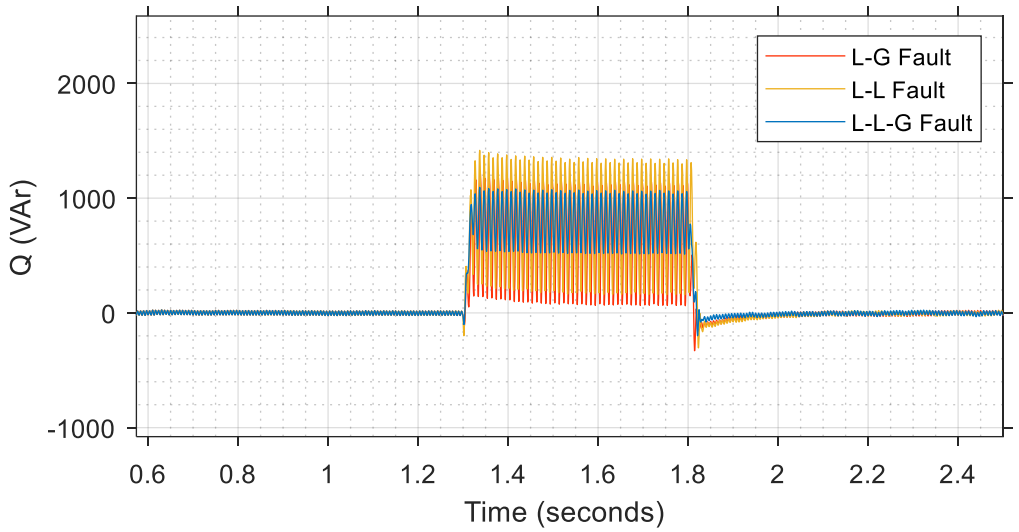

Figure 6. 34:Power supplied by and DER 2 under L-L fault

Table 6. 15:Active Power Generation by the DERs within the microgrid

	L-G Fault		L-L Fault		L-L-G Fault	
Time (s)	**DER 1 (W)**	**DER 2 (W)**	**DER 1 (W)**	**DER 2 (W)**	**DER 1 (W)**	**DER 2 (W)**
1.30	10063.3245	5072.0227	10063.3245	5016.1134	10060.4253	2016.1134
1.31	9877.6796	4966.6776	9468.8383	4799.7237	8990.4254	4561.1338
1.32	9620.7312	4862.9151	9217.9192	4692.6115	8587.0979	4238.3960
1.33	9507.9702	4786.6664	9368.8144	4723.1733	8642.2986	4342.2461
1.40	9432.8465	4727.7862	9232.2647	4665.8828	8533.7782	4308.2264
1.60	9456.3368	4744.2408	9253.8580	4693.7061	8563.7859	4344.3242
1.80	9537.2463	4749.3026	9395.5638	4682.3980	8729.7577	4324.3510
1.81	9864.0143	5015.3247	9455.0987	4807.5814	9578.3749	4880.9652
1.82	10110.8144	5071.6403	10029.6859	5076.2135	10183.2832	5097.9147
1.83	10114.5749	5068.8985	10145.7384	5088.7441	10173.9020	5094.5776

Table 6. 16:Reactive Power Generation by the DERs within the microgrid

	L-G Fault		L-L Fault		L-L-G Fault	
Time (s)	**DER 1 (VAr)**	**DER 2 (VAr)**	**DER 1 (VAr)**	**DER 2 (VAr)**	**DER 1 (VAr)**	**DER 2 (VAr)**
1.30	-159.6578	-108.8270	-368.5216	-79.7195	-175.8124	-60.1054
1.31	751.3095	116.0625	725.8762	583.2065	718.1926	607.0751
1.32	692.1361	146.8782	681.3997	627.0508	1413.64	748.5618
1.33	1883.6241	1159.9937	2719.3370	1105.7338	2088.0339	937.0625
1.40	1241.6137	462.0502	545.4306	216.2318	1113.6079	535.1339
1.60	2247.8738	1019.4420	2239.2572	901.5914	1896.4272	901.5914
1.80	2232.5847	965.0492	2221.5844	1144.6011	1895.0333	965.0492
1.81	306.7914	339.7883	502.0136	1309.7123	418.6162	680.5204
1.82	060.1403	-157.2360	1100.5944	-305.0239	218.6192	-81.5873
1.83	-219.4128	-129.4043	-425.7867	-138.0991	-115.2041	-63.2967

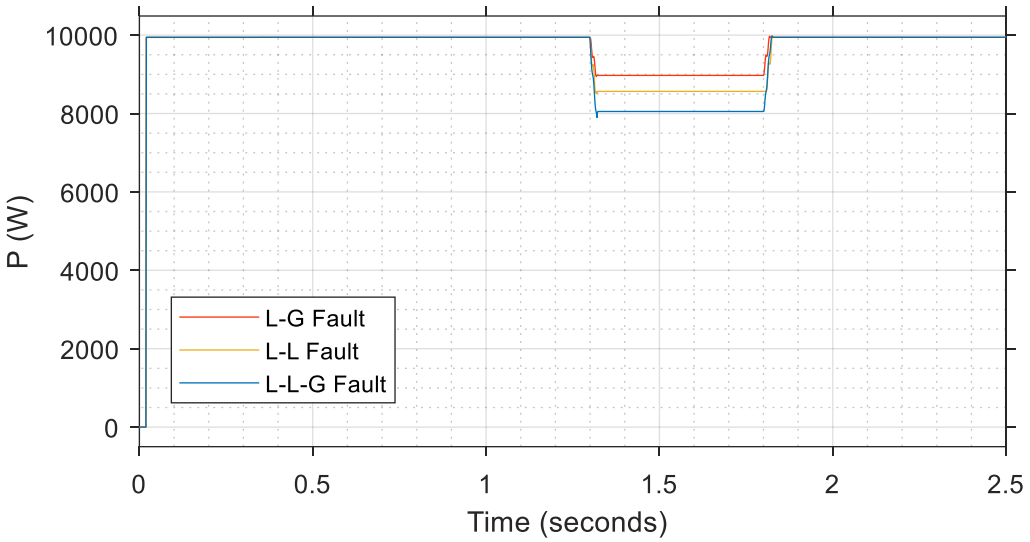

Figure 6. 35:Power supplied to the local microgrid load under L-G fault

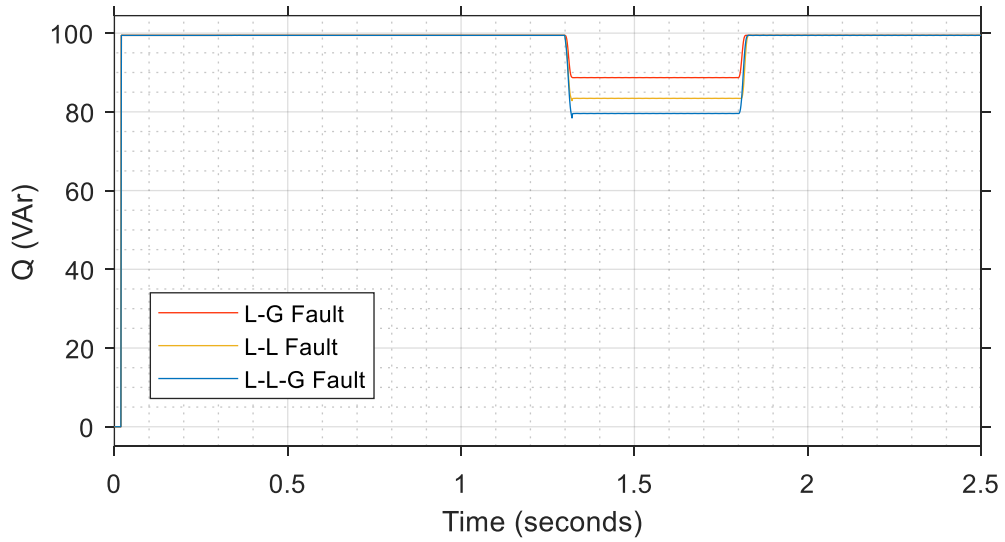

Figure 6. 36:Power supplied to the local microgrid load under L-L-G fault

Table 6. 17:Power supplied to the local microgrid load under L-L fault

	L-G Fault		L-L Fault		L-L-G Fault	
Time(s)	**P (W)**	**Q (VAr)**	**P (W)**	**Q (VAr)**	**P (W)**	**Q (VAr)**
1.30	9944.1066	99.4410	9944.1066	99.4411	9944.1060	99.4411
1.31	9349.2730	95.9595	8846.2618	91.5224	8491.6106	90.2416
1.32	8953.0741	88.9924	8564.2977	83.3398	7999.7550	79.4111
1.33	8973.0095	88.6851	8565.1092	83.4201	8052.5465	79.5717
1.80	8972.9928	88.7040	8565.0905	83.4382	8052.5306	79.5913
1.81	9634.3516	90.1817	9073.3267	83.4221	9150.6043	80.5932
1.82	9965.3190	99.2649	9256.6600	91.5642	9545.7745	95.6701
1.83	9944.0793	99.4403	9944.0793	99.4635	9944.0844	99.4556
1.84	9944.1047	99.4394	9944.0830	99.4637	9944.0970	99.4468

6.4 Conclusion

Using the DSC, the sequence detection algorithm is implemented to detect negative sequences and instances of fault in 0.1515 ms to activate the proposed FRT secondary control to comply with the grid code stipulations. The DSC has a faster convergence time with improved separation of the positive and negative sequences being feasible. The results of the simulation confirm the performance and effectiveness of the proposed strategy.

The proposed FRT control strategy in this work is integrated at the hierarchical control structure's secondary level. Consequently, the FRT scheme ensures that the inverter-based microgrid requires no mode switching from grid feeding (active and reactive power generation control) to grid forming (frequency and voltage control). The transition from one mode to another will introduce severe transients in the system. The inverter interfaced microgrids can ride through faults or transient disturbances on the host utility grid without loss of synchronization. As a result, no distinct control arrangements are required to ensure the transition from constant grid feeding (P–Q) mode to constant grid forming (ω–V) mode and vice versa.

Furthermore, an acceptable power quality for the local sensitive loads during fault duration is ascertained irrespective of the grid condition. Previous FRT schemes in literature have not taken the power quality of the local load into consideration. Though throughout this scenario, the active power supply to the local sensitive load is continuous under fault. Similarly, due to the high R/X ratio of a typical low voltage (LV) distribution line, injecting reactive power during the faults may not substantially contribute to the voltage recovery. Therefore, this work has been able to deploy an adequately sized anti-parallel IGBT-diode switched inductance in PCC with a grid to reduce the R/X ratio and effectively support grid voltage under disturbance. The theoretical framework for the determination of this value is developed in this work.

Lastly, this work introduces a droop-based control for the reactive and active power reference of an inverter-based microgrid with a DC-DC converter. This droop interfaces the primary control of the PV inverter with the proposed secondary control. This is further implemented by extending the grid-connected PV system's dynamic functions where the MPPT provides active power referencing. This enables active power-sharing and collective participation in voltage and frequency regulation of the host grid.

CHAPTER SEVEN
FRT CONTROL IMPLEMENTATION IN INVERTER-BASED MICROGRID WITH PV

7.1 Introduction

FRT is one of the critical technical issues in large-scale PV grid integration with a less-thorough investigation. Consequently, reference [126] proposes a detailed strategy with external devices for a single-stage PV source system to boost FRT capability based on the stipulations of current grid code interconnection conditions. The suggested control mitigates over-voltage in DC-link and AC over-current, which causes DC-AC inverter disconnection or damage. The fault current limiter and chopper are deployed as external devices to limit excessive AC grid current and absorb the excess DC link voltage, respectively. This thesis earlier introduced an approach to limit the active power reference generated by the MPPT is an inverter-based microgrid with a DC-DC converter, as in the case of a double-stage PV system in Chapter 5. A specific control action is implemented to curtail the DC-source power generation and equip the interface converters with fault ride-through capabilities to avoid activating the DC-link overvoltage protection scheme. This is achieved without shutting down the voltage boosting operation of the converter. The DC-DC and DC-AC converter's DC bus voltage is controlled during the AC grid voltage sag cycle. Consequently, the solutions proposed in this study curtailed the usual momentous DC voltage increase in the DC bus under the transient process. Chapter 7 simulated the FRT approach proposed in Chapter 5 on a grid supporting the inverter-based microgrid model with a DC-DC converter presented in Chapter 4. A typical example of this is a double stage PV system with DC-DC and DC-AC converters. Therefore, the grid code FRT compliance of the system is evaluated based on the same parameters as given in Chapter 6 while simultaneously solving the unique challenges introduced as a result of a PV source. Table 7.1 gives the critical system parameters at uniform 25 ^{0}C temperature and 1000 W/m^2 irradiance. The system is connected to a medium voltage level with a nominal voltage of 11 kV.

The grid-connected inverter-based microgrid with DC-DC converter interfacing the PV. The system consisting of a PV based DERs and local load, as depicted in Figure 7.1. The fault is simulated on the main grid to cause 50%, 60%, and 70% voltage sags at the PCC, switched at time t = 1.3 s, and assumed to be automatically cleared at t = 1.8 s.

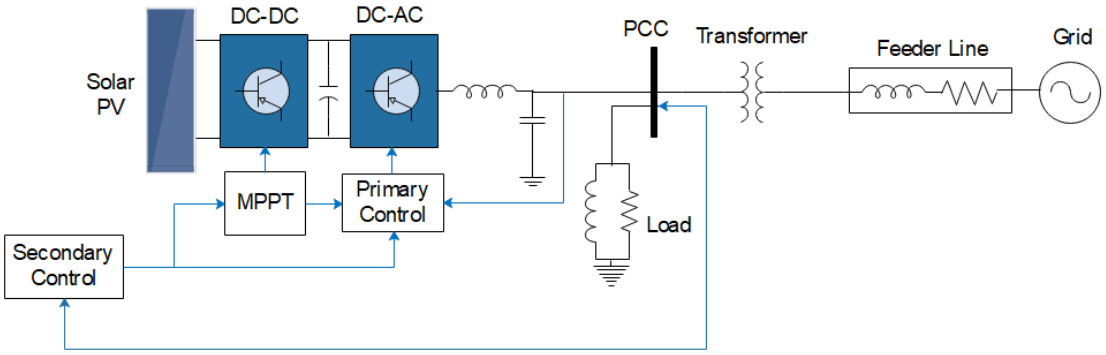

Figure 7. 1:The examined topology of the double stage PV system used to form a microgrid with a local load

The double stage PV system serving as the microgrid DER supplies a 21 kW local load with a 0.90 power factor. The surplus generated power by PV in the microgrid is exported into the main grid system, whereas the primary control also participates in the grid voltage and frequency regulations. A phase-phase RMS rated 0.400/11 kV step-up transformer is installed at the PCC, through which the spare generation is supplied to the utility grid.

Table 7. 1:PV Inverter primary and secondary control parameters

Parameters	**Descriptions**	**Values**
ω_{cut}	Cut-off angular frequency	100π
E	Single-phase voltage reference	330 V
$K_{p\,I}$	Direct-quadrature current loop P gain	100
$K_{i\,I}$	Direct-quadrature current loop I gain	1000
$K_{p\,VDC}$	Outer loop DC voltage P gain	5
$K_{i\,VDC}$	Outer loop DC voltage I gain	800
$K_{p\,PCC+-}$	Positive sequence and negative sequence P gain	0.0125
$K_{i\,PCC+-}$	Positive sequence and negative sequence I gain	2
f_{PWM}	DC-AC inverter PWM switching frequency	10 kHz

7.2. Fault

7.2.1 DC Side Analysis

The drop in the PCC voltage due to a fault caused the proposed secondary control to re-evaluate the primary control references provided the voltage drop is within the FRT curve envelope. As a result of this drop, the PV power generated, power in the DC link, and power delivered to the AC grid is unbalanced. Consequently, this imbalance portends an unwarranted transient voltage at the

PV side and DC link while excessive current is witnessed at the AC side, as shown in Figures 7.2, 7.3, 7.4, 7.5, 7.6, 7.7, 7.8, 7.9, and 7.10. The exponential increment in the voltage at the DC link is due to the capacitor's energy build-up. Figures 7.1, 7.2, and 7.3 show the PV voltage, DC link voltage, and average DC link current flow under fault without and with the proposed secondary control under 50% voltage sags.

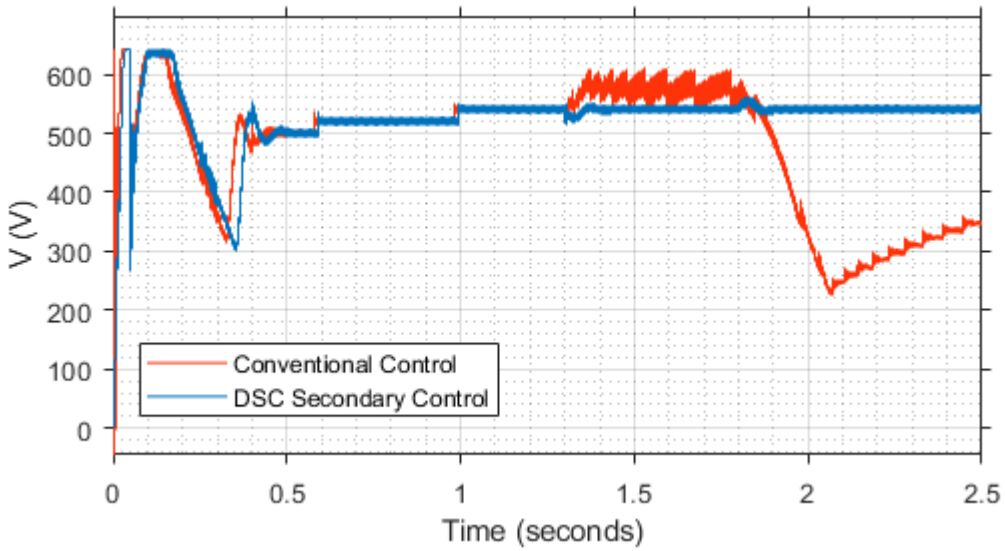

Figure 7. 2:PV voltage under 50% grid voltage sag

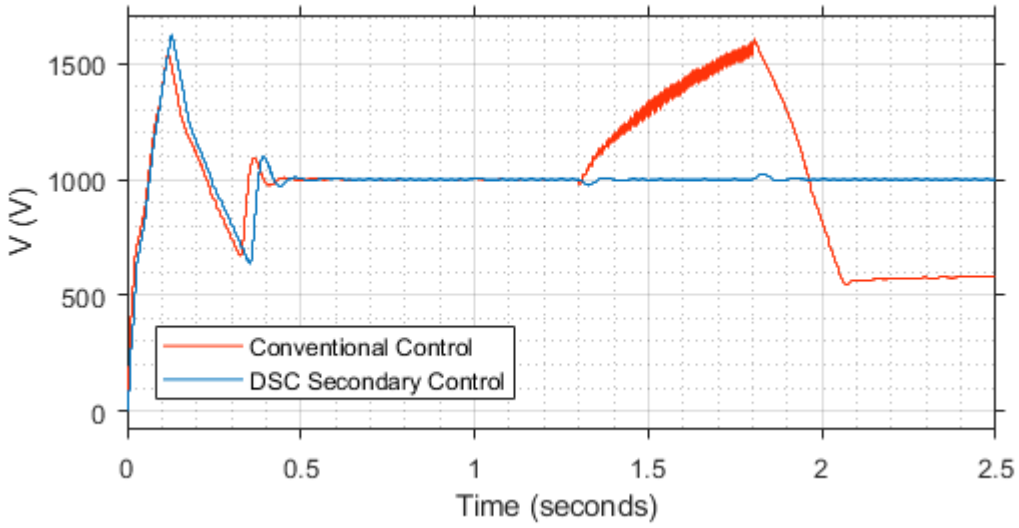

Figure 7. 3:DC link voltage under 50% grid voltage sag

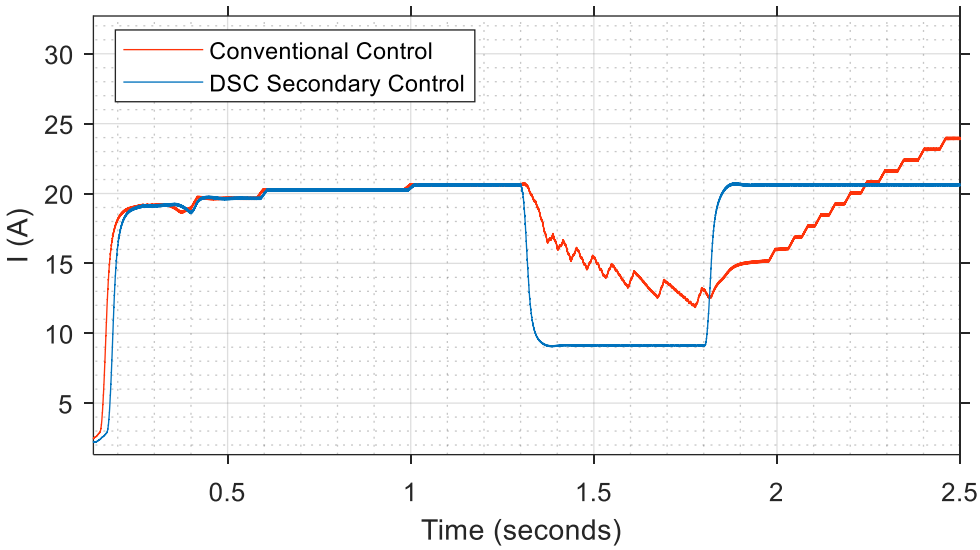

Figure 7. 4:Average DC link current under 50% grid voltage sag

When a disturbance is sensed in the grid, the MPPT function is deactivated, as shown in the DC side's current drop depicted in Figures 7.4 and 7.7. This infers that the operating point is transitioned to the FRT mode. Immediately upon the fault detection, the PV system starts reactive power injection into the grid per the voltage sag demands and grid code requirements. Similarly, the active power generation is limited in compliance with the limit imposed by the ratings and complex power requirements. Furthermore, Figures 7.5, 7.6, and 7.7 show that the PV voltage, DC bus voltage, and average DC link current flow under fault with and without the proposed secondary control under 60% voltage sags.

The limitation of active power is not necessarily the requirement of grid codes; however, it is done out of concern in simultaneously fulfilling the key objective of the grid-supporting schemes of fault ride-through (by remaining in grid connection mode), providing grid support services to expedite grid recovery. Thus, reactive power injection without a commensurate drop in the active power generation triggers the system to activate overcurrent protection for safe disconnection. As a result, the active power is limited under FRT operation as shown in the average DC flow in the DC link, as shown in Figures 7.4 and 7.7

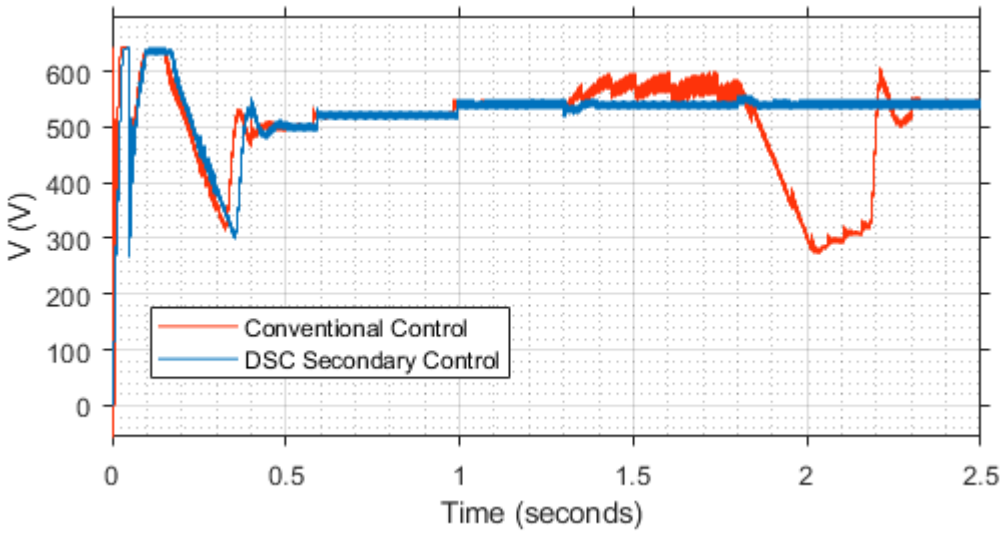

Figure 7. 5:PV voltage under 60% grid voltage sag

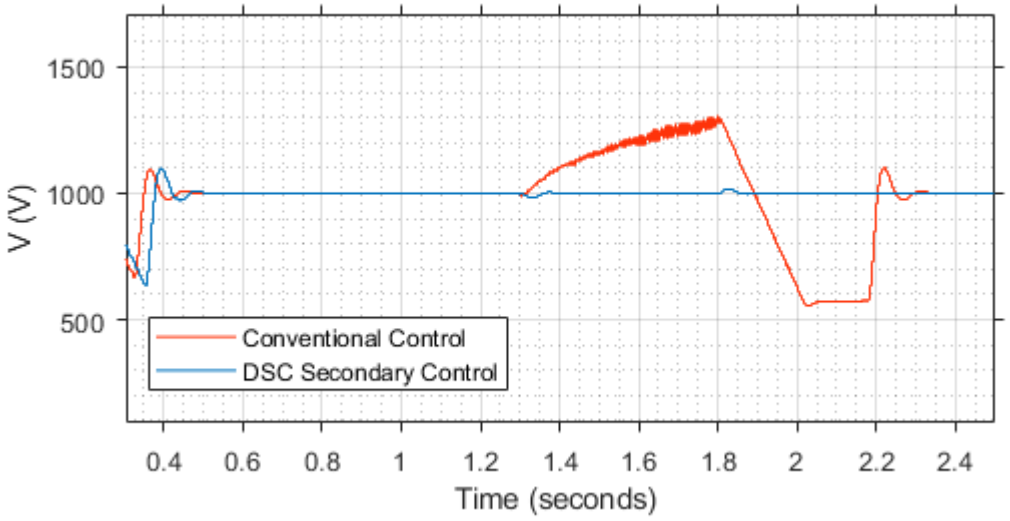

Figure 7. 6:DC link voltage under 60% grid voltage sag

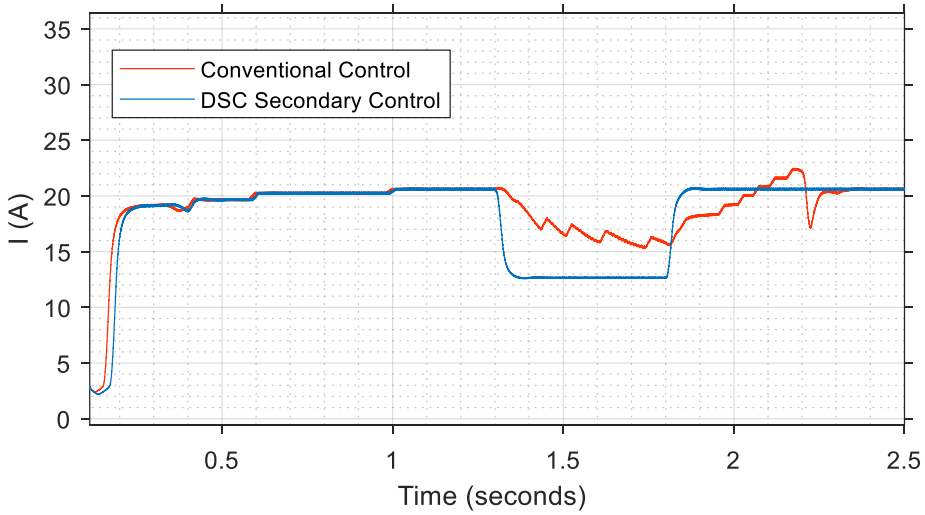

Figure 7. 7:Average DC link current under 60% grid voltage sag

Under the Spanish grid code, the fault is recognized to be cleared as soon as the voltage level rises to 90% of the nominal grid voltage value. Hence the system is recognized to have returned to the normal operation mode. Consequently, the PV system immediately returned to its MPPT mode and tracked the PV panels' maximum output power. It took a short period for the incremental conductance MPPT used to adjust to the transients caused by the AC grid fault, and this is evident in the responses reported in Figures 7.2-7.10.

Furthermore, PV module voltage and current, PV diode current, DC link voltage, average DC link current, and by extension, DC link power require a considerable period to regain the pre-fault stable value, as shown in Figures 7.2-7.10. However, the proposed secondary control significantly mitigated the increase in voltage at the DC link.

The developed models and the FRT control have demonstrated that the active power and reactive power regulation can facilitate the FRT capability of the three-phase grid- supporting converter when the operating mode of MPPT is shifted to minimize the generation of active power throughout the fault period. The secondary control developed for the system shifted the operating point hinge on the voltage-sag depth, reducing the PV power generated and DC power delivered at the DC link. This, in the long run, provided adequate protection for the inverter/converter switches from potential damage, which could be caused by the excessive AC grid current and hike in DC voltage. Without the proposed secondary control, the increasing DC link voltage causes the operating point to shift and limit DC link current. The DC bus voltage failed to be maintained at the reference even after fault clearance, thereby hampering power delivery.

Furthermore, the control of DC generated power by the PV, and, by extension, the AC grid active power transmitted is associated with the depth of voltage dip the AC grid. The active power control is based on a droop relationship between these two parameters, and the inverse proportionate relationship and requirements are exploited in the development of the proposed strategy. Hence the AC grid voltage was closely monitored with the DSC algorithm. The information obtained is directly utilized in the converter's MPPT for alternation between the MPP and FRT operations.

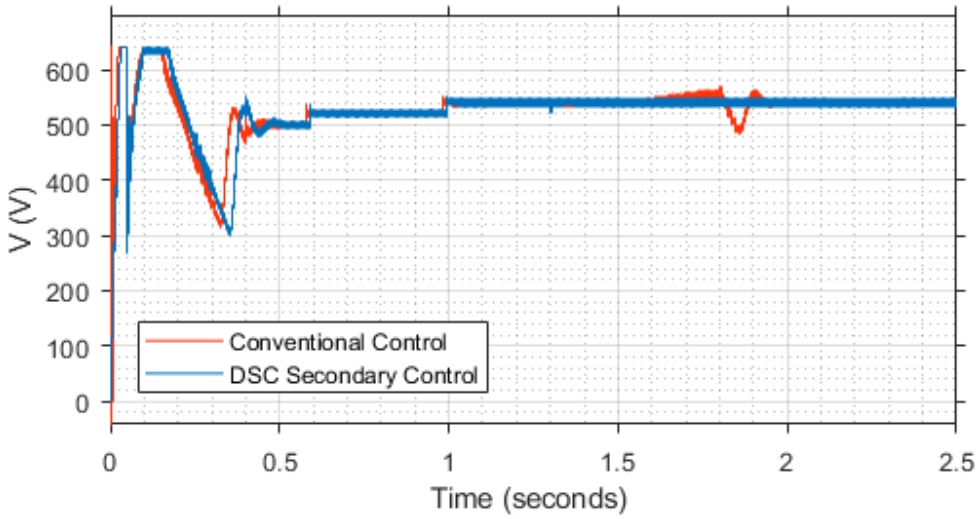

Figure 7. 8:PV voltage under 70% grid voltage sag

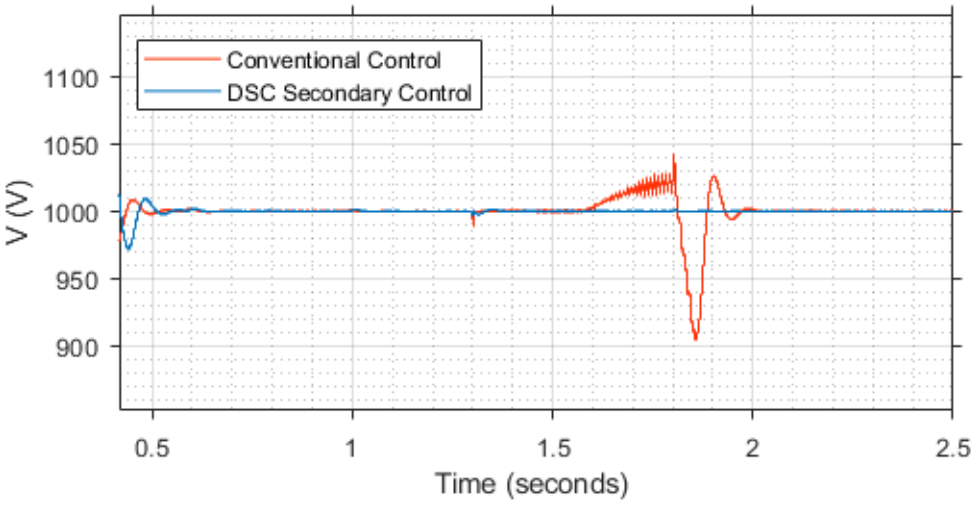

Figure 7. 9:DC link voltage under 70% grid voltage sag

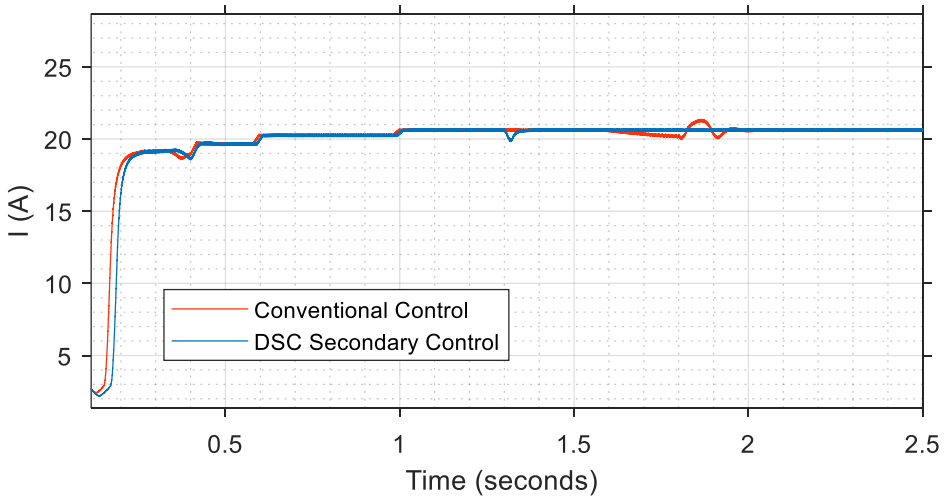

Figure 7. 10:Average DC link current under 70% grid voltage sag

Table 7. 2: PV Voltage under 50%, 60% and 70% voltage sags

	50% voltage sag		60% voltage sag		70% voltage sag	
Time (s)	**Proposed Secondary Control**	**Proposed Secondary Control**	**Proposed Secondary Control**	**Conventional Control**	**Proposed Secondary Control**	**Conventional Control**
1.30	532.1	534.0	548.0	548.0	548.0	532.7
1.34	536.6	571.8	540.1	565.1	548.5	548.3
1.38	542.2	570.5	536.9	556.8	548.0	548.2
1.42	534.0	576.4	538.6	575.7	536.6	536.4
1.46	547.5	601.7	547.6	584.9	548.0	548.1
1.50	536.2	581.4	534.1	572.1	548.0	548.3
1.54	537.6	567.4	537.6	566.9	537.5	537.7
1.58	545.6	607.2	545.7	588.9	548.0	548.2
1.62	533.1	553.7	532.9	552.5	532.8	536.4
1.66	542.8	587.5	532.8	547.3	548.0	555.3
1.70	534.4	566.6	547.7	554.0	543.8	551.4
1.74	534.2	570.5	532.8	533.2	548.0	538.6
1.78	547.3	577.1	532.8	551.9	547.6	555.2
1.82	553.5	553.2	541.4	538.4	548.0	544.8
1.86	534.0	537.0	547.9	518.0	534.5	486.7
1.90	547.8	495.7	532.6	442.0	548.0	545.4
1.94	536.6	415.2	548.1	392.4	548.0	545.5
1.98	540.1	361.7	547.9	343.1	537.4	538.3
2.02	546.2	296.8	533.7	283.1	548.0	548.1
2.06	532.9	233.7	547.9	307.5	548.0	548.0
2.10	543.8	251.7	548.0	300.4	547.9	548.0
2.14	546.1	276.1	545.4	312.2	543.9	543.9
2.18	532.9	268.7	547.9	324.4	533.0	533.0
2.22	543.8	288.0	548.0	586.7	546.1	546.2
2.26	540.2	297.9	536.4	517.4	543.0	543.0
2.30	533.2	307.9	546.9	514.8	534.6	534.5

Table 7. 3:DC Link Voltage under 50%, 60% and 70% voltage sags

	50% voltage sag		60% voltage sag		70% voltage sag	
Time (s)	**Proposed Secondary Control**	**Proposed Secondary Control**	**Proposed Secondary Control**	**Conventional Control**	**Proposed Secondary Control**	**Conventional Control**
1.30	998.8	998.8	1000.5	1000.5	1000.4	1000.5
1.34	985.4	985.4	985.5	1039.4	999.9	1001.0
1.38	1005.2	1005.2	1004.3	1086.3	1000.4	1000.0
1.42	998.3	998.3	999.2	1107.5	1000.5	999.8
1.46	1000.1	1000.1	999.9	1130.4	1000.6	1000.3
1.50	1000.0	1000.0	1000.2	1168.6	999.6	1000.9
1.54	1000.1	1000.1	1000.0	1186.8	1000.6	999.1
1.58	999.7	999.7	999.7	1217.9	1000.5	999.9
1.62	1000.1	1000.1	1000.4	1193.1	1000.6	1005.5
1.66	999.8	999.8	999.7	1241.3	999.6	1013.6
1.70	999.9	999.9	1000.3	1225.5	999.6	1017.7

1.74	1000.2	1000.2	1000.3	1281.0	999.5	1025.7
1.78	999.9	999.9	1000.3	1279.5	1000.6	1012.6
1.82	1021.6	1021.6	1013.7	1254.5	1000.2	989.6
1.86	998.9	998.9	1001.0	1115.9	1000.5	904.1
1.90	999.0	999.0	999.6	977.0	1000.5	1024.7
1.94	1000.5	1000.5	1000.0	853.8	1000.5	996.4
1.98	999.9	999.9	1000.5	709.3	1000.4	1001.4
2.02	999.9	999.9	1000.5	566.5	1000.5	1000.6
2.06	1000.4	1000.4	999.6	568.9	999.5	999.7
2.10	1000.0	1000.0	1000.6	569.9	1000.5	999.8
2.14	1000.0	1000.0	1000.5	572.6	1000.6	1000.6
2.18	1000.1	1000.1	999.5	576.4	1000.5	1000.5
2.22	999.7	999.7	1000.5	1100.2	999.5	1000.5
2.26	1000.2	1000.2	1000.5	982.1	1000.4	1000.4
2.30	1000.1	1000.1	1000.5	1002.3	1000.5	1000.5

Table 7. 4: Average DC Current under 50%, 60%, and 70% voltage sags

	50% voltage sag		**60% voltage sag**		**70% voltage sag**	
Time (s)	**Proposed Secondary Control**	**Proposed Secondary Control**	**Proposed Secondary Control**	**Conventional Control**	**Proposed Secondary Control**	**Conventional Control**
1.30	20.7	20.7	20.7	20.7	20.7	20.7
1.34	9.8	9.8	13.3	20.1	20.6	20.7
1.38	9.1	9.1	12.7	19.3	20.5	20.5
1.42	9.2	9.2	12.7	17.6	20.7	20.7
1.46	9.2	9.2	12.7	17.8	20.5	20.5
1.50	9.2	9.2	12.6	16.6	20.7	20.7
1.54	9.2	9.2	12.7	17.2	20.7	20.7
1.58	9.2	9.2	12.7	16.3	20.7	20.7
1.62	9.2	9.2	12.6	16.5	20.7	20.6
1.66	9.1	9.1	12.7	16.4	20.7	20.5
1.70	9.1	9.1	12.7	15.8	20.7	20.4
1.74	9.1	9.1	12.6	15.3	20.7	20.3
1.78	9.1	9.1	12.7	16.1	20.7	20.3
1.82	14.5	14.5	17.1	16.0	20.7	20.5
1.86	20.3	20.3	20.4	17.8	20.7	21.3
1.90	20.7	20.7	20.7	18.3	20.7	20.4
1.94	20.5	20.5	20.6	18.2	20.7	20.7
1.98	20.7	20.7	20.7	19.2	20.7	20.7
2.02	20.6	20.6	20.7	19.7	20.7	20.7
2.06	20.5	20.5	20.7	20.3	20.7	20.7
2.10	20.7	20.7	20.7	20.9	20.7	20.7
2.14	20.7	20.7	20.7	21.7	20.7	20.7
2.18	20.5	20.5	20.7	22.5	20.7	20.7
2.22	20.6	20.6	20.7	18.8	20.7	20.7
2.26	20.5	20.5	20.7	20.4	20.7	20.7
2.30	20.7	20.7	20.7	20.3	20.7	20.7

7.2.2 Grid AC Side Analysis

7.2.2.1 AC Grid and Microgrid Voltage

Figures 7.11, 7.12 and 7.13 illustrate the voltage drop's depth on the main grid, which also compels a consequent rise in the current magnitude as in Figures 7.14, 7.15, and 7.16. The immediate current magnitude limitation is created by the secondary power reference integrated into the proposed secondary control FRT scheme of the DC-AC inverter and DC-DC Converter, as shown in Figures 7.14, 7.15 and 7.16. At-fault inception, the references for active and reactive current are changed instantly. Correspondingly, with suitable tuning, all references are preserved automatically after fault clearance. Thereby, Figures 7.11. 7.12 and 7.13 demonstrate a seamless transition from pre-fault to a fault and then from fault to post-fault. Therefore, the LC filter's current output from the PV system is adequately constrained, as seen in Figures 7.14, 7.15, and 7.16. The 50 percent voltage drop rate detected at the PCC to the grid is then enhanced within 93.32 percent in the microgrid. The grid voltage sag is detected at 0.1515 ms at the PCC, less than half of the first fault incidence cycle. This indicates that the fault is observed in 1.3001515 s as revealed in the positive half cycle and in the negative half cycle 1.300 on the point. Consequently, the FRT scheme fault mode operation is activated with simultaneous switching of the IGBT-diode switched reactor in series with all the phases for balanced transient conditions and series with only the affected phase in unbalanced conditions. Implementing the FRT solutions for PV source in the microgrid application meant that the microgrid voltage would be compensated for the microgrid's efficient operation independent of the specific transient grid state.

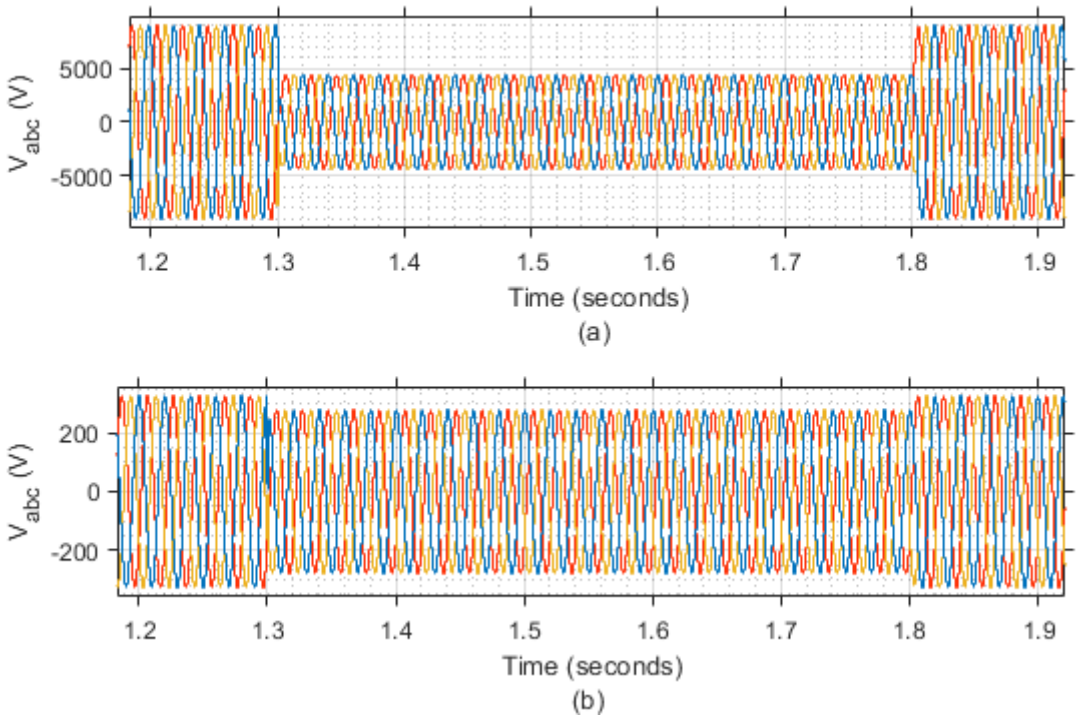

Figure 7. 11:Voltages in the grid and microgrid at grid voltage sag of 50% produced by L-L-L-G fault

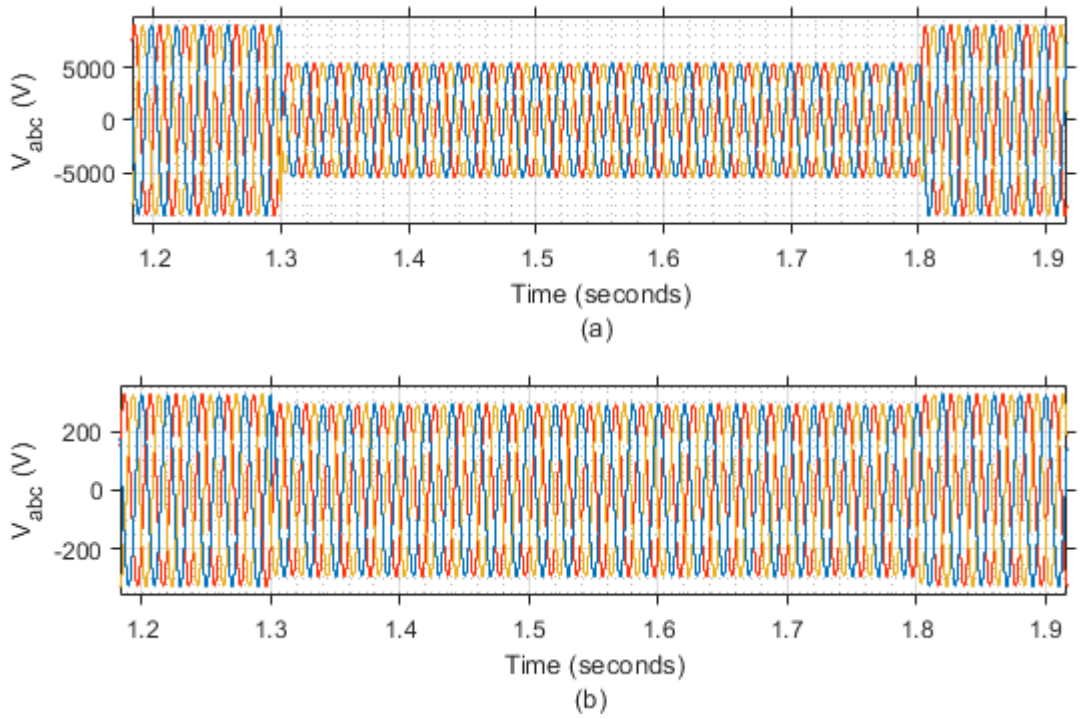

Figure 7. 12:Voltages in the grid and microgrid at grid voltage sag of 60% produced by L-L-L-G fault

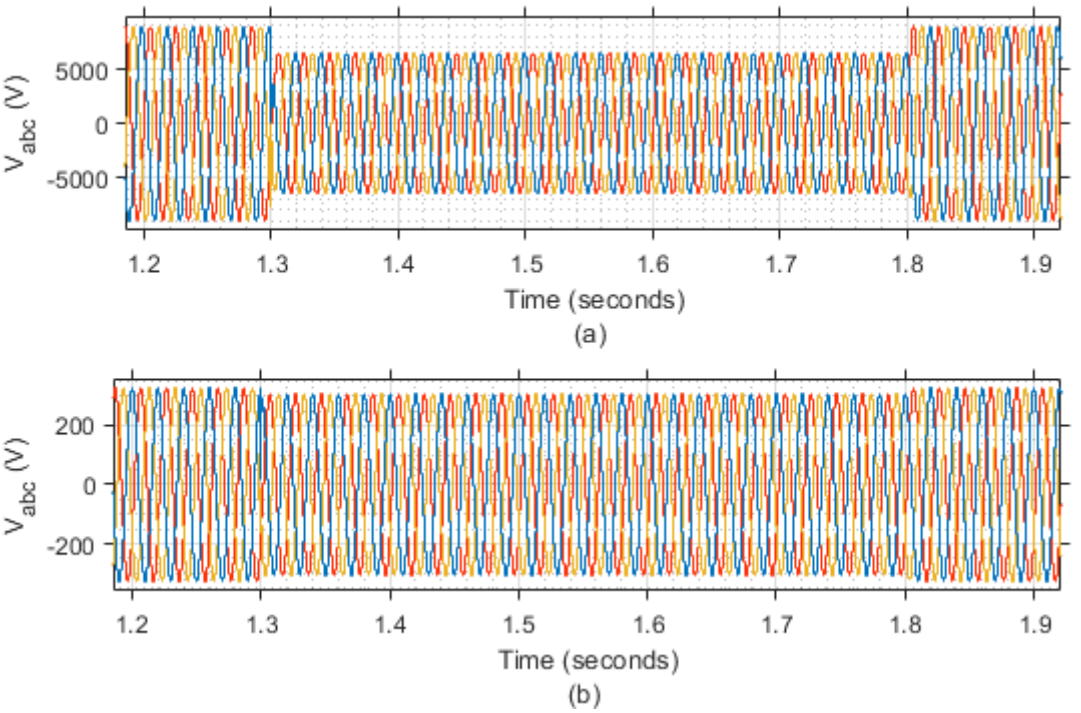

Figure 7. 13:Voltages in the grid and microgrid at grid voltage sag of 70% produced by L-L-L-G fault

7.2.2.2 AC Grid and Microgrid Current

Based on its kVA rated values, the fault current restricting this secondary control's potential contributes to the main grid voltage support using reactive power injected. Figures 7.14, 7.15, and

7.16 illustrate the corresponding PV based DER current output waveforms with and without the secondary control under 50 percent voltage sags at the PCC. The current output within the microgrid is appropriately constrained with no substantial distortion in the PV-DER current signals than when the proposed secondary control is not present. Thus, it is clear that the inverter currents are appropriately limited in the first cycle after fault inception at 1.3 s. Consequently, the inverter currents are at 1.3 s adequately constrained within the first cycle after fault commencement. The 0.00016 delay after the proposed control activation fault is small and negligible. Nevertheless, the inverter semiconductor switches cannot be affected by overcurrent generated between 1.30000 and 1.30016 s. In particular, grid faults occur practically around the filter capacitor, and the transient current peak at fault commencement disappears almost immediately and thus is overlooked. It should be stated that the excess current in the event of transient interruption is absolutely attenuated where the converters are connected to an electrically weak grid far from the inverter stem placement.

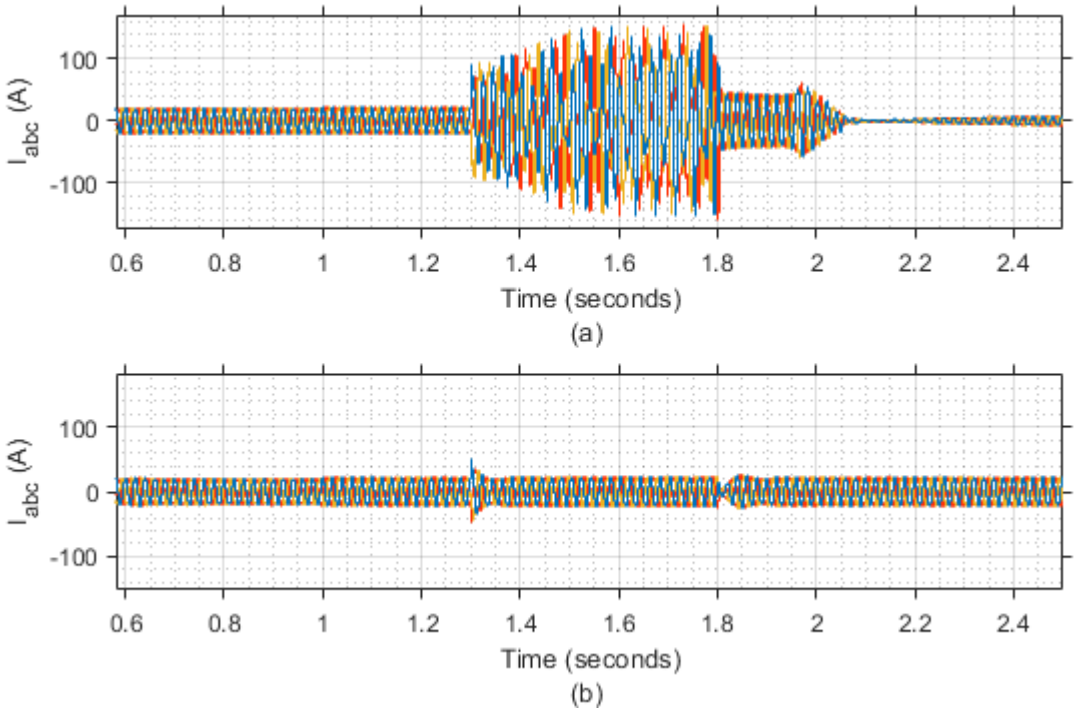

Figure 7. 14:Current at the PCC with and without the proposed secondary control 50% voltage sag

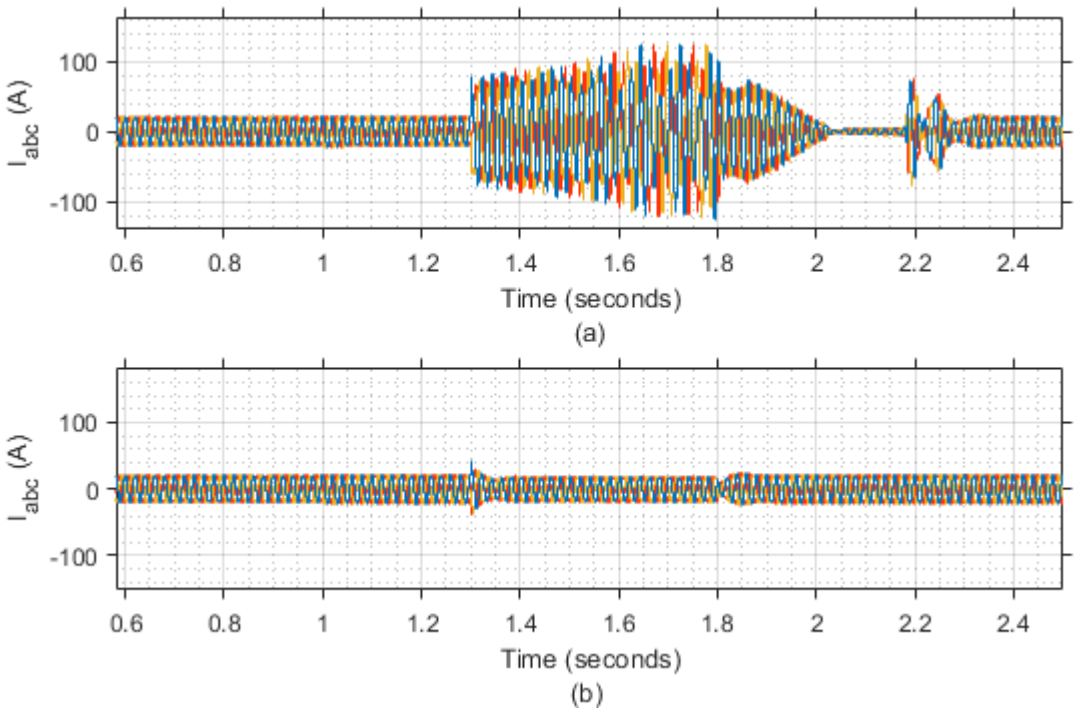

Figure 7. 15:Current at the PCC with and without the proposed secondary control 60% voltage sag

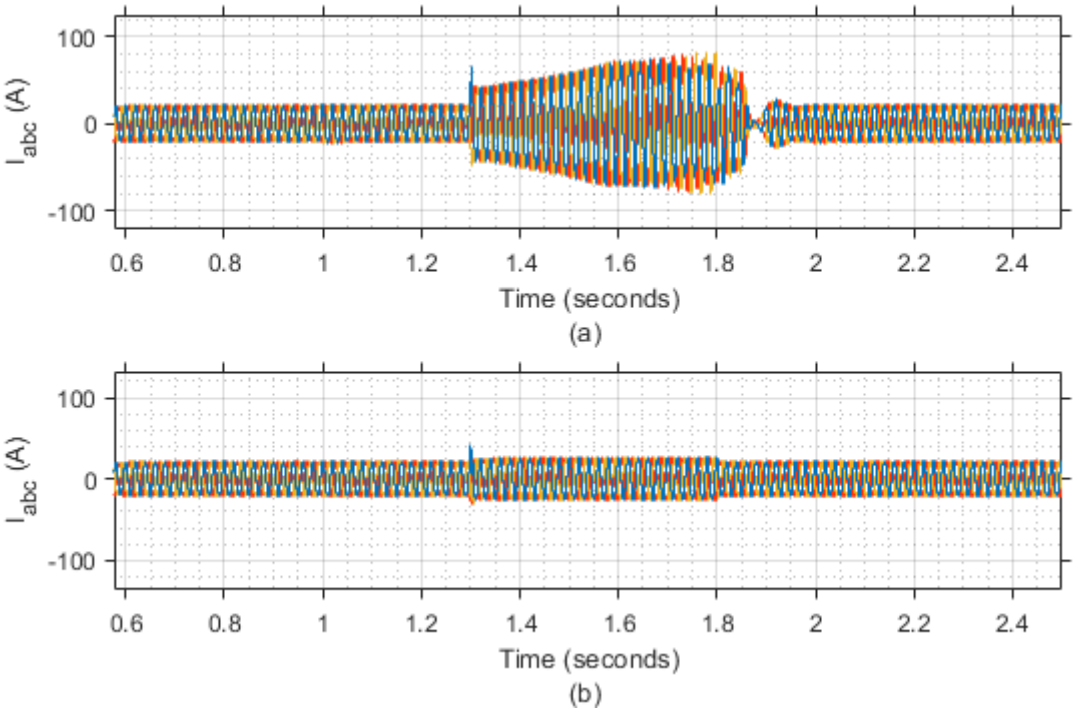

Figure 7. 16:Current at the PCC with and without the proposed secondary control 70% voltage sag

7.2.2.3 PV Inverter Current and Voltage Harmonics

Following the EN50160 standard for all the phases, the THD of any generating unit's output voltage waveforms shall not exceed 8 percent [207]. Subsequently, the THDs (before fault, during

the fault, and after fault clearance for different fault types causing 50 percent and 60 percent voltage sags) of PV voltage signals and output current waveforms are revealed in Table 7.1 and Figures 7.17 and 7.18. The THD is evaluated in MATLAB using a quick analysis of the fast Fourier transformation. As reflected in the low THDs of the PV system output current and voltages, the good signal quality confirms the satisfactory performance of the FRT strategy. As examined, the microgrid voltage display significant-quality waveforms, PV system voltage output, and current. Regarding the output current harmonics, the voltage harmonics are relatively negligible. The reported low THD indicates high efficiency, significant power factor, and low peak current. This demonstrates the efficacy of this proposed FRT approach for secondary control and IEC 61000-3-2 standard compliance [208]

Table 7. 5:Average (THD) of voltage and current waveforms of the DERs.

Voltage Sag	**Signal**	**Total Harmonic Distortion (%)**								
		Pre-Fault			**Fault**			**Post-Fault**		
		L_1	**L_2**	**L_3**	**L_1**	**L_2**	**L_3**	**L_1**	**L_2**	**L_3**
50%	Voltage	0.329	0.321	0.327	1.165	1.160	1.169	0.327	0.322	0.325
	Current	2.007	2.001	2.009	2.149	2.142	2.140	1.982	1.983	1.987
60%	Voltage	0.314	0.312	0.313	1.190	1.192	1.191	0.328	0.320	0.323
	Current	2.059	2.054	2.058	2.056	2.057	2.050	2.083	2.085	2.082
70%	Voltage	0.310	0.315	0.311	1.243	1.249	1.249	0.321	0.328	0.329
	Current	2.052	2.053	2.056	2.045	2.046	2.043	2.099	2.079	2.067

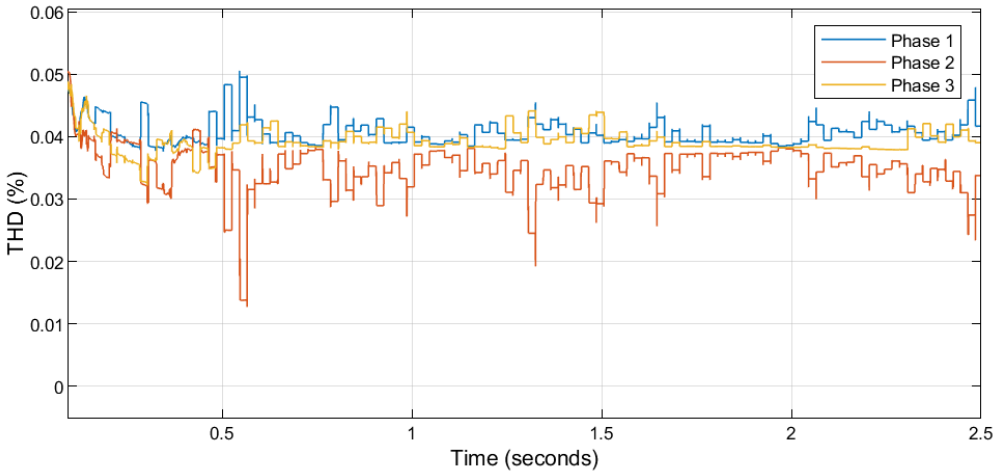

Figure 7. 17:THD at 50 % voltage sag with secondary control

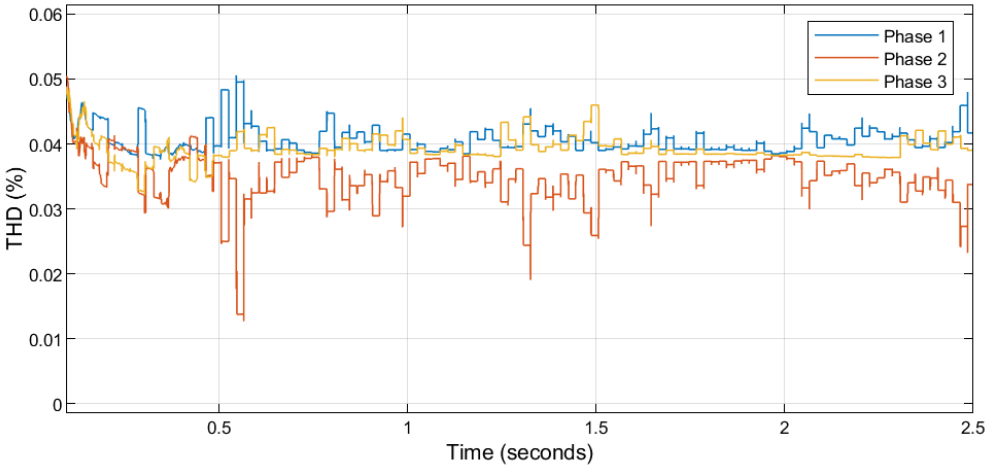

Figure 7. 18:THD at 60 % voltage sag with secondary control

7.2.2.3 Power Generation and Delivery

Following the grid codes, the FRT control structures ensure comparable reactive power is delivered to support grid voltage sag, thus performing a PV system ride through disturbances. The system seamless switch from grid synchronous to an isolated mode of service is therefore prevented. The rise in reactive power requirement restricts active power generation for the PV inverters to comply with the FRT approach's apparent power threshold and inverter ratings. The active power curtailment under 50% voltage sag is Figures 7.19, 7.21, and 7.22. The reactive power injected supports the voltage recovery within the microgrid and at the PCC through the active power generation and reactive power injection per the depth of voltage sag at the PCC. The improved reactive power production ensures the microgrid voltage is controlled to an appropriate voltage magnitude during the fault duration. At the moment t = 1.8 s, the FRT system automatically detects the rise in the main grid voltage to an allowable point of 0.90–1.10 at the PCC. The reactive power injection is thus limited according to the extent of voltage increase, as shown in Figures 7.20, 7.22, and 7.24. Figures 7.19, 7.21, and 7.22 and Figures 7.20, 7.22, and 7.24 indicate the rise in injected reactive capacity, as well as a sharp proportional decrease in active power. This FRT regulation's deployment with the DSC algorithms monitors the main grid disruption using the voltage sag sensed at the PCC. The FRT technique restricts active and reactive references in the PV system as needed to trigger microgrid voltage change without major distortion to the DER output current and voltage waveforms. The active power generated by the PV system under 50%, 60%, and 70% voltage sags are summarized in Table 7. 6. Similarly, the PV's reactive power under 50%, 60%, and 70% voltage sags is shown in Table 7. 7.

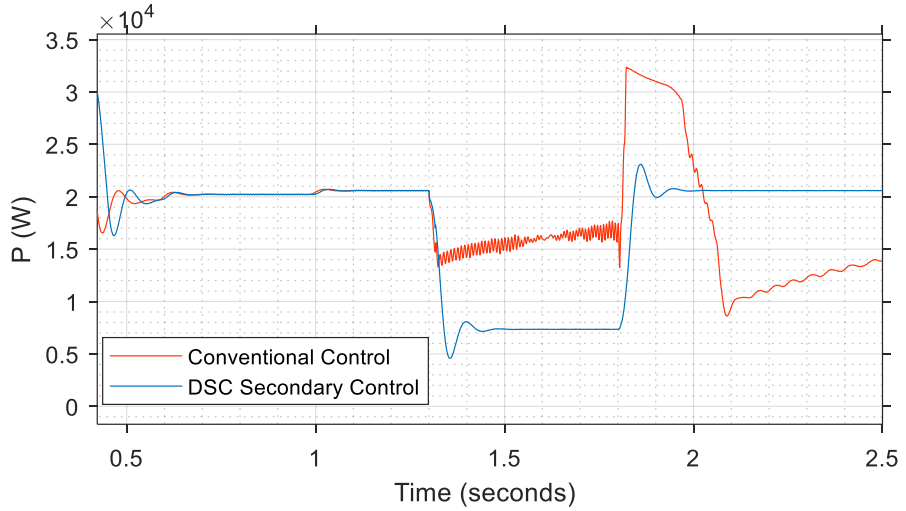

Figure 7. 19:Active Power supplied by PV under voltage sag of 50%

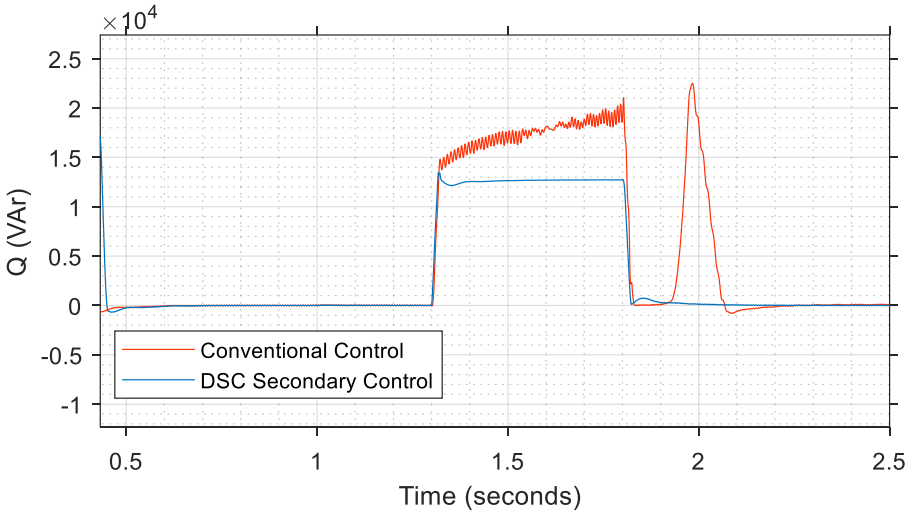

Figure 7. 20:Reactive Power supplied by PV under voltage sag of 50%

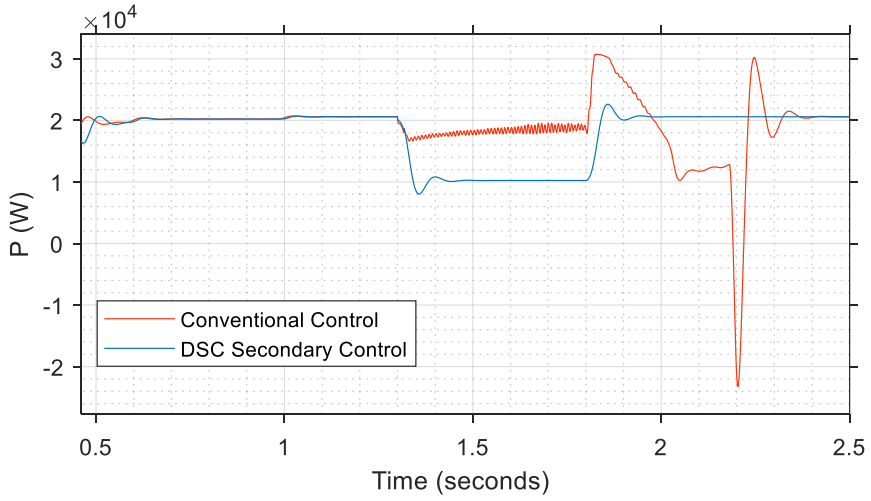

Figure 7. 21:Active Power supplied by PV under voltage sag of 60%

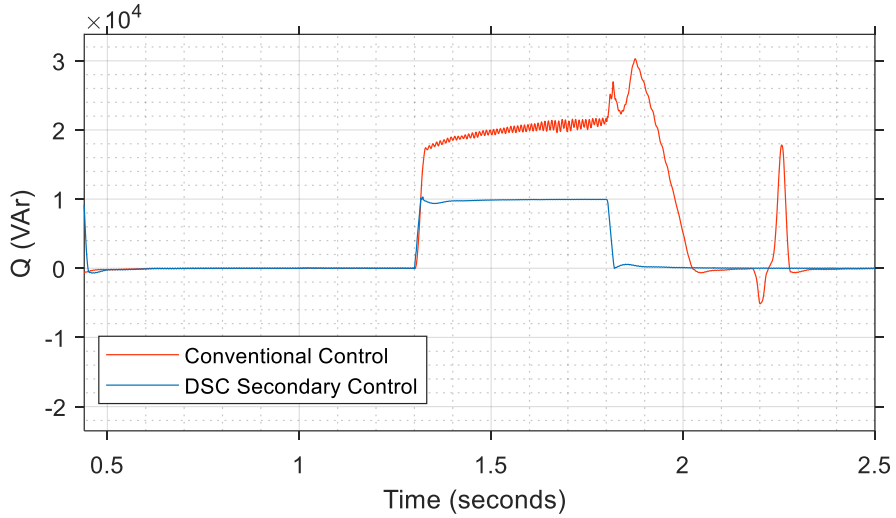

Figure 7. 22:Reactive Power supplied by PV under voltage sag of 60%

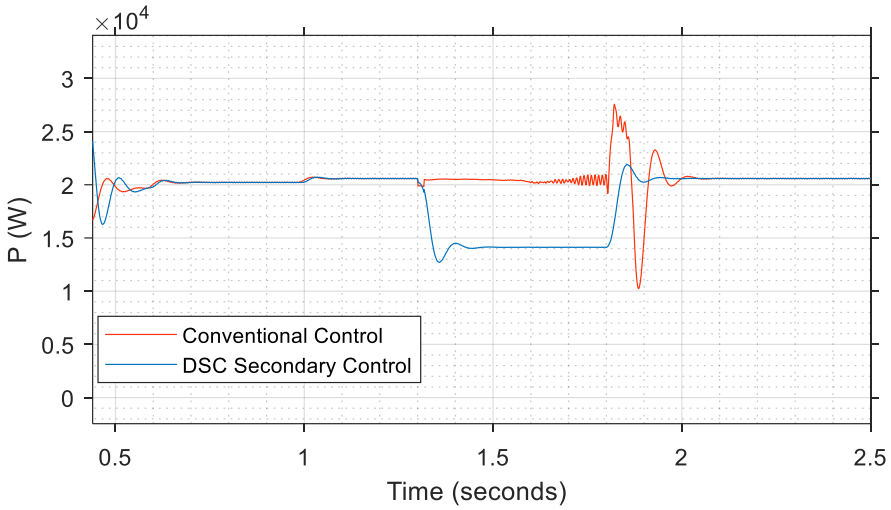

Figure 7. 23:Active Power supplied by PV under voltage sag of 70%

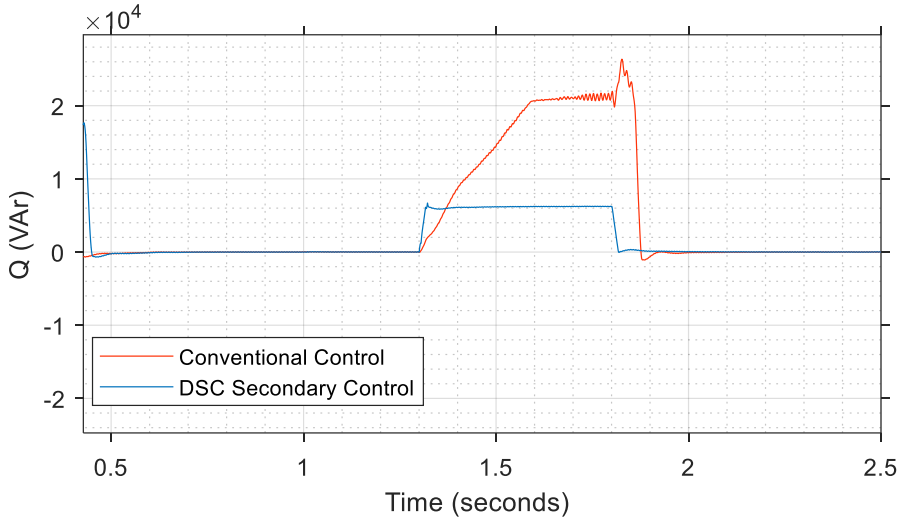

Figure 7. 24:Reactive Power supplied by PV under voltage sag of 70%

Table 7. 6: Active Power P Generation under voltage sag

Time (s)	Active Power P (kW)					
	50% Voltage Sag		60% Voltage Sag		70% Voltage Sag	
	Proposed Secondary Control	Conventional Control	Proposed Secondary Control	Conventional Control	Proposed Secondary Control	Conventional Control
1.30	20.590	20.590	20.600	20.600	20.590	20.590
1.34	07.222	14.580	10.600	16.700	14.380	20.480
1.38	07.101	14.070	09.870	17.100	13.870	20.540
1.42	07.498	15.160	10.400	17.900	14.240	20.530
1.46	07.274	15.030	10.200	18.000	14.080	20.500
1.50	07.364	15.930	10.300	17.700	14.140	20.470
1.54	07.347	16.090	10.200	18.300	14.120	20.450
1.58	07.343	15.930	10.200	17.800	14.120	20.400
1.62	07.356	16.130	10.200	19.000	14.110	20.210
1.66	07.364	16.420	10.200	17.800	14.130	20.320
1.70	07.341	16.640	10.300	17.900	14.120	20.320
1.74	07.339	16.790	10.200	18.100	14.130	19.970
1.78	07.337	16.580	10.200	19.500	14.120	20.890
1.82	09.493	24.990	12.300	27.900	15.470	25.060
1.86	22.960	31.700	22.600	30.300	21.810	24.290
1.90	19.960	31.020	20.100	26.900	20.230	14.120
1.94	20.700	30.440	20.700	23.500	20.680	22.500
1.98	30.560	26.030	20.500	20.100	20.560	19.940
2.02	20.580	21.010	20.600	16.200	20.600	20.770
2.06	20.590	15.840	20.600	10.600	20.590	20.540
2.10	20.590	09.482	20.600	11.700	20.600	20.620
2.14	20.600	10.400	20.600	12.400	20.590	20.590
2.18	20.590	11.030	20.600	12.800	20.590	20.590
2.22	20.600	11.550	20.600	17.600	20.590	20.580
2.26	20.580	12.020	20.600	28.400	20.570	20.570
2.30	20.590	12.280	20.600	17.500	20.590	20.580

Table 7. 7:Reactive Power Q Generation under voltage sag

Time (s)	Reactive Power Q (kVAr)					
	50% Voltage Sag		60% Voltage Sag		70% Voltage Sag	
	Proposed Secondary Control	Conventional Control	Proposed Secondary Control	Conventional Control	Proposed Secondary Control	Conventional Control
1.30	-0.259	-0.279	-02.59	-0.279	-0.026	-0.029
1.34	12.300	15.100	9.470	17.700	5.920	3.030
1.38	12.400	16.000	09.58	18.500	6.003	6.870
1.42	12.500	15.700	09.74	18.700	6.130	9.840
1.46	12.600	17.300	09.81	18.800	6.130	12.100
1.50	12.600	17.000	09.88	20.000	6.160	14.500
1.54	12.700	12.700	09.89	21.100	6.180	17.400
1.58	12.700	17.800	09.91	20.300	6.190	19.900
1.62	12.700	17.800	09.92	20.400	6.200	20.800
1.66	12.700	18.300	09.96	21.000	6.200	20.900

1.70	12.700	18.900	09.94	21.000	6.230	21.200
1.74	12.700	18.600	09.90	21.000	6.220	20.900
1.78	12.400	19.800	09.940	21.200	6.210	21.400
1.82	02.870	08.100	03.150	25.800	-0.040	24.100
1.86	0.684	00.06	00.509	26.100	0.269	20.100
1.90	0.272	00.06	00.249	27.200	0.083	-0.657
1.94	0.274	03.010	00.155	18.500	0.118	0.003
1.98	0.182	22.500	00.127	10.900	0.034	-0.180
2.02	0.142	13.100	00.044	00.636	0.012	0.089
2.06	0.102	01.470	-00.525	00.002	0.004	-0.078
2.10	0.244	-06.27	0.008	-0.297	-0.008	-0.049
2.14	0.004	-03.50	0.005	-0.142	-0.007	-0.053
2.18	-0.005	-01.88	0.005	-0.056	0.039	0.001
2.22	-0.007	-00.83	-0.015	-0.423	-0.002	-0.004
2.26	-0.015	-00.17	-0.027	17.306	-0.026	-0.034
2.30	0.020	00.420	-0.022	-0.588	0.035	0.020

As a result of the voltage sag induced by grid fault, the PV system's total active power supply is reduced. The PV system is controlled to initially inject an active power quantity that satisfies local load demand and thus lessens the active power injection into the faulty main grid, as shown in Figures 7.25, 7.26, 7.27, 7.28, 7.29, and 7.30. The amplitude of the system voltage declined during voltage sags. The fault current's intensity is reduced, and the microgrid voltage is enhanced to transmit the active power to the local load. The active power generated is limited to the rated value of the local load under severe voltage sag. Each time an over-generation happens, the excess is transmitted to the failed system. Nevertheless, no active power can be generated for the local microgrid load and main grid load in the severe occurrence voltage sag. Subsequently, the PV system reactive power output maximizes host system voltage according to Spanish grid codes. The microgrid voltage is regulated within the operating range (0.9–1.1 Spanish grid code) to ensure continuous active power delivery to local sensitive loads, as seen in Figures 7.25, 7.26, 7.27, 7.28, 7.29 and 7.30.

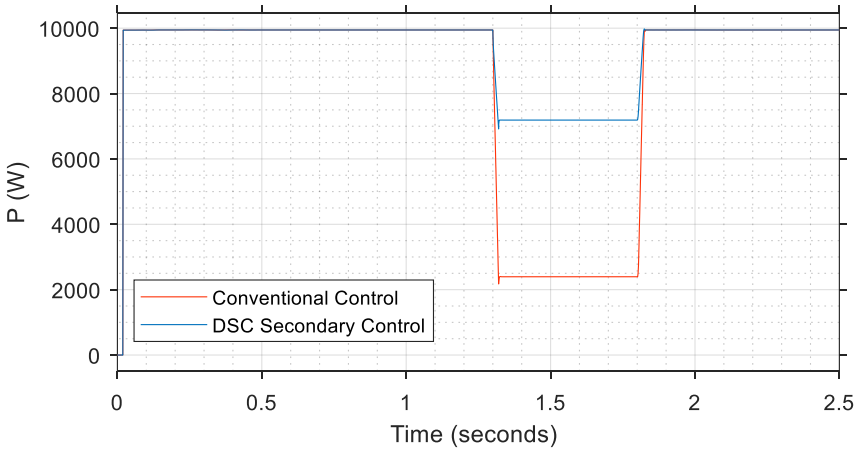

Figure 7. 25: Active power supply to local microgrid load under voltage sag of 50%

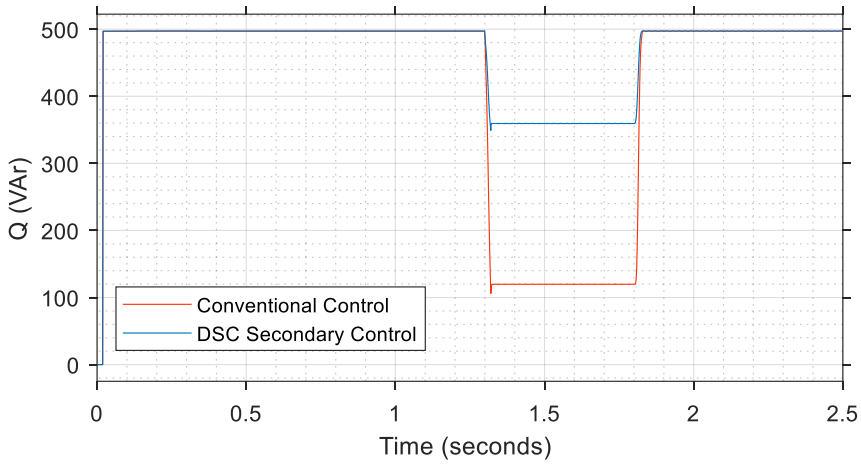

Figure 7. 26: Reactive power supply to local microgrid load under voltage sag of 50%

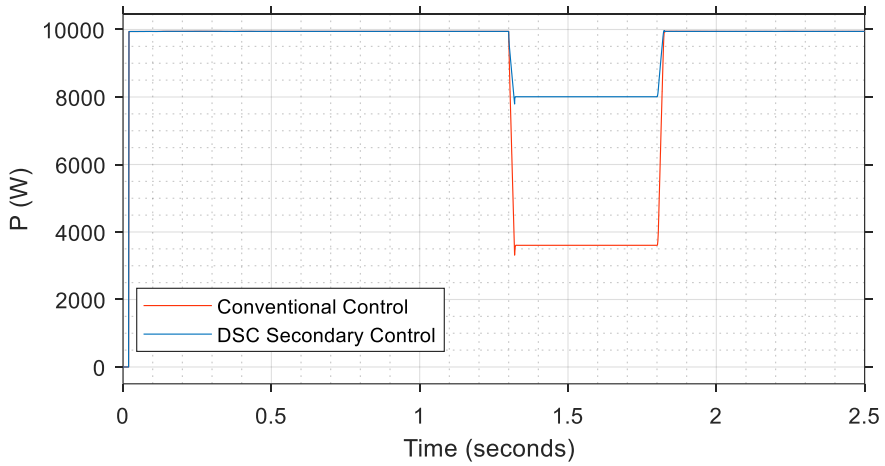

Figure 7. 27:Active power supply to local microgrid load under voltage sag of 60%

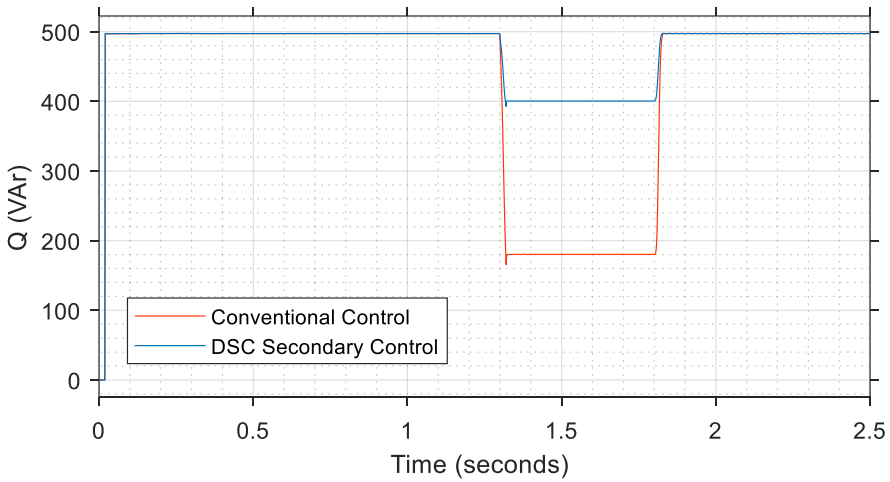

Figure 7. 28: Reactive power supply to local microgrid load under voltage sag of 60%

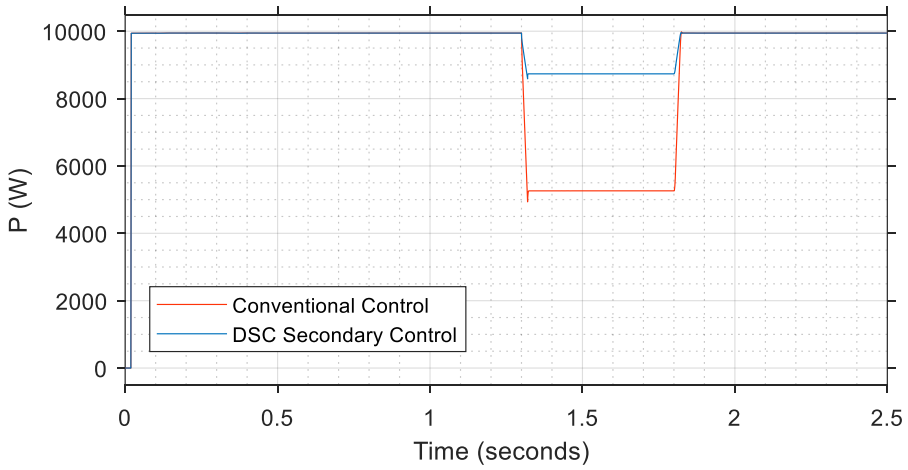

Figure 7. 29:Active power supply to local microgrid load under voltage sag of 70%

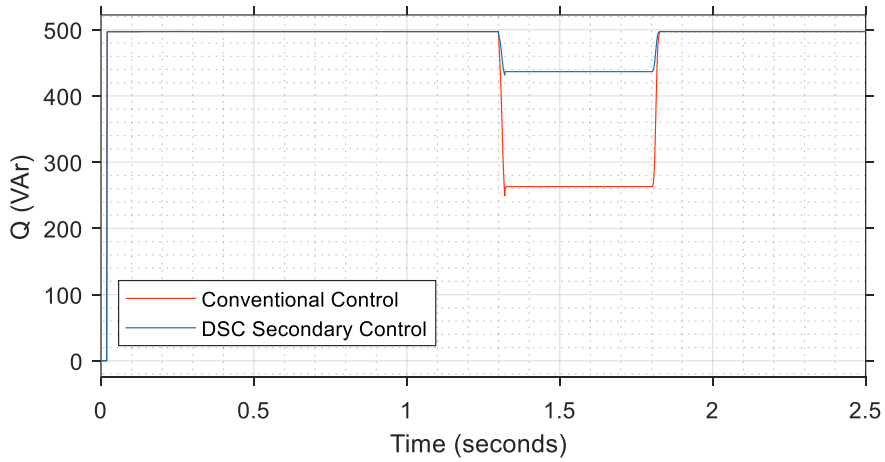

Figure 7. 30: Reactive power supply to local microgrid load under voltage sag of 70%

The active and reactive power consumptions in the local load are summarized in Tables 7.8 and 7.9, respectively.

Table 7. 8:Active Power (kW) Consumption in the Load

Time (s)	**50% Voltage Sag**		**60% Voltage Sag**		**70% Voltage Sag**	
	Proposed Secondary Control	**Conventional Control**	**Proposed Secondary Control**	**Conventional Control**	**Proposed Secondary Control**	**Conventional Control**
1.30	9.944	9.944	9.944	9.944	9.944	9.944
1.31	8.277	5.921	8.748	6.456	9.182	7.251
1.32	6.917	2.176	7.792	3.316	8.586	4.934
1.33	7.188	2.396	8.008	3.605	8.734	5.260
1.80	7.188	2.395	8.007	3.606	8.734	5.261
1.81	8.288	4.842	8.801	5.803	9.241	7.007
1.82	9.655	8.613	9.761	8.963	9.840	9.336
1.83	9.944	9.945	9.944	9.947	9.944	9.947
1.84	9.944	9.945	9.944	9.947	9.944	9.947

Table 7. 9: Reactive Power (VAr) Consumption in the Load

	50% Voltage Sag		60% Voltage Sag		70% Voltage Sag	
Time (s)	**Proposed Secondary Control**	**Conventional Control**	**Proposed Secondary Control**	**Conventional Control**	**Proposed Secondary Control**	**Conventional Control**
1.30	497.2	497.2	497.2	497.2	497.2	497.2
1.31	421.1	311.1	442.6	336.9	462.5	374.0
1.32	349.1	106.2	392.5	165.7	431.5	249.1
1.33	359.4	119.7	400.4	180.2	436.7	263.0
1.80	359.4	119.8	400.4	180.3	436.7	263.1
1.81	387.3	162.9	421.1	225.2	450.3	303.4
1.82	483.6	483.3	488.4	453.8	492.1	469.8
1.83	497.3	497.5	497.3	497.6	497.3	497.5
1.84	497.1	497.0	497.1	497.2	497.2	497.2

7.3. Conclusion

To summarize the proposition implemented in the chapter and by extension, this thesis, Figure 7.31, appropriately depicts a grid-supporting solar PV system's trajectories interfaced with the main grid via DC-DC and DC-AC converters during a fault in the grid. The seamlessly switching is achieved between the MPPT (normal operating condition) and FRT (fault operating condition) operating modes with fast dynamics.

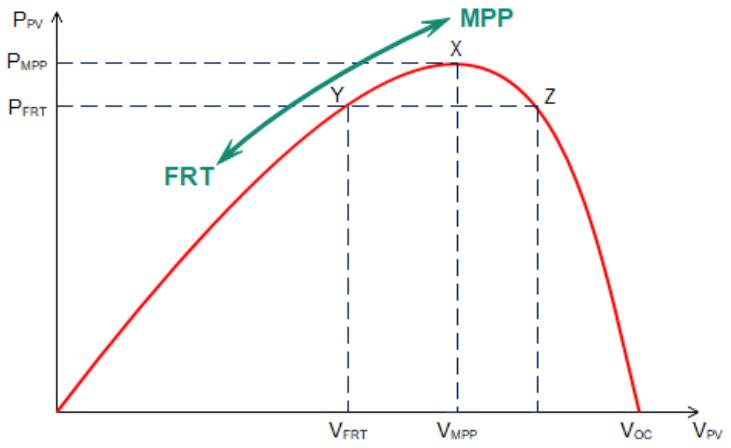

Figure 7. 31; The seamless switching between MPP and FRT operation based on P-V characteristics

The primary and the proposed secondary control for the double stage PV sourced microgrid implements an FRT using the DSC fault detection algorithm. Strategic amendments to the traditional primary control system of a grid-supporting system are made. This controller is designed as per the Spanish grid codes stipulations for reactive power injection in achieving a secondary voltage control with an operation that is valid and significant in the transient fault period. The injected reactive power complies with the required reactive currents based on the percentage voltage drop as specified in the emerging grid codes under different depths of voltage

sags caused by faults. This scheme prevents the transient AC overcurrent in the microgrid and DC link overvoltage during the AC grid fault. Simultaneously, the DC side over-voltage and AC side over-current are mitigated through active power decrease and current amplitude curtailing strategies in compliance with the complex/apparent power ratings. The DSC algorithms allow for separating the sequence components for dual control at the PCC of the positive-sequence and negative-sequence components during the primary grid disturbance.

The continuous supply to microgrid local sensitive load is ensured while meeting the grid code FRT requirement. Furthermore, the control of DC generated power and, by extension, the AC grid active power transmitted is linked to the depth of voltage dip the AC grid. The active power control is based on a droop relationship between these two parameters, and the inverse proportionate relationship and requirements are exploited in the development of the proposed shift in the operating point of the MPPT from MPP to FRT operation. To identify negative sequences and instances of fault in 0.1515 ms, the DSC's sequence identification algorithm is applied to enable the proposed secondary FRT scheme to conform to the grid code stipulations. The DSC detects the grid restoration after fault clearance, and the system switches back to the normal MPPT operating condition.

CHAPTER EIGHT

CONCLUSION AND RECOMMENDATION

8.1 Conclusion

The conclusions of this thesis are as follows:

- With the ever-increasing penetration of RESs, RESs must possess dynamic characteristics and resilience proposed in this work as their disconnection portends a critical system instability.
- The existing microgrid's hierarchical control structure can be leveraged to address the FRT challenges in grid supporting inverter-based microgrids. The secondary FRT system provides power injection reference and dynamic voltage supports for the inverter-based systems' primary control using the droop interface. The implementation should be in strict compliance with the grid code requirements, apparent power limits, and technical stipulations for the power inverters.
- The grid voltage monitoring and prompt sag detection of fault are crucial as the system's control, compensation, active power curtailment, dynamic voltage supports, and FRT. Thus, a fast DSC algorithm detects a fault and injects the commensurate amount of reactive current for grid supports per the depth of voltage sag under the Grid Codes. The DSC detects the grid restoration after fault clearance, and the system switches back to the normal MPPT operating condition. The DSC algorithms allow for separating the sequence components for dual control at the PCC of the positive-sequence and negative-sequence components during a disturbance in the main grid.
- The secondary control level is essential to coordinate the primary control activities and sets prompt references for effective transient operations, especially under faults. The reference current generated at any point in time, especially under the FRT operation, does not comprise the inverter system protections for both overvoltage and overcurrent by incessant triggering. This prevents the transient AC overcurrent and DC link overvoltage under the AC grid fault. Simultaneously, the DC side over-voltage and AC side over-current can be mitigated through active power decrease, and current amplitude curtailment approaches in compliance with the apparent power ratings.
- The conventional MPPT operating limit should be shifted to another point other than the MPP for efficient FRT mode operation in an inverter-based system with a DC-DC converter. The FRT point presented is a non-MPP mode that ensured that the PV voltage is brought down to the required value, which corresponds to a particular active power value. This active power value corresponds to a value required to ensure compliance with

the complex power limit when a given reactive current is injected into the grid for grid support purposes.

- Before developing an FRT scheme for a grid-supporting system, it is imperative to put an efficient model for valid investigation in place. The grid forming and grid feeding models provided a veritable platform for a grid supporting system development with essential dynamic features and study investigation, and efficient power-sharing, using droop controls. Furthermore, this droop is implemented in a PV system with an MPPT control for its DC-DC converter to participate in grid frequency and voltage regulation between the outer loop DC link voltage control and inner current loop control.
- The maintenance of the qualitative power supply to the local microgrid load is critical at all times, and this forms one of the design goals of the secondary FRT scheme. Consequently, irrespective of the transient main grid condition, the scheme ensures protection from grid voltage dip's adverse effects and the continuous supply to microgrid local sensitive load. The switched inductance significantly alleviates this; thus, the local load's load requirements are met irrespective of transient grid condition.
- Furthermore, the inductance's switching under fault provides an improved value for the *X/R* ratio, which enhanced the reactive power injection into the main grid. As a result of the low *X/R* ratio of the feeder line between the inverter-based microgrid PCC and the main grid, the reactive power injection may not be efficient. The injection may not significantly influence the grid voltage recovery. The proposed IGBT switched inductance increased the *X/R* ratio under fault. The switched inductance behaves as an open circuit under the normal operating mode, which does not hamper active power export into the main utility grid under normal operating conditions. This controller performance is further enhanced with an IGBT-diode switched AC reactor to improve the voltage and prevent the transient overcurrent in the microgrid during the grid fault.
- The inverters' complex/apparent power ratings must be taken into strict consideration for effective fault ride-through and system protection schemes. The grid codes necessarily do not demand the limitation or reduction in the active power generated under fault. However, the complex/apparent power limit must not be exceeded to avoid activation of the protection scheme and the inverter's disconnection.
- The control of generated RES power can be linked to the AC grid voltage dip depth for FRT operation. The active power control is based on a droop relationship between these two parameters, and the inverse proportionate relationship and requirements are exploited in the development of the proposed strategy. The seamlessly switching is achieved between the MPPT (normal operating condition) and FRT (fault operating condition) operating modes with fast dynamics.

8.2 Recommendations and Future Works

The following areas are suggested for future work:

- The droop control scheme offers no inertia support expected. Consequently, the virtual synchronous generator control method is recommended in place of droop control. Before this, the impact of the droop control's inadequacies must first be investigated on the fault ride-through capabilities to establish the need for a more robust artificial inertia. Virtual inertia schemes permit the synthetic imitation of synchronous generators' steady-state and dynamic characteristics by the converters.
- Consequently, this work recommends a review and amendment of the existing national grid codes' standards and requirements for DER systems and renewable energy-based microgrids to comply with some of the features developed for better and efficient grid integration.
- This work can be extended to an inverter-based microgrid with a grid supporting grid forming dynamic attributes. This system makes use of a virtual impedance emulated in its loop. Similarly, incorporating the DC-DC converter validates the proposed scheme's effectiveness on an ideal DC energy source such as PV arrays. Similarly, virtual impedance can be exploited and used to replace the IGBT switched inductance proposed in this work. Consequently, the need for an additional cost is removed.
- The investigation and comparative analysis of fast Delayed Signal Cancellation algorithm for DERs control and coordination to fulfil FRT in a centralized, distributed, and decentralized secondary control arrangement in an AC Microgrid.

REFERENCES

[1] E. Buraimoh, I. E. Davidson, and F. Martinez-Rodrigo, "Fault Ride-Through Enhancement of Grid Supporting Inverter-Based Microgrid Using Delayed Signal Cancellation Algorithm Secondary Control," *Energies*, vol. 12, no. 20, p. 3994, Oct. 2019.

[2] E. Buraimoh and I. E. Davidson, "Fault Ride - Through Analysis of Current and Voltage Source - Models of Grid Supporting Inverter - Based Microgrid," *IEEE Canadian Journal of Electrical and Computer Engineering/Journal canadien de genie electrique et informatique*, vol. 44, no. 1, pp. 1–10, 2020.

[3] E. Buraimoh and I. E. Davidson, "Investigation of the Low Voltage Ride-Through of Inverter Using Virtual Inertia Methods in Microgrid," *International Journal of Engineering Research in Africa*, vol. 44, no. 1, pp. 200–212, 2019.

[4] E. Buraimoh, F. K. Ariyo, M. O. Omoigui, and I. E. Davidson, "Investigation of Combined SVC and TCSC Versus IPFC in Enhancing Power System Static Security," *International Journal of Engineering Research in Africa*, vol. 40, pp. 119–135, 2018.

[5] E. Buraimoh and I. E. Davidson, "Modelling and Assessment of the Fault Ride- Through Capabilities of Grid Supporting Inverter- Based Microgrids," in *Clemson University Power Systems Conference (PSC 2020)*, 2020, pp. 1–7.

[6] E. Buraimoh and I. E. Davidson, "Modeling and Analysis of Standalone Inverter-Based Microgrid with Grid-Supporting Voltage-Source Control under Changing Load," in *2020 IEEE PES/IAS PowerAfrica*, 2020, pp. 1–5.

[7] E. Buraimoh and I. E. Davidson, "Comparative Analysis of the Fault Ride-Through Capabilities of the VSG Methods of Microgrid Inverter Control under Faults," in *Proceedings - 2019 Southern African Universities Power Engineering Conference/Robotics and Mechatronics/Pattern Recognition Association of South Africa, SAUPEC/RobMech/PRASA*, 2019, pp. 400–405.

[8] E. Buraimoh and I. E. Davidson, "Development of an IGBT-Diode based Fault Current Limiter for Fault Ride-Through Enhancement in Microgrid Application," in *IEEE PES/IAS PowerAfrica*, 2019, pp. 190–195.

[9] E. Buraimoh, F. K. Ariyo, and I. E. Davidson, "Power System Static Security Enhancement Through Interline Power Flow Controller," in *IEEE PES & IAS Power Africa Conference*, 2018, pp. 1–6.

[10] E. Kianmehr, S. Nikkhah, V. Vahidinasab, D. Giaouris, and P. C. Taylor, "A Resilience-Based Architecture for Joint Distributed Energy Resources Allocation and Hourly Network Reconfiguration," *IEEE Transactions on Industrial Informatics*, vol. 15, no. 10, pp. 5444–5455, 2019.

[11] O. Palizban and K. Kauhaniemi, "Hierarchical control structure in microgrids with

distributed generation: Island and grid-connected mode," *Renewable and Sustainable Energy Reviews*, vol. 44, pp. 797–813, 2015.

[12] S. Vadi, S. Padmanaban, R. Bayindir, F. Blaabjerg, and L. Mihet-Popa, "A Review on Optimization and Control Methods Used to Provide Transient Stability in Microgrids," *Energies*, vol. 12, no. 18, p. 3582, Sep. 2019.

[13] R. Viral and D. K. Khatod, "Optimal planning of distributed generation systems in distribution system: A review," *Renewable and Sustainable Energy Reviews*, vol. 16, no. 7, pp. 5146–5165, Sep. 2012.

[14] H. A. Saleem, "Microgrid Modeling and Grid Interconnection Studies," 2014.

[15] K. Rahbar, C. C. Chai, and R. Zhang, "Energy cooperation optimization in microgrids with renewable energy integration," *IEEE Transactions on Smart Grid*, vol. 9, no. 2, pp. 1482–1493, 2018.

[16] X. Lu, J. Wang, S. Member, and J. M. Guerrero, "Virtual Impedance Based Fault Current Limiters for Inverter Dominated AC Microgrids," *IEEE Transaction on Smart Grid*, vol. 3053, no. 6, pp. 1599–1612, 2018.

[17] B. Kroposki, C. Pink, R. DeBlasio, H. Thomas, M. Simões, and P. K. Sen, "Benefits of Power Electronic Interfaces for Distributed Energy Systems," *IEEE Transactions on Energy Conversion*, vol. 25, no. 3, pp. 901–908, Sep. 2010.

[18] S. I. Gkavanoudis and C. S. Demoulias, "A Control Strategy for Enhancing the Fault Ride-Through Capability of a Microgrid During Balanced and Unbalanced Grid Voltage Sags," *Sustainable Energy, Grids and Networks*, vol. 3, pp. 1–11, 2015.

[19] A. Q. Al-Shetwi, M. A. Hannan, K. P. Jern, M. Mansur, and T. M. I. Mahlia, "Grid-connected renewable energy sources: Review of the recent integration requirements and control methods," *Journal of Cleaner Production*, vol. 253, p. 119831, Apr. 2020.

[20] Y. Yang, P. Enjeti, F. Blaabjerg, and H. Wang, "Wide-scale adoption of photovoltaic energy: Grid code modifications are explored in the distribution grid," *IEEE Industry Applications Magazine*, vol. 21, no. 5, pp. 21–31, Sep. 2015.

[21] E. Buraimoh and I. E. Davidson, "Comparative Analysis of the Fault Ride-Through Capabilities of the VSG Methods of Microgrid Inverter Control under Faults," in *SAUPEC/RobMech/PRASA 2019*, 2019, pp. 400–405.

[22] T. Kerdphol, F. S. Rahman, and Y. Mitani, "Virtual inertia control application to enhance frequency stability of interconnected power systems with high renewable energy penetration," *Energies*, vol. 11, no. 4, 2018.

[23] X. Xu, Z. Yan, M. Shahidehpour, H. Wang, and S. Chen, "Power System Voltage Stability Evaluation Considering Renewable Energy With Correlated Variabilities," *IEEE Transactions on Power Systems*, vol. 33, no. 3, pp. 3236–3245, 2018.

[24] M. J. Morshed and A. Fekih, "A Novel Fault Ride Through Scheme for Hybrid Wind/PV

Power Generation Systems," *IEEE Transactions on Sustainable Energy*, vol. PP, no. c, pp. 1–1, 2019.

[25] K. V. Ramana Reddy, N. Ramesh Babu, and P. Sanjeevikumar, "A Review on Grid Codes and Reactive Power Management in Power Grids with WECS," Springer, Singapore, 2018, pp. 525–539.

[26] X. Zhao, J. M. Guerrero, M. Savaghebi, J. C. Vasquez, X. Wu, and K. Sun, "Low-Voltage Ride-Through Operation of Power Converters in Grid-Interactive Microgrids by Using Negative-Sequence Droop Control," vol. 32, no. 4, pp. 3128–3142, 2017.

[27] Y. Yang, K. A. Kim, F. Blaabjerg, and A. Sangwongwanich, "Advanced control of PV systems under anomaly grid conditions," in *Advances in Grid-Connected Photovoltaic Power Conversion Systems*, 1st ed., Cambridge: Woodhead Publishing, 2018, pp. 113–152.

[28] X. Wang, Z. Yang, B. Fan, and W. Xu, "Control Strategy of Three-Phase Photovoltaic Inverter under Low-Voltage Ride-Through Condition," *Mathematical Problems in Engineering*, vol. 2015, pp. 1–23, 2015.

[29] Y. Bae, T. K. Vu, and R. Y. Kim, "Implemental control strategy for grid stabilization of grid-connected PV system based on German grid code in symmetrical low-to-medium voltage network," *IEEE Transactions on Energy Conversion*, vol. 28, no. 3, pp. 619–631, 2013.

[30] A. Molina-García, A. Honrubia-Escribano, T. García-Sánchez, E. Gómez-Lázaro, and E. Muljadi, "Power quality surveys of photovoltaic power plants: characterisation and analysis of grid-code requirements," *IET Renewable Power Generation*, vol. 9, no. 5, pp. 466–473, Jul. 2015.

[31] Y. Yang, P. Enjeti, F. Blaabjerg, and H. Wang, "Suggested grid code modifications to ensure wide-scale adoption of photovoltaic energy in distributed power generation systems," in *Conference Record - IAS Annual Meeting (IEEE Industry Applications Society)*, 2013, pp. 1–8.

[32] M. Tarafdar Hagh and T. Khalili, "A review of fault ride through of PV and wind renewable energies in grid codes," *International Journal of Energy Research*, vol. 43, no. 4, pp. 1342–1356, Mar. 2019.

[33] P. H. A. Barra, D. V. Coury, and R. A. S. Fernandes, "A survey on adaptive protection of microgrids and distribution systems with distributed generators," *Renewable and Sustainable Energy Reviews*, vol. 118, no. June 2019, p. 109524, 2020.

[34] M. A. Hossain, H. R. Pota, M. J. Hossain, and F. Blaabjerg, "Evolution of microgrids with converter-interfaced generations: Challenges and opportunities," *International Journal of Electrical Power and Energy Systems*, vol. 109, no. February, pp. 160–186, 2019.

[35] E. Yildirim, Ş. Saraç, and A. Aslan, "Energy consumption and economic growth in the

USA: Evidence from renewable energy," *Renewable and Sustainable Energy Reviews*, vol. 16, no. 9, pp. 6770–6774, 2012.

[36] P. N. P. Barbeiro *et al.*, "Sizing and siting static synchronous compensator devices in the Portuguese transmission system for improving system security," *IET Generation, Transmission and Distribution*, vol. 9, no. 10, pp. 957–965, 2015.

[37] M. Alberdi, M. Amundarain, A. J. Garrido, I. Garrido, and F. J. Maseda, "Fault-ride-through capability of oscillating-water-column-based wave-power-generation plants equipped with doubly fed induction generator and airflow control," *IEEE Transactions on Industrial Electronics*, vol. 58, no. 5, pp. 1501–1517, 2011.

[38] Y. A. R. I. Mohamed and A. A. Radwan, "Hierarchical control system for robust microgrid operation and seamless mode transfer in active distribution systems," *IEEE Transactions on Smart Grid*, vol. 2, no. 2, pp. 352–362, 2011.

[39] S. M. Ashabani and Y. A. R. I. Mohamed, "A flexible control strategy for grid-connected and islanded microgrids with enhanced stability using nonlinear microgrid stabilizer," *IEEE Transactions on Smart Grid*, vol. 3, no. 3, pp. 1291–1301, 2012.

[40] G. Pepermans, J. Driesen, D. Haeseldonckx, R. Belmans, and W. D'haeseleer, "Distributed generation: Definition, benefits and issues," *Energy Policy*, vol. 33, no. 6, pp. 787–798, 2005.

[41] A. G. Anastasiadis, G. P. Kondylis, and G. A. Vokas, "Effect of augmented distributed generation in distribution networks," *Energy Reports*, no. September, 2019.

[42] V. Das, S. Padmanaban, K. Venkitusamy, R. Selvamuthukumaran, F. Blaabjerg, and P. Siano, "Recent advances and challenges of fuel cell based power system architectures and control – A review," *Renewable and Sustainable Energy Reviews*, vol. 73, no. November 2016, pp. 10–18, 2017.

[43] P. C. Sekhar and S. Mishra, "Storage Free Smart Energy Management for Frequency Control in a Diesel-PV-Fuel Cell-Based Hybrid AC Microgrid," *IEEE Transactions on Neural Networks and Learning Systems*, vol. 27, no. 8, pp. 1657–1671, 2016.

[44] J. Peirs, D. Reynaerts, and F. Verplaetsen, "A microturbine for electric power generation," *Sensors and Actuators, A: Physical*, vol. 113, no. 1, pp. 86–93, Jun. 2004.

[45] P. A. Pilavachi, "Mini- and micro-gas turbines for combined heat and power," *Applied Thermal Engineering*, vol. 22, no. 18, pp. 2003–2014, 2002.

[46] D. Papadaskalopoulos, D. Pudjianto, and G. Strbac, "Decentralized coordination of microgrids with flexible demand and energy storage," *IEEE Transactions on Sustainable Energy*, vol. 5, no. 4, pp. 1406–1414, 2014.

[47] J. Xiao, P. Wang, and L. Setyawan, "Multilevel Energy Management System for Hybridization of Energy Storages in DC Microgrids," *IEEE Transactions on Smart Grid*, vol. 7, no. 2, pp. 847–856, 2016.

[48] A. Naderipour, M. R. Miveh, and J. M. Guerrero, *Grid-Connected Inverter for Distributed Generation in Microgrid*, no. 7. 2017.

[49] U. Tamrakar, D. Shrestha, M. Maharjan, B. P. Bhattarai, T. M. Hansen, and R. Tonkoski, "Virtual inertia: Current trends and future directions," *Applied Sciences (Switzerland)*, vol. 7, no. 7, pp. 1–29, 2017.

[50] J. M. Guerrero, L. GarciadeVicuna, J. Matas, M. Castilla, and J. Miret, "A Wireless Controller to Enhance Dynamic Performance of Parallel Inverters in Distributed Generation Systems," *IEEE Transactions on Power Electronics*, vol. 19, no. 5, pp. 1205–1213, Sep. 2004.

[51] A. M. Roslan, K. H. Ahmed, S. J. Finney, and B. W. Williams, "Improved Instantaneous Average Current-Sharing Control Scheme for Parallel-Connected Inverter Considering Line Impedance Impact in Microgrid Networks," *IEEE Transactions on Power Electronics*, vol. 26, no. 3, pp. 702–716, Mar. 2011.

[52] T. Caldognetto and P. Tenti, "Microgrids Operation Based on Master–Slave Cooperative Control," *IEEE Journal of Emerging and Selected Topics in Power Electronics*, vol. 2, no. 4, pp. 1081–1088, Dec. 2014.

[53] C. N. Papadimitriou, E. I. Zountouridou, and N. D. Hatziargyriou, "Review of hierarchical control in DC microgrids," *Electric Power Systems Research*, vol. 122, pp. 159–167, May 2015.

[54] U. B. Tayab, M. A. Bin Roslan, L. J. Hwai, and M. Kashif, "A review of droop control techniques for microgrid," *Renewable and Sustainable Energy Reviews*, vol. 76, no. 5, pp. 717–727, 2017.

[55] J. Jia, G. Yang, A. H. Nielsen, and P. Rønne-Hansen, "Study of control strategies of power electronics during faults in microgrids," in *Hybrid-renewable energy systems in microgrids: Integration, developments and control*, Elsevier Ltd, 2018, pp. 109–146.

[56] J. Rocabert, A. Luna, F. Blaabjerg, and P. Rodriguez, "Control of Power Converters in AC Microgrids," *IEEE Transactions on Power Electronics*, vol. 27, no. 11, pp. 4734–4749, 2012.

[57] G. K. Venayagamoorthy, R. K. Sharma, P. K. Gautam, and A. Ahmadi, "Dynamic Energy Management System for a Smart Microgrid," *IEEE Transactions on Neural Networks and Learning Systems*, vol. 27, no. 8, pp. 1643–1656, 2016.

[58] N. Pogaku, M. Prodanović, and T. C. Green, "Modeling, analysis and testing of autonomous operation of an inverter-based microgrid," *IEEE Transactions on Power Electronics*, vol. 22, no. 2, pp. 613–625, 2007.

[59] N. A. Ahmed, M. Miyatake, and A. K. Al-Othman, "Power fluctuations suppression of stand-alone hybrid generation combining solar photovoltaic/wind turbine and fuel cell systems," *Energy Conversion and Management*, vol. 49, no. 10, pp. 2711–2719, 2008.

[60] A. Mehrizi-Sani and R. Iravani, "Potential-function based control of a microgrid in islanded and grid-connected modes," *IEEE Transactions on Power Systems*, vol. 25, no. 4, pp. 1883–1891, 2010.

[61] S. Adhikari and F. Li, "Coordinated V-f and P-Q control of solar photovoltaic generators with MPPT and battery storage in microgrids," *IEEE Transactions on Smart Grid*, vol. 5, no. 3, pp. 1270–1281, 2014.

[62] I. Sadeghkhani, G. S. Member, M. Esmail, and H. Golshan, "A Current Limiting Strategy to Improve Fault Ride-Through of Inverter Interfaced Autonomous Microgrids," *IEEE Transaction on Smart Grid*, vol. 8, no. 5, pp. 2138–2148, 2017.

[63] H. R. Baghaee, M. Mirsalim, G. B. Gharehpetian, and H. A. Talebi, "A new current limiting strategy and fault model to improve fault ride-through capability of inverter interfaced DERs in autonomous microgrids," *Sustainable Energy Technologies and Assessments*, vol. 24, pp. 71–81, Dec. 2017.

[64] A. Bidram and A. Davoudi, "Hierarchical Structure of Microgrids Control System," *IEEE Transactions on Smart Grid*, vol. 3, no. 4, pp. 1963–1976, 2012.

[65] O. Palizban, K. Kauhaniemi, and J. M. Guerrero, "Microgrids in active network management—Part I: Hierarchical control, energy storage, virtual power plants, and market participation," *Renewable and Sustainable Energy Reviews*, vol. 36, pp. 428–439, Aug. 2014.

[66] A. Bidram and A. Davoudi, "Hierarchical structure of microgrids control system," *IEEE Transactions on Smart Grid*, vol. 3, no. 4, pp. 1963–1976, 2012.

[67] L. Hassaine, E. Olias, J. Quintero, and V. Salas, "Overview of power inverter topologies and control structures for grid connected photovoltaic systems," *Renewable and Sustainable Energy Reviews*, vol. 30, pp. 796–807, 2014.

[68] J. Rocabert, A. Luna, F. Blaabjerg, and P. Rodrıguez, "Control of Power Electronic Converters in AC Microgrid," *IEEE Transactions on Power Electronics*, vol. 27, no. 11, pp. 329–355, 2012.

[69] F. Blaabjerg, R. Teodorescu, M. Liserre, and A. V. Timbus, "Overview of control and grid synchronization for distributed power generation systems," *IEEE Transactions on Industrial Electronics*, vol. 53, no. 5. pp. 1398–1409, Oct-2006.

[70] Y. Yang, K. A. Kim, F. Blaabjerg, and A. Sangwongwanich, "Power electronic technologies for PV systems," in *Advances in Grid-Connected Photovoltaic Power Conversion Systems*, 2019, pp. 15–43.

[71] X. Wang, X. Lu, B. Liu, D. Chen, Y. Tong, and G. Shen, "Flexible energy-storage devices: Design consideration and recent progress," *Advanced Materials*, vol. 26, no. 28, pp. 4763–4782, 2014.

[72] M. Savaghebi, A. Jalilian, J. C. Vasquez, and J. M. Guerrero, "Secondary control for

voltage quality enhancement in microgrids," *IEEE Transactions on Smart Grid*, vol. 3, no. 4, pp. 1893–1902, 2012.

[73] C. Ahumada, R. Cárdenas, D. Sáez, and J. M. Guerrero, "Secondary Control Strategies for Frequency Restoration in Islanded Microgrids With Consideration of Communication Delays," *IEEE Transactions on Smart Grid*, vol. 7, no. 3, pp. 1430–1441, 2016.

[74] A. M. Salamah, S. J. Finney, and B. W. Williams, "Three-phase phase-lock loop for distorted utilities," *IET Electric Power Applications*, vol. 1, no. 6, p. 937, 2007.

[75] M. Mao, P. Jin, N. D. Hatziargyriou, and L. Chang, "Multiagent-based hybrid energy management system for microgrids," *IEEE Transactions on Sustainable Energy*, vol. 5, no. 3, pp. 938–946, 2014.

[76] F. Blaabjerg, Y. Yang, D. Yang, and X. Wang, "Distributed Power-Generation Systems and Protection," *Proceedings of the IEEE*, vol. 105, no. 7. Institute of Electrical and Electronics Engineers Inc., pp. 1311–1331, 01-Jul-2017.

[77] X. Wang and F. Blaabjerg, "Harmonic Stability in Power Electronic-Based Power Systems: Concept, Modeling, and Analysis," *IEEE Transactions on Smart Grid*, vol. 10, no. 3, pp. 2858–2870, 2019.

[78] Y. Yang, K. A. Kim, F. Blaabjerg, and A. Sangwongwanich, *Advances in Grid-Connected Photovoltaic Power Conversion Systems*. .

[79] X. Wang, F. Blaabjerg, and W. Wu, "Modeling and analysis of harmonic stability in an AC power-electronics- based power system," *IEEE Transactions on Power Electronics*, vol. 29, no. 12, pp. 6421–6432, 2014.

[80] H. Xiao and S. Xie, "Leakage current analytical model and application in single-phase transformerless photovoltaic grid-connected inverter," *IEEE Transactions on Electromagnetic Compatibility*, vol. 52, no. 4, pp. 902–913, 2010.

[81] B. Yang, W. Li, Y. Gu, W. Cui, and X. He, "Improved transformerless inverter with common-mode leakage current elimination for a photovoltaic grid-connected power system," *IEEE Transactions on Power Electronics*, vol. 27, no. 2, pp. 752–762, 2012.

[82] Y. Zhou and H. Li, "Analysis and suppression of leakage current in cascaded-multilevel-inverter-based PV systems," *IEEE Transactions on Power Electronics*, vol. 29, no. 10, pp. 5265–5277, 2014.

[83] B. Xiao, L. Hang, J. Mei, C. Riley, L. M. Tolbert, and B. Ozpineci, "Modular Cascaded H-Bridge Multilevel PV Inverter with Distributed MPPT for Grid-Connected Applications," *IEEE Transactions on Industry Applications*, vol. 51, no. 2, pp. 1722–1731, 2015.

[84] H. Almasi, J. Panterlis, M. Alian, and M. Alian, "Comparison between two 10MW Solar Plant with Central and Distributed Inverters," in *ICEE 2019 - 27th Iranian Conference on Electrical Engineering*, 2019, pp. 831–835.

[85] M. Díez-Mediavilla, M. I. Dieste-Velasco, M. C. Rodríguez-Amigo, T. García-Calderón, and C. Alonso-Tristán, "Performance of grid-tied PV facilities based on real data in Spain: Central inverter versus string system," *Energy Conversion and Management*, vol. 86, pp. 1128–1133, 2014.

[86] R. Dogga and M. K. Pathak, "Recent trends in solar PV inverter topologies," *Solar Energy*, vol. 183, no. February, pp. 57–73, 2019.

[87] M. Z. C. Wanik, A. A. Jabbar, N. K. Singh, and A. P. Sanfilippo, "Comparison on the Impact of 0.4 MW PV with Central Inverter vs String Inverter on Distribution Network Operation," in *2018 IEEE 7th International Conference on Power and Energy, PECon 2018*, 2018, pp. 162–167.

[88] SMA, "Decentralized Inverter Technology in Large-Scale PV Plants," *Advisory Guide*, 2019. .

[89] Y. Yang, K. A. Kim, F. Blaabjerg, and A. Sangwongwanich, "PV system modeling, monitoring, and diagnosis," in *Advances in Grid-Connected Photovoltaic Power Conversion Systems*, Cambridge: Woodhead Publishing, 2018, pp. 45–74.

[90] M. Di Piazza and G. Vitale, *Photovoltaic sources: modeling and emulation*. London: Springer, 2012.

[91] M. G. Villalva, J. R. Gazoli, and E. R. Filho, "Comprehensive approach to modeling and simulation of photovoltaic arrays," *IEEE Transactions on Power Electronics*, vol. 24, no. 5, pp. 1198–1208, 2009.

[92] A. Ortiz-Conde, D. Lugo-Muñoz, and F. J. García-Sánchez, "An explicit multiexponential model as an alternative to traditional solar cell models with series and shunt resistances," *IEEE Journal of Photovoltaics*, vol. 2, no. 3, pp. 261–268, 2012.

[93] M. Hejri, H. Mokhtari, M. R. Azizian, M. Ghandhari, and L. Söder, "On the parameter extraction of a five-parameter double-diode model of photovoltaic cells and modules," *IEEE Journal of Photovoltaics*, vol. 4, no. 3, pp. 915–923, 2014.

[94] K. A. Kim, C. Xu, L. Jin, and P. T. Krein, "A dynamic photovoltaic model incorporating capacitive and reverse-bias characteristics," *IEEE Journal of Photovoltaics*, vol. 3, no. 4, pp. 1334–1341, 2013.

[95] X. H. Mai, S. K. Kwak, J. H. Jung, and K. A. Kim, "Comprehensive electric-thermal photovoltaic modeling for power-hardware-in-the-loop simulation (PHILS) applications," *IEEE Transactions on Industrial Electronics*, vol. 64, no. 8, pp. 6255–6264, Aug. 2017.

[96] N. Karami, N. Moubayed, and R. Outbib, "General review and classification of different MPPT Techniques," *Renewable and Sustainable Energy Reviews*, vol. 68, no. September 2016, pp. 1–18, 2017.

[97] V. Sridhar and S. Umashankar, "A comprehensive review on CHB MLI based PV inverter and feasibility study of CHB MLI based PV-STATCOM," *Renewable and Sustainable*

Energy Reviews, vol. 78, no. March, pp. 138–156, 2017.

[98] Q. Li, S. Zhao, M. Wang, Z. Zou, B. Wang, and Q. Chen, "An improved perturbation and observation maximum power point tracking algorithm based on a PV module four-parameter model for higher efficiency," *Applied Energy*, vol. 195, pp. 523–537, 2017.

[99] T. Esram and P. L. Chapman, "Comparison of photovoltaic array maximum power point tracking techniques," *IEEE Transactions on Energy Conversion*, vol. 22, no. 2, pp. 439–449, Jun. 2007.

[100] B. N. Alajmi, K. H. Ahmed, S. J. Finney, and B. W. Williams, "Fuzzy-logic-control approach of a modified hill-climbing method for maximum power point in microgrid standalone photovoltaic system," *IEEE Transactions on Power Electronics*, vol. 26, no. 4, pp. 1022–1030, 2011.

[101] S. Jain and V. Agarwal, "A new algorithm for rapid tracking of approximate maximum power point in photovoltaic systems," *IEEE Power Electronics Letters*, vol. 2, no. 1, pp. 16–19, 2004.

[102] T. Tafticht and K. Agbossou, "Development of a MPPT method for photovoltaic systems," 2004, pp. 1123–1126.

[103] P. Sivakumar, A. Abdul Kader, Y. Kaliavaradhan, and M. Arutchelvi, "Analysis and enhancement of PV efficiency with incremental conductance MPPT technique under non-linear loading conditions," *Renewable Energy*, vol. 81, pp. 543–550, 2015.

[104] S. Twaha, J. Zhu, Y. Yan, B. Li, and K. Huang, "Performance analysis of thermoelectric generator using dc-dc converter with incremental conductance based maximum power point tracking," *Energy for Sustainable Development*, vol. 37, pp. 86–98, 2017.

[105] A. Reza Reisi, M. Hassan Moradi, and S. Jamasb, "Classification and comparison of maximum power point tracking techniques for photovoltaic system: A review," *Renewable and Sustainable Energy Reviews*, vol. 19, pp. 433–443, 2013.

[106] K. Ishaque and Z. Salam, "A review of maximum power point tracking techniques of PV system for uniform insolation and partial shading condition," *Renewable and Sustainable Energy Reviews*, vol. 19, pp. 475–488, 2013.

[107] H. A. Sher, A. F. Murtaza, A. Noman, K. E. Addoweesh, K. Al-Haddad, and M. Chiaberge, "A New Sensorless Hybrid MPPT Algorithm Based on Fractional Short-Circuit Current Measurement and P&O MPPT," *IEEE Transactions on Sustainable Energy*, vol. 6, no. 4, pp. 1426–1434, 2015.

[108] D. Baimel, S. Tapuchi, Y. Levron, and J. Belikov, "Improved fractional open circuit voltage MPPT methods for PV systems," *Electronics (Switzerland)*, vol. 8, no. 3, pp. 1–20, 2019.

[109] A. Nadeem, H. A. Sher, and A. F. Murtaza, "Online fractional open-circuit voltage maximum output power algorithm for photovoltaic modules," *IET Renewable Power*

Generation, vol. 14, no. 2, pp. 188–198, Feb. 2020.

[110] M. M. Algazar, H. Al-Monier, H. A. El-Halim, and M. E. E. K. Salem, "Maximum power point tracking using fuzzy logic control," *International Journal of Electrical Power and Energy Systems*, vol. 39, no. 1, pp. 21–28, 2012.

[111] W. I. Hameed, A. L. Saleh, B. A. Sawadi, Y. I. A. Al-Yasir, and R. A. Abd-Alhameed, "Maximum power point tracking for photovoltaic system by using fuzzy neural network," *Inventions*, vol. 4, no. 3, 2019.

[112] K. Loudiyi, A. Berrada, H. G. Svendsen, and K. Mentesidi, "Grid code status for wind farms interconnection in Northern Africa and Spain: Descriptions and recommendations for Northern Africa," *Renewable and Sustainable Energy Reviews*, vol. 81. Elsevier Ltd, pp. 2584–2598, 01-Jan-2018.

[113] M. T. Hagh and T. Khalili, "A Review of Fault Ride-Through of PV and Wind Renewable Energies in Grid Codes," *International Journal of Energy Research*, vol. 43, no. 12, pp. 1342–1356, 2018.

[114] A. M. Howlader and T. Senjyu, "A comprehensive review of low voltage ride through capability strategies for the wind energy conversion systems," *Renewable and Sustainable Energy Reviews*, vol. 56, pp. 643–658, 2016.

[115] D. M. Vilathgamuwa, P. C. Loh, and Y. Li, "Protection of microgrids during utility voltage sags," *IEEE Transactions on Industrial Electronics*, vol. 53, no. 5, pp. 1427–1436, 2006.

[116] X. Yingcheng and T. Nengling, "Review of contribution to frequency control through variable speed wind turbine," *Renewable Energy*, vol. 36, no. 6, pp. 1671–1677, 2011.

[117] M. Mohseni and S. M. Islam, "Review of international grid codes for wind power integration: Diversity, technology and a case for global standard," *Renewable and Sustainable Energy Reviews*, vol. 16, no. 6, pp. 3876–3890, 2012.

[118] M. T. Hagh and T. Khalili, "A review of fault ride through of PV and wind renewable energies in grid codes," *International Journal of Energy Research*, vol. 43, no. 4, pp. 1342–1356, 2019.

[119] A. Q. Al-Shetwi, M. Z. Sujod, F. Blaabjerg, and Y. Yang, "Fault ride-through control of grid-connected photovoltaic power plants: A review," *Solar Energy*, vol. 180, no. November 2018, pp. 340–350, 2019.

[120] M. Nasiri, J. Milimonfared, and S. H. Fathi, "A review of low-voltage ride-through enhancement methods for permanent magnet synchronous generator based wind turbines," *Renewable and Sustainable Energy Reviews*, vol. 47. Elsevier Ltd, pp. 399–415, 01-Jul-2015.

[121] J. I. Y. Ota, T. Sato, and H. Akagi, "Enhancement of performance, availability, and flexibility of a battery energy storage system based on a modular multilevel cascaded converter (MMCC-SSBC)," *IEEE Transactions on Power Electronics*, vol. 31, no. 4, pp.

2791–2799, Apr. 2016.

[122] Y. W. Shen, D. P. Ke, W. Qiao, Y. Z. Sun, D. S. Kirschen, and C. Wei, "Transient Reconfiguration and Coordinated Control for Power Converters to Enhance the LVRT of a DFIG Wind Turbine with an Energy Storage Device," *IEEE Transactions on Energy Conversion*, vol. 30, no. 4, pp. 1679–1690, Dec. 2015.

[123] W. Guo, L. Xiao, and S. Dai, "Enhancing low-voltage ride-through capability and smoothing output power of DFIG with a superconducting fault-current limiter-magnetic energy storage system," *IEEE Transactions on Energy Conversion*, vol. 27, no. 2, pp. 277–295, 2012.

[124] N. Saadat, S. S. Choi, and D. M. Vilathgamuwa, "A statistical evaluation of the capability of distributed renewable generator-energy-storage system in providing load low-voltage ride-through," *IEEE Transactions on Power Delivery*, vol. 30, no. 3, pp. 1128–1136, Jun. 2015.

[125] L. G. Meegahapola, T. Littler, and D. Flynn, "Decoupled-DFIG fault ride-through strategy for enhanced stability performance during grid faults," *IEEE Transactions on Sustainable Energy*, vol. 1, no. 3, pp. 152–162, Oct. 2010.

[126] A. Q. Al-shetwi, M. Zahim, and F. Blaabjerg, "Low voltage ride-through capability control for single-stage inverter-based grid-connected photovoltaic power plant," *Solar Energy*, vol. 159, no. November 2017, pp. 665–681, 2018.

[127] A. Al-Durra, Y. Fayyad, S. M. Muyeen, and F. Blaabjerg, "Fault Ride-through of a Grid-connected Photovoltaic System with Quasi Z Source Inverter," *Electric Power Components and Systems*, vol. 44, no. 16, pp. 1786–1800, 2016.

[128] G. Pannell, B. Zahawi, D. J. Atkinson, and P. Missailidis, "Evaluation of the performance of a DC-link brake chopper as a DFIG low-voltage fault-ride-through device," *IEEE Transactions on Energy Conversion*, vol. 28, no. 3, pp. 535–542, 2013.

[129] L. S. Barros and C. M. V. Barros, "An internal model control for enhanced grid-connection of direct-driven PMSG-based wind generators," *Electric Power Systems Research*, vol. 151, pp. 440–450, 2017.

[130] A. Q. Al-Shetwi and M. Z. Sujod, "Modeling and Control of Grid-Connected Photovoltaic Power Plant with Fault Ride-Through Capability," *Journal of Solar Energy Engineering, Transactions of the ASME*, vol. 140, no. 2, pp. 1–9, 2018.

[131] M. J. Hossain, H. R. Pota, and M. A. Mahmud, "Decentralized STATCOM/ESS Control for Wind Generators," *Power Systems*, vol. 53, pp. 401–437, 2012.

[132] A. Moghadasi, A. Sarwat, and J. M. Guerrero, "A comprehensive review of low-voltage-ride-through methods for fixed-speed wind power generators," *Renewable and Sustainable Energy Reviews*, vol. 55, pp. 823–839, 2016.

[133] A. Movahedi, A. Halvaei Niasar, and G. B. Gharehpetian, "LVRT improvement and

transient stability enhancement of power systems based on renewable energy resources using the coordination of SSSC and PSSs controllers," *IET Renewable Power Generation*, vol. 13, no. 11, pp. 1849–1860, Aug. 2019.

[134] H. Kuang, L. Zheng, S. Li, and X. Ding, "Voltage stability improvement of wind power grid-connected system using TCSC-STATCOM control," *IET Renewable Power Generation*, vol. 13, no. 2, pp. 215–219, Feb. 2019.

[135] L. Chen *et al.*, "Comparison of Superconducting Fault Current Limiter and Dynamic Voltage Restorer for LVRT Improvement of High Penetration Microgrid," *IEEE Transactions on Applied Superconductivity*, vol. 27, no. 4, 2017.

[136] A. Luna *et al.*, "Grid Voltage Synchronization for Distributed Generation Systems Under Grid Fault Conditions," *IEEE Transactions on Industry Applications*, vol. 51, no. 4, pp. 3414–3425, Jul. 2015.

[137] M. Rezkallah, A. Chandra, A. Hamadi, H. Ibrahim, and M. Ghandour, "Power Quality in Smart Grids," in *Pathways to a Smarter Power System*, Elsevier Ltd., 2019, pp. 225–245.

[138] R. A. J. Amalorpavaraj, P. Kaliannan, S. Padmanaban, U. Subramaniam, and V. K. Ramachandaramurthy, "Improved fault ride through capability in DFIG based wind turbines using dynamic voltage restorer with combined feed-forward and feed-back control," *IEEE Access*, vol. 5, pp. 20494–20503, 2017.

[139] X. Chen, L. Yan, X. Zhou, and H. Sun, "A Novel DVR-ESS-Embedded Wind-Energy Conversion System," *IEEE Transactions on Sustainable Energy*, vol. 9, no. 3, pp. 1265–1274, 2018.

[140] P. Mitra and G. K. Venayagamoorthy, "An adaptive control strategy for DSTATCOM applications in an electric ship power system," *IEEE Transactions on Power Electronics*, vol. 25, no. 1, pp. 95–104, 2010.

[141] M. S. Ali, M. M. Haque, and P. Wolfs, "A review of topological ordering based voltage rise mitigation methods for LV distribution networks with high levels of photovoltaic penetration," *Renewable and Sustainable Energy Reviews*, vol. 103, no. December 2017, pp. 463–476, 2019.

[142] T. Ghanbari and E. Farjah, "Unidirectional fault current limiter: An efficient interface between the microgrid and main network," *IEEE Transactions on Power Systems*, vol. 28, no. 2, pp. 1591–1598, 2013.

[143] L. Kovalsky, X. Yuan, K. Tekletsadik, A. Keri, J. Bock, and F. Breuer, "Applications of Superconducting Fault Current Limiters in Electric Power Transmission Systems," *IEEE Transactions on Appiled Superconductivity*, vol. 15, no. 2, pp. 2130–2133, 2005.

[144] I. Sadeghkhani, M. E. Hamedani Golshan, J. M. Guerrero, and A. Mehrizi-Sani, "A Current Limiting Strategy to Improve Fault Ride-Through of Inverter Interfaced Autonomous Microgrids," *IEEE Transactions on Smart Grid*, vol. 8, no. 5, pp. 2138–

2148, Sep. 2017.

[145] H. He *et al.*, "Application of a SFCL for Fault Ride-Through Capability Enhancement of DG in a Microgrid System and Relay Protection Coordination," *IEEE Transactions on Applied Superconductivity*, vol. 26, no. 7, pp. 1–8, Oct. 2016.

[146] D. H. Choi, J. I. Yoo, D. Kim, S. H. Lee, and J. W. Park, "Analysis on Effect of SFCL Applied to an Isolated Microgrid with a Dynamic Load Model," *IEEE Transactions on Applied Superconductivity*, vol. 27, no. 4, 2017.

[147] S. B. Naderi, M. Negnevitsky, A. Jalilian, M. Tarafdar Hagh, and K. M. Muttaqi, "Optimum Resistive Type Fault Current Limiter: An Efficient Solution to Achieve Maximum Fault Ride-Through Capability of Fixed-Speed Wind Turbines During Symmetrical and Asymmetrical Grid Faults," *IEEE Transactions on Industry Applications*, vol. 53, no. 1, pp. 538–548, Jan. 2017.

[148] G. Rashid and M. H. Ali, "Fault ride through capability improvement of DFIG based wind farm by fuzzy logic controlled parallel resonance fault current limiter," *Electric Power Systems Research*, vol. 146, pp. 1–8, May 2017.

[149] T. Ghanbari and E. Farjah, "Unidirectional Fault Current Limiter : An Ef fi cient Interface Between the Microgrid and Main Network," vol. 28, no. 2, pp. 1591–1598, 2013.

[150] M. A. Zamani, S. Member, A. Yazdani, S. Member, and T. S. Sidhu, "A Control Strategy for Enhanced Operation of Inverter-Based Microgrids Under Transient Disturbances and Network Faults," *IEEE Transactions on Power Delivery*, vol. 27, no. 4, pp. 1737–1747, 2012.

[151] D. Shin, K. J. Lee, J. P. Lee, D. W. Yoo, and H. J. Kim, "Implementation of fault ride-through techniques of grid-connected inverter for distributed energy resources with adaptive low-pass notch PLL," *IEEE Transactions on Power Electronics*, vol. 30, no. 5, pp. 2859–2870, 2015.

[152] D. Çelik and M. E. Meral, "Voltage support control strategy of grid-connected inverter system under unbalanced grid faults to meet fault ride through requirements," *IET Generation, Transmission & Distribution*, vol. 14, no. 16, pp. 3198–3210, 2020.

[153] P. H. Huang, M. S. El Moursi, and S. A. Hasen, "Novel Fault Ride-Through Scheme and Control Strategy for Doubly Fed Induction Generator-Based Wind Turbine," *IEEE Transactions on Energy Conversion*, vol. 30, no. 2, pp. 635–645, 2015.

[154] M. Mirhosseini, J. Pou, and V. G. Agelidis, "Single- and Two-Stage Inverter-Based Grid-Connected Photovoltaic Power Plants With Ride-Through Capability Under Grid Faults," *IEEE Transactions on Sustainable Energy*, vol. 6, no. 3, pp. 1150–1159, 2015.

[155] A. Merabet, L. Labib, and A. M. Y. M. Ghias, "Robust model predictive control for photovoltaic inverter system with grid fault ride-through capability," *IEEE Transactions on Smart Grid*, vol. 9, no. 6, pp. 5699–5709, 2018.

[156] A. Mojallal and S. Lotfifard, “Enhancement of Grid Connected PV Arrays Fault Ride Through and Post Fault Recovery Performance,” *IEEE Transactions on Smart Grid*, vol. 10, no. 1, pp. 546–555, 2019.

[157] M. Easley, S. Jain, M. B. Shadmand, and H. A. Abu-Rub, “Autonomous Model Predictive Controlled Smart Inverter with Proactive Grid Fault Ride-Through Capability,” *IEEE Transactions on Energy Conversion*, vol. 8969, no. c, pp. 1–12, 2020.

[158] W. Kou and D. Wei, “Fault ride through strategy of inverter-interfaced microgrids embedded in distributed network considering fault current management,” *Sustainable Energy, Grids and Networks*, vol. 15, pp. 43–52, Sep. 2018.

[159] P. Piya, M. Ebrahimi, M. Karimi-Ghartemani, and S. A. Khajehoddin, “Fault Ride-Through Capability of Voltage-Controlled Inverters,” *IEEE TRANSACTIONS ON INDUSTRIAL ELECTRONICS*, vol. 65, no. 10, pp. 7933–7943, 2018.

[160] O. Palizban, K. Kauhaniemi, and J. M. Guerrero, “Microgrids in active network management – part II: System operation, power quality and protection,” *Renewable and Sustainable Energy Reviews*, vol. 36, pp. 440–451, Aug. 2014.

[161] Y. Yang and F. Blaabjerg, “Low-voltage ride-through capability of a single-stage single-phase photovoltaic system connected to the low-voltage grid,” *International Journal of Photoenergy*, vol. 2013, 2013.

[162] F. Yang, L. Yang, and X. Ma, “An advanced control strategy of PV system for low-voltage ride-through capability enhancement,” *Solar Energy*, vol. 109, pp. 24–35, 2014.

[163] A. Q. Al-Shetwi and M. Z. Sujod, “Voltage Sag Detection in Grid-Connected Photovoltaic Power Plant for Low Voltage Ride-Through Control,” *Recent Advances in Electrical & Electronic Engineering (Formerly Recent Patents on Electrical & Electronic Engineering)*, vol. 12, no. 4, pp. 384–392, Jun. 2018.

[164] A. Khoshkbar Sadigh and K. M. Smedley, “Fast and precise voltage sag detection method for dynamic voltage restorer (DVR) application,” *Electric Power Systems Research*, vol. 130, pp. 192–207, 2016.

[165] S. Alepuz *et al.*, “Control strategies based on symmetrical components for grid-connected converters under voltage dips,” *IEEE Transactions on Industrial Electronics*, vol. 56, no. 6, pp. 2162–2173, 2009.

[166] M. B. Latran and A. Teke, “A novel wavelet transform based voltage sag/swell detection algorithm,” *International Journal of Electrical Power and Energy Systems*, vol. 71, pp. 131–139, 2015.

[167] M. Bollen, M. Olofsson, A. Larsson, S. Rönnberg, and M. Lundmark, “Standards for supraharmonics (2 to 150 kHz),” *IEEE Electromagnetic Compatibility Magazine*, vol. 3, no. 1, pp. 114–119, Mar. 2014.

[168] Y. Kumsuwan and Y. Sillapawicharn, “FRAME-BASED VOLTAGE SAG DETECTION

UNDER PRACTICAL GRID VOLTAGES FOR VOLTAGE SAG COMPENSATION SYSTEMS," in *6th IET International Conference on Power Electronics, Machines and Drives (PEMD 2012)*, 2012, pp. 1–3.

[169] K. E. Paratane and V. P. Dhote, "Review On Single Phase Voltage Sag Detection Methods," *International Journal of Advanced Research in Electrical, Electronics and Instrumentation Engineering*, vol. 5, no. 1, pp. 117–121, 2016.

[170] K. Ding *et al.*, "A Novel Detection Method for Voltage Sags," in *2nd International Conference on Power Electronics Systems and Applications*, 2006, pp. 250–255.

[171] T. Ngo, K. W. Min, and T. Vu, "Comparative Study of Fault Detection Methods Based on Time Domain RMS Calculation," *IEEE Power and Energy Society General Meeting*, vol. 2019-Augus, pp. 1–5, 2019.

[172] J. C. Gu and S. L. Yu, "Removal of DC offset in current and voltage signals using a novel Fourier filter algorithm," *IEEE Transactions on Power Delivery*, vol. 15, no. 1, pp. 73–79, Jan. 2000.

[173] H. Liu, H. Hu, H. Chen, L. Zhang, and Y. Xing, "Fast and Flexible Selective Harmonic Extraction Methods Based on the Generalized Discrete Fourier Transform," *IEEE Transactions on Power Electronics*, vol. 33, no. 4, pp. 3484–3496, Apr. 2018.

[174] C. Ma, F. Gao, G. He, and G. Li, "A Voltage Detection Method for the Voltage Ride-Through Operation of Renewable Energy Generation Systems under Grid Voltage Distortion Conditions," *IEEE Transactions on Sustainable Energy*, vol. 6, no. 3, pp. 1131–1139, 2015.

[175] A. Vinayagam, K. S. V. Swarna, S. Y. Khoo, A. T. Oo, and A. Stojcevski, "PV Based Microgrid with Grid-Support Grid-Forming Inverter Control-(Simulation and Analysis)," *Smart Grid and Renewable Energy*, vol. 08, no. 01, pp. 1–30, 2017.

[176] W. Yuan, Y. Wang, D. Liu, F. Deng, and Z. Chen, "Efficiency-Prioritized Droop Control Strategy of AC Microgrid," *IEEE Journal of Emerging and Selected Topics in Power Electronics*, vol. 6777, no. c, pp. 1–16, 2020.

[177] L. Che, M. Shahidehpour, A. Alabdulwahab, and Y. Al-Turki, "Hierarchical Coordination of a Community Microgrid With AC and DC Microgrids," *IEEE Transactions on Smart Grid*, vol. 6, no. 6, pp. 3042–3051, Nov. 2015.

[178] P. Rodriguez, C. Citro, J. I. Candela, J. Rocabert, and A. Luna, "Flexible Grid Connection and Islanding of SPC-Based PV Power Converters," *IEEE Transactions on Industry Applications*, vol. 54, no. 3, pp. 2690–2702, 2018.

[179] A. M. Bouzid, J. M. Guerrero, A. Cheriti, M. Bouhamida, P. Sicard, and M. Benghanem, "A survey on control of electric power distributed generation systems for microgrid applications," *Renewable and Sustainable Energy Reviews*, vol. 44, pp. 751–766, 2015.

[180] A. M. Dissanayake and N. C. Ekneligoda, "Transient Optimization of Parallel Connected

Inverters in Islanded AC Microgrids," *IEEE Transactions on Smart Grid*, vol. PP, no. c, pp. 1–12, 2018.

[181] B. Wei, J. M. Guerrero, J. C. Vásquez, and X. Guo, "A Circulating-Current Suppression Method for Parallel Connected Voltage Source Inverters (VSI) with Common DC and AC Buses Xiaoqiang Guo," *IEEE Transactions on Industry Applications*, vol. 9994, no. c, pp. 1–11, 2017.

[182] Y. Sun, X. Hou, J. Yang, H. Han, M. Su, and J. M. Guerrero, "New Perspectives on Droop Control in AC Microgrid," *IEEE Transactions on Industrial Electronics*, vol. 64, no. 7, pp. 5741–5745, Jul. 2017.

[183] A. Arzani and G. K. Venayagamoorthy, "Computational approach to enhance performance of photovoltaic system inverters interfaced to utility grids," *IET Renewable Power Generation*, vol. 12, no. 1, pp. 112–124, 2018.

[184] K. Ishaque, Z. Salam, H. Taheri, and Syafaruddin, "Modeling and simulation of photovoltaic (PV) system during partial shading based on a two-diode model," *Simulation Modelling Practice and Theory*, vol. 19, no. 7, pp. 1613–1626, 2011.

[185] M. Uzunoglu, O. C. Onar, and M. S. Alam, "Modeling, control and simulation of a PV/FC/UC based hybrid power generation system for stand-alone applications," *Renewable Energy*, vol. 34, no. 3, pp. 509–520, 2009.

[186] S. R. Madeti and S. N. Singh, "Modeling of PV system based on experimental data for fault detection using kNN method," *Solar Energy*, vol. 173, no. March, pp. 139–151, 2018.

[187] A. R. Jordehi, "Parameter estimation of solar photovoltaic (PV) cells: A review," *Renewable and Sustainable Energy Reviews*, vol. 61, pp. 354–371, 2016.

[188] T. Suntio and A. Kuperman, "Comments on 'An efficient partial power processing DC/DC converter for distributed PV architectures,'" *IEEE Transactions on Power Electronics*, vol. 30, no. 4, p. 2372, Apr. 2015.

[189] H. Choi, M. Ciobotaru, M. Jang, and V. G. Agelidis, "Performance of Medium-Voltage DC-Bus PV System Architecture Utilizing High-Gain DC-DC Converter," *IEEE Transactions on Sustainable Energy*, vol. 6, no. 2, pp. 464–473, Apr. 2015.

[190] A. Ravi, P. S. Manoharan, and J. Vijay Anand, "Modeling and simulation of three phase multilevel inverter for grid connected photovoltaic systems," *Solar Energy*, vol. 85, no. 11, pp. 2811–2818, 2011.

[191] A. Morales, X. Robe, M. Sala, P. Prats, C. Aguerri, and E. Torres, "Advanced grid requirements for the integration of wind farms into the Spanish transmission system," *IET Renewable Power Generation*, vol. 2, no. 1, pp. 47–59, 2008.

[192] F. Jiménez, E. Gómez-Lázaro, J. A. Fuentes, A. Molina-García, and A. Vigueras-Rodríguez, "Validation of a double fed induction generator wind turbine model and wind farm verification following the Spanish grid code," *Wind Energy*, vol. 15, no. 4, pp. 645–

659, May 2012.

[193] M. Bakkar, S. Bogarra, F. Córcoles, J. Saura, and M. Moreno, “Power Control Strategies During Voltage Sags According to Spanish Grid Code,” *Renewable Energy and Power Quality Journal*, vol. 1, no. 16, pp. 493–498, 2018.

[194] D. Ramirez, F. Martinez-Rodrigo, S. de Pablo, and L. Carlos Herrero-de Lucas, “Assessment of a non linear current control technique applied to MMC-HVDC during grid disturbances,” *Renewable Energy*, vol. 101, pp. 945–963, Feb. 2017.

[195] E. Buraimoh, I. E. Davidson, and F. Martinez-Rodrigo, “Fault ride-through enhancement of grid supporting inverter-based microgrid using delayed signal cancellation algorithm secondary control,” *Energies*, vol. 12, no. 20, pp. 7–8, 2019.

[196] J. Svensson, M. Bongiorno, and A. Sannino, “Practical implementation of delayed signal cancellation method for phase-sequence separation,” *IEEE Transactions on Power Delivery*, vol. 22, no. 1, pp. 18–26, Jan. 2007.

[197] X. Chen, Y. Zhang, S. Wang, J. Chen, and C. Gong, “Impedance-Phased Dynamic Control Method for Grid-Connected Inverters in a Weak Grid,” *IEEE Transactions on Power Electronics*, vol. 32, no. 1, pp. 274–283, Jan. 2017.

[198] M. Davari and Y. A.-R. I. Mohamed, “Robust Vector Control of a Very Weak-Grid-Connected Voltage-Source Converter Considering the Phase-Locked Loop Dynamics,” *IEEE Transactions on Power Electronics*, vol. 32, no. 2, pp. 977–994, Feb. 2017.

[199] I. Sadeghkhani, M. Esmail, H. Golshan, A. Mehrizi-sani, and J. M. Guerrero, “Low-Voltage Ride-Through of A Droop-Based Three-Phase Four-Wire Grid-Connected Microgrid,” *IET Generation, Transmission & Distribution*, vol. 12, no. 8, pp. 1906–1914, 2018.

[200] A. Camacho, M. Castilla, J. Miret, J. C. Vasquez, and E. Alarcon-Gallo, “Flexible Voltage Support Control for Three-Phase Distributed Generation Inverters Under Grid Fault,” *IEEE Transactions on Industrial Electronics*, vol. 60, no. 4, pp. 1429–1441, Apr. 2013.

[201] A. Camacho, M. Castilla, J. Miret, A. Borrell, and L. G. de Vicuna, “Active and Reactive Power Strategies With Peak Current Limitation for Distributed Generation Inverters During Unbalanced Grid Faults,” *IEEE Transactions on Industrial Electronics*, vol. 62, no. 3, pp. 1515–1525, Mar. 2015.

[202] M. M. Haque and P. Wolfs, “A review of high PV penetrations in LV distribution networks: Present status, impacts and mitigation measures,” *Renewable and Sustainable Energy Reviews*, vol. 62, pp. 1195–1208, Sep. 2016.

[203] Y. Yang, H. Wang, and F. Blaabjerg, “Reactive Power Injection Strategies for Single-Phase Photovoltaic Systems Considering,” vol. 9994, no. c, 2014.

[204] G. P. V Inverters and E. Current, “Control Strategy for Three-Phase Limitation Under Unbalanced Faults,” *Ieee Transactions on Industrial Electronics*, vol. 64, no. 11, pp.

8908–8918, 2017.

[205] X. Li, H. Zhang, M. B. Shadmand, and R. S. Balog, “Model Predictive Control of a Voltage-Source Inverter with Seamless Transition between Islanded and Grid-Connected Operations,” *IEEE Transactions on Industrial Electronics*, vol. 64, no. 10, pp. 7906–7918, Oct. 2017.

[206] A. Micallef, M. Apap, C. Spiteri-Staines, and J. M. Guerrero, “Single-Phase Microgrid with Seamless Transition Capabilities between Modes of Operation,” *IEEE Transactions on Smart Grid*, vol. 6, no. 6, pp. 2736–2745, Nov. 2015.

[207] EN Std, “Voltage Characteristics of Electricity Supploed by Public Distribution Systems,” 2001.

[208] International Electrotechnical Commission, “Limits for Harmonic Current Emissions,” 2000.

[209] I. Sadeghkhani, M. E. H. Golshan, A. Mehrizi-Sani, J. M. Guerrero, and A. Ketabi, “Transient Monitoring Function-Based Fault Detection for Inverter-Interfaced Microgrids,” *IEEE Transactions on Smart Grid*, vol. 9, no. 3, pp. 2097–2107, May 2018.

[210] S. Dhar, R. K. Patnaik, and P. K. Dash, “Fault Detection and Location of Photovoltaic Based DC Microgrid Using Differential Protection Strategy,” *IEEE Transactions on Smart Grid*, vol. 9, no. 5, pp. 4303–4312, Sep. 2018.

[211] A. Q. Al-Shetwi, M. Z. Sujod, and N. L. Ramli, “A review of the fault ride through requirements in different grid codes concerning penetration of PV system to the electric power network,” *ARPN Journal of Engineering and Applied Sciences*, vol. 10, no. 21, pp. 9906–9912, 2015.

[212] M. G. Taul, X. Wang, P. Davari, and F. Blaabjerg, “Current Reference Generation based on Next Generation Grid Code Requirements of Grid-Tied Converters during Asymmetrical Faults,” *IEEE Journal of Emerging and Selected Topics in Power Electronics*, vol. 19, pp. 1–1, Jul. 2019.

[213] A. B. Rey-Boué, N. F. Guerrero-Rodríguez, J. Stöckl, and T. I. Strasser, “Modeling and Design of the Vector Control for a Three-Phase Single-Stage Grid-Connected PV System with LVRT Capability according to the Spanish Grid Code,” *Energies*, vol. 12, no. 15, p. 2899, Jul. 2019.

APPENDIX A: COUNTRIES' GRID CODE FAULT RIDE-THROUGH REQUIREMENT

The FRT provision ensures that every power plant's ability will stay linked under those limits during fault situations or low voltage [112]. E. ON and VE-T first suggested FRT specifications in 2003 German transmission operators. This condition is generally called FRT, and the voltage vs. time characteristics are shown in Figure 1. The PV power plant should also deliver reactive power during voltage sags to improve the point of common coupling (PCC) voltage level until system stability is regained after its clearance. The disengagement of RESs beneath 80% of the rated voltage allows an unacceptable portion of the lost energy output. For example, the FRT specifications of the PV system method have been introduced for low FRT demands in wind turbine generations. They are revised in several countries as a consequence of increased efficiency and PV systems penetration levels. The overall FRT specifications of PV schemes concentrate on maintaining sustained grid-connection of DC-AC inverters without over-current generation but, in the meantime, offer dynamic reactive power support to aid grid recovery under different faulty conditions. Because of its benefits in voltage recovery and frequency stability, the FRT requirements are accepted and widely spread, ignoring the impacts of a high-penetration grid on transient stability.

A.1 Fault Ride-Through in Countries

The grid codes specify that the Solar PV should tolerate grid voltage sag to a certain fraction of rated voltage, as in some instances for a specified time down to zero [211]. PV units will typically operate within this period without any disconnection. After removing faults, the PV system needs to maintain both active and reactive power quickly enough to pre-fault value. Some codes stipulate that, like conventional synchronous generators, the PV system must supply the grid with the reactive current to support the grid voltage. Figure 2.8 presents a sample of the LVRT capability curve. The grid codes LVRT curves of various countries are comparatively similar, with variance in their features and specific requirements. Whenever a generating unit is operating in normal mode (V_n), its PCC voltage is in area A. When there is a fault occurring at time t_0, the generating unit encounters a voltage sag (V_0) at the PCC. Generating units in area B have to endure the voltage drop until a particular time and remain grid-connected. If the generating unit experiences a substantial voltage decrease in which the voltage exceeded region C, the generating unit has the freedom to detach from the power grid. Upon removal of fault at the time past period (t_0), the voltage is requested to return to V_{n0}. Various grid code operators decide the required time for their respective grid-connected units to withstand different voltage sags levels, possibly up to 0 V, for a considerable period [118].

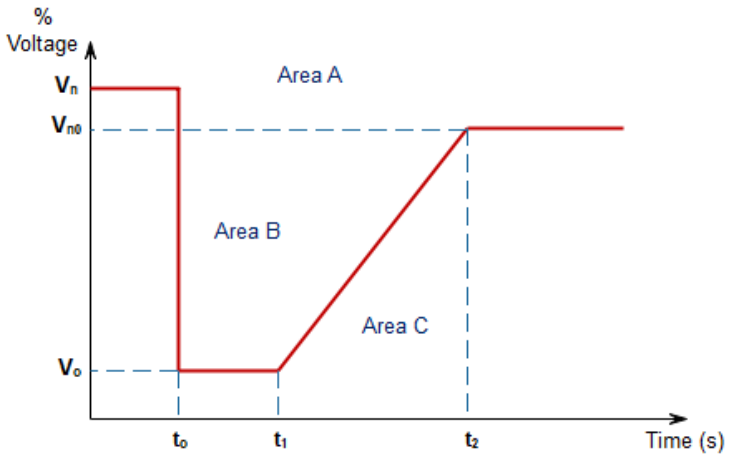

Figure A. 1:Generic FRT/LVRT curve

The German grid code [212] specified the FRT when the voltage dropped to zero for a maximum duration of 150 ms, followed by the voltage recovery to 90 percent of the nominal voltage at PCC in 1.5 seconds, as revealed in Figure 2.9. Germany gives incentives to renewable energy farm operators to possess FRT enhancements and capabilities. The new renewable energy entries must make adequate preparation for FRT amidst evolving grid code regulations. The LVRT grid code for Germany comprises two lines. For example, the wind system must not disconnect from the grid over Germany's borderline 1 line. The disconnection of generating unit at voltage sag values of above borderline 1 may lead to instability. The voltage sags between borderlines 1 and 2 are encouraged to be ridden through; however, a plant may temporarily detach and re-join for up to 2 seconds is a fault occurs between borderlines. This is usually determined based on an agreement between the plant owners and network operators. The energy-generating unit can always disconnect shortly below the borderline 2 lines. Units are not expected to disconnect under a 0% voltage drop that only persists for a duration less or equal to 150 microseconds. However, the requirement stipulates the grid-connected system's compulsory disconnection for any condition under the blue line, as shown.

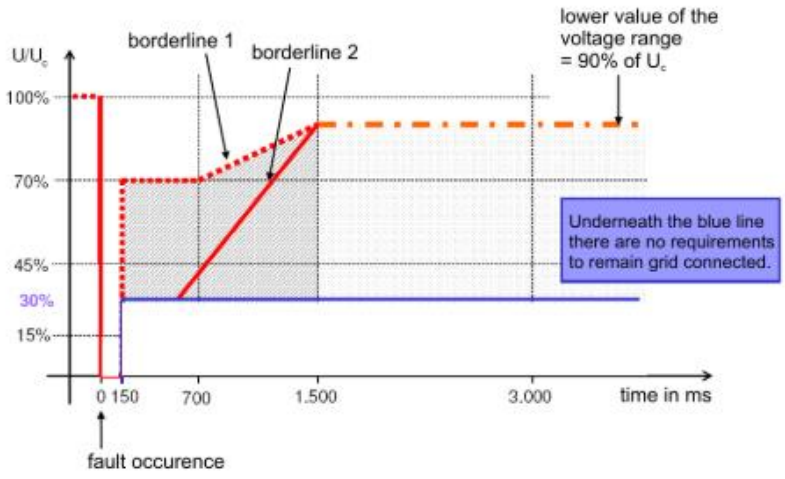

Figure A. 2:LVRT Curves of Germany

The solar PV systems are required to withstand faults and are still connected to the system within 200 microseconds when the voltage at the PV system's connection point drops to zero in the Italian grid code. If the voltage at the connection point is recovered to 85% of the rated voltage within 1.5 s after fault occurrence, the photovoltaic units shall remain in continuous operation without disengagement. The Spanish grid code requirements are less cumbersome than German, which requests PV systems to withstand grid disturbance with 20% voltage sag for 500 ms with a voltage restoration stipulation of up to 80% in the subsequent period of 1 s [213]. Spain, just like Germany, gives incentives to energy generating units operating with FRT capability. The Danish grid code concerning wind farms is used for the PV system. FRT specifications for the classification of grid codes such as those in France rely heavily on the voltage level of the fault occurrence.

The grid code in Japan implements one of the world's highly restrictive FRT regulatory requirements. The generating units in Japan are required to remain grid-connected for up to 0 percent of the rated voltage for 1 second under different types of faults and return to an acceptable voltage level of up to 2 seconds. Subsequently, the voltage must rise to a convenient voltage after the fault at 3.5 seconds. The U.S. grid code requires the voltage to decrease to zero for a period of 0.625 microseconds and afterward reduce to 15 percent from the rated voltage value accompanied by the voltage recovery to 90% in 3 s. The grid code Australia also comes with strict stipulations, which require that after a drop in voltage to 0 % within a period of 450 microseconds, it has also required to increase the voltage to 80 percent simultaneously. FRT specifications for classification of grid codes such as those in India also rely heavily on the voltage level of the fault occurrence. The South African grid code LVRT requirements require the generating units not to disconnect from the grid for voltages above the LVRT curve if power clearing capability after the fault is sustained. These stipulations apply to different fault types, and the minimum voltage which the LVRT curve signifies is applicable in all the phases. The generating units are

expected to reconnect to the grid within 1 second after the voltage recovery to 90 % of the rated grid voltage after disconnecting due to fault. Table 2.3 summarizes the prescribed LVRT requirement for PV grid integration in the countries earlier discussed and some other selected countries.

Table A. 1:Prescribed LVRT for countries

	National Grid Codes	**Fault**		**Post Fault**	
		V_{min} (pu)	**t_{max} (ms)**	**V_{min} (pu)**	**t_{max} (ms)**
1	South Africa	0.00	150	0.85	2000
2	Spain	0.20	500	0.80	1000
3	Italy	0.00	200	0.85	1500
4	Japan	0.30	1000	0.80	1500
5	Germany (3 phase)	0.00	150	0.90	1500
6	United States	0.15	625	0.90	3000
7	United Kingdom	0.15	140	0.90	2500
8	Australia	0.00	450	0.80	450
9	Ireland	0.15	625	0.90	3000
10	Belgium (small voltage dips)	0.70	1500	0.92	1500
11	Belgium (large voltage dips)	0.00	200	0.92	700
12	New Zealand	0.00	140	0.90	3000
13	Sweden (< 100 MW)	0.25	250	0.90	250
14	Sweden (> 100 MW)	0.00	250	0.90	750
15	Canada (Hydro-Quebec)	0.00	150	0.85	2000
16	Denmark	0.10	500	0.85	1500
17	Hungary (3 phase)	0.45	150	0.90	1500
18	China	0.00	150	0.90	2000
19	Taiwan	0.15	625	0.90	3000
20	Norway (nominal < 220 kV)	0.00	400	0.85	1000
21	Norway (nominal ≥ 220 kV)	0.15	200	0.90	1000
22	Greece	0.15	150	0.90	1500
23	Poland	0.15	600	0.80	3000
24	Finland	0.00	250	0.90	750
25	India	0.15	300	0.85	3000
26	France (400kV)	0.00	150	1.00	1500
27	France (63-225kV)	0.05	250	0.90	1100
28	Turkey	0.15	500	0.90	3000

29	Romania	0.15	625	0.90	3000
30	Cyprus	0.15	650	0.90	3000

A.2 High Voltage Ride-Through in Countries

Sometimes, a single line to ground fault and the switching of large power factor correction capacitor banks cause a swell in the grid voltage. However, compared to grid voltage sags, a surge in the grid voltage resulting from these grid disturbances is less frequent. HVRT capability is less acknowledged in the grid codes due to the extreme protection difficulties. The HVRT stipulation prescribes that generating units must possess HVRT capability to sustain a grid voltage swell while the remaining grid-connected under such conditions. However, most grid codes do not set out the rules for HVRT capability. The HVRT guidelines obtainable are set out in Figure 2.10 and Table 2.4. Under this transient period, the generating unit's resiliency strongly depends on its components' dynamic features.

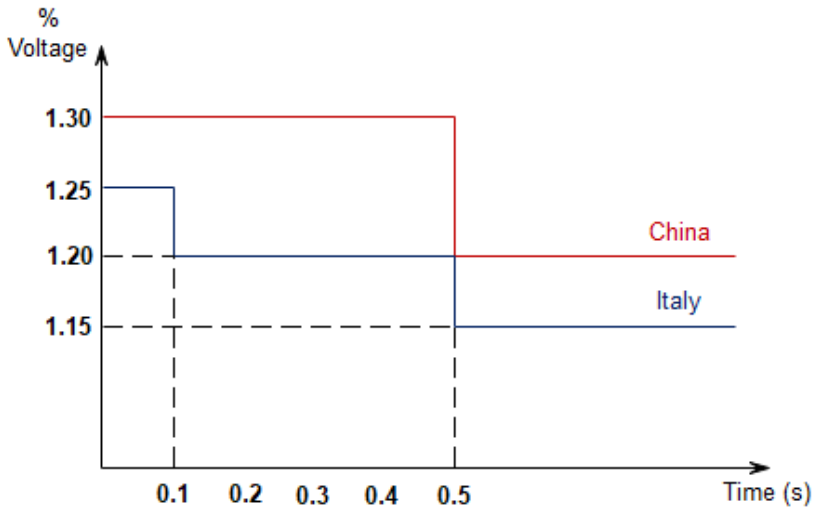

Figure A. 3: HVRT Curves for Italy and China

Table A. 2:Prescribed HVRT for countries

	National Grid Codes	Fault	
		V_{max} (pu)	**t_{max} (ms)**
1	China	1.30	500
2	Spain	1.30	250
3	Italy	1.25	100
4	Germany	1.20	100
5	Australia	1.30	600
6	United States	1.20	1000
7	Denmark	1.20	100

To keep the network safe and efficient, grid codes solve this problem by acquiring generating unit's HVRT specifications which have no synchronous generators. The HVRT specifications are clarified in Table 2 for the listed countries. Spain, Australia, and China have the most stringent regulations requiring a PV system to withstand a voltage swell of 130% of rated grid voltage. The Italian CEI 0-21 allows a PV device to sustain disruptions and to remain grid-tied under 125% voltage swell within 100 ms; the stipulated grid voltage recovery of 115 % is required in 0.5 seconds.

A.3 Dynamic Grid Voltage Support in Countries

Ensuring voltage stability in the grid is crucial to meeting the FRT requirement, and this is therefore achieved by dynamic grid support during voltage drops or voltage swell. Consequently, generating units must be capable of: remaining grid-connected in the event of a grid fault, supporting the voltage by providing reactive power (inductive or capacitive) during the fault; and consume the same or less reactive power after clearance of the fault.

PV system, for instance, is expected to inject a considerable amount of reactive current at the PCC during LVRT and HVRT operation, as given in Figure 3. This additional reactive current in crucial to mitigating the effect of voltage sag or swell as the case may be under faults. In Figure 3, the dynamic voltage support operation is activated in the event of a voltage drop of more than ±10% of the nominal voltage. Depending on the depth of voltage sag, for instance, the grid code stipulates possible supply reactive current of at least 100% of the rated current, as shown in Figure 3. The grid codes require that PV systems through their interface power electronic inverters to actively participate in the faster restoration of the grid voltage by generating reactive power during grid fault within the inverter apparent power limit.

The grid codes of Spain, Germany, and Denmark stipulate that the reactive current can only be injected outside the dead band (between 0.90 pu and 1.10 pu of the nominal voltage) by ± 10% [212]. The maximum time expected for dynamic voltage support operation to be activated after the inception of faults is between 20 to 30 microseconds. After the fault clearance, the PV system should avoid reactive current absorption to prevent undesirable consequences. For instance, in the Spanish grid code, the PV generating unit is expected to be disconnected in the event of a fault, which caused voltage swell above 1.30 pu of the nominal voltage.

Dynamic voltage support is distinct from static voltage supports, and they must not be confused with each other. The latter is concerned with power factor correction under steady-state operation. In contrast, the former is concerned with the dynamic operation of the generating system, especially in the event of a grid fault. All the grid codes are cohesive, and all agreed on the optimal grid supports for stability and rapid responses under grid disturbance. However, all the requirements imposed on the PV generating systems are done to the grid operators' advantage and

at the expense of the power electronic inverter interfacing the PV modules with the grid. Consequently, interface inverters are poised to face numerous challenges in their designs and grid-connected operation. The inverter will be expected to promptly adjust their active and reactive current references in fulfilling the FRT requirements. This, therefore, poses potential voltage instability and overcurrent issues for the inverter system.

A.4 Spanish FRT Grid Code Requirements and specifics

The voltage-time curve describing the voltage level and period of maximum allowable voltage sags are given in Figure 2.8. The existing Spanish P.O.12.3 requires no blue band disconnections, as shown in Figure 2.11. This dip-time voltage curve was determined using the stability simulations by the Red Eléctrica de España (REE) grid operators under specific protection criteria [191]:

1. The estimated 20% minimum is derived through REE's simulations for stability, and the active power (maximum) generated that can be loosened by the Spanish power grid when a short-circuit transmission system suffers.

2. According to the Spanish electrical system's general safety requirements, the voltage dip's time interval of 500 ms stems through the information provided on the required time of distance protection activation.

3. The time for voltage sag recovery specified for within 1 second is the product of traditional generation units ' under-voltage safety, enabled if the voltage is less than 80% of the nominal value for a period span exceeding 1s.

The P.O.12.3 also includes applications relating to the capabilities of reactive and active control. Nevertheless, under grid fault and subsequent recovery, active and reactive power requirements are strictly regulated. The global time interval varies from failure incidence (and below 85% voltage sags) to restoration time to operating range.

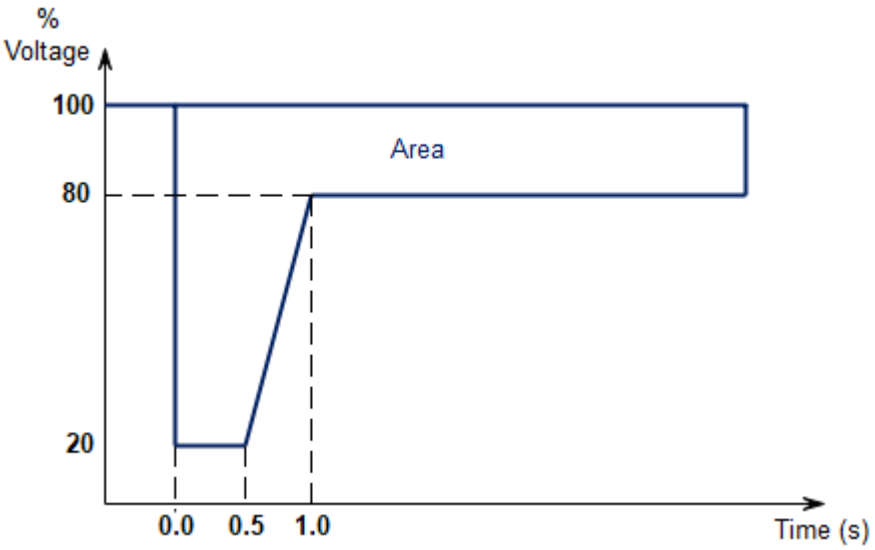

Figure A. 4:Spanish voltage-dip requirements at PCC:

PV power plants and wind farms are expected to generate maximum current at the PCC under grid fault and voltage recovery after the fault clearance. This current must, in any case, be within the blue band in Figure 2.12. The PV power plants and wind farms should generate reactive current when the level of voltage falls below 0.85 pu only. Consequently, the pre-fault active power generation must match the post-fault active power generation.

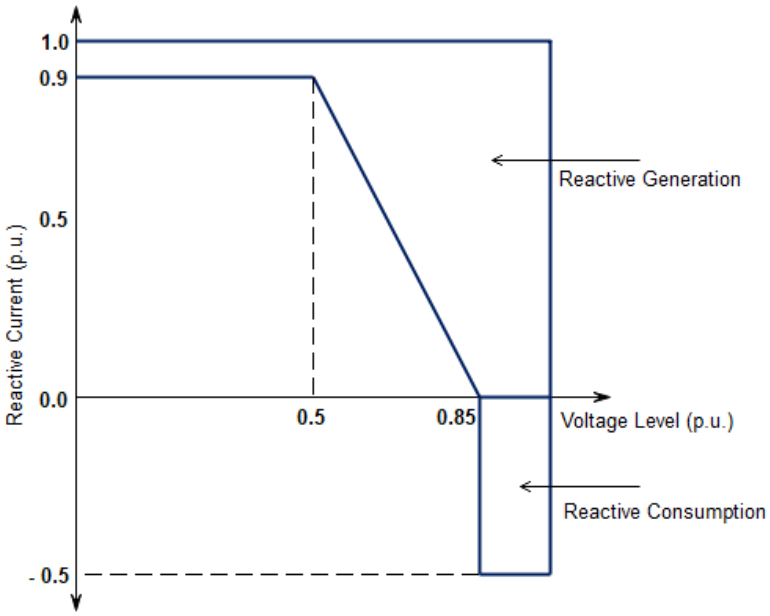

Figure A. 5:Stipulated reactive current ranges (generated or consumed) with respect to the voltage level

A.5 Fault Ride-Through Requirements and Ancillary Services.

The FRT ability is primarily reflected in the voltage-times chart that shows the required voltage disturbance capacity for a power generating sub-system due to failure to guarantee the protection of the systems. The aim of using FRT is to avert loss of generation within the confinement of

technical and non-technical feasibilities [113]. FRT's illustration is diverse across countries [114]. Units must remain connected to the grid at a given voltage irrespective of the grid conditions. Vilathgamuwa et al. [115] address its safety process and protection procedures in the event of a collapse in the main grid voltage.

The design of relays and some protective appliances rely heavily on low voltage ride-through requirements. A generation unit injects maximum reactive power during a fault without reaching the stipulated transient limit. Consequently, a system's FRT capability is enhanced in the face of different depths of voltage sags [18].

Symmetrical and asymmetrical disturbances have varying effects on the amplitude of three-phase voltage, and as a result, the impact on the FRT ability differs. Generally, the nature of the generating unit and as well as its application and location all have a crucial effect on FRT analysis and applications. Lastly, the constituent generating units' grid resilience and dynamics have significant influences on the draft of grid code guidelines pertaining to FRT. [113].

A.6 Low Voltage and High Voltage Ride-Through

The system operation needs to possess LVRT capabilities because of the high RES penetration level. The absence of automatic voltage regulation of a typical synchronous generator in RES based generating units has raised interest in WT and solar PV LVRT capability. Implementing this feature on wind turbines and solar PV is a fundamental challenge in sustaining a network connection [114] [116]. The operating cost compels the steady power generation during situations such as LVRT. The reactive current power injection standards under the grid fault for generating units is presented in this work. The switching high-capacity capacitors lead to voltage swell. Similarly, grid codes establish a new rule for faults causing an increase in voltage for power generating systems, excluding synchronous generators [117]. Although this nature of fault rarely occurs and capability, as prescribed by the grid code, is known as high voltage ride through (HVRT).

APPENDIX B: EXTRA EQUATIONS

B.1 Phase-Locked Loop Basic Model Equation

System input signal

$$v = V\sin(\theta) = V\sin(\omega t + \phi)$$

Signal generated by a voltage controlled oscillator

$$v' = \cos(\theta') = \cos(\omega' t + \phi')$$

The error of the multiple phase detector output

$$\varepsilon_{pd} = Vk_{pd}\sin(\omega t + \phi)\cos(\omega' t + \phi')$$

$$\bar{\varepsilon}_{pd} = \frac{Vk_{pd}}{2}\sin(\omega - \omega')t + (\phi + \phi')$$

$$\bar{\varepsilon}_{pd} = \frac{Vk_{pd}}{2}\sin(\phi - \phi')$$

$$\bar{\varepsilon}_{pd} = \frac{Vk_{pd}}{2}(\phi - \phi')$$

Frequency of voltage controlled oscillator

$$\bar{\omega}' = (\omega_c + \Delta\bar{\omega}') = (\omega_c + k_{osc}\bar{v}_{lf})$$

$$\bar{\omega}' = k_{osc}\bar{v}_{if})$$

The phase angle is therefore

$$\bar{\theta}'(t) = \int \bar{\omega}' dt = \int k_{oscillator}\bar{v}_{if}\, dt$$

B.2 Phase-Locked Loop small-signal model

The small-signal model of the phase detector

$$E_{pd}(s) = \frac{V}{2}\left(\Theta(s) - \Theta'(s)\right)$$

The small-signal model of the loop filter

$$V_{lf}(s) = k_p\left(1 + \frac{1}{sT_i}\right)\varepsilon_{pd}(s)$$

The small-signal model of the controlled oscillator

$$\Theta'(s) = \frac{1}{s}V_{lf}(s)$$

The transfer function for phase (open-loop)

$$T_{OL}(s) = PD(s) \cdot LF(s) \cdot VCO(s) = k_{in} \frac{k_p\left(1 + \frac{1}{sT_i}\right)}{s} = \frac{k_p s + \frac{k_p}{T_i}}{s^2}$$

The transfer function for phase (closed-loop)

$$H_\theta(s) = \frac{\Theta'(s)}{\Theta(s)} = \frac{LF(s)}{s + LF(s)} = \frac{k_p s + \frac{k_p}{T_i}}{s^2 + k_p s + \frac{k_p}{T_i}}$$

The transfer function for error (closed-loop)

$$E_\theta(s) = 1 - H_\theta(s) = \frac{E_{pd}(s)}{\Theta(s)} = \frac{s}{s + LP(s)} = \frac{s^2}{s^2 + k_p s + \frac{k_p}{T_i}}$$

When $\omega_n = \sqrt{\frac{K_p}{T_i}}$ and $\xi = \frac{\sqrt{K_p T_i}}{2}$

Thus, the transfer functions in the second-order are

$$H_\theta(s) = \frac{2\xi\omega_n s + \omega_n^2}{s^2 + 2\xi\omega_n s + \omega_n^2}$$

$$E_\theta(s) = \frac{s^2}{s^2 + 2\xi\omega_n s + \omega_n^2}$$

Total Harmonic Distortion Calculation

$$THD = \frac{\sqrt{V_1 + V_2 + V_3 + V_4 + \ldots\ldots + V_n}}{V_F}$$

The internal inductance of the grid

$$L = \frac{V_{base}^2}{P_{sc}} \cdot \frac{1}{2\pi f}$$

The internal resistance R

$$R = \frac{X}{\left(X/R\right)} = \frac{2\pi f L}{X/R}$$

B.2 PID Controller

The transfer function of the PID controller used in the discrete-time models is

$$C_{id}(z) = P\left[1 + I\alpha(z) + D\frac{N}{1 + N\beta(z)}\right]$$

The α(z) and β(z) are determined by integrator and filter parameter, respectively.

The sampling time influences the performance of the effect of the P, I, D, and N coefficients of the controller.

The integral term of the controller transfer function is Iα(z), and α(z) could be determined by the following equations

$$\alpha(z) = \frac{T_s}{z-1}$$

$$\alpha(z) = \frac{T_s z}{z-1}$$

$$\alpha(z) = \frac{T_s}{2}\frac{z+1}{z-1}$$